Advances in Aero-Propulsive Modeling for Fixed-Wing and eVTOL Aircraft Using Experimental Data

Benjamin M. Simmons

Dissertation submitted to the Faculty of the
Virginia Polytechnic Institute and State University
in partial fulfillment of the requirements for the degree of

Doctor of Philosophy
in
Aerospace Engineering

Craig A. Woolsey, Chair
Eugene A. Morelli, Co-chair
K. Todd Lowe
Mark L. Psiaki

April 25, 2023
Blacksburg, Virginia

Keywords: System Identification, Flight Dynamics, Response Surface Methods, VTOL, Advanced Air Mobility, UAV, Distributed Electric Propulsion, Flight Test, Wind Tunnel

Advances in Aero-Propulsive Modeling for Fixed-Wing and eVTOL Aircraft Using Experimental Data

Benjamin M. Simmons

(ABSTRACT)

Small unmanned aircraft and electric vertical takeoff and landing (eVTOL) aircraft have recently emerged as vehicles able to perform new missions and stimulate future air transportation methods. This dissertation presents several system identification research advancements for these modern aircraft configurations enabling accurate mathematical model development for flight dynamics simulations based on wind-tunnel and flight-test data. The first part of the dissertation focuses on advances in flight-test system identification methods using small, fixed-wing, remotely-piloted, electric, propeller-driven aircraft. A generalized approach for flight dynamics model development for small fixed-wing aircraft from flight data is described and is followed by presentation of novel flight-test system identification applications, including: aero-propulsive model development for propeller aircraft and nonlinear dynamic model identification without mass properties. The second part of the dissertation builds on established fixed-wing and rotary-wing aircraft system identification methods to develop modeling strategies for transitioning, distributed propulsion, eVTOL aircraft. Novel wind-tunnel experiment designs and aero-propulsive modeling approaches are developed using a subscale, tandem tilt-wing, eVTOL aircraft, leveraging design of experiments and response surface methodology techniques. Additionally, a method applying orthogonal phase-optimized multisine input excitations to aircraft control effectors in wind-tunnel testing is developed to improve test efficiency and identified model utility. Finally, the culmination of this dissertation is synthesis of the techniques described throughout the document to form a flight-test system identification approach for eVTOL aircraft that is demonstrated using a high-fidelity flight dynamics simulation. The research findings highlighted throughout the dissertation constitute substantial progress in efficient empirical aircraft modeling strategies that are applicable to many current and future aeronautical vehicles enabling accurate flight simulation development, which can subsequently be used to foster advancement in many other pertinent technology areas.

Advances in Aero-Propulsive Modeling for Fixed-Wing and eVTOL Aircraft Using Experimental Data

Benjamin M. Simmons

(GENERAL AUDIENCE ABSTRACT)

Small, electric-powered airplanes flown without an onboard pilot, as well as novel electric aircraft configurations with many propellers that operate at a wide range of speeds, referred to as electric vertical takeoff and landing (eVTOL) aircraft, have recently emerged as aeronautical vehicles able to perform new tasks for future airborne transportation methods. This dissertation presents several mathematical modeling research advancements for these modern aircraft that foster accurate description and prediction of their motion in flight. The mathematical models are developed from data collected in wind-tunnel tests that force air over a vehicle to simulate the aerodynamic forces in flight, as well as from data collected while flying the aircraft. The first part of the dissertation focuses on advances in mathematical modeling approaches using flight data collected from small traditional airplane configurations that are controlled by a pilot operating the vehicle from the ground. A generalized approach for mathematical model development for small airplanes from flight data is described and is followed by presentation of novel modeling applications, including: characterization of the coupled airframe and propulsion aerodynamics and model development when vehicle mass properties are not known. The second part of the dissertation builds on established airplane, helicopter, and multirotor mathematical modeling methods to develop strategies for characterization of the flight motion of eVTOL aircraft. Innovative data collection and modeling approaches using wind-tunnel testing are developed and applied to a subscale eVTOL aircraft with two tilting wings. Statistically rigorous experimentation strategies are employed to allow the effects of many individual controls and their interactions to be simultaneously distinguished while also allowing expeditious test execution and enhancement of the mathematical model prediction capability. Finally, techniques highlighted throughout the dissertation are combined to form a mathematical modeling approach for eVTOL aircraft using flight data, which is demonstrated using a realistic flight simulation. The research findings described throughout the dissertation constitute substantial progress in efficient aircraft modeling strategies that are applicable to many current and future vehicles enabling accurate flight simulator development, which can subsequently be used for many research applications.

Dedication

To those who have and will tenaciously pursue advances in flight dynamics research.

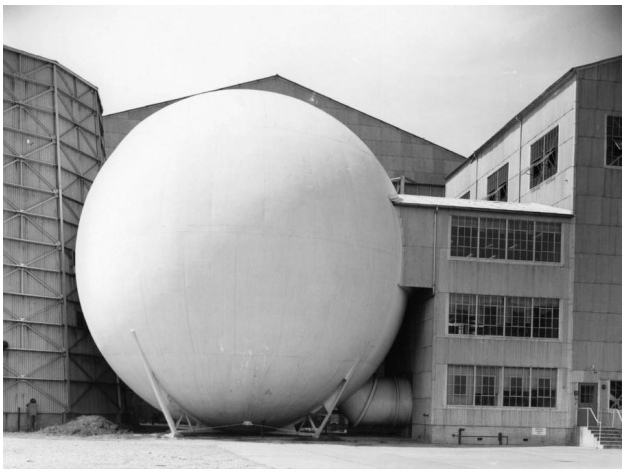

Langley 12-Foot Low-Speed Tunnel
(operation: 1939 – present)

Langley Flight Dynamics Research Facility
(construction progress: May 4, 2023)

Acknowledgments

Firstly, I would like to thank Professor Craig Woolsey for being an outstanding advisor throughout my graduate studies. Dr. Woolsey is the individual I undoubtedly credit most with guiding my research and career trajectory. I am very grateful for his subtle yet impactful persuasion for me to pursue a Ph.D. after completion of my Master's degree and his recognition of the specific benefits for me personally to pursue doctoral studies. Dr. Woolsey was very supportive of my unconventional Ph.D. track as a distance student working full-time and influentially guided my efforts to produce a successful final result. I am incredibly grateful for his commitment and time invested in my technical development, as well as his advice, mentorship, teaching, and encouragement throughout my graduate studies and this dissertation.

Next, I would like to thank Dr. Eugene Morelli for being a tremendous co-advisor throughout my Ph.D. and an extraordinary colleague at NASA. Dr. Morelli's work is what ultimately inspired me to pursue research and a Ph.D. focused on aircraft system identification. I can attribute a large majority of my knowledge of the subject to his publications, software, and courses, as well as many technical discussions we have had over the past few years. I am supremely grateful for Dr. Morelli's time and effort committed to provide mentorship, technical guidance, rigorous paper reviews, and support fostering my development as a researcher and bolstering the content presented in this dissertation.

Both Dr. Woolsey and Dr. Morelli set a phenomenal example of how to be an exceptional research leader in their respective vocations. I am very fortunate to have had the opportunity to learn from both of them and will strive to follow their examples in my career.

I would also like to thank Professors Todd Lowe and Mark Psiaki for their time and commitment invested in serving on my Ph.D. advisory committee. I am grateful for the helpful feedback they provided during my Ph.D. milestones that helped to form this dissertation and for the knowledge that I gained from their respective courses.

Thank you to additional mentors who have made a substantial impact on my academic and professional career: Roger Chang, Pat Artis, Marge Draper-Donley, Alex Kokolios, and Pat Murphy. The knowledge and skills that I learned from each of you has had a profound influence on my technical and professional development.

Thank you to all those in the Nonlinear Systems Laboratory (NSL) who have provided coursework companionship and research support during my pursuit of a Ph.D., including: James Gresham, Jeremy Hopwood, Jean-Michel Fahmi, Mekonen Halefom, Dennis Marquis, Chris Gahan, Garrett Asper, and Patrick Corrigan. In particular, thank you to James Gresham for being a phenomenal primary research and coursework collaborator throughout my doctoral studies. I am very grateful for the serendipitous opportunity presented to work

with James and combine our skill sets to advance flight-test system identification research for small unmanned aircraft. Thank you to Dr. Woolsey for facilitating these collaborations despite my geographic distance from the NSL for my doctoral studies.

Thank you to those who have helped me to thrive in my current position of a Research Engineer in the Flight Dynamics Branch at NASA Langley Research Center while pursuing this degree. Thank you to my former supervisors, Mike Fremaux and Vanessa Aubuchon, for hiring me, guiding my research focus into modeling eVTOL aircraft, and laying the foundation for me to seamlessly pursue a Ph.D while working at NASA. Thank you to my current supervisors, Corey Diebler and Tom Ivanco, for their steadfast encouragement and support of my pursuit of this degree, as well as their persistent efforts to put me in a position to succeed. Thank you to my project leadership, Steve Riddick, Irene Gregory, Mike Acheson, and Vanessa Aubuchon, for enabling and supporting a large amount of the research described in this dissertation. To that end, I am grateful for research funding support from the NASA Aeronautics Research Mission Directorate Transformational Tools and Technologies project; I am also grateful to the NASA Langley Research Center Advanced Degree Program, led by Phil Kandel, for funding my degree. Furthermore, thank you to many colleagues who have provided advice, encouragement, technical suggestions, and research support contributing to the work presented in this dissertation, including: Gene Morelli, Pat Murphy, Jake Cook, Jared Grauer, John Foster, Ron Busan, Steve Geuther, Dave North, Greg Howland, George Altamirano, Wes O'Neal, Pieter Buning, Kasey Ackerman, Tom Britton, Rosie Weinstein, David Hartman, Garrett Asper, Jason Welstead, Siena Whiteside, Nat Blaesser, Sue Grafton, David Hatke, Earl Harris, Clinton Duncan, and Lee Pollard. Additionally, thank you to former colleagues and supervisors who have substantially invested in my career and technical development: Marge Draper-Donley, Cindy Romano, Ryan Paul, John Leonard, Joe Allen, Steve Hynes, Tosh Jain, Bob Hanley, Jess Holmberg, Susan Polsky, John Walker, Rich Spadaccini, and Joan Marano-Goyco.

Thank you to my parents and family for their encouragement and support through the past few intense years of pursuing this degree and throughout my life. Lastly, and *very* importantly, thank you to my wife, Lauren, for her unwavering support and encouragement for my graduate studies, this dissertation, and all my other pursuits. I am eternally grateful for her backing of me pursuing this degree and everything she contributed to make it possible.

Contents

List of Figures

List of Tables

Nomenclature

a_x, a_y, a_z	=	body-axis translational acceleration, ft/s^2 or g
b	=	projected wingspan, ft
C_X, C_Y, C_Z	=	body-axis force coefficients
C_l, C_m, C_n	=	body-axis moment coefficients
C_T	=	propeller thrust coefficient
C_Q	=	propeller torque coefficient
$\bar{c}$	=	mean aerodynamic chord, ft
D	=	propeller diameter, ft
g	=	gravitational acceleration, ft/s^2
h_x, h_y, h_z	=	body-axis propulsion system angular momentum components, slug·ft^2/s
I_x, I_y, I_z, I_{xz}	=	aircraft moments of inertia, slug·ft^2
J	=	advance ratio
L, M, N	=	applied body-axis moments, ft·lbf
m	=	aircraft mass, slug
n	=	propulsor rotational speed, revolutions/s
p, q, r	=	body-axis angular velocity, rad/s or deg/s
$\bar{q}$	=	dynamic pressure, lbf/ft^2
S	=	wing reference area, ft^2
T	=	thrust, lbf
u, v, w	=	body-axis translational velocity, ft/s
V	=	true airspeed, ft/s
X, Y, Z	=	applied body-axis forces, lbf
x_E, y_E, z_E	=	earth-fixed position, ft
α	=	angle of attack, rad or deg
β	=	angle of sideslip, rad or deg
$\delta_{(\cdot)}$	=	control surface deflection, rad or deg
$\eta_{(\cdot)}$	=	control effector command, normalized or μs
ϕ, θ, ψ	=	Euler angles, rad or deg
ρ	=	air density, slug/ft^3

Superscripts

^{T}	=	transpose
$\dot{}$	=	time derivative
$^{-1}$	=	matrix inverse
$\tilde{}$	=	Fourier transform
†	=	complex conjugate transpose

Chapter 1

Introduction

Recent technology advancements have resulted in new aeronautical vehicles being used for a variety of missions. These aircraft include:

1. small, low-cost, unmanned aerial vehicles (UAVs) and
2. electric vertical takeoff and landing (eVTOL) vehicles.

Over the past several years, there has been a substantial increase in the accessibility and use of small unmanned aircraft for commercial, military, and research applications. Specific applications leveraging UAVs include package delivery, surveillance, imagery, and atmospheric sensing, among many others [1]. Small UAVs can also serve as low-risk surrogate research platforms to demonstrate technology intended to be used on larger aircraft. With the increasing prevalence of small, low-cost UAV operations, there is an increasing need to develop flight dynamics models characterizing their motion in flight to support tasks such as control system design, flight simulation, and airworthiness certification.

The cost and risk associated with full-scale, manned aircraft justifies the investment of significant time, resources, and experience to develop high-quality dynamic models using computational fluid dynamics (CFD), wind-tunnel testing, and flight testing. Conversely, small unmanned aircraft flight dynamics model development is often constrained by limited time and resources, as well as inherent physical challenges. Expensive wind-tunnel tests and/or CFD may not be practical for small aircraft, requiring that a model be developed only from flight data; however, small aircraft still present multiple challenges which complicate identification of an adequate model. Small, inexpensive UAVs are typically equipped with lower-quality instrumentation, which incorporates fewer, less capable sensors and therefore provides less accurate measurements. Neglecting budgetary considerations, small UAVs also have payload weight and volume constraints that prohibit the use of high-quality sensing and data acquisition systems for system identification. In any case, a costly instrumentation system defeats the purpose of a low-cost UAV. Furthermore, small UAVs are more susceptible to atmospheric disturbances, especially within the planetary boundary layer where these aircraft are often used. Additionally, compared to full-scale aircraft, small UAVs exhibit high maneuverability, large power-to-weight ratios, and lower Reynolds number aerodynamics. These attributes reduce the quality of experimental data, which in turn degrades the quality of the model that is obtained through flight-test system identification. Despite the increased challenges of model identification for small UAVs, system identification using flight data has proven to be a useful method for model development [2–10], but still required further

research to improve small UAV system identification strategies.

In parallel to small UAV advancements and integration into the national airspace, many complex distributed hybrid and electric propulsion aircraft concepts have emerged to enable future Advanced Air Mobility (AAM) transportation missions [11–16]. There are many design concepts with a variety of Urban Air Mobility (UAM) and Regional Air Mobility (RAM) mission profiles, which include vertical takeoff and landing (VTOL), short takeoff and landing (STOL), and conventional takeoff and landing (CTOL) configurations. Common characteristics of these modern aircraft include the use of many control surfaces and propulsors, as well as significant propulsion-airframe interactions.

Vehicles supporting UAM operations require precise hover and efficient cruise capabilities as well as the ability to safely transition between flight regimes. Hybrid and electric VTOL aircraft are a clear fit for this new transportation model. In general, eVTOL aircraft are a combination of traditional fixed-wing and rotary-wing aircraft leveraging certain attributes from each type of vehicle. Rotary-wing aircraft features provide the ability to takeoff and land vertically, hover, and precisely maneuver in confined areas. Longer endurance, better efficiency, and the ability to operate at high speeds is derived from fixed-wing aircraft attributes. Distributed hybrid and electric propulsion technology used in many eVTOL aircraft concepts has further broadened the traditional aeronautical vehicle design space and resulted in many unique vehicle designs. As of April 2023, Reference [16] lists 810 known eVTOL aircraft concepts.

Although the operational utility of eVTOL aircraft has great potential [17], there are several research areas to be addressed prior to introduction into a UAM environment [18]. eVTOL vehicle technical challenges include airworthiness certification, air traffic management, pilot-operator interface, handling qualities, simplified vehicle operations, contingency management, vehicle autonomy, and flight control strategies. One essential research area is accurate eVTOL vehicle aero-propulsive modeling enabling flight dynamics simulation development to support flight control system design and certification, research on practical flight operations, and many other areas, as reflected in Figure 1.1. Efficient and accurate eVTOL vehicle aero-propulsive model development, however, is largely unexplored and is challenged by several vehicle attributes, including: many control surfaces and propulsors, propulsion-airframe interactions, propulsor-propulsor interactions, high-incidence angle propulsor aerodynamics, vehicle instability, rapidly changing aerodynamics through transition, and a wide range of operational flight conditions to characterize. Compared to many conventional aircraft, eVTOL aircraft designs exhibit greater aero-propulsive complexity and many interacting factors requiring development of new testing and model development strategies. For conventional fixed-wing aircraft, the propulsion aerodynamics and airframe aerodynamics can generally be studied separately because the interaction effects are relatively small. In contrast, integrated aero-propulsive modeling is performed for eVTOL aircraft because the propulsion aerodynamics, airframe aerodynamics, and propulsion-airframe interactional aerodynamics are generally highly coupled. Thus, development of high-fidelity aero-propulsive models for eVTOL configurations is a new, critical area of research where

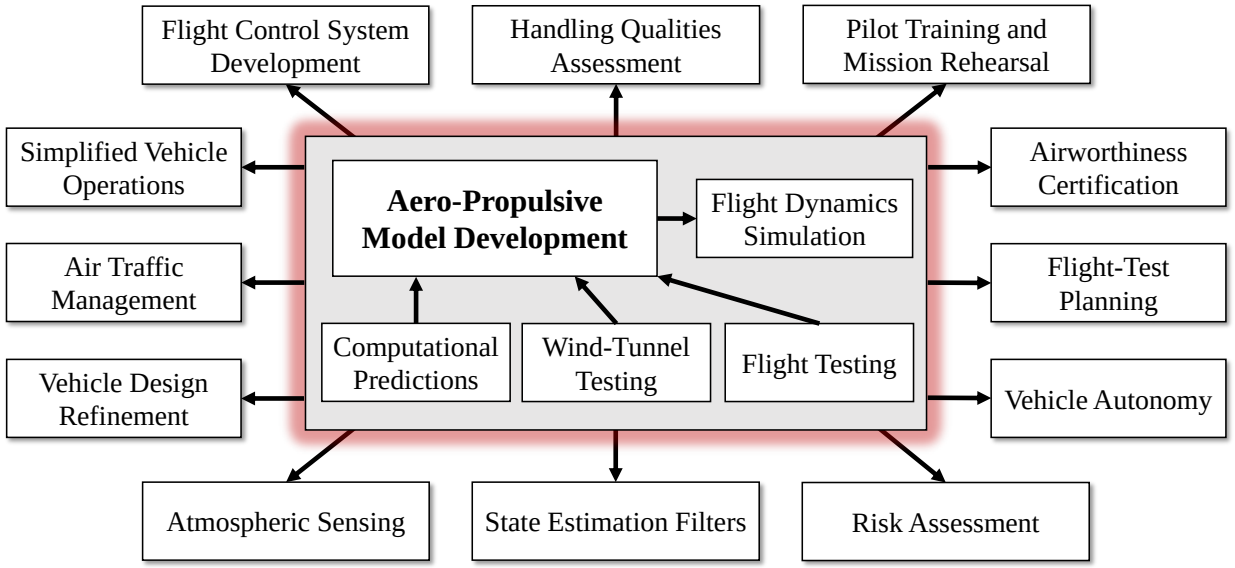

Figure 1.1: Research applications supported by accurate aero-propulsive model development.

novel modeling strategies are needed to appropriately represent pertinent aerodynamic phenomena specific to these unique vehicles.

This dissertation presents several novel flight dynamics modeling advancements for small, low-cost, remotely-piloted, fixed-wing aircraft and transitioning eVTOL aircraft using flight-test and wind-tunnel data. Consequently, the fundamental theme of the dissertation is methods used to develop aircraft mathematical models from experimental data, termed aircraft system identification [19–21]. The dissertation is organized into two parts to provide a thorough development and assessment of new system identification approaches for small fixed-wing aircraft and eVTOL aircraft. Part I focuses on advances in flight-test system identification methods developed using small, unmanned, fixed-wing aircraft. Chapter 2 presents generic flight-test system identification methods for small, fixed-wing UAVs. Chapter 3 describes aero-propulsive model development strategies for propeller aircraft. Chapter 4 develops a method for nonlinear dynamic modeling without mass properties information. The overall conclusions for Part I are summarized in Chapter 5.

Building on the material presented in Part I and established fixed-wing and rotary-wing aircraft system identification techniques, Part II concentrates on advances in eVTOL aircraft system identification. Chapter 6 develops an empirical aero-propulsive model development strategy for eVTOL aircraft using static eVTOL aircraft wind-tunnel testing conducted using design of experiments (DOE) and response surface methodology (RSM) techniques. Development of an improved response surface experiment design approach for distributed propulsion aircraft is then presented in Chapter 7. Next, Chapter 8 describes a more efficient wind-tunnel testing and novel model identification strategy leveraging dynamic programmed test input (PTI) excitations. The assortment of techniques discussed in this dissertation are

synthesized in Chapter 9 to propose a method for flight-test system identification for eVTOL aircraft, which is then demonstrated using a high-fidelity flight dynamics simulation. The overall conclusions for Part II are summarized in Chapter 10.

Research Contributions

The primary novel research contributions presented in this dissertation include:

1. Development of a generalized approach for small, fixed-wing, unmanned aircraft system identification [22] (Chapter 2).
2. Development of two aero-propulsive modeling approaches for fixed-wing aircraft with propellers using flight data [23, 24] (Chapter 3).
3. Development of a nonlinear dynamic modeling approach for aircraft without known mass properties using flight data [25, 26] (Chapter 4).
4. Development of empirical aero-propulsive modeling approaches for eVTOL aircraft using wind-tunnel data [27, 28] (Chapter 6).
5. Development, evaluation, and justification for the nested I-optimal response surface experiment design for distributed propulsion aircraft aero-propulsive modeling [29] (Chapter 7).
6. Development of a hybrid DOE/RSM–PTI wind-tunnel testing and two-step modeling approach enabling rapid wind-tunnel testing for eVTOL aircraft [30] (Chapter 8).
7. Development of a flight-test system identification strategy for transitioning eVTOL aircraft, which is demonstrated using a high-fidelity flight dynamics simulation [31, 32] (Chapter 9).

Additional novel research contributions by the author that are briefly mentioned in the dissertation include:

8. Development and assessment of a method for small aircraft system identification using a combination of flight testing and computational aerodynamic predictions [33, 34].
9. Development of an approach for modeling eVTOL aircraft propellers operating at high incidence angles [35–37].
10. Development of an efficient wind-tunnel response surface experiment design strategy for characterizing variable-pitch eVTOL aircraft propellers [38].

Furthermore, collaborative research contributions where the author has substantially contributed to the methodology development, writing, and technical-depth include:

11. Development of reduced-order model identification strategies using computational experiments for multiple applications: transitioning eVTOL aircraft aero-propulsive mod-

eling [39], propeller aerodynamic and aeroacoustic modeling [40], and bare airframe aerodynamic modeling [41].

12. Development and assessment of a remote uncorrelated pilot input (UPI) technique for unmanned fixed-wing aircraft aerodynamic modeling [42, 43].
13. Development of an approach for spin aerodynamic model identification for fixed-wing aircraft using flight data [44, 45].
14. Development of advanced wind-tunnel test techniques for eVTOL aircraft applications [30, 46].
15. Development and refinement of an automated algorithm employing DOE/RSM theory and a unique sequential modeling algorithm to identify aerodynamic models meeting specific prediction error requirements [47, 48].

Part I

System Identification for Small Fixed-Wing Aircraft

Chapter 2

Flight-Test System Identification Approach for Small, Low-Cost, Fixed-Wing Aircraft

This chapter provides an overview of a general flight-test system identification approach tailored to small, inexpensive, remote-controlled, fixed-wing aircraft that has been recently developed and refined within the Nonlinear Systems Laboratory (NSL) at Virginia Tech. The general aircraft system identification methods are outlined with details provided on the experiment design methods, instrumentation systems, flight-test operations, data processing techniques, and model identification methods enabling development of nonlinear flight dynamics models for small aircraft. Custom flight research and data processing software leveraging Pixhawk flight computers running the PX4 firmware [49] and the System IDentification Programs for AirCraft (SIDPAC) software toolbox [19, 50] are employed for system identification. Flight-test experiments are conducted using both piloted inputs and computer-generated inputs with various waveforms. The model structure and parameter estimates are determined offline using both equation-error and output-error methods supporting nonlinear model development. Specific small aircraft system identification challenges are overcome, including low-cost control surface servo-actuators and instrumentation systems, as well as a greater sensitivity to atmospheric disturbances and limited piloting cues. Four recent system identification research advancements using the general system identification process are featured in this chapter and subsequent chapters, including:

1. application of uncorrelated pilot inputs to remotely piloted aircraft [42, 43],
2. aerodynamic modeling in a spin [44, 45],
3. aero-propulsive model development for propeller aircraft [23, 24] (Chapter 3), and
4. nonlinear dynamic modeling without mass properties information [25, 26] (Chapter 4).

A significant portion of the content in this chapter will also appear in a to-be-published, invited journal article [22]. Although these methods are described in the context of fixed-wing aircraft, certain material in this chapter also applies to eVTOL aircraft model identification, as will be discussed in Part II.

The chapter is organized as follows: Section 2.1 gives an overview of the flight-test research facility, research aircraft, and flight-test operations. Section 2.2 summarizes the

general small aircraft flight-test system identification approach, followed by detailed descriptions of the techniques used for experiment design (Section 2.3), flight data collection (Section 2.4), data processing (Section 2.5), and model identification (Section 2.6). Specific flight-test system identification research advancements are featured in Section 2.7, as well as Chapter 3 and Chapter 4.

2.1 Flight-Test Research Facility, Aircraft, and Operations

This section provides an overview of the NSL flight research facilities, aircraft, and operational procedures. This infrastructure fosters an environment for rapid flight-test research advancements, including the system identification studies described throughout Part I of this dissertation.

2.1.1 Kentland Experimental Aerial Systems (KEAS) Laboratory

Flight-test research in the NSL is primarily conducted at the Kentland Experimental Aerial Systems (KEAS) Laboratory at Virginia Tech [51]. The facility hosts numerous unmanned aircraft researchers, including those affiliated with the Mid-Atlantic Aviation Partnership, the Virginia Tech steward of a Federal Aviation Administration (FAA) designated unmanned aircraft systems (UAS) test site. The KEAS Laboratory is used for a variety of flight research in areas such as system identification, flight controls, atmospheric sensing, and agricultural monitoring. The focal point of the facility is a 300 x 70 ft paved runway and a flight-test environment above an 1800-acre agricultural research facility that provides ample maneuvering airspace to perform flight testing for experimental aircraft. The KEAS Laboratory also provides hangar space that facilitates storage, flight preparation, post-flight data handling, repair work, and rapid modification for research aircraft. Internet connectivity throughout the hangar and runway area enables field updates for firmware, research code, and map data for the ground station and flight computers. Weather monitoring is available from a WeatherSTEM device [52] and a wind sock located adjacent to the runway. Furthermore, the KEAS Laboratory airspace is approximately a 20-minute drive from Virginia Tech's primary Blacksburg campus allowing research flight testing to be a part of students' and faculty members' daily schedule. Ground and aerial photographs of the KEAS Laboratory are shown in Figure 2.1.

(a) KEAS Laboratory runway and airspace

(b) KEAS Laboratory runway and hangar

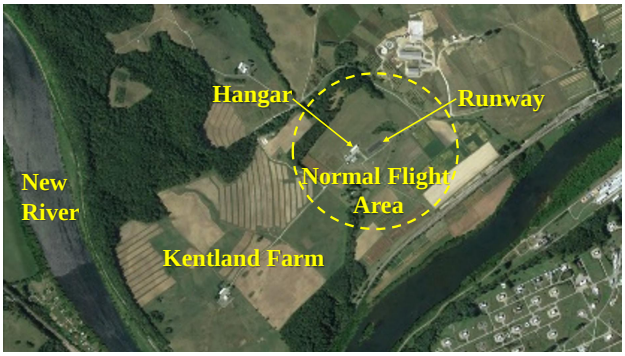

(c) Overhead view of KEAS Laboratory airspace

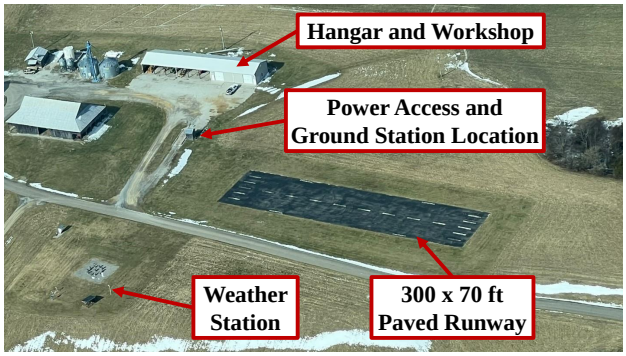

(d) Overhead view of KEAS Laboratory facilities

Figure 2.1: Photographs of KEAS Laboratory facilities and airspace.

2.1.2 Research Aircraft

The NSL aircraft used for the system identification research described in this dissertation include the off-the-shelf My Twin Dream (MTD) and Carbon-Z Cessna 150 (CZ-150), pictured in Figures 2.2-2.3. The aircraft are small, fixed-wing, remote controlled (RC) unmanned aircraft with traditional control surfaces: an elevator, ailerons, and a rudder (with deflection angles respectively denoted δ_e, δ_a, and δ_r). The MTD is powered by two electric motors that drive APC sport 10-inch diameter, 6-inch pitch, counter-rotating propellers mounted to the front of the wing. The CZ-150 has a single electric motor mounted on the front of the fuselage that drives an Aero-Naut CAM carbon folding, two-bladed, 16-inch diameter, 8-inch pitch propeller. Recent work has also been conducted in parallel to modernize Virginia Tech's custom-built electric Small Platform for Autonomous Aerial Research Operations (eSPAARO) aircraft initially developed and characterized as described in References [53–55]. The current eSPAARO aircraft, shown in Figure 2.4, has an inverted V-tail with ruddervator and aileron control surfaces. The aircraft is powered by a single electric motor mounted on the rear of the fuselage which drives an APC 22-inch diameter, 12-inch pitch pusher propeller. Compared to other NSL aircraft, the eSPAARO vehicle provides

Figure 2.2: MTD aircraft.

Figure 2.3: CZ-150 aircraft.

Figure 2.4: eSPAARO aircraft.

a larger scale research platform with a greater payload capacity for future research efforts. Geometric and inertial properties for the described NSL research aircraft, as configured for model identification, are given in Table 2.1. For each aircraft, the mass was determined using a commercial scale and the moments of inertia were determined using a compound pendulum [56].

Table 2.1: Research aircraft inertial and geometric properties

Property	MTD	CZ-150	eSPAARO	Units
m	0.211	0.336	1.40	slug
I_x	0.216	0.403	5.47	slug·ft^2
I_y	0.182	0.317	6.27	slug·ft^2
I_z	0.340	0.591	9.39	slug·ft^2
I_{xz}	0.036	0.049	0.131	slug·ft^2
$\bar{c}$	0.833	1.05	1.83	ft
b	5.91	6.97	12.0	ft
S	4.92	7.32	22.0	ft^2

The NSL research aircraft are equipped with an onboard Pixhawk flight computer used

for data acquisition and an onboard companion computer connected via Universal Serial Bus (USB) used for automated injection of control inputs for system identification and custom control law implementation [57]. The Pixhawk flight computer is a CubePilot Cube Orange flight controller [58] running PX4 firmware (version 1.11.3) [49]. The companion computer is a Raspberry Pi 4 running the Ubuntu Linux distribution which communicates with the Pixhawk using the MAVLink communication protocol [59]. The documentation and code used to implement automated system identification inputs and enable custom control law integration using the companion computer are publicly-available in an NSL GitHub repository [60]. It is worth noting that an alternative approach allowing a Simulink® model to be deployed directly onto the Pixhawk flight computer using the MathWorks® UAV Toolbox and its Support Package for PX4 Autopilots is currently being explored for system identification input injection and custom control law integration [61]; however, the implementation and utility of this alternate approach is not described further in this dissertation.

The research aircraft instrumentation package includes an attitude and heading reference system (AHRS), a pitot-static probe, and a Here+ Real-Time Kinematic (RTK) GPS receiver. Notably, the aircraft instrumentation suite lacks an air-data sensor to measure the aerodynamic angles α and β. The PX4 software includes an extended Kalman filter (EKF) used to estimate vehicle state variables, including attitude angles and Earth-relative velocity [62]. Using the EKF states to calculate signals traditionally derived from air-data sensors has been successfully applied in multiple NSL system identification efforts and is a typical approach used for NSL flight-test system identification because of its practical utility for small, low-cost aircraft system identification. The use of inertial, EKF-derived air-data signals assumes that there is no wind and, accordingly, flight testing used for model identification is only conducted in negligible wind conditions. Pulse width modulation (PWM) control signals applied to the control surface actuators are recorded and mapped to control surface deflection angles using a servo-actuator model, as will be discussed further in Section 2.5.3. The propeller rotational speed is measured by sampling a signal from the electronic speed controller (ESC) proportional to the brushless motor rotational frequency. The sample rate for the translational acceleration and angular velocity measurements is 200 Hz. The sample rate for the EKF-derived data is 100 Hz. The control effector PWM commands and the propeller rotational speed are sampled at approximately 50 Hz. Minor modifications to a Pixhawk startup file and PX4 parameters are required prior to flight testing to ensure that the desired flight data are recorded at sufficient sample rates for system identification [60]. The data processing techniques used to condition the flight data for model identification will be described later in this chapter (Section 2.5).

2.1.3 Flight-Test Operations

Flight-test operations at the NSL are conducted with meticulous pre-flight, in-flight, and post-flight procedures to ensure safe, efficient, and productive small aircraft operations for a variety of research applications. Concurrently, the low-risk operation of small unmanned

aircraft at low altitudes over university-owned farmland, along with the relatively permissive university research environment, enables rapid development and testing of new control laws and investigation of off-nominal flight conditions, such as spins. Irreparable aircraft damage, although not a desirable outcome, is accepted as a possible outcome for most NSL flight testing; injuries to people or damage to property outside of the research aircraft, however, are carefully avoided through a scrupulous safety management process. The streamlined and flexible flight-test environment stimulates rapid flight dynamics and controls research advancement.

Prior to each flight-test effort, a test plan and test matrix are developed to safely and efficiently achieve the flight-test research objectives. The National Weather Service hourly forecast [63] is used to predict wind speeds, precipitation, and visibility for test scheduling. Negligible wind, considered at or below one knot, is desired for system identification flight tests. Early morning flight testing typically provides the most benign atmospheric conditions. Prior to each day of flight testing, a detailed pre-flight briefing and aircraft inspection are conducted with an established checklist to ensure consistent thoroughness. The briefing guide, pre-flight checklist, and emergency procedures are documented in the appendix of Reference [56].

During flight testing, real-time airspace and telemetry monitoring with persistent communication between flight-test personnel are emphasized for successful testing and safe operations. The Pixhawk and RFD900+ telemetry module provide aircraft state information to a ground station laptop which is displayed with QGroundControl, a commercially available ground station software [64]. At least three flight-test personnel are desired for flight operations including a test pilot, a ground station operator, and an observer; although, flight testing can still be safely and effectively conducted with only two people present. The pilot is responsible for safely operating the aircraft, as well as activating and augmenting flight research algorithms. The ground station operator is responsible for monitoring altitude, airspeed, battery power remaining, and geographic location within the airspace, while also communicating pertinent information to the pilot via wireless headsets. Warnings and PX4 mode changes are also announced by the ground station software for the pilot and flight crew awareness. The observer is responsible for monitoring for air traffic and runway obstructions, as well as performing any extra tasks that would otherwise distract the pilot. To further reduce the risk of a UAV collision with a manned aircraft, the ground station operator monitors a display of local air traffic. The geographic display includes a local FlightAware PiAware system [65] which processes data from Automatic Dependent Surveillance-Broadcast (ADS-B) and Mode-S transponder broadcast signals. The pilot uses an aviation transceiver radio to monitor local Very High Frequency (VHF) aviation communications and communicate with airborne pilots, if required. The increased situational awareness and ability to communicate with airborne pilots are essential capabilities to reduce risk during research flights operating under an FAA UAS altitude limit waiver.

After flight testing, data logs are downloaded from the Pixhawk flight computer and uploaded to an NSL flight-test data repository for archiving and team accessibility. A corre-

sponding flight report is prepared on the same day as testing to provide an archival document of the personnel, weather, flight-test objectives and outcomes, pertinent details of each flight, and next steps. The flight report is archived alongside the data and emailed to all laboratory personnel for awareness and bookkeeping. Although the NSL flight-test operations are conducted in a university environment, the flight testing is conducted with a level of diligence and professionalism reflective of industry and government flight-test centers. Collectively, these capabilities greatly enhance flight-test safety, productivity, and data quality.

2.2 General System Identification Approach

System identification is the process of developing a useful mathematical model of a system using input and output data measured from the system [66, 67]. More specifically, aircraft system identification is the process for developing a dynamic model of an aircraft using measured input and output data collected using informative experiments [19–21]. In this portion of the dissertation, the focus is placed on the flight-test system identification process for small, fixed-wing aircraft.

2.2.1 Aircraft Equations of Motion

A standard aircraft motion model is adopted, which incorporates several simplifying assumptions [19, 68]. The aircraft is considered to be a six degree-of-freedom rigid body subject to external forces and moments due to gravity, aerodynamics, and thrust. The Earth is assumed to be flat and fixed in inertial space, where there is assumed to be no atmospheric wind and constant acceleration due to gravity. The aircraft mass m is constant, and the x–z plane is a plane of symmetry so that the I_{xy} and I_{yz} products of inertia are negligible. Thrust T is assumed to be aligned with the aircraft longitudinal axis, and rotational effects from the aircraft propulsion system are neglected (although, they are accounted for in the aero-propulsive modeling approach discussed in Chapter 3 and in Reference [24]). The translational kinematics equations are:

$$\dot{x}_E = u\cos\theta\cos\psi + v(\sin\theta\cos\psi\sin\phi - \sin\psi\cos\phi) + w(\sin\theta\cos\psi\cos\phi + \sin\psi\sin\phi) \quad (2.1)$$

$$\dot{y}_E = u\cos\theta\sin\psi + v(\sin\theta\sin\psi\sin\phi + \cos\psi\cos\phi) + w(\sin\theta\sin\psi\cos\phi - \cos\psi\sin\phi) \quad (2.2)$$

$$\dot{z}_E = -u\sin\theta + v\cos\theta\sin\phi + w\cos\theta\cos\phi \quad (2.3)$$

The rotational kinematics equations are:

$$\dot{\phi} = p + (q\sin\phi + r\cos\phi)\tan\theta \quad (2.4)$$

$$\dot{\theta} = q\cos\phi - r\sin\phi \quad (2.5)$$

$$\dot{\psi} = (q\sin\phi + r\cos\phi)\sec\theta \quad (2.6)$$

The translational dynamics equations are:

$$\dot{u} = rv - qw - g\sin\theta + X/m + T/m \tag{2.7}$$

$$\dot{v} = pw - ru + g\cos\theta\sin\phi + Y/m \tag{2.8}$$

$$\dot{w} = qu - pv + g\cos\theta\cos\phi + Z/m \tag{2.9}$$

The rotational dynamics equations are:

$$I_x\dot{p} - I_{xz}\dot{r} = L + (I_y - I_z)qr + I_{xz}pq \tag{2.10}$$

$$I_y\dot{q} = M + (I_z - I_x)pr + I_{xz}(r^2 - p^2) \tag{2.11}$$

$$I_z\dot{r} - I_{xz}\dot{p} = N + (I_x - I_y)pq - I_{xz}qr \tag{2.12}$$

2.2.2 Aerodynamic Forces and Moments

For fixed-wing aircraft, the aerodynamic forces and moments are generally expressed in nondimensional form to remove the dependence on dynamic pressure ($\bar{q} = \frac{1}{2}\rho V^2$) and aircraft scale:

$$C_X = \frac{X}{\bar{q}S},\quad C_Y = \frac{Y}{\bar{q}S},\quad C_Z = \frac{Z}{\bar{q}S},\quad C_l = \frac{L}{\bar{q}Sb},\quad C_m = \frac{M}{\bar{q}S\bar{c}},\quad C_n = \frac{N}{\bar{q}Sb} \tag{2.13}$$

When performing modeling from flight data, it is generally better to formulate the structure of the aerodynamic model in terms of C_X and C_Z as opposed to the lift coefficient

$$C_L = C_X\sin\alpha - C_Z\cos\alpha \tag{2.14}$$

and drag coefficient

$$C_D = -C_X\cos\alpha - C_Z\sin\alpha \tag{2.15}$$

because the measured angle of attack α is also required to calculate C_L and C_D, which increases measurement error [19]. Because the structure of the dynamic equations is known from physical principles, aircraft system identification involves determining explicit expressions for the nondimensional aerodynamic force and moment coefficients in terms of the state and input variables. Although the force and moment coefficients are defined as the response variables, these quantities cannot be measured directly in flight and must be inferred from other measurements and known aircraft properties [19]. The body-axis force coefficients are calculated as:

$$C_X = \frac{ma_x - T}{\bar{q}S},\quad C_Y = \frac{ma_y}{\bar{q}S},\quad C_Z = \frac{ma_z}{\bar{q}S} \tag{2.16}$$

Translational accelerometer measurements must be recorded at the aircraft center of gravity location or corrected to the aircraft center of gravity location [19, 69] to be used in Equation (2.16). The body-axis moment coefficients are calculated using the aircraft rotational

dynamics equations:

$$C_l = \frac{1}{\bar{q}Sb}\left[I_x\dot{p} - I_{xz}\dot{r} + (I_z - I_y)qr - I_{xz}pq\right] \tag{2.17}$$

$$C_m = \frac{1}{\bar{q}S\bar{c}}\left[I_y\dot{q} + (I_x - I_z)pr + I_{xz}(p^2 - r^2)\right] \tag{2.18}$$

$$C_n = \frac{1}{\bar{q}Sb}\left[I_z\dot{r} - I_{xz}\dot{p} + (I_y - I_x)pq + I_{xz}qr\right] \tag{2.19}$$

The body-axis angular accelerations ($\dot{p}$, $\dot{q}$, $\dot{r}$) within Equations (2.17)-(2.19) are calculated using smoothed numerical differentiation of the body-axis angular rates because angular accelerations are typically not measured directly, or if they are measured, the measurements are generally low quality [19, 70].

The explanatory variables used to develop a functional representation of the body-axis force and moment coefficients typically include angle of attack α in radians, angle of sideslip β in radians, dimensionless angular rates

$$\hat{p} = \frac{pb}{2V}, \quad \hat{q} = \frac{q\bar{c}}{2V}, \quad \hat{r} = \frac{rb}{2V} \tag{2.20}$$

and control surface deflection angles (e.g., δ_e, δ_a, δ_r) in radians. The dimensionless angle of attack rate

$$\hat{\dot{\alpha}} = \frac{\dot{\alpha}\bar{c}}{2V} \tag{2.21}$$

and angle of sideslip rate

$$\hat{\dot{\beta}} = \frac{\dot{\beta}b}{2V} \tag{2.22}$$

can also be included as explanatory variables to aid in modeling unsteady aerodynamic phenomena. Furthermore, the dimensionless airspeed ($\hat{V} = V/V_o$, where V_o is a reference airspeed) can be included as an explanatory variable to model airspeed effects that are not captured by the dynamic pressure scaling used to compute the force and moment coefficients. The air-data variables V, α, and β are related to the body-axis translational velocity components u, v, and w by

$$V = \sqrt{u^2 + v^2 + w^2} \tag{2.23}$$

$$\alpha = \tan^{-1}(w/u) \tag{2.24}$$

$$\beta = \sin^{-1}(v/V) \tag{2.25}$$

and:

$$u = V\cos\alpha\cos\beta \tag{2.26}$$

$$v = V\sin\beta \tag{2.27}$$

$$w = V\sin\alpha\cos\beta \tag{2.28}$$

For the aircraft system identification work described in this dissertation, the models for each response variable are expressed as nonlinear polynomial equations, reminiscent of a multivariate Taylor series expansion, in which the estimated parameters represent sensitivities of the response variables to changes in the explanatory variables or combinations of them. The selection of model terms typically reflects an assumed separation of longitudinal and lateral-directional effects, which is motivated by considerations of symmetry and empirical observations [71]. As will be seen in a later example, this assumption is relaxed in certain flight regimes that exhibit significant coupling.

2.2.3 Equations of Motion for Flight Simulation

Solutions to the nonlinear aircraft equations of motion shown in Equations (2.1)-(2.12) cannot be determined analytically and, thus, require using numerical integration algorithms. A set of first-order ordinary differential equations in state-space form

$$\dot{\boldsymbol{x}} = \boldsymbol{f}(\boldsymbol{x}, \boldsymbol{u}) \tag{2.29}$$

are needed to apply numerical integration techniques such as Runge-Kutta schemes [19, 20, 72]. Here, $\boldsymbol{x}$ is the state vector

$$\boldsymbol{x} = [x_E \quad y_E \quad z_E \quad \phi \quad \theta \quad \psi \quad u \quad v \quad w \quad p \quad q \quad r]^T$$

and $\boldsymbol{u}$ is the input vector pertaining to the particular aircraft configuration. Equations (2.1)-(2.6) are already in the correct form with a single state derivative on the left side of each equation. Assuming that the aerodynamic forces are not a function of state derivatives, Equations (2.7)-(2.9) are also in the correct form. However, Equations (2.10)-(2.12) need to be rearranged using algebraic manipulation to isolate $\dot{p}$, $\dot{q}$, and $\dot{r}$. Assuming that the aerodynamic moments are not a function of state derivatives, the rotational dynamics equations become:

$$\dot{p} = \frac{I_z L + I_{xz} N + (I_y I_z - I_z^2 - I_{xz}^2) qr + I_{xz}(I_x - I_y + I_z) pq}{I_x I_z - I_{xz}^2} \tag{2.30}$$

$$\dot{q} = \frac{M + (I_z - I_x) pr + I_{xz}(r^2 - p^2)}{I_y} \tag{2.31}$$

$$\dot{r} = \frac{I_x N + I_{xz} L + (I_x^2 - I_x I_y + I_{xz}^2) pq - I_{xz}(I_x - I_y + I_z) qr}{I_x I_z - I_{xz}^2} \tag{2.32}$$

In summary, assuming that the aerodynamic forces and moments are not a function of state derivatives, Equations (2.1)-(2.9) and (2.30)-(2.32) are in the form of Equation (2.29) and are suitable for computing solutions to the initial value problem via numerical integration. This is important for performing flight simulations and applying parameter estimation methods that required numerical integration, such as the time-domain output-error

method (see Section 2.6.1.3). Note that there is a singularity in Equations (2.4) and (2.6) at $\theta = \pm 90$ deg, which is called gimbal lock [73]. This singularity is not generally encountered in normal flight maneuvers or maneuvers used for system identification; however, if the $\theta = \pm 90$ deg condition is expected, then a formulation of the rotational kinematics equations that uses quaternions can be implemented to avoid the problem.

If the aerodynamic forces and moments within the translational dynamics and rotational dynamics equations are a function of state derivatives, then additional algebraic manipulation is needed to construct equations in the form of Equation (2.29) (i.e., writing the equations in a form where a single state derivative appears on the left side of each equation). This is, for example, necessary when the aerodynamic forces and/or moments are a function of $\dot{\alpha}$ and/or $\dot{\beta}$ to model unsteady effects. To demonstrate how this is done, assume that the model structures for C_X, C_Z, and C_m each include a linear $\hat{\dot{\alpha}}$ model term. The steady and unsteady terms can be separated as

$$C_X = C_{X_\mathrm{S}} + C_{X_\mathrm{U}} = C_{X_\mathrm{S}} + C_{X_{\dot{\alpha}}}\hat{\dot{\alpha}} \tag{2.33}$$

$$C_Z = C_{Z_\mathrm{S}} + C_{Z_\mathrm{U}} = C_{Z_\mathrm{S}} + C_{Z_{\dot{\alpha}}}\hat{\dot{\alpha}} \tag{2.34}$$

$$C_m = C_{m_\mathrm{S}} + C_{m_\mathrm{U}} = C_{m_\mathrm{S}} + C_{m_{\dot{\alpha}}}\hat{\dot{\alpha}} \tag{2.35}$$

with the "S" and "U" subscripts representing the steady and unsteady contributions, respectively. The steady components (C_{X_S}, C_{Z_S}, and C_{m_S}) are general nonlinear functions of state and control variables; the unsteady terms are:

$$C_{X_\mathrm{U}} = C_{X_{\dot{\alpha}}}\hat{\dot{\alpha}}, \qquad C_{Z_\mathrm{U}} = C_{Z_{\dot{\alpha}}}\hat{\dot{\alpha}}, \qquad C_{m_\mathrm{U}} = C_{m_{\dot{\alpha}}}\hat{\dot{\alpha}}$$

Using Equations (2.13) and (2.21), the dimensional aerodynamic forces and moment in Equations (2.7), (2.9), and (2.11) can be expressed as

$$X = \bar{q}SC_X = \bar{q}S\left(C_{X_\mathrm{S}} + C_{X_{\dot{\alpha}}}\hat{\dot{\alpha}}\right) = X_\mathrm{S} + \bar{q}SC_{X_{\dot{\alpha}}}\frac{\dot{\alpha}\bar{c}}{2V} = X_\mathrm{S} + X_\mathrm{U}\dot{\alpha} \tag{2.36}$$

$$Z = \bar{q}SC_Z = \bar{q}S\left(C_{Z_\mathrm{S}} + C_{Z_{\dot{\alpha}}}\hat{\dot{\alpha}}\right) = Z_\mathrm{S} + \bar{q}SC_{Z_{\dot{\alpha}}}\frac{\dot{\alpha}\bar{c}}{2V} = Z_\mathrm{S} + Z_\mathrm{U}\dot{\alpha} \tag{2.37}$$

$$M = \bar{q}S\bar{c}C_m = \bar{q}S\bar{c}\left(C_{m_\mathrm{S}} + C_{m_{\dot{\alpha}}}\hat{\dot{\alpha}}\right) = M_\mathrm{S} + \bar{q}S\bar{c}C_{m_{\dot{\alpha}}}\frac{\dot{\alpha}\bar{c}}{2V} = M_\mathrm{S} + M_\mathrm{U}\dot{\alpha} \tag{2.38}$$

where:

$$X_\mathrm{S} = \bar{q}SC_{X_\mathrm{S}}, \quad Z_\mathrm{S} = \bar{q}SC_{Z_\mathrm{S}}, \quad M_\mathrm{S} = \bar{q}S\bar{c}C_{m_\mathrm{S}}$$

$$X_\mathrm{U} = \frac{\bar{q}S\bar{c}}{2V}C_{X_{\dot{\alpha}}}, \quad Z_\mathrm{U} = \frac{\bar{q}S\bar{c}}{2V}C_{Z_{\dot{\alpha}}}, \quad M_\mathrm{U} = \frac{\bar{q}S\bar{c}^2}{2V}C_{m_{\dot{\alpha}}}$$

To rearrange Equations (2.7), (2.9), and (2.11) into the form of Equation (2.29), it is necessary to express $\dot{\alpha}$ in terms of the body-axis velocity states and state derivatives

$$\dot{\alpha} = \frac{u\dot{w} - w\dot{u}}{u^2 + w^2} \tag{2.39}$$

which is obtained by taking the time derivative of Equation (2.24). Inserting Equations (2.36)-(2.39) into Equations (2.7), (2.9), and (2.11) and solving for $\dot{u}$, $\dot{w}$, and $\dot{q}$ yields a form of the equations suitable for numerical integration:

$$\begin{aligned}\dot{u} = \Big[&\Big(ru^2v - qu^2w - qw^3 + rvw^2 - u^2g\sin\theta - w^2g\sin\theta\Big)m^2 \\ &+ \Big(Tu^2 + Tw^2 + X_{\mathrm{S}}u^2 + X_{\mathrm{S}}w^2 + X_{\mathrm{U}}qu^2 - X_{\mathrm{U}}puv + Z_{\mathrm{U}}quw - Z_{\mathrm{U}}ruv \\ &+ Z_{\mathrm{U}}ug\sin\theta + X_{\mathrm{U}}ug\cos\theta\cos\phi\Big)m \\ &+ X_{\mathrm{U}}Z_{\mathrm{S}}u - X_{\mathrm{S}}Z_{\mathrm{U}}u - TZ_{\mathrm{U}}u\Big] \Big/ \Big[\Big(u^2 + w^2\Big)m^2 + \Big(X_{\mathrm{U}}w - Z_{\mathrm{U}}u\Big)m\Big]\end{aligned} \tag{2.40}$$

$$\begin{aligned}\dot{w} = \Big[&\Big(qu^3 - pu^2v - pvw^2 + quw^2 + u^2g\cos\theta\cos\phi + w^2g\cos\theta\cos\phi\Big)m^2 \\ &+ \Big(Z_{\mathrm{S}}u^2 + Z_{\mathrm{S}}w^2 + Z_{\mathrm{U}}qw^2 - X_{\mathrm{U}}pvw + X_{\mathrm{U}}quw - Z_{\mathrm{U}}rvw \\ &+ Z_{\mathrm{U}}wg\sin\theta + X_{\mathrm{U}}wg\cos\theta\cos\phi\Big)m \\ &+ X_{\mathrm{U}}Z_{\mathrm{S}}w - X_{\mathrm{S}}Z_{\mathrm{U}}w - TZ_{\mathrm{U}}w\Big] \Big/ \Big[\Big(u^2 + w^2\Big)m^2 + \Big(X_{\mathrm{U}}w - Z_{\mathrm{U}}u\Big)m\Big]\end{aligned} \tag{2.41}$$

$$\begin{aligned}\dot{q} = \Big[&\Big(M_{\mathrm{S}}u^2 + M_{\mathrm{S}}w^2 - I_{xz}p^2u^2 - I_{xz}p^2w^2 + I_{xz}r^2u^2 + I_{xz}r^2w^2 + M_{\mathrm{U}}qu^2 \\ &+ M_{\mathrm{U}}qw^2 - M_{\mathrm{U}}puv - M_{\mathrm{U}}rvw - I_xpru^2 + I_zpru^2 - I_xprw^2 + I_zprw^2 \\ &+ M_{\mathrm{U}}wg\sin\theta + M_{\mathrm{U}}ug\cos\theta\cos\phi\Big)m \\ &+ M_{\mathrm{S}}X_{\mathrm{U}}w - M_{\mathrm{U}}Tw - M_{\mathrm{S}}Z_{\mathrm{U}}u - M_{\mathrm{U}}X_{\mathrm{S}}w + M_{\mathrm{U}}Z_{\mathrm{S}}u - I_{xz}X_{\mathrm{U}}p^2w \\ &+ I_{xz}Z_{\mathrm{U}}p^2u + I_{xz}X_{\mathrm{U}}r^2w - I_{xz}Z_{\mathrm{U}}r^2u - I_xX_{\mathrm{U}}prw + I_xZ_{\mathrm{U}}pru \\ &+ I_zX_{\mathrm{U}}prw - I_zZ_{\mathrm{U}}pru\Big] \Big/ \Big[I_y\Big(\big(u^2 + w^2\big)m + X_{\mathrm{U}}w - Z_{\mathrm{U}}u\Big)\Big]\end{aligned} \tag{2.42}$$

A similar process could be followed to derive forms of Equations (2.8), (2.10), and (2.12) suitable for numerical integration if Y, L, and/or N are a function of β.

2.2.4 Aircraft System Identification Process

The general process for the small aircraft system identification research described in Part I of this dissertation follows the set of steps outlined in Figure 2.5. System identification efforts are often motivated by an application that requires an accurate dynamic model, such as model-based wind estimation [74–77] or control law design [57, 78–81]. The desired model accuracy and range of applicability for the intended application set objectives for the aircraft system identification effort and can inform the specific aircraft configuration. The next step is to install any required hardware modifications and the flight-test instrumentation discussed in Section 2.1.2. Ground testing is then conducted to determine the aircraft mass

properties, geometry, and servo-actuator models. Next, a flight-test experiment is designed and conducted to excite the aircraft dynamics over the range of desired model applicability. After collecting the flight data, a series of data processing steps are used to assess the data quality and condition the measured flight data for model identification. The model structure is then determined from the measured data and model parameters within the model structure are estimated. The identified model is subsequently validated to assess its accuracy and prediction capability, as well as the adequacy of the model for its intended application. If the model is inadequate, then remedial plans are developed for additional testing that can provide the data required to identify an adequate model. If the model is deemed sufficient, then it may be used for an intended application. The following sections provide additional information on the flight-test experimentation, data processing, and model identification methods applied for NSL aircraft system identification.

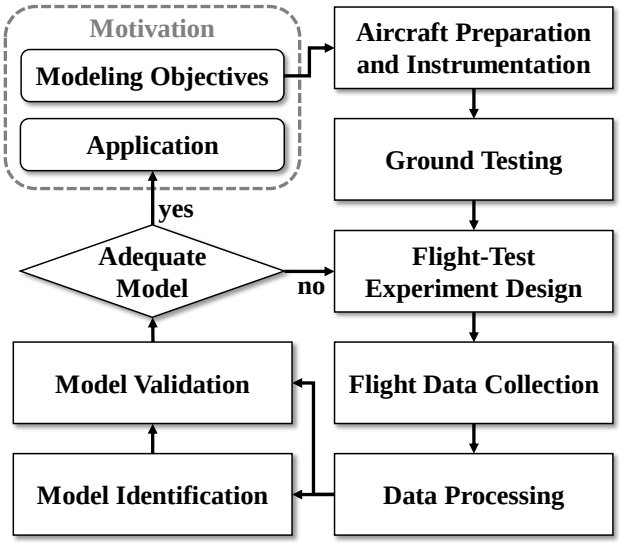

Figure 2.5: Flight-test system identification process for small unmanned aircraft.

2.3 Flight-Test Experiment Design

Specific maneuvers are used for aircraft system identification to excite the natural dynamic motion of an aircraft and facilitate collection of informative flight data for model identification [19–21]. NSL flight-test experiments have involved using several different piloted and automated input types, including multistep, multisine, and frequency sweep inputs. Sample automated system identification inputs are shown in Figure 2.6. Automated excitations are designed using the input design tools available in SIDPAC [19, 50]. For initial flight testing of a new aircraft, piloted doublet maneuvers are flown to develop preliminary estimates of the aircraft dynamic modes. The amplitude and frequency of the doublet in-

puts are adjusted in flight based on the aircraft response observed by the test pilot. The preliminary estimates of the aircraft dynamics inform the design of more complex system identification inputs discussed in the following paragraphs.

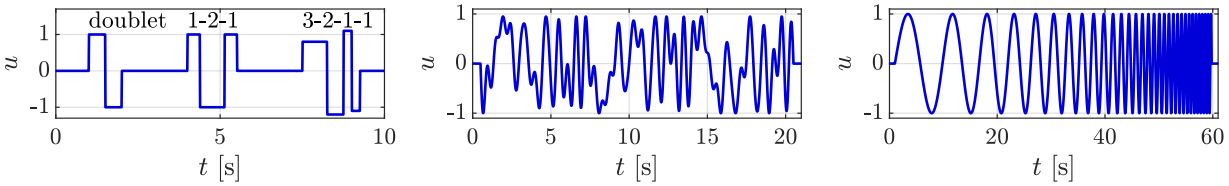

(a) Multistep inputs (b) Multisine input (c) Frequency sweep input

Figure 2.6: Sample aircraft system identification inputs.

2.3.1 Multistep Inputs

Multistep inputs are the simplest maneuver type used to collect modeling data, which include doublet (1-1), 1-2-1, and 3-2-1-1 inputs [19, 20]; the integers in these multistep input labels describe the relative time length of alternating-sign step changes in the input signal. Sample square wave multistep inputs are shown in Figure 2.6a. The elevator and rudder input step lengths are designed to excite the natural frequencies of the short period and dutch roll modes. The aileron step lengths are designed to induce a bank excitation from level flight to approximately 30 to 60 deg and back to level flight. The main advantage of multistep inputs is their implementation simplicity. A skilled pilot can implement these inputs directly and can vary the pulse widths and amplitude of the input in real-time. A computer can be programmed for repeatable automated maneuvers with *a priori* knowledge of the aircraft dynamics, and the excitation pulse widths and amplitude can be adjusted in real-time from the observed aircraft response. However, some engineering development effort is necessary to implement computer-generated inputs for a new aircraft. The quickest and easiest experiment design to gather data for modeling a new aircraft, while still providing adequate modeling results, is to execute piloted multistep inputs. Using several repeated multistep input maneuvers, preferably with different polarity and amplitude, is a good approach for obtaining adequate modeling results for small unmanned aircraft. In addition to aircraft dynamic model identification, the use of automated multistep inputs has proven to be a useful technique to develop control surface servo-actuator models in flight, which will be discussed further in Section 2.5.3.

2.3.2 Multisine Inputs

The orthogonal phase-optimized multisine input [19, 82–85] is another input type commonly used in NSL system identification flight testing. A sample multisine input is shown

in Figure 2.6b. A multisine input is defined as a sum of multiple sinusoidal functions with different amplitudes, frequencies, and phase angles, where the frequencies are chosen to encompass the frequency range corresponding to the system dynamics of interest. To make all inputs orthogonal in both the time domain and frequency domain, the multisine signal for the jth control effector is assigned sinusoids with a unique subset K_j of discrete harmonic frequency indices selected from the complete set of K available frequency indices. The available frequencies in Hz are $f_k = k/T,\ k = 1, 2, ..., K$, where T is the fundamental period and K/T is the highest excitation frequency. For m total control effectors, the jth input signal $\boldsymbol{u}_j$ is defined as

$$\boldsymbol{u}_j = \sum_{k \in K_j} A_j \sqrt{P_k} \sin\left(\frac{2\pi k \boldsymbol{t}}{T} + \phi_k\right), \quad j = 1, 2, ..., m \tag{2.43}$$

where A_j is the signal amplitude, P_k is the kth power fraction (with $\sum_{k \in K_j} P_k = 1$), ϕ_k is the kth phase angle defined on the interval $(-\pi, +\pi]$, and $\boldsymbol{t}$ is the time vector containing N discrete points. The relative peak factor (RPF), defined as

$$\text{RPF}\left(\boldsymbol{u}_j\right) = \frac{1}{\sqrt{2}} \frac{\left[\max\left(\boldsymbol{u}_j\right) - \min\left(\boldsymbol{u}_j\right)\right] / 2}{\sqrt{\boldsymbol{u}_j^T \boldsymbol{u}_j / N}} \tag{2.44}$$

is the range of input amplitude divided by the root-mean-square of the signal, referenced to the peak factor for a single frequency sinusoidal signal. An RPF value near one is preferred for system identification to prevent perturbing the system far from the reference flight condition. Minimizing RPF also approximately minimizes the peak-to-peak amplitude of the multisine signals, which keeps the rate of change low. This is beneficial for repeated dynamic use of the control surface actuators and electric motors during testing. The relative peak factor for a multisine signal is minimized by optimizing the phase angles using the simplex algorithm because the optimization problem is not convex [82]. A phase-optimized multisine signal retains the same high input energy as a signal composed of the same amplitude and frequency sinusoidal functions without optimized phase angles, while also helping to keep the system close to its nominal flight trajectory. Mutual orthogonality of different input signals is preserved regardless of the phase angles selected [19, 83]. After phase angle optimization, phase shifts are added so the periodic multisine signal starts and ends at a value of zero [85].

Because multiple inputs and all aircraft dynamics of interest are simultaneously excited, the use of multisine inputs allows execution of highly efficient and informative flight testing. A single flight maneuver can be used to develop a comprehensive aircraft dynamic model around a nominal flight condition including nonlinear aerodynamic phenomena and control interaction effects. The use of multisine inputs does, however, require an automated input injection capability, which requires initial development time and expertise to design the signals and integrate the signals into a flight computer. Another technique that maintains many of the advantages of programmed multisine inputs, but does not require the engineering development effort to integrate automated control inputs, is known as uncorrelated pilot inputs (UPI) [86–88]. This technique, adapted for application to small aircraft

system identification, will be summarized later in this chapter (Section 2.7.1). In general, computer-generated multisine inputs are the preferred input type for small aircraft system identification because of their efficiency, repeatability, rich information content, and utility for identifying nonlinear aerodynamic models.

2.3.3 Frequency Sweep Inputs

Frequency sweeps are another input type that has been used to collect data for system identification [19, 21]. A sample frequency sweep input is shown in Figure 2.6c. An automated logarithmic frequency sweep input signal covering the frequency range $[\omega_{\min}, \omega_{\max}]$ rad/s is

$$\boldsymbol{u} = A \sin\left[\omega_{\min}\boldsymbol{t} + C_2\left(\omega_{\max} - \omega_{\min}\right)\left(\frac{T}{C_1}e^{C_1\boldsymbol{t}/T} - \boldsymbol{t}\right) + \phi_0\right] \tag{2.45}$$

where $C_1 = 4$ and $C_2 = 0.0187$ are constant rule-of-thumb parameters [21]. The parameter ϕ_0 is a phase shift to make the input have a starting value of zero and the end time of the signal is adjusted to have an ending value of zero. Similar to multisine inputs, frequency sweeps excite a broad range of frequencies. In contrast to multisine inputs, frequency sweeps can only be conducted using a single control input at a time. Concurrent to the work described in this dissertation, frequency sweeps have been used for actuator characterization in ground tests, preliminary investigation of aircraft dynamics, frequency response estimation, and investigation of structural modes. However, the initial low frequency excitations coupled with the relatively high excitation amplitude needed to obtain a good signal-to-noise ratio for small aircraft, tend to perturb the aircraft away from the initial trimmed flight condition. Also, the long duration maneuvers must be executed for each axis separately, resulting in large flight-test times. Furthermore, the single-axis excitation prevents identification of control interaction effects and is not well-suited for nonlinear model identification. For these reasons, in general, using multistep or multisine inputs are preferred for small aircraft system identification.

2.4 Flight Data Collection

The NSL system identification flight testing described in this dissertation was conducted with a ground-based pilot using a Spektrum DX20 20-channel RC transmitter. The transmitter switch layout is depicted in Figure 2.7 and described further in Table 2.2. Piloted system identification excitation inputs are flown in the PX4 Manual Flight Mode, which disables feedback stabilization. Artificial stabilization is undesirable for system identification because it suppresses the natural aircraft response that the system identification maneuvers are designed to excite, distorts optimally designed control inputs, and leads to correlation between explanatory variables [19]. For automated system identification maneuvers using

programmed test input (PTI) excitations, the PX4 Offboard Flight Mode is used to allow the companion computer to inject control inputs. The input excitation signals are summed with the pilot commands so that the inputs are symmetric about the trim settings, while also allowing the pilot to make corrections if the aircraft starts to significantly deviate from the original trimmed flight condition. This method also permits the pilot to center the excitation around an unusual flight condition such as a stall or a spin, as will be discussed in Section 2.7.2.

Figure 2.7: RC transmitter programmed for system identification flight testing.

Table 2.2: RC transmitter channel descriptions for system identification flight testing

Channel	Functionality	Selection	Switch Type
1	Pilot Input	Aileron Command	Right Stick (↔)
2	Pilot Input	Elevator Command	Right Stick (↕)
3	Pilot Input	Throttle Command	Left Stick (↕)
4	Pilot Input	Rudder Command	Left Stick (↔)
5	PX4 Flight Mode	Stabilized, Manual, Offboard	3-Position Switch
6	PTI Activation	Off or On	2-Position Switch
7	PTI Mode	Input Type (See Figure 2.8)	3-Position Switch
8	PTI Submode	Input Type (See Figure 2.8)	3-Position Switch
9	Control Surface PTI Amplitude	0% to 100%	Rotary Knob
10	Propulsion PTI Amplitude	0%, 10%, or 20%	3-Position Switch

Following the development and verification of automated PTI injection capabilities, most NSL system identification flight testing has been conducted using automated inputs. As shown in Figure 2.7 and Table 2.2, multiple channels on the RC transmitter are used to conduct system identification flight testing. Figure 2.8 depicts the hierarchy of system identification flight modes. The automated system identification inputs are initiated when the

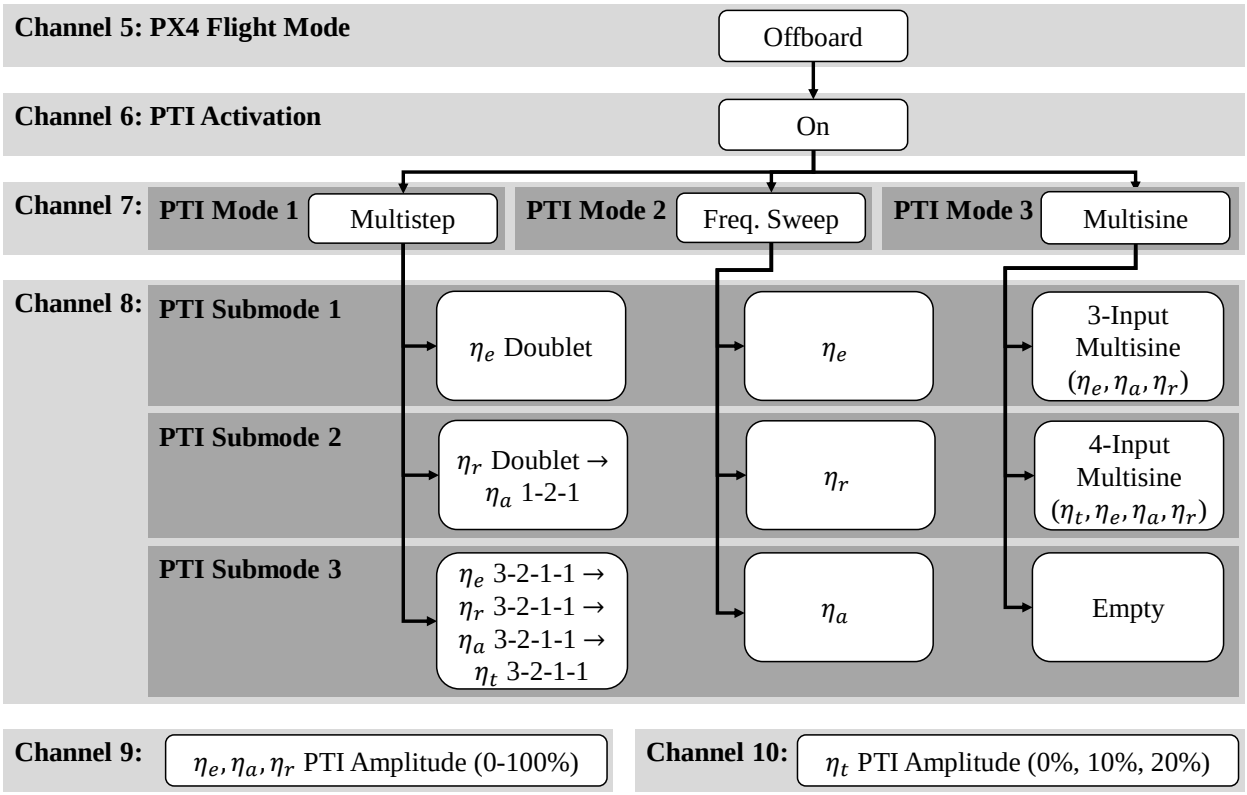

Figure 2.8: System identification PTI mode hierarchy.

PTI activation switch is engaged in the PX4 Offboard Flight Mode. The type of PTI injection is determined by the PTI mode and PTI submode, which are controlled using two different 3-position switches on the RC transmitter. There are three PTI mode options available: multistep mode, frequency sweep mode, and multisine mode. Each PTI mode then has three available submodes. For the multistep PTI mode, the submode options are (1) an elevator doublet, (2) a rudder doublet followed by an aileron 1-2-1 input, and (3) a sequence of elevator, rudder, aileron, and throttle 3-2-1-1 inputs. To provide additional input variety, the polarity of the inputs is reversed for each successive multistep input sequence. The frequency sweep submodes include elevator, aileron, and rudder sweeps. The multisine submodes include a 3-input control surface multisine design for bare airframe aerodynamic modeling and a 4-input propulsion and control surface multisine for aero-propulsive modeling. For each mode and submode, a rotary knob on the transmitter sets the control surface PTI amplitude between 0% to 100%. For a given rotary knob setting, the amplitude command for each control surface can be the same value or scaled based on the relative effectiveness and range of each control surface. An additional three-position switch is used to set the propulsion input amplitude between three discrete settings of 0%, 10%, and 20%. The PWM signal value for each channel shown in Figure 2.8 is used to implement this hierarchy in the companion computer automation code. Discrete mode settings are determined

by the channel signal being within certain PWM threshold values, and continuous amplitude settings are commanded by converting the PWM signal to normalized signals that scale the control effector commands. For parallel research efforts, the RC transmitter has also been programmed to conduct control law testing using a similar hierarchical framework.

2.5 Data Processing

Post-flight data processing is a critical step in the system identification process to condition measured flight data for model identification. The steps include smoothing data, correcting time delays, calculating unmeasured signals, and data compatibility analysis and corrections. Although tedious and often overlooked, proper signal conditioning is necessary to obtain good modeling results. A data processing methodology for system identification of aircraft equipped with the Pixhawk flight computer has been developed and refined by the author in the recent NSL system identification efforts described in this dissertation. The current version of the data processing methodology is presented in this section, which expands on the foundational methodology presented in References [33, 57].

The overall data processing objective is to convert the raw PX4 "ULog" message logging format [89] to a MATLAB® data format suitable for use with the employed system identification tools. Several other intermediate signal processing steps must be taken because the raw PX4 output measurement signals are not adequate for model development for several reasons, including: (1) message topics have different sample rates, (2) message topic sample intervals are not constant, (3) raw signals are not expressed as the state and control variables needed for modeling, (4) raw signals contain bias errors and relative time skews, and (5) the data include measurement noise. Several data processing steps are needed to provide sufficient data quality for system identification and the steps are different depending on the particular signal. The general steps are summarized in the flowchart shown in Figure 2.9. The result is processed flight data stored in an `fdata` matrix, which is the standard data format used in SIDPAC [19, 50]. Each step in the flowchart is described in the remainder of this section. A MATLAB® code, developed using MATLAB® release R2021a, implementing the steps shown in Figure 2.9 has been used for data processing for multiple NSL system identification efforts. Note that it is important to include an extra second of time at the start and end of the data being processed to be able to remove initial filter transients and numerical differentiation startup inaccuracies, as well as to shift time series. After applying the data processing steps, the extra second of time included at the beginning and end of the data is removed before performing further analysis.

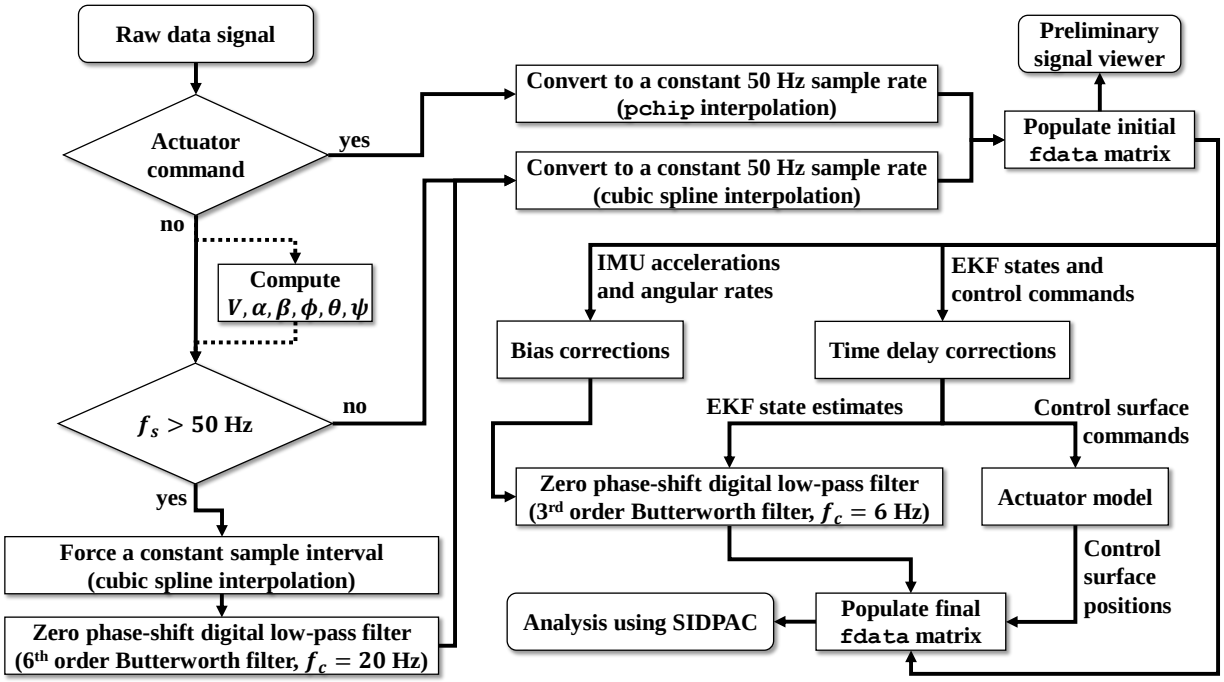

Figure 2.9: Flight data processing flowchart.

2.5.1 Data Importing, Resampling, and Formatting

The data are first imported into the MATLAB® workspace from the "ULog" format using the `ulogreader` function available in the MathWorks® UAV Toolbox [90]. The output is a "`ulogreader` object" which is then passed to the `readTopicMsgs` function to extract the data. When the Pixhawk flight computer with PX4 firmware was first flight tested in the NSL, all variants of available signals needed for flight dynamics analyses were compared to determine the best measurements and state estimates to use for post-flight system identification and real-time control applications. The signals selected for post-flight system identification are shown in Table 2.3, with modifications needed for real-time applications included in the table footer.

After the data have been imported into the MATLAB® workspace, the raw signals are converted to have a constant sample rate of $f_s = 50$ Hz. Control surface actuator command signals are converted to a 50 Hz sample rate using shape-preserving piecewise cubic interpolation [92, 93] with the `pchip` function in MATLAB® [90]. Shape-preserving piecewise cubic interpolation is preferred over cubic spline interpolation for actuator commands (which can be sharp inputs or square waves) because shape-preserving piecewise cubic interpolation tends to avoid overshoot and oscillatory behavior. Anti-alias protection is not needed for resampling the actuator commands because the PWM signals are recorded digital data that do not have wideband measurement noise. For all other measured or estimated signals, the

Table 2.3: Sources of key system identification measurements from PX4 flight data logs

Measurement Name	Source/Type	Data Field	Symbol	Default Units	Sample Rate
Body-Axis Accelerations	Accelerometers	sensor_combined	a_x, a_y, a_z	m/s^2	200 Hz
Body-Axis Angular Velocities	Rate Gyros	sensor_combined	p, q, r	rad/s	200 Hz
Earth-Fixed Velocities	EKF*	estimator_status*	V_N, V_E, V_D	m/s	100 Hz
Orientation (Quaternions)	EKF*	estimator_status*	q_0, q_x, q_y, q_z	—	100 Hz
Control Signals	PWM Signals	actuator_outputs	$\eta_e, \eta_a, \eta_r, \eta_t$	μs	50 Hz
Motor Rotational Speed	ESC	rpm	n	rpm	50 Hz
Air Density	Air Data	vehicle_air_data	ρ	kg/m^3	20 Hz

*For real-time applications, the "vehicle_local_position" and "vehicle_attitude" data fields (PX4 output predictor states) sampled at 50 Hz are used in place of "estimator_status" to reduce time delay. Further information about the PX4 EKF and output predictor algorithm can be found in References [62, 91].

data are resampled using cubic spline interpolation. If the median sample rate of the original signal is less than 50 Hz, the signal is upsampled using cubic spline interpolation directly. If the median sample rate of the original signal is greater than 50 Hz, the data are resampled to have a constant sample interval at the raw signal median sample interval, smoothed, and then downsampled to 50 Hz. This process removes higher frequency content that would cause aliasing when downsampling the data. The data are smoothed using a zero phase-shift digital filtering technique with a digital sixth-order low-pass Butterworth filter applied both forward and backward in time [94] using the `filtfilt` MATLAB® function available in the MathWorks® Signal Processing Toolbox [90]. The resampling filter cutoff frequency was selected as $f_c = 20$ Hz to provide at least -20 dB of attenuation at the Nyquist frequency of 25 Hz for the final sampling frequency of $f_s = 50$ Hz. Figure 2.10 shows the frequency response gain on a decibel and linear scale for four different initial sampling frequencies with $f_c = 20$ Hz, where it is observed that at least -23 dB of attenuation is achieved at 25 Hz for sample rates up to 1000 Hz.

Within these initial processing steps, the quaternion states are converted to Euler orientation angles, the body-axis translational velocity components are computed as

$$\begin{bmatrix} u \\ v \\ w \end{bmatrix} = \begin{bmatrix} \cos\theta\cos\psi & \cos\theta\sin\psi & -\sin\theta \\ \cos\psi\sin\theta\sin\phi - \cos\phi\sin\psi & \cos\phi\cos\psi + \sin\theta\sin\phi\sin\psi & \cos\theta\sin\phi \\ \cos\psi\sin\theta\cos\phi + \sin\phi\sin\psi & \sin\theta\cos\phi\sin\psi - \sin\phi\cos\psi & \cos\theta\cos\phi \end{bmatrix} \begin{bmatrix} V_N \\ V_E \\ V_D \end{bmatrix} \tag{2.46}$$

and the air-data signals (V, α, β) are computed using Equations (2.23)-(2.25). These equations assume that there is no wind, which is a reasonable assumption because the modeling data are deliberately collected in negligible wind conditions.

For small, low-cost aircraft, it is hypothesized that using EKF-derived air data is just as accurate, if not more accurate, than using an air-data vane or probe of reasonable cost relative to the inexpensive aircraft on a day with negligible wind. However, the use of inertial,

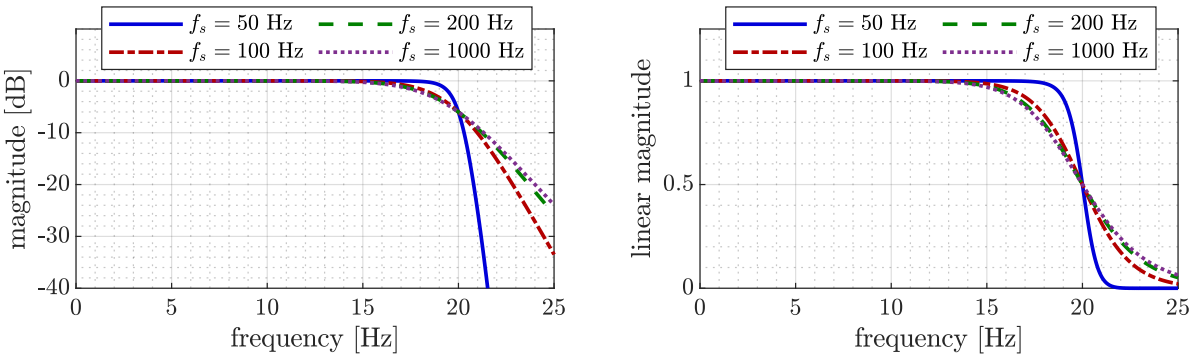

(a) Frequency response gain (dB scale)

(b) Frequency response gain (linear scale)

Figure 2.10: Comparison of the zero phase-shift digital sixth-order low-pass Butterworth filters with $f_c = 20$ Hz applied for resampling data collected with different sample rates.

EKF-derived air-data signals, as opposed to measured signals, could raise the question if these reconstructed data have sufficient accuracy for model development. As will be shown in the next subsection, the reconstructed air data derived from the EKF agree very well kinematically with the IMU measurements (as would be expected when using inertial air-data estimates on a day with negligible wind). Flight data from an MTD aircraft equipped with a developmental, low-cost air-data vane[1] used for other related research efforts was used to compare measured and reconstructed air-data signals. Figure 2.11 shows a comparison of measured and estimated angle of sideslip signals for a rudder doublet maneuver executed on a low-wind day. The signals shown on the plot are:

1. the EKF-derived angle of sideslip that would be used for system identification,
2. reconstructed angle of sideslip computed using integrated accelerometer and rate gyro measurements used to check kinematic consistency (see Section 2.5.2), and
3. airflow angle vane measurements corrected to the CG position [95].

The match between the EKF-derived and reconstructed sideslip angle are visually identical, as would be expected. The sideslip angle measured by the air-data vane is close to the EKF-derived and reconstructed signals, providing confidence that each signal is a good representation of the true sideslip angle.

After all signals are resampled and computed, the data are stored in an initial `fdata` matrix. The data at this point are examined using a strip chart viewer to determine the start and end times of each maneuver and assess maneuver quality, but further steps are needed before using the data for model development.

[1]Credit: Jeremy W. Hopwood

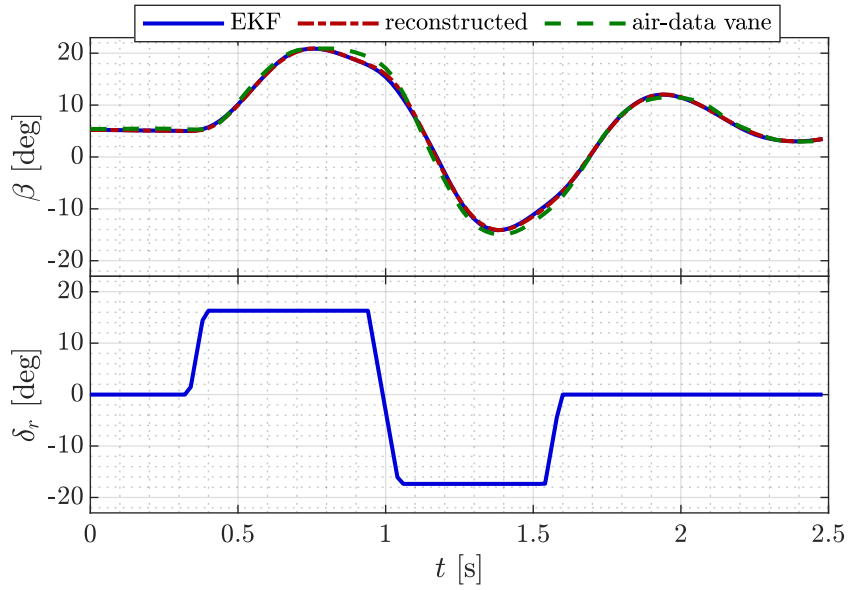

Figure 2.11: Comparison of angle of sideslip signals for an MTD rudder doublet maneuver.

2.5.2 Data Compatibility Analysis and Corrections

Data compatibility analysis is the process of validating that kinematic signals are consistent using the aircraft equations of motion. Performing model identification from kinematically inconsistent data precludes estimation of model parameters that accurately represent aircraft dynamics. Thus, ensuring that flight data are kinematically consistent is essential to obtaining useful system identification results. Kinematic consistency analysis is performed using the rotational kinematics equations [Equations (2.4)-(2.6)] and translational dynamics equations [Equations (2.7)-(2.9)] with a_x, a_y, and a_z used in place of $X/m+T/m$, Y/m, and Z/m, respectively.

Data compatibility analysis is performed using a numerical integration and/or differentiation procedure. The numerical integration method is performed by integrating Equations (2.4)-(2.9) using the body-axis translational accelerations and angular rates as inputs. Reconstructed air-data signals are subsequently calculated from the reconstructed body-axis velocity components using Equations (2.23)-(2.25). The reconstructed Euler attitude angles and air-data signals are then compared to the corresponding measured signals to assess kinematic consistency. An alternative procedure is to substitute measured Euler angles, body-axis angular rates, and body-axis velocity, as well as computed time derivatives of Euler angles and body-axis velocity, into a rearranged form of the translational dynamics and rotational kinematics equations

$$a_x = \dot{u} + qw - rv + g\sin\theta \tag{2.47}$$

$$a_y = \dot{v} + ru - pw - g\cos\theta\sin\phi \tag{2.48}$$

$$a_z = \dot{w} + pv - qu - g\cos\theta\cos\phi \tag{2.49}$$

$$p = \dot{\phi} - \dot{\psi}\sin\theta \tag{2.50}$$

$$q = \dot{\theta}\cos\phi + \dot{\psi}\sin\phi\cos\theta \tag{2.51}$$

$$r = \dot{\psi}\cos\phi\cos\theta - \dot{\theta}\sin\phi \tag{2.52}$$

to obtain the reconstructed translational accelerations and angular rates. If the reconstructed and measured signals match, then the data are kinematically consistent. If data are found to be kinematically inconsistent from this analysis, corrective measures must be taken before proceeding in system identification analysis. Potential errors may include bias errors in translational acceleration and angular rate measurements, bias errors and scale factor errors in Euler attitude angles and air-data signals, and errors in acceleration and air-data signals from not correcting for sensor locations relative to the aircraft center of gravity (CG) [19]. Additionally, time skews between measurements corrupt the system identification analysis [96], because parameter estimation methods assume that all signals are sampled at the same time [97].

The necessary data compatibility corrections made for data recorded by the Pixhawk flight computer include correction of bias in the translational accelerations and angular rates measurements, correction for time delays in Euler angles and air-data signals, and correction for time delays in control signals as a part of servo-actuator models (see Section 2.5.3). Scale factors and biases in Euler angles and air-data signals are also usually considered in data compatibility corrections [19]; however, these states obtained from the PX4 EKF do not have this deficiency. The acceleration and angular rate biases are corrected by subtracting the median difference between the measured and reconstructed signals. Time lags for aircraft states are estimated visually by comparing measured signals and reconstructed signals used for data compatibility analysis, but they could also be determined by finding the peak of the cross-correlation function between signals or modeling the time delay parameter using the frequency-domain approach described in Reference [97]. Translational acceleration and angular rate signals are generally acquired from the same data stream, making their time stamps a good grounding value [97]. For NSL aircraft, the instrumentation system inertial measurement unit (IMU) is secured at the aircraft CG, so position corrections are not necessary. Placing the IMU at the aircraft CG is generally straightforward for electric aircraft that have constant mass properties (as is the case for the NSL aircraft).

Figure 2.12 shows example CZ-150 data compatibility analysis plots for multistep maneuvers and a spin maneuver with multisine excitations active. The plots display corrected flight data used for system identification analysis, raw data obtained from the instrumentation system, and reconstructed signals computed from other measurements as described previously, to confirm validity of the kinematic consistency corrections. The corrected measured signals and reconstructed signals agree well, indicating that the data have been sufficiently conditioned for model identification.

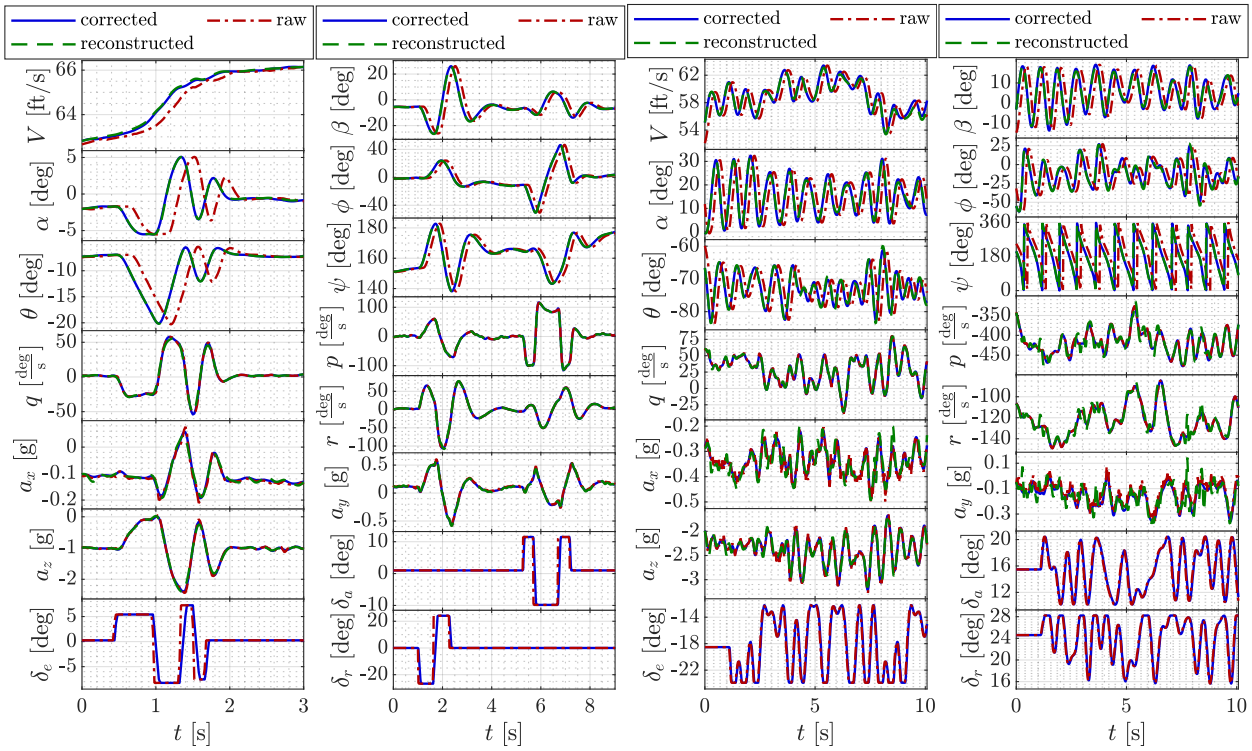

(a) Elevator 3-2-1-1 (b) Rudder 1-1, Aileron 1-2-1 (c) Spin maneuver with multisine inputs

Figure 2.12: Comparison of measured CZ-150 flight data to reconstructed signals for data compatibility assessment.

2.5.3 Control Surface Servo-Actuator Model

Small, low-cost aircraft are generally not instrumented to measure control surface deflection angles directly. Consequently, control surface servo-actuator characterization from ground and flight testing is performed to develop static and dynamic servo-actuator models. The static actuator model relates the PWM command, η, to the control surface deflection angle after all transients have ended, which is referred to as the commanded deflection angle, ξ. The dynamic actuator model describes the actuator dynamic response to changes in the commanded deflection angle to compute the control surface deflection angle, δ. A block diagram for the actuator model is shown in Figure 2.13. Development of an accurate model to predict control surface deflections is important because parameter estimation methods commonly used for aircraft system identification assume that the control inputs are known without error.

The ground testing used to develop the static and dynamic actuator models consists of cascaded square wave pulses of 10 different amplitudes applied to each control surface, as shown in Figure 2.14. Frequency sweep and multisine inputs are also useful for establish-

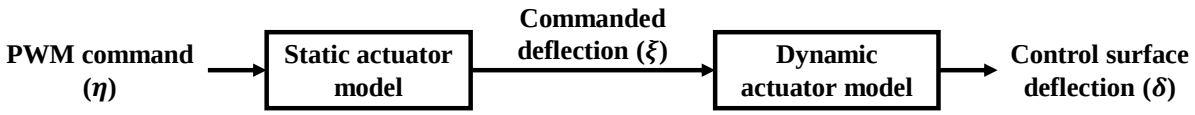

Figure 2.13: Control surface servo-actuator model block diagram.

ing a baseline understanding of actuator characteristics (although, the reader is cautioned against applying multisine inputs with frequency components well above the actuator break frequency because persistent high-frequency excitation can damage the actuator). Actuator ground testing is performed using the same Pixhawk flight computer used in flight as the measurement device. The Pixhawk is affixed to each individual control surface using double-sided foam adhesive tape, as shown in Figure 2.15. This approach has been proven on multiple aircraft to be both resourceful and accurate. The strategy requires no additional sensors than are used in flight testing, which is useful for characterizing low-cost aircraft systems; the strategy is also more accurate than using a protractor. Additionally, because the Pixhawk flight computer is used as the measurement device, the method allows for accurate characterization of time delays relative to other signals measured by the Pixhawk. Note that, visually, the presence of the Pixhawk on the control surface appears to have a negligible effect on the actuator dynamics (especially relative to the change in the actuator dynamic response expected under aerodynamic loading in flight).

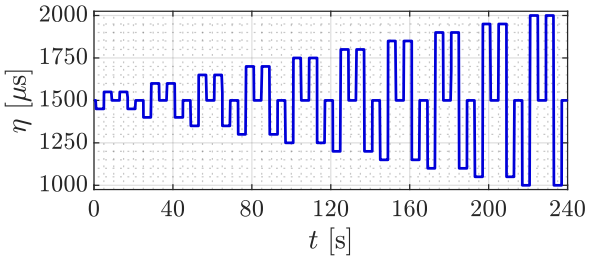

Figure 2.14: Cascaded square wave control surface servo-actuator input for ground testing.

The angular velocity signal about the axis of control surface rotation is integrated to reconstruct the deflection angle. The EKF orientation angle estimate about the axis of rotation is also available from the Pixhawk data log, however, these signals appeared to be flawed due to the abnormal use of the measurement hardware out of its intended application and were discarded for analysis. The measured angular velocity signal generally contains a small bias error, which results in the integrated deflection angle signal drifting over time. Because all control surface inputs start and end at zero deflection, the trend of the numerically integrated signal is removed, so that the starting and ending deflection angles are both zero. The detrended signal is considered the measured output used for a sequential optimization procedure leveraging the output-error parameter estimation method (see Section 2.6.1.3) to correct the angular velocity bias since there is no measured position signal available. This procedure yields an accurate deflection angle solution. The process

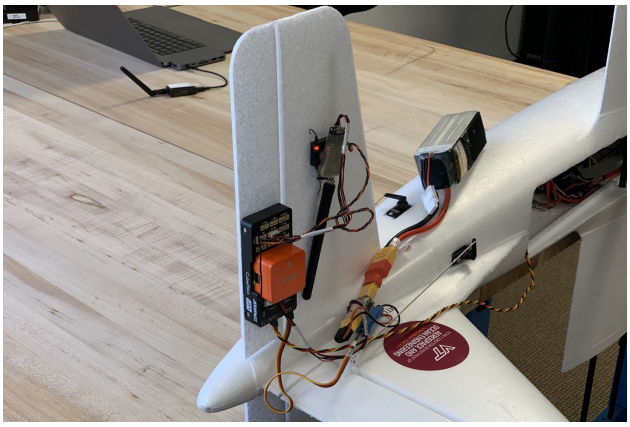

Figure 2.15: Pixhawk affixed to the MTD elevator for servo-actuator characterization ground testing.

is reflected in Figure 2.16 for an MTD rudder square wave input. The bias in the rudder deflection rate $\dot{\delta}_r$ measurement (i.e., the Pixhawk angular velocity measurement along the axis of rotation) appears small, but clearly affects the reconstructed deflection angle δ_r. This procedure was performed independently for each doublet square wave input to estimate a deflection angle signal used to identify both the static and dynamic actuator models.

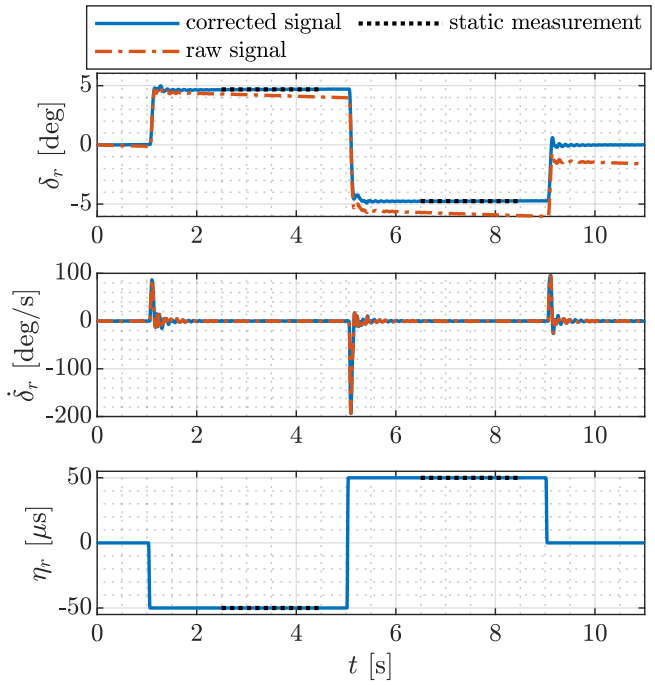

Figure 2.16: MTD rudder response to a square wave input in ground testing.

2.5.3.1 Static Actuator Model

The static actuator model is developed as a polynomial mapping between the PWM command sent to the actuator, η, and the commanded control surface deflection angle, ξ. Deflection angle data are taken as an averaged value from the static portions of each square wave pulse, as shown in Figure 2.16. A polynomial model is then fit to the data to characterize the relationship between PWM command and deflection angle. The polynomial model order is determined using the data taken from a particular control surface actuator using statistical metrics and analyst judgment. The data used to develop the deflection angle mapping and the polynomial model for an MTD rudder and eSPAARO aileron control surface are shown in Figure 2.17, where close model fits are observed. This process is repeated for each individual control surface on each aircraft.

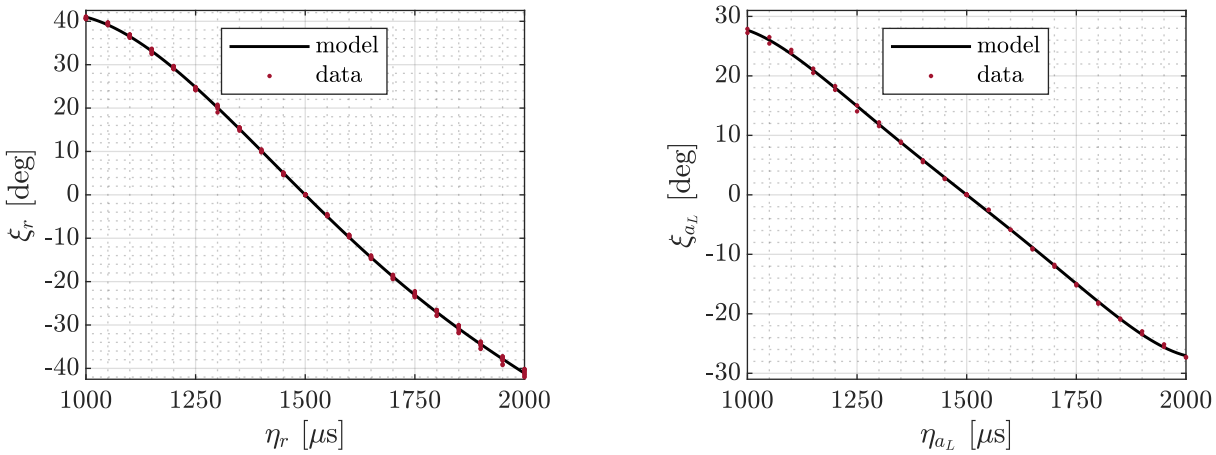

(a) MTD rudder

(b) eSPAARO left aileron

Figure 2.17: Sample static control surface servo-actuator data and model fit.

2.5.3.2 Dynamic Actuator Model

Two dynamic model forms were investigated to characterize the dynamic response of control surface servo-actuators. The first model is a linear first-order dynamic model with a pure time delay. The transfer functions is

$$\delta(s) = \frac{e^{-\tau_0 s}}{\tau_1 s + 1}\xi(s) \tag{2.53}$$

where τ_0 is the time delay and τ_1 is the first-order time constant. The second model consists of a rate limit and a pure time delay, which is a nonlinear model.

The parameters in the dynamic servo-actuators models were identified using both ground testing and flight testing. For ground testing, the commanded deflection angle, ξ, is the input and the reconstructed deflection angle, δ, is the output. The model parameters are optimized to determine the values that minimize the mean squared error between the deflection angle data and the modeled deflection angle. The parameter values for each control surface dynamic model are taken to be the averaged values computed across the range of amplitudes tested.

Example dynamic modeling results for an MTD control surface are shown for the first-order dynamics model in Figure 2.18a and for the rate limit model in Figure 2.18b. The model fit for both model forms are good; however, the rate limit model is observed to have a superior visual model fit demonstrated by the modeling residuals shown on the lower subplot and the closer model fit in the transient regions seen in the magnified portion of the plot. It has also been noted that the estimated first-order model time constant parameter increases with increasing input amplitude, whereas the estimated rate limit parameter is generally constant across the range of input amplitudes tested. Furthermore, it has been observed that the estimate of the time constant parameter and the time delay parameter are somewhat confounded, whereas the rate limit parameter and time delay parameter are decoupled. These results suggest that the rate limit model is a more accurate representation of the physical electric servo-actuator behavior which typically exhibits a trapezoidal response to step commands. Although a linear dynamics model is more convenient for controller design and tuning, the rate limit model appears to be a better representation when the objective is to most accurately estimate control surface deflection angles, and thus, is the preferred model for system identification. For this reason, the rate limit model is used as the dynamic control surface servo-actuator model henceforth in Part I.

Another example of dynamic modeling results from ground testing is shown for an eS-PAARO aileron control surface in Figure 2.19, where the rate limit model is seen to accurately predict the deflection angle. The lower subplot in Figure 2.19 also shows that use of only the commanded deflection angle results in significant error compared to the measured deflection angle near step changes, highlighting the importance of using the dynamic model.

Although the dynamic actuator characterization ground experiments yield good initial models, the actuator dynamics typically change under aerodynamic loading in flight. Consequently, characterization of control surface actuator dynamic behavior using flight data leads to improved actuator models. To characterize the actuator dynamic response in flight, the rate limit model parameters are estimated alongside an aerodynamic model identified using single-axis multistep maneuvers. The actuator dynamics for each control surface are identified separately using a model for the response variable where the control surface influence is most prominent. For example, the aileron actuator model is identified with the nondimensional aerodynamic rolling moment (C_l) response. Actuator model parameters are optimized to obtain minimum mean squared error between the measured and modeled response variable. The aerodynamic model structure can be fixed, or updated using an automated model structure selection procedure for each set of actuator model parameter

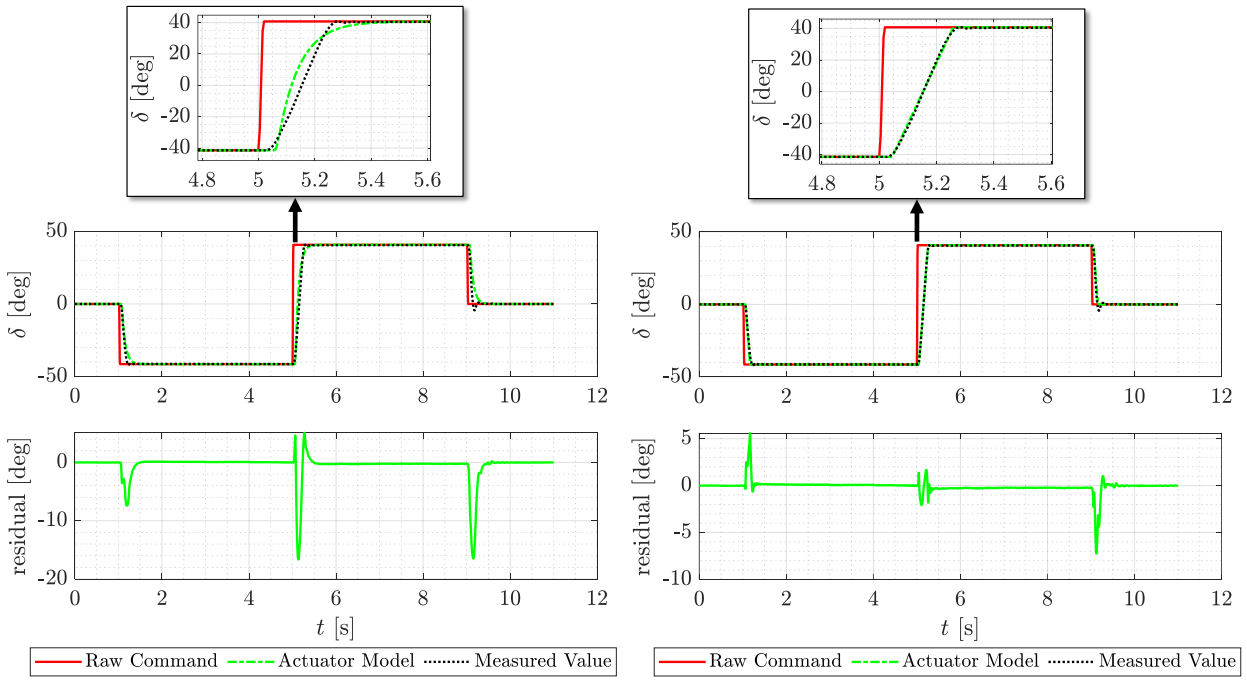

(a) First-order dynamics model (b) Rate limit model

Figure 2.18: MTD actuator command and modeled actuator response compared to the measured deflection angle.

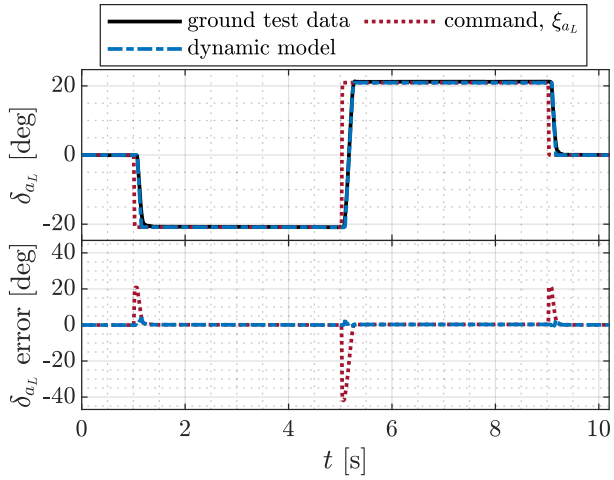

Figure 2.19: Modeled eSPAARO left aileron actuator response compared to the measured deflection angle.

values (see Section 2.6.2). Figure 2.20 shows example results for dynamic actuator modeling for the eSPAARO aileron using flight data. The C_l flight data are compared to a linear C_l aerodynamic model estimated with a dynamic actuator model identified from flight data

and using the uncorrected commanded aileron deflection. The C_l modeling residuals and δ_a deflection angles for each model are also shown. Clearly, the C_l model fit is much better when the dynamic actuator model is included, demonstrating the importance of identifying an accurate dynamic actuator model.

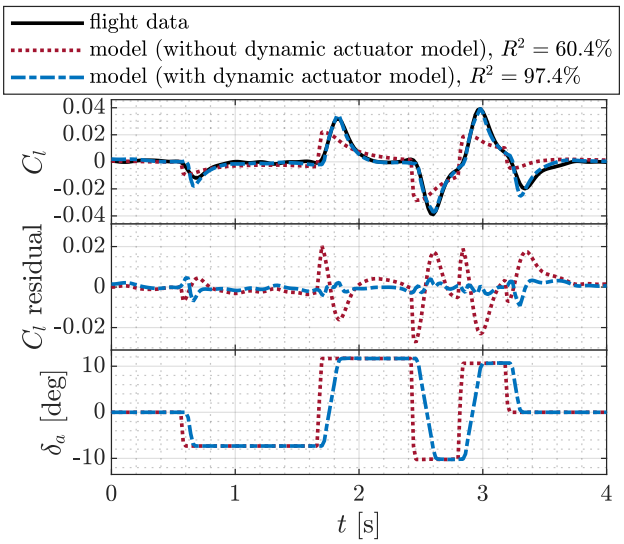

Figure 2.20: Modeled eSPAARO C_l response with and without an aileron dynamic servo-actuator model.

The ground-test and flight-test dynamic actuator modeling results using the rate limit model for the eSPAARO aileron are compared in Table 2.4, including the mean parameter value $\hat{\theta}$ and the standard deviation s estimated from several repeated dynamic actuator characterization experiments. The flight derived model has a slower rate limit and a shorter time delay. These general trends have been observed for multiple small aircraft and are attributed to the control surfaces being under persistent aerodynamic loading in flight. The dynamic actuator model identified using flight data serves as the final dynamic model for each actuator.

Table 2.4: Comparison of dynamic aileron servo-actuator model parameters for the eSPAARO aircraft

	Time Delay [s]	Rate Limit [deg/s]
Method	$\hat{\theta} \pm s$	$\hat{\theta} \pm s$
Ground Testing	0.0683 ± 0.0051	235 ± 19
Flight Testing	0.0462 ± 0.0030	178 ± 21

2.5.4 Data Smoothing

After all above steps are completed, the flight data, excluding the control surface signals, are smoothed by applying a third-order Butterworth filter both forward and backward in time [94] using the `filtfilt` function in MATLAB® [90]. Measured flight data contain noise, which can compromise the accuracy of system identification. Smoothing helps satisfy the assumed noise characteristics of data used for time-domain parameter estimation [19, 20]. Additionally, it is best to smooth data before performing numerical differentiation, which is required to compute analysis signals such as the body-axis angular accelerations [19]. A cutoff frequency of $f_c = 6$ Hz is used to preserve lower frequency information needed for modeling, but also to reject most higher frequency noise. The zero phase-shift nature of digital smoothing allows a lower cutoff frequency, and thus further noise attenuation, without distorting the deterministic information content used for modeling.

A comparison of the zero phase-shift digital third-order low-pass Butterworth filter and a global optimal Fourier smoothing technique [19, 98] with a cutoff frequency of $f_c = 6$ Hz applied gradually using a Wiener filter is shown in Figure 2.21. Figures 2.21a-2.21b compare the frequency response gain on a decibel and linear scale, where it is observed that the gain variation with frequency and roll-off characteristics are very similar. Phase is not shown because there is no phase lag across the frequency range for both the zero phase-shift digital filter and the global optimal Fourier smoother. The absence of phase lag distinguishes the digital smoothing techniques from a digital filter that is applied only forward in time. Figure 2.21c shows the frequency response gain on a linear scale zoomed in near the passband, where it observed that both smoothers have a flat passband with no ripple. Figure 2.21d shows that the step response for each smoother is visually identical.

The intent of Figure 2.21 is to show that the selected zero phase-shift digital low-pass Butterworth filter has very similar smoothing character compared to the global optimal Fourier smoother [19, 98] with a specified cutoff frequency of $f_c = 6$ Hz applied gradually using a Wiener filter.[2] This analysis helps to justify using the selected digital smoother design based on its similarity in performance to the global optimal Fourier smoother, which has been successfully applied in many previous aircraft system identification efforts. The main reason the Butterworth smoother approach was used for this work was for computational speed when batch processing full flights. This approach is faster because it used the built-in MATLAB® `filtfilt` function. Both techniques are excellent smoothers and the use of either smoothing approach will result in practically the same modeling results.

After completing all data processing steps, the data are stored in an updated `fdata` matrix and then used to perform model identification.

[2]Note that `smoo`, the function in SIDPAC [19, 50] that implements the global optimal Fourier smoother, also has options to automatically determine the cutoff frequency based on the data and apply an ideal (sharp) filter cutoff, which are features that are not available in `filtfilt`.

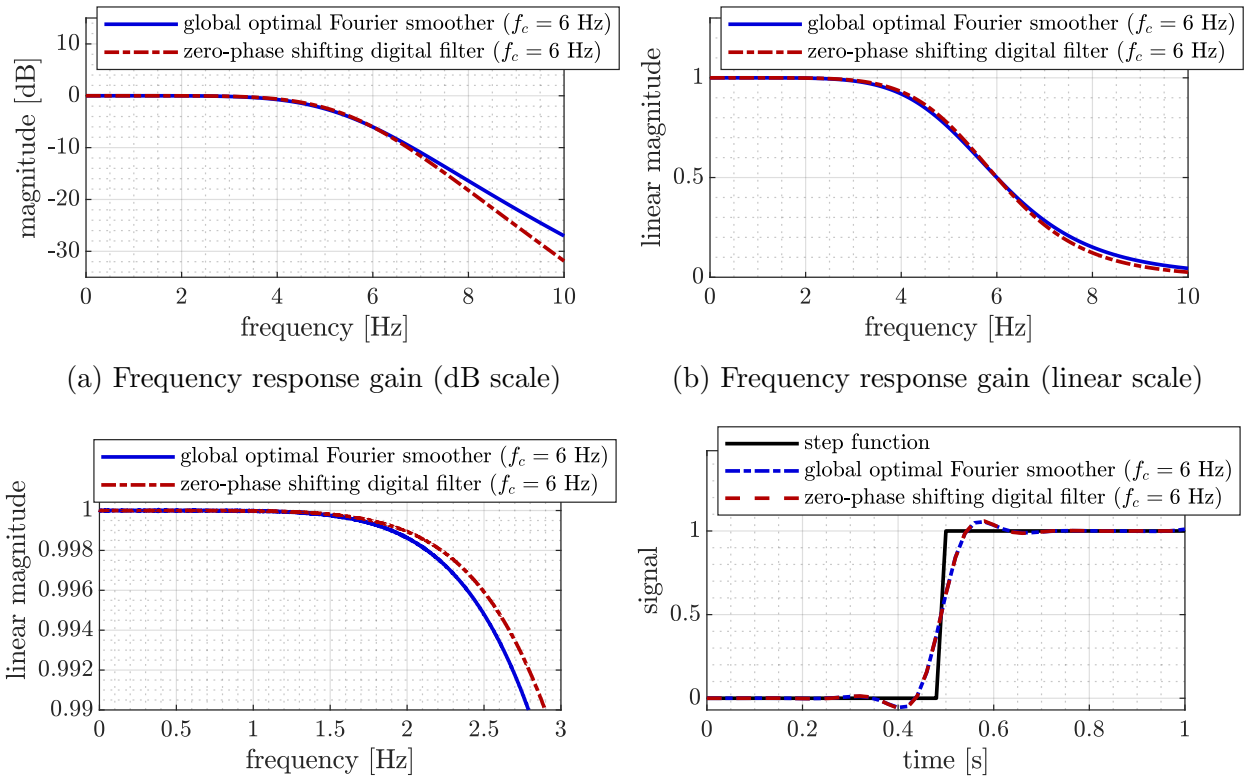

(a) Frequency response gain (dB scale)

(b) Frequency response gain (linear scale)

(c) Passband frequency response gain (linear)

(d) Step response

Figure 2.21: Comparison of the zero phase-shift digital third-order low-pass Butterworth filter and the global optimal Fourier smoother [19, 98].

2.6 Model Identification

The model identification process commences after flight data have been acquired and conditioned, and involves developing an adequate model structure for each response variable, estimating model parameters, and validating the identified model. Model identification methods that support nonlinear model development are employed for NSL aircraft because of the desire to characterize a broad range of aerodynamic conditions. Also, as a result of the challenges discussed in Chapter 1, small aircraft require large control inputs to obtain sufficient signal-to-noise ratios for model identification, which generally perturbs the aircraft to the extent that nonlinear aerodynamic phenomena are exhibited. The model structure identification and parameter estimation methods used in this work were adapted from the SIDPAC software toolbox [19, 50]. A comprehensive description of these techniques, among other system identification methods, is given in Reference [19].

2.6.1 Parameter Estimation

The parameter estimation methods used for this dissertation include the equation-error method formulated in the time domain and frequency domain, as well as the output-error method in the time domain [19]. Each of these parameter estimation methods supports identification of nonlinear models and has unique utility for different modeling problems. These methods provide a parameter estimation solution, but an adequate model structure must be assumed or determined to obtain a good model. The following subsection (Section 2.6.2) discusses model structure determination methods built on the equation-error methods discussed in this section.

2.6.1.1 Time-Domain Equation-Error Method

The time-domain equation-error method can be applied using ordinary least-squares regression to estimate a vector $\boldsymbol{\theta}$ of n_p unknown model parameters for a given model $\boldsymbol{y} = \boldsymbol{X\theta}$ [19]. Here $\boldsymbol{y}$ is the length N model response vector and $\boldsymbol{X}$ is a $N \times n_p$ matrix consisting of column vectors of regressors assumed to be measured without error. The regression equation, including a measurement of the response variable $\boldsymbol{z}$, corrupted by constant variance, zero-mean, and uncorrelated measurement error $\boldsymbol{\nu}$, is:

$$\boldsymbol{z} = \boldsymbol{X\theta} + \boldsymbol{\nu} \tag{2.54}$$

For least-squares parameter estimation, the optimal estimate of the unknown parameters $\boldsymbol{\theta}$ is determined by minimizing the cost function:

$$J(\boldsymbol{\theta}) = \frac{1}{2}\left(\boldsymbol{z} - \boldsymbol{X\theta}\right)^T\left(\boldsymbol{z} - \boldsymbol{X\theta}\right) \tag{2.55}$$

For fixed-wing aircraft system identification, the method generally minimizes the difference between the aerodynamic force and moment coefficients computed from flight-test data and those predicted by the mathematical model. The optimal estimate of the unknown parameters is:

$$\hat{\boldsymbol{\theta}} = \left(\boldsymbol{X}^T\boldsymbol{X}\right)^{-1}\boldsymbol{X}^T\boldsymbol{z} \tag{2.56}$$

Assuming uncorrelated measurement errors and that an adequate model structure is used to compute a modeled response $\hat{\boldsymbol{y}} = \boldsymbol{X}\hat{\boldsymbol{\theta}}$, a length n_p vector of standard errors $\boldsymbol{s}(\hat{\boldsymbol{\theta}})$ corresponding to the estimated parameters $\hat{\boldsymbol{\theta}}$ is:

$$\boldsymbol{s}(\hat{\boldsymbol{\theta}}) = \sqrt{\left(\frac{\left(\boldsymbol{z} - \hat{\boldsymbol{y}}\right)^T\left(\boldsymbol{z} - \hat{\boldsymbol{y}}\right)}{N - n_p}\right)\operatorname{diag}\left[\left(\boldsymbol{X}^T\boldsymbol{X}\right)^{-1}\right]} \tag{2.57}$$

where "diag( )" indicates the column vector of diagonal elements of a square matrix. Because modeling residuals are typically colored when using flight data, a modified form of Equation (2.57) is needed to compute a more accurate estimate of parameter uncertainty [19, 99].

As an example of the setup of an equation-error estimation problem, consider the following pitching moment coefficient model structure:

$$C_m = C_{m_\alpha}\alpha + C_{m_q}\hat{q} + C_{m_{\delta_e}}\delta_e + C_{m_{\alpha^2}}\alpha^2 + C_{m_{\alpha\delta_e}}\alpha\delta_e + C_{m_o}$$

To apply least-squares regression with N total data points collected from an informative experiment, the measured response vector is

$$\boldsymbol{z} = \begin{bmatrix} C_m(1) & C_m(2) & \dots & C_m(N) \end{bmatrix}^T$$

the regressor matrix is

$$\boldsymbol{X} = \begin{bmatrix} \alpha(1) & \hat{q}(1) & \delta_e(1) & \alpha^2(1) & \alpha(1)\delta_e(1) & 1 \\ \alpha(2) & \hat{q}(2) & \delta_e(2) & \alpha^2(2) & \alpha(2)\delta_e(2) & 1 \\ \vdots & \vdots & \vdots & \vdots & \vdots & \vdots \\ \alpha(N) & \hat{q}(N) & \delta_e(N) & \alpha^2(N) & \alpha(N)\delta_e(N) & 1 \end{bmatrix}$$

and the vector of $n_p = 6$ unknown model parameters is:

$$\boldsymbol{\theta} = \begin{bmatrix} C_{m_\alpha} & C_{m_q} & C_{m_{\delta_e}} & C_{m_{\alpha^2}} & C_{m_{\alpha\delta_e}} & C_{m_o} \end{bmatrix}^T$$

The parameter estimates and corresponding standard errors can then be determined using Equation (2.56) and Equation (2.57), respectively.

The equation-error method applied in the time domain is advantageous for its simplicity and computational efficiency for processing longer-duration, high-amplitude flight maneuvers, enabling rapid investigation of model structures. The equation-error method is also a maximum likelihood estimator if the regressors are error-free and the response variable is corrupted by white, Gaussian, constant variance measurement noise [19]. However, one principal disadvantage of the equation-error method is the assumption that the regressors are known perfectly, which is always violated when using experimental flight data and results in biased parameter estimates [19, 70]. Fortunately, parameter estimation biases encountered using least-squares regression can be mitigated by smoothing the explanatory variables before performing model identification. This strategy results in equation-error parameter estimates that are similar in accuracy to parameter estimates obtained using the output-error method [70]. As discussed in Section 2.5.4, the flight data used for model identification are smoothed using a zero phase-shift digital filtering technique [90, 94]. This approach effectively smooths the modeling data and results in unbiased parameter estimates.

2.6.1.2 Frequency-Domain Equation-Error Method

The equation-error method can also be formulated in the frequency domain using ordinary least-squares regression with the complex regressor and response data [19, 70, 100]. To

apply the frequency-domain modeling technique, the regressor and response variable data are first detrended; subsequently, the data are transformed into the frequency domain using a Fourier transform technique leveraging time-domain cubic interpolation and the chirp-z transform to produce a high-accuracy transform with an arbitrary frequency range and resolution [19, 101]. The transform frequencies are selected to encompass the aircraft dynamics of interest. The use of a restricted frequency range for modeling effectively smooths the data and allows estimation of nearly unbiased parameter estimates when the regressors contain noise [19, 70, 100]. Additional benefits of model identification in the frequency domain include accurate parameter uncertainty estimation, increased computational speed, and least-squares weighting based on frequency components as opposed to individual data points.

Parameter estimation using ordinary least-squares regression with the complex regressor and response data is similar to application of ordinary least-squares regression using real-valued data in the time domain. For complex least-squares regression, p unknown model parameters in a parameter vector $\boldsymbol{\theta}$ are estimated for a given model $\tilde{\boldsymbol{y}} = \tilde{\boldsymbol{X}}\boldsymbol{\theta}$, where $\tilde{\boldsymbol{y}}$ is the length M complex model response vector and $\tilde{\boldsymbol{X}}$ is a $M \times p$ matrix consisting of column vectors of the complex regressors assumed to be error-free [19]. The regression equation is

$$\tilde{\boldsymbol{z}} = \tilde{\boldsymbol{X}}\boldsymbol{\theta} + \tilde{\boldsymbol{\nu}} \tag{2.58}$$

where $\tilde{\boldsymbol{z}}$ is the complex measured response variable corrupted by constant variance, zero-mean, and uncorrelated complex error $\tilde{\boldsymbol{\nu}}$. For complex least-squares parameter estimation, the optimal estimate of the unknown parameters $\boldsymbol{\theta}$ is determined by minimizing the cost function:

$$J(\boldsymbol{\theta}) = \frac{1}{2}\left(\tilde{\boldsymbol{z}} - \tilde{\boldsymbol{X}}\boldsymbol{\theta}\right)^{\dagger}\left(\tilde{\boldsymbol{z}} - \tilde{\boldsymbol{X}}\boldsymbol{\theta}\right) \tag{2.59}$$

It follows that the solution to compute an optimal estimate of the unknown real-valued parameters is

$$\hat{\boldsymbol{\theta}} = \left[Re\left(\tilde{\boldsymbol{X}}^{\dagger}\tilde{\boldsymbol{X}}\right)\right]^{-1} Re\left(\tilde{\boldsymbol{X}}^{\dagger}\tilde{\boldsymbol{z}}\right) \tag{2.60}$$

where $\hat{\boldsymbol{\theta}}$ is a vector of p estimated parameters [19]. The modeled response variable vector is:

$$\hat{\tilde{\boldsymbol{y}}} = \tilde{\boldsymbol{X}}\hat{\boldsymbol{\theta}} \tag{2.61}$$

A length p vector of standard errors $\boldsymbol{s}(\hat{\boldsymbol{\theta}})$ corresponding to the estimated parameters $\hat{\boldsymbol{\theta}}$ is given as:

$$\boldsymbol{s}(\hat{\boldsymbol{\theta}}) = \sqrt{\left(\frac{1}{2T\left(f_{\max} - f_{\min}\right)} Re\left[\left(\tilde{\boldsymbol{z}} - \hat{\tilde{\boldsymbol{y}}}\right)^{\dagger}\left(\tilde{\boldsymbol{z}} - \hat{\tilde{\boldsymbol{y}}}\right)\right]\right) \quad \text{diag}\left(\left[Re\left(\tilde{\boldsymbol{X}}^{\dagger}\tilde{\boldsymbol{X}}\right)\right]^{-1}\right)} \tag{2.62}$$

This form of $\boldsymbol{s}(\hat{\boldsymbol{\theta}})$ accounts for the fact that an arbitrary frequency range is used for analysis [100].

After complex least-squares parameter estimation is completed, an additional step is needed to identify the bias term in a model equation because the detrended data used to estimate the model parameters contain only dynamic information [19, 100]. The scalar bias parameter estimate $\hat{\theta}_o$ is found as the mean value of $(\boldsymbol{z} - \boldsymbol{X}\hat{\boldsymbol{\theta}})$, where $\boldsymbol{z}$ is the measured response variable in the time domain, $\boldsymbol{X}$ is a matrix consisting of column vectors of the regressors in the time domain, and $\hat{\boldsymbol{\theta}}$ is the model parameter vector estimated previously in Equation (2.60) using complex least-squares regression. The bias parameter standard errors are best estimated by accounting for colored residuals using the method described in References [19, 99] to compute a more realistic estimate of parameter uncertainty.

2.6.1.3 Time-Domain Output-Error Method

The output-error method is a maximum likelihood estimator that minimizes the weighted sum of squared differences between measured aircraft outputs and modeled outputs computed through numerical integration of the proposed dynamic model [19, 20]. This method is a more computationally intensive, iterative, nonlinear optimization problem. Consequently, the output-error method is not well suited for model structure selection and requires using an assumed model structure or a model structure developed using equation-error methods. The output-error method accounts for zero-mean, white, Gaussian measurement noise, but assumes that there is no process noise (i.e., no disturbances such as atmospheric turbulence). Because the output-error is the minimization criterion, the models produced using output-error parameter estimation generally result in more accurate prediction of aircraft outputs, and thus, more accurate flight simulations. The following overview of the output-error method is presented considering the deterministic nonlinear dynamic system:

$$\dot{\boldsymbol{x}} = \boldsymbol{f}\left(\boldsymbol{x}(t), \boldsymbol{u}(t), \boldsymbol{\theta}\right), \quad \boldsymbol{x}(0) = \boldsymbol{x}_0 \tag{2.63}$$

$$\boldsymbol{y} = \boldsymbol{g}\left(\boldsymbol{x}(t), \boldsymbol{u}(t), \boldsymbol{\theta}\right) \tag{2.64}$$

where the state equations $\boldsymbol{f}$ and output equations $\boldsymbol{g}$ can be nonlinear functions of states $\boldsymbol{x}(t)$, inputs $\boldsymbol{u}(t)$, and unknown parameters $\boldsymbol{\theta}$, subject to initial states $\boldsymbol{x}_0$. The N discrete measurements of the dynamic system are

$$\boldsymbol{z}(k) = \boldsymbol{y}(k) + \boldsymbol{\nu}(k), \quad k = 1, 2, ..., N \tag{2.65}$$

where the system output $\boldsymbol{y}$ is corrupted by zero-mean, Gaussian, white measurement noise $\boldsymbol{\nu}$ with measurement noise covariance $\boldsymbol{R}$.

To minimize the output-error between the measured output $\boldsymbol{z}$ and modeled output $\boldsymbol{y}$, the output-error cost function $J(\boldsymbol{\theta})$ is formulated as

$$J(\boldsymbol{\theta}) = \frac{1}{2}\sum_{k=1}^{N}\left[\boldsymbol{z}(k) - \boldsymbol{y}(k)\right]^T \hat{\boldsymbol{R}}^{-1}\left[\boldsymbol{z}(k) - \boldsymbol{y}(k)\right] \tag{2.66}$$

for a given estimate of the measurement noise covariance $\hat{\boldsymbol{R}}$ [19]. The $\hat{\boldsymbol{R}}$ matrix, which essentially weights each output based on noise level and signal units, is estimated as:

$$\hat{\boldsymbol{R}} = \frac{1}{N}\sum_{k=1}^{N}\left[\boldsymbol{z}(k) - \boldsymbol{y}(k)\right]\left[\boldsymbol{z}(k) - \boldsymbol{y}(k)\right]^T \tag{2.67}$$

Minimization of $J(\boldsymbol{\theta})$ constitutes a nonlinear optimization problem that can be approached using the modified Newton-Raphson (Gauss-Newton) method. Optimization proceeds by computing the cost function gradient and Hessian estimate:

$$\frac{\partial J}{\partial \boldsymbol{\theta}} = -\sum_{k=1}^{N}\left[\frac{\partial \boldsymbol{y}(k)}{\partial \boldsymbol{\theta}}\right]^T \hat{\boldsymbol{R}}^{-1}\left[\boldsymbol{z}(k) - \boldsymbol{y}(k)\right] \tag{2.68}$$

$$\frac{\partial^2 J}{\partial \boldsymbol{\theta}^2} \approx \sum_{k=1}^{N}\left[\frac{\partial \boldsymbol{y}(k)}{\partial \boldsymbol{\theta}}\right]^T \hat{\boldsymbol{R}}^{-1}\left[\frac{\partial \boldsymbol{y}(k)}{\partial \boldsymbol{\theta}}\right] \tag{2.69}$$

The estimated parameters $\hat{\boldsymbol{\theta}}$ at each jth iteration are then updated by

$$\Delta\hat{\boldsymbol{\theta}} = -\left[\left(\frac{\partial^2 J}{\partial \boldsymbol{\theta}^2}\right)_j\right]^{-1}\left(\frac{\partial J}{\partial \boldsymbol{\theta}}\right)_j \tag{2.70}$$

where the new parameter estimates are $\hat{\boldsymbol{\theta}}_{j+1} = \hat{\boldsymbol{\theta}}_j + \Delta\hat{\boldsymbol{\theta}}$. A more detailed description of this output-error method algorithm is presented in Reference [19].

The theoretical best accuracy of output-error parameter estimates is given by the Cramér-Rao lower bounds for the parameter standard errors:

$$\boldsymbol{s}(\hat{\boldsymbol{\theta}}) = \sqrt{\operatorname{diag}\left(\left[\frac{\partial^2 J}{\partial \boldsymbol{\theta}^2}\right]^{-1}_{\boldsymbol{\theta}=\hat{\boldsymbol{\theta}}}\right)} \tag{2.71}$$

The standard Cramér-Rao bounds are generally too optimistic because the output residuals are typically colored when using flight data. A method to correct for the presence of colored residuals and compute a more realistic estimate of parameter uncertainty is described in References [19, 99].

As an example of the setup of an output-error estimation problem, consider the following lateral-direction aerodynamic model structure from Reference [71] including bias parameters:

$$C_Y = C_{Y_\beta}\beta + C_{Y_p}\hat{p} + C_{Y_r}\hat{r} + C_{Y_{\delta_a}}\delta_a + C_{Y_{\delta_r}}\delta_r + C_{Y_o}$$

$$C_l = C_{l_\beta}\beta + C_{l_p}\hat{p} + C_{l_r}\hat{r} + C_{l_{\delta_a}}\delta_a + C_{l_{\delta_r}}\delta_r + C_{l_o}$$

$$C_n = C_{n_\beta}\beta + C_{n_p}\hat{p} + C_{n_r}\hat{r} + C_{n_{\delta_a}}\delta_a + C_{n_{\delta_r}}\delta_r + C_{n_{\beta 2}}\beta^2 + C_{n_{\beta 3}}\beta^3 + C_{n_o}$$

When applying the output-error method, typically the parameters within multiple dynamics equations are estimated simultaneously, which differs from the equation-error method where the set of parameters for each force or moment coefficient are usually estimated separately. In this example, the unknown parameters in the C_Y, C_l, and C_n model structures are estimated together and, accordingly, the unknown model parameter vector is:

$$\boldsymbol{\theta} = \begin{bmatrix} C_{Y_\beta} & C_{Y_p} & C_{Y_r} & C_{Y_{\delta_a}} & C_{Y_{\delta_r}} & C_{Y_o} & C_{l_\beta} & C_{l_p} & C_{l_r} & C_{l_{\delta_a}} & C_{l_{\delta_r}} & C_{l_o} \\ & & & & & & C_{n_\beta} & C_{n_p} & C_{n_r} & C_{n_{\delta_a}} & C_{n_{\delta_r}} & C_{n_{\beta 2}} & C_{n_{\beta 3}} & C_{n_o} \end{bmatrix}^T$$

The lateral-directional outputs, for which the error will be minimized, can be selected as β, p, r, ϕ and a_y. The lateral-directional control inputs are δ_a and δ_r, both of which should be varied in an informative flight maneuver that excites the lateral-directional dynamics. Initial model parameter values obtained using the equation-error method or prior information and initial conditions from the flight maneuver also need to be specified. The modified Newton-Raphson method can then be applied to estimate the unknown model parameters by minimizing the weighted sum of squared differences between measured outputs and predicted outputs, which involves integration of the rotational kinematics equations [Equations (2.4)-(2.6)], translational dynamics equation [Equations (2.7)-(2.9)], and rotational dynamics equations [Equations (2.30)-(2.32)]. Because only the lateral-directional dynamics are being modeled in this example, the longitudinal states (V, α, q, θ), as well as the longitudinal force and moment coefficients (C_X, C_Z, C_m), from the collected flight data can be substituted into the dynamics equations during the integration process.

2.6.2 Model Structure Determination

Two common methods for model structure determination are multivariate orthogonal function (MOF) modeling [19, 102] and stepwise regression [19, 103]. First, a set of candidate model terms is postulated. The candidate model terms are often defined as polynomial expansions of pertinent explanatory variables for the particular response, including nonlinear and cross terms; although, the model structure determination algorithms support using any arbitrary nonlinear functions of the explanatory variables specified by the user as candidate model terms. For MOF modeling, the predefined set of candidate regressors is orthogonalized which allows independent assessment of the potential of each orthogonalized candidate regressor to model the response variable. The orthogonal regressors are then ranked based on their ability to improve the model, and the model terms that significantly contribute to model effectiveness are retained in the model. For stepwise regression, the candidate terms are added or removed from the model one-by-one to assess the significance of including each model term. Linear terms in the polynomial model structure are generally incorporated first, followed by nonlinear terms, which is referred to as modified stepwise regression. An effective strategy used to efficiently and effectively develop model structures is a combination of MOF modeling and stepwise regression. First, MOF modeling is executed for several

separate flight maneuvers. The model structures developed from each flight maneuver are compared, and the model terms appearing in a majority of the maneuvers are retained in the model. As a final step, the MOF results are reviewed by an analyst using stepwise regression to assess whether to include or exclude fringe model terms. This combined strategy was applied to the aircraft system identification efforts described in Part I. The remainder of this subsection provides a more in-depth description of the MOF and stepwise regression modeling techniques.

2.6.2.1 Multivariate Orthogonal Function (MOF) Modeling

The MOF modeling approach [19, 102] starts by orthogonalizing a predefined set of candidate regressors using an algorithm such as Gram-Schmidt orthogonalization or QR decomposition. Orthogonal regressors are convenient for model structure development because of the ability to independently assess the candidate regressors potential to model the response variable—this facilitates only including model terms that significantly contribute to model effectiveness. Upon orthogonalization of candidate regressors, the least-squares regression equation can be reformulated as

$$\boldsymbol{z} = \boldsymbol{P}\boldsymbol{a} + \boldsymbol{\nu} \tag{2.72}$$

where $\boldsymbol{P}$ is a $N \times n_p$ matrix consisting of column vectors holding orthogonal regressors $\boldsymbol{p}_i$ from $i = 1, 2, ..., n_p$, and $\boldsymbol{a}$ is a vector of n_p unknown parameters. The least-squares cost function becomes

$$J(\boldsymbol{a}) = \frac{1}{2}(\boldsymbol{z} - \boldsymbol{P}\boldsymbol{a})^T(\boldsymbol{z} - \boldsymbol{P}\boldsymbol{a}) \tag{2.73}$$

following Equation (2.55). Similarly, the least-squares solution and uncertainty estimates emulate the form of Equation (2.56) and Equation (2.57) by substituting in the orthogonal regressor matrix $\boldsymbol{P}$, the parameter estimates $\hat{\boldsymbol{a}}$, and the modeled response variable vector $\hat{\boldsymbol{y}} = \boldsymbol{P}\hat{\boldsymbol{a}}$. Because the matrix $\boldsymbol{P}^T\boldsymbol{P}$ is diagonal due to the mutual orthogonality of the regressors, the least-squares estimate for the ith parameter decouples and takes the form

$$\hat{a}_i = \frac{\boldsymbol{p}_i^T\boldsymbol{z}}{\boldsymbol{p}_i^T\boldsymbol{p}_i} \tag{2.74}$$

to obtain a vector of estimated parameters, $\hat{\boldsymbol{a}} = \left[\hat{a}_1, \hat{a}_2, ..., \hat{a}_{n_p}\right]^T$. It follows that the least-squares cost function can be rewritten as

$$J(\hat{\boldsymbol{a}}) = \frac{1}{2}\left(\boldsymbol{z}^T\boldsymbol{z} - \sum_{i=1}^{n_p}\frac{\left(\boldsymbol{p}_i^T\boldsymbol{z}\right)^2}{\boldsymbol{p}_i^T\boldsymbol{p}_i}\right) \tag{2.75}$$

which highlights the fact that the contribution of each orthogonal regressor to improve the least-squares model fit can be assessed independently from other orthogonal regressors in a particular model structure. This allows a model structure to be identified without iteration [19].

Using the above developments, the regressors are ranked from highest to lowest decrease in the mean squared fit error (MSFE):

$$\text{MSFE} = \frac{1}{N}\left(\boldsymbol{z} - \hat{\boldsymbol{y}}\right)^T\left(\boldsymbol{z} - \hat{\boldsymbol{y}}\right) \tag{2.76}$$

This is reflected by the $\left(\boldsymbol{p}_i^T\boldsymbol{z}\right)^2/\boldsymbol{p}_i^T\boldsymbol{p}_i$ term for each regressor in Equation (2.75). In other words, the regressors are ranked from highest to lowest ability to improve the model. Candidate regressors are brought into the model structure in this rank order.

Deciding which terms to include in the final model can then be done using one or more statistical metrics. A common threshold for MOF modeling is to minimize the predicted squared error (PSE) [19, 104]. The PSE is the sum of the MSFE [Equation (2.76)] and a model complexity penalty related to the number of terms included in the model

$$\text{PSE} = \text{MSFE} + \sigma_{\text{max}}^2\frac{p}{N} \tag{2.77}$$

where p is the number of terms in the current model structure and σ_{max}^2 is an estimate of the upper-bound of the mean squared error for the model prediction of data that were not used to develop the model. The quantity σ_{max}^2 can be estimated using the variance of measured responses between repeated data points in wind-tunnel experiments or from the variance between the measured response $\boldsymbol{z}$ and mean measured response $\bar{\boldsymbol{z}}$:

$$\sigma_{\text{max}}^2 = \frac{1}{N-1}\sum_{i=1}^{N}\left[\boldsymbol{z}(i) - \bar{z}\right]^2 \tag{2.78}$$

When the orthogonalized regressors are ranked as stated above, the PSE metric is guaranteed to have a single global minimum [19].

Another statistical metric that has been used as a stopping criterion for MOF modeling is the coefficient of determination R^2 [105, 106]. The R^2 metric quantifies the model fit by characterizing the fraction of variation of the response variable about its mean that is described by the model. The R^2 metric, which is generally expressed as a percentage, is calculated as:

$$R^2 = \frac{\hat{\boldsymbol{y}}^T\boldsymbol{z} - N\bar{z}^2}{\boldsymbol{z}^T\boldsymbol{z} - N\bar{z}^2} \tag{2.79}$$

The R^2 metric will typically increase with addition of new orthogonal model terms. Consequently, it is important that each model term added on the basis of the R^2 metric significantly improves modeling performance. A common threshold to justify addition of a given model term is an R^2 increase of 0.5% [19]. This means that the model term describes at least 0.5% of the total variation about the mean response.

For this dissertation, both PSE and R^2 were used as a cutoff threshold for candidate model terms to include in the final model structure. After determining the model terms to include in the model structure, the final parameter values were estimated using least-squares regression with ordinary regressors. The MOF modeling process used for model structure determination is summarized in Figure 2.22.

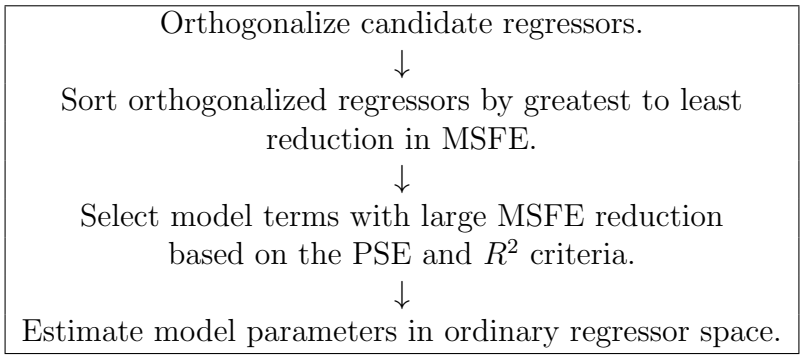

Figure 2.22: Summary of the MOF modeling process used for model structure determination.

2.6.2.2 Stepwise Regression

The stepwise regression algorithm used here for model structure development is based on the algorithm described in Reference [103]. This algorithm is a combination of forward selection and backwards elimination of candidate regressors where a single regressor is either added to or removed from the model at each iteration. The procedure is started with only a bias parameter included in the model structure. The first step is adding the candidate regressor with the highest correlation to the unmodeled portion of the response variable into the model. The process is continued by adding excluded candidate model terms with the highest partial correlation r_i into the model. For the ith model term excluded from the model structure, r_i is calculated using the equation for the correlation coefficient. For two arbitrary vectors $\boldsymbol{\xi}_i$ and $\boldsymbol{\xi}_j$, the correlation coefficient r_{ij} is defined as:

$$r_{ij} = \frac{(\boldsymbol{\xi}_i - \bar{\xi}_i)^T(\boldsymbol{\xi}_j - \bar{\xi}_j)}{\sqrt{(\boldsymbol{\xi}_i - \bar{\xi}_i)^T(\boldsymbol{\xi}_i - \bar{\xi}_i)}\sqrt{(\boldsymbol{\xi}_j - \bar{\xi}_j)^T(\boldsymbol{\xi}_j - \bar{\xi}_j)}} \tag{2.80}$$

For stepwise regression, $\boldsymbol{\xi}_i$ represents the ith model term residual vector resulting from being regressed on the terms included in the current model, with mean denoted $\bar{\xi}_i$; $\boldsymbol{\xi}_j$ represents the difference between the measured response variable and the response modeled by the current regressors in the model, with mean denoted $\bar{\xi}_j$.

At each stepwise regression iteration, terms included in the model are considered to be removed from the model if their partial F-statistic, F_{0_i}, falls below a cutoff threshold $F_{\text{out}} = F(\alpha_p, 1, N - n_p)$ prescribed by a partial F-test for significance at an α_p significance level with n_p included model regressors. For the ith model term included in the current iteration of the model structure, F_{0_i} is calculated as

$$F_{0_i} = \frac{\hat{\theta}_i^2}{s^2(\hat{\theta}_i)} \tag{2.81}$$

where $\hat{\theta}_i$ is the respective parameter estimate and $s^2(\hat{\theta}_i)$ is the respective parameter variance. In the statistics literature, the significance level α_p is commonly chosen as $\alpha_p = 0.05$, or

95% confidence that a model term is significant; however, this threshold has been noted to admit a large number of model terms that lack physical justification for aircraft modeling problems (which often have a large number of data points relative to the number of estimated model parameters). Over-parameterizing a model is undesirable because the model can yield unrealistic response predictions and unnecessary curvature. To mitigate this problem, the SIDPAC [19, 50] stepwise regression algorithm includes a conservative constant partial F-statistic cutoff value of $F_{\text{out}} = 20$ which, for a large value of $N - n_p$, corresponds to $\alpha_p = 0.000008$ or 99.9992% confidence that a model term is significant. This can also be interpreted as requiring the parameter estimate magnitude to be at least $\sqrt{20} \approx 4.5$ times greater than the estimated standard error for a candidate regressor to remain in the model, meaning that the parameter estimate has a very high probability of being nonzero. The best significance level to use is somewhat subjective and depends on the particular modeling problem.

The stepwise regression algorithm can be run automatically or manually. Automatic execution is more efficient and is generally effective in predicting dominant terms, but can have more difficulty determining which borderline terms are worthy of inclusion in the model structure (a task that would be more obvious to a subject matter expert based on physical insight). Manual execution of the stepwise regression algorithm allows a subject matter expert to be given the ability to add insight into the modeling process by adding or removing model terms based on physical vehicle insight and statistical metrics introduced previously.

2.6.2.3 Model Structure Determination in the Frequency Domain

The MOF modeling and stepwise regression model structure identification algorithms that use real-valued data in the time domain can also be formulated in the frequency domain, while still allowing nonlinear model terms to be considered for the model structure [100, 107, 108]. The key modifications, developed in References [107, 108] for MOF modeling, are applied to the candidate regressor and response variable data used in each model structure selection algorithm. The nonlinear candidate regressors are assembled in the time domain using detrended explanatory variables and are subsequently detrended again before transforming the candidate regressor data into the frequency domain. After the Fourier transform is applied to the candidate regressor data, the real and imaginary components of the complex candidate regressor matrix $\tilde{\boldsymbol{X}}$ are concatenated to form a real vector:

$$\boldsymbol{X}' = \begin{bmatrix} Re(\tilde{\boldsymbol{X}}) \\ Im(\tilde{\boldsymbol{X}}) \end{bmatrix} \tag{2.82}$$

Similarly, the detrended response variable vector is transformed to the frequency domain and then the real and imaginary components of the complex response variable vector $\tilde{\boldsymbol{z}}$ are concatenated to form a real vector:

$$\boldsymbol{z}' = \begin{bmatrix} Re(\tilde{\boldsymbol{z}}) \\ Im(\tilde{\boldsymbol{z}}) \end{bmatrix} \tag{2.83}$$

The real candidate regressor matrix $\boldsymbol{X}'$ and response variable vector $\boldsymbol{z}'$ assembled from complex data are then used in the standard model structure identification algorithms described earlier. This approach also applies for parameter estimation in the frequency domain with nonlinear model terms.

2.6.2.4 Data Collinearity

Within the model structure determination step, it is important to avoid including terms in the model structure that are highly correlated. Inclusion of highly-correlated terms in a model can result in data collinearity, or correlation between model terms high enough to cause corrupted model identification [19]. Data collinearity causes parameter estimation deficiencies because the effects of certain highly-correlated model terms on the output response cannot be distinguished, resulting in inaccurate parameter estimates and high uncertainties from the poorly conditioned estimation problem. The identified model structure should be examined for evidence of data collinearity using correlation metrics (e.g., see Section 7.2.2 and References [19, 20, 109]) before proceeding to estimate the final model parameter values. If data collinearity is detected, the model structure should be adjusted or the flight-test experiment should be redesigned; alternatively, *a priori* information can be used to resolve data collinearity problems. The topic of data collinearity is discussed further in Sections 6.4.2 and 7.2.2.

Note that the MOF modeling approach automatically protects against data collinearity when selecting a model structure. If there is high correlation between candidate regressors, after the first candidate regressor is orthogonalized, any other highly-correlated candidate regressors will be close to zero after passing through the orthogonalization process, which will prevent the latter model terms from being included in the model structure [19]. In other words, this prevents highly-correlated model terms from being included in the model together.

2.6.3 Model Validation

After estimating model parameters, model validation procedures are used to determine whether the identified model will be satisfactory for its intended use. This includes assessing the ability of the model to predict aircraft motion and inspecting identified model parameters.

Validation flight data withheld from model identification are used to assess model prediction accuracy. This is best accomplished using flight data with input waveforms differing from the modeling data that also excites the aircraft dynamics and perturbs the aircraft through a substantial portion of the explanatory variable space characterized by the model to provide a rigorous prediction test. The model should provide a close match to the validation flight data, with a similar level of accuracy as the data used for model identification.

The prediction quality of the model can be further assessed by analyzing the residual characteristics graphically and using metrics such as the root-mean-square error (RMSE):

$$\text{RMSE} = \sqrt{\frac{(\boldsymbol{z} - \hat{\boldsymbol{y}})^T (\boldsymbol{z} - \hat{\boldsymbol{y}})}{N}} \tag{2.84}$$

The RMSE metric can be given further interpretability by normalization. The normalized root-mean-square error (NRMSE), expressed as a percentage and normalized by the range of response variable measurements used to identify the model

$$\text{range}(\boldsymbol{z}_m) = \max(\boldsymbol{z}_m) - \min(\boldsymbol{z}_m) \tag{2.85}$$

is calculated as:

$$\text{NRMSE} = 100 \times \frac{1}{\text{range}(\boldsymbol{z}_m)} \sqrt{\frac{(\boldsymbol{z} - \hat{\boldsymbol{y}})^T (\boldsymbol{z} - \hat{\boldsymbol{y}})}{N}} \tag{2.86}$$

The range-normalized NRMSE is a good metric for model validation because it

1. permits quantitative assessment and comparison of the model fit and prediction performance,
2. allows a fair comparison of longitudinal and lateral-directional model response quality (because longitudinal responses are generally biased above or below zero, whereas lateral-directional responses are generally centered around zero), and
3. is straightforward to interpret as a percent error quantity.

The range-normalized NRMSE is used to quantify the prediction capability of the identified models for much of the work described in this dissertation. Although an NRMSE threshold value to determine if a model is adequate depends on the aircraft and application, a general rule of thumb to strive for is obtaining NRMSE values of less than 5% to 10% for most model outputs, which could, respectively, be used as *desired* and *adequate* model performance thresholds. It is also important to ensure that the corresponding modeling and validation NRMSE values for each output response are similar to provide confidence that the model has good prediction capability.

The individual model parameters are also assessed to ensure that their values agree with physical intuition and that the parameter uncertainty values are within a reasonable bound. Because the models are identified for small, low-cost aircraft with inexpensive instrumentation, the model parameters are expected to have a higher uncertainty compared to larger aircraft with more expensive, higher-quality instrumentation systems. The increased uncertainty in the parameter estimates can be partially mitigated by performing several repeated maneuvers for model identification, which is typically inexpensive and easy to justify for small, low-cost aircraft. Despite the higher uncertainty, the flight-derived models are generally more accurate than models developed using other computational or experimental techniques and are usually fit for the purpose of the intended model-based application.

2.7 Small Fixed-Wing Aircraft Modeling Applications

Multiple fixed-wing aircraft system identification advancements have been enabled by the core set of techniques and tools described above. These applications include: remote uncorrelated piloted inputs [43], aerodynamic modeling in a spin [44], aero-propulsive modeling [24], and nonlinear dynamic modeling without mass properties [26]. The first two applications were collaborative efforts primarily executed by James Gresham, and are summarized in this section (with many additional details provided in References [43, 44] and Gresham's dissertation [56]). The latter two applications were efforts primarily executed by the author and are presented in Chapter 3 and Chapter 4, respectively.

2.7.1 Remote Uncorrelated Piloted Inputs

During flight-test experiments, it is sometimes advantageous for a human pilot to perform system identification maneuvers, as opposed to injecting computer-generated inputs. For example, piloted input excitations are appealing when cost or programmatic speed is important because they circumvent the engineering effort needed to design and integrate an automated excitation input injection capability for a new aircraft. Multistep inputs, which were discussed in Section 2.3, are easy for a pilot to execute but the information content in the data is deficient compared to using orthogonal phase-optimized multisine inputs. Reference [43] investigated a remote uncorrelated pilot input (UPI) technique that facilitates efficient collection of high-quality flight data for dynamic model identification with a ground-based test pilot. Multi-axis UPI excitations, which were first developed and applied for manned aircraft in References [86–88], are composed of pseudo-random piloted excitation of the aircraft dynamics in all axes simultaneously. In essence, the UPI is an approximation of computer-generated orthogonal phased-optimized multisine inputs executed by the pilot with the objective to decorrelate the inputs and excite the aircraft over a broad range of frequencies consistent with the aircraft dynamics. The UPI maintains many of the advantages of multisine inputs, but does not require the engineering development effort to integrate automated control inputs. Although the UPI is an effective technique, pilot training is required to properly execute the inputs and the inputs are generally not mutually orthogonal, as is the case for a computer-generated multisine.

The advancements presented in Reference [43] included the development of procedures and best practices for application of the remote UPI technique to small, unmanned, fixed-wing aircraft. The remote UPI technique was demonstrated and refined with a novice and an expert ground-based pilot. The novice pilot had limited prior experience flying RC aircraft and had no formal flight-test training; the expert pilot had significant experience flying RC aircraft and was a trained flight-test professional. Simulator-based pilot training with the RC transmitter used for flight testing was found to be essential for pilots to build muscle memory for generating remote UPI excitations with proper input character in flight experiments.

Figure 2.23 shows the near real-time pilot display used for the pilot training simulations, which included plots of the normalized pilot input signals as well as the input signal frequency spectra and pairwise cross plots with the correlation coefficient. The simulator training objectives included creating diverse frequency content for each control effector within the frequency band of common aircraft rigid-body dynamics (e.g., below 2 Hz), achieving low absolute values of the pairwise correlation coefficient r (e.g., $|r| < 0.3$), and distributing control signal data throughout the cross plots. The most successful training technique was to perform a three-axis maneuver, while focusing on improvement of one control input at a time. Using this training philosophy and the near real-time visual feedback shown in Figure 2.23, both pilots' abilities to successfully perform the remote UPI maneuver rapidly improved; each pilot achieved consistent inputs meeting the training objectives in less than 10 simulated UPI excitations.

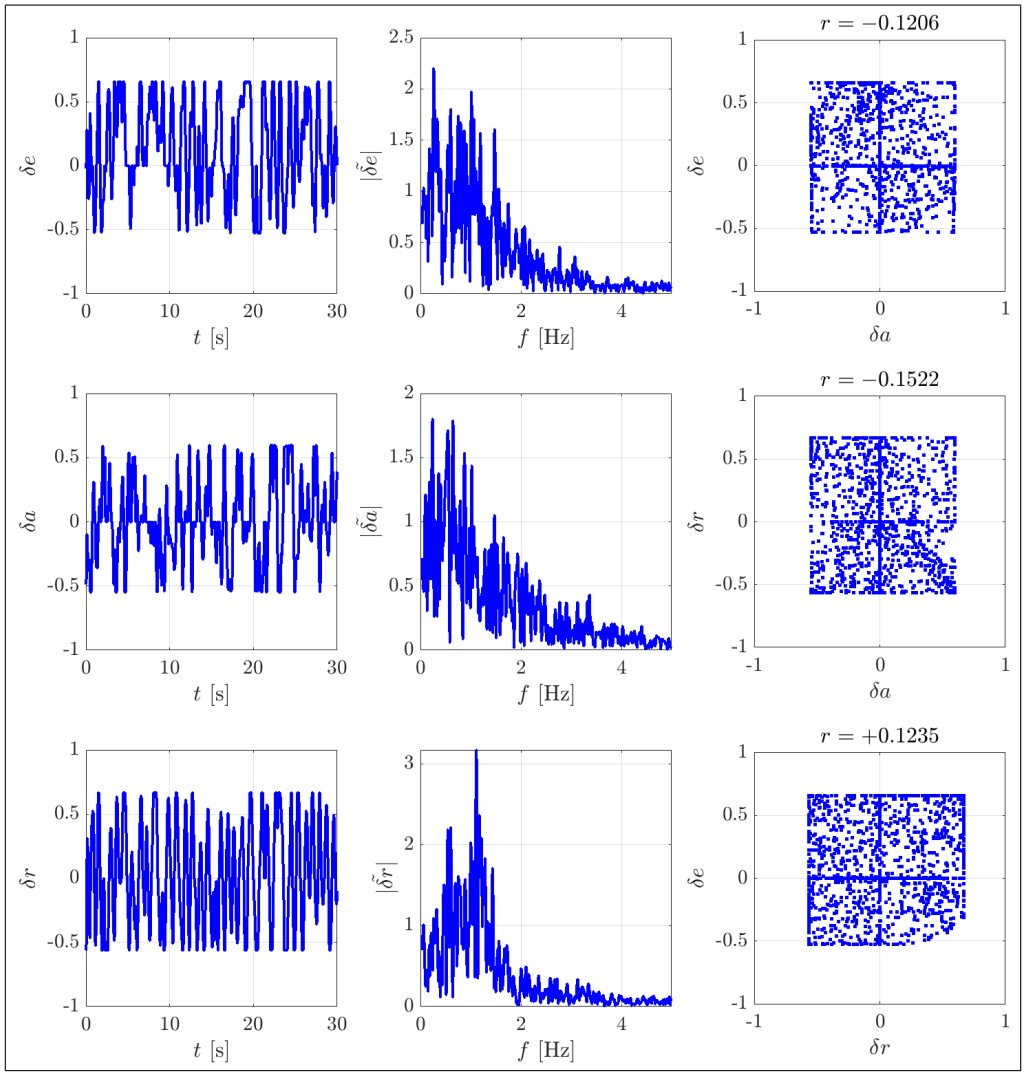

Figure 2.23: Remote UPI simulator training display [43].

Following the simulator-based training campaign, both pilots successfully executed the remote UPI maneuvers in flight. The added challenge during flight experiments included keeping the aircraft near its original trimmed flight condition with the limited physiological, auditory, and visual cues available to a ground-based pilot. This challenge was overcome by occasionally referencing the attitude display on the ground station telemetry data, and could be further aided by a future first person view (FPV) video feed. With practice, the pilots produced uncorrelated inputs with broad frequency content while remaining in the desired operational envelope. The models obtained using the remote UPI maneuver were found to have similar predictive performance to models developed using computer-generated multisine inputs, as well as piloted and automated multistep inputs (which are less time-efficient and less information-rich), providing confidence that the remote UPI flight data were well-suited for system identification. The remote UPI technique was validated as an efficient excitation technique that can be applied in nonlinear aerodynamic regions without the complications of incorporating computer-generated inputs.

2.7.2 Spin Aerodynamic Model Identification

Aerodynamic model development for spinning motion is typically accomplished from data collected in wind-tunnel testing or using CFD. Reference [44] presented an alternative method for identifying a nonlinear, quasi-steady, coupled, aerodynamic model for a fixed-wing aircraft in a spinning descent using flight-test data. Identification of a model for the aircraft dynamics and control authority in the neighborhood of a stable, oscillatory spin is helpful to accurately describe and simulate the motion of an aircraft for spin path control law development. One related application was development of a robust, model-based spin path control law for use in a flight termination system for an unmanned fixed-wing aircraft [80]. Although the novel control scheme proposed in Reference [80] was effective in controlling a descending spiral trajectory toward a designated impact area using a model developed for nominal wings-level flight, it was also helpful to have a dedicated spin flight dynamics model to compare to the nominal flight dynamics model. In Reference [44], a flight experiment was designed and conducted using automated orthogonal phase-optimized multisine inputs active on the elevator, aileron, and rudder control surfaces while in a stable spin to excite all rigid-body dynamics concurrently. The efficient excitation capability of multisine inputs is well suited for the short duration stall-spin maneuvers as well as the need to characterize numerous interaction effects. For each spin maneuver, the pilot progressed through a series of scripted test inputs as follows:

1. Initiate benign, wings-level, power-off stall by gradually applying 70% elevator deflection trailing-edge up and applying aileron and rudder inputs as required to level the wings.

2. At the stall break, initiate prescribed spin inputs of 70% left rudder, 70% trailing-edge up elevator, and 50% left aileron.

3. After two spin rotations, initiate multisine excitations.
4. At a predetermined safe recovery altitude, terminate the multisine excitations and recover to resume normal flight.

The precise control surface deflections were obtained during test maneuvers by modifying the pilot commanded input limits to allow the pilot to maintain a precise spin by holding the maximum control inputs on the RC transmitter. These input settings were selected to ensure the controls were not saturated with the multisine inputs active and that the aircraft remained in a spin during multisine excitations. The flight path from a nominal CZ-150 spin flight maneuver is shown in Figure 2.24 with the aircraft orientation depicted at 1-second intervals.

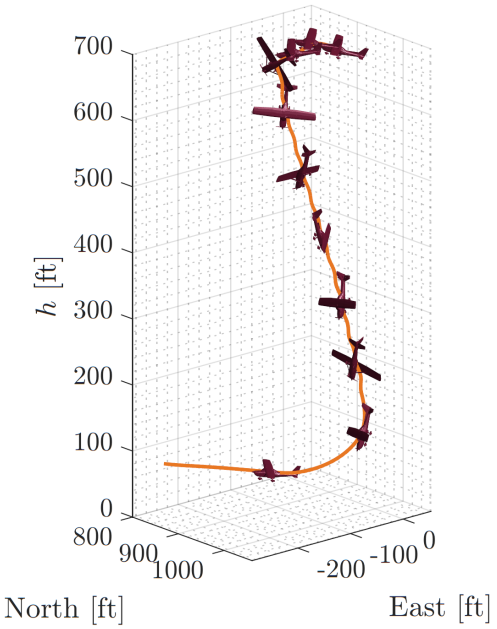

Figure 2.24: Flight data from a nominal CZ-150 spin maneuver [44].

The spin model was developed using the flight data from several repeated spin maneuvers with multisine excitations active on each control surface. The short maneuver length and aerodynamic complexity of the spinning flight regime necessitated the use of data from several flight maneuvers for adequate spin modeling. Stall-spins are aggressive out-of-plane flight maneuvers best described by a nonlinear flight dynamics model where the equations of motion are fully coupled due to complex aerodynamics and rotating reference frame effects. Initially, the typical explanatory variables used to develop an aerodynamic model for a fixed-wing aircraft (i.e., α, β, p, q, r, δ_a, δ_e, δ_r) were considered for spin modeling; however, the resulting model was inadequate for describing the aircraft dynamics in a spin. Inspired by previous spin aerodynamic modeling work leveraging wind-tunnel testing [110–112], one essential modification to adequately characterize the spin aerodynamics was to transform

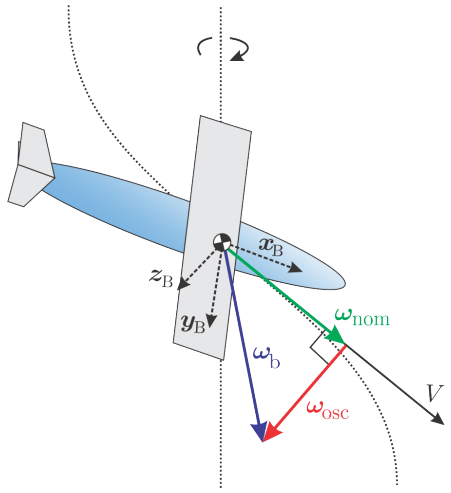

Figure 2.25: Decomposition of body-axis rotation rates in a perturbed spin [44].

the body-axis angular velocity to states better suited to describe the spinning motion. As depicted in Figure 2.25, the body-axis angular velocity vector $\boldsymbol{\omega}_b$ was decomposed into components along ($\boldsymbol{\omega}_{nom}$) and orthogonal to ($\boldsymbol{\omega}_{osc}$) the instantaneous wind vector. The figure shows an aircraft perturbed from a nominal spin to visualize the angular velocity vector components, which is important because the modeling approach excites the aircraft dynamics around the nominal spin states. This results in four new explanatory variables: the wind-axis angular rate Ω and the complementary body-axis oscillatory components p_{osc}, q_{osc}, and r_{osc}, which replace the body-axis angular velocity components for model identification. This transformation, based on aerodynamic spin theory, resulted in significantly improved modeling results. Furthermore, based on demonstrated spin model improvement by including unsteady effects [113], $\dot{\alpha}$ and $\dot{\beta}$ terms were considered, which significantly improved the predictive performance of the dynamic model. Using these additional explanatory variables, as well as α, β, δ_a, δ_e, and δ_r, to represent the aerodynamic force and moment coefficients in a nonlinear polynomial expansion resulted in an accurate aerodynamic spin model valid around a perturbation range from the nominal spin. The model captures longitudinal and lateral-directional coupling, post-stall effects, and spin dynamics.

After identification of the spin aerodynamic model, the model prediction performance was assessed using spin flight data withheld from model identification and was compared to the model performance of a nonlinear aerodynamic model of the aircraft developed for nominal trimmed, steady, level flight. The spin aerodynamic model adequately matched validation spin flight data and substantially outperformed the nominal model which predicted an exaggerated aircraft response in a spin. This illustrated the utility and necessity of the proposed spin aerodynamic modeling approach to accurately characterize the spin dynamics.

Acknowledgment of Collaborative Research

The research described in this chapter was completed in collaboration with James Gresham. The small unmanned aircraft system identification process, including the generalized flight-test experiment design and modeling approach, was jointly formulated. The control surface modeling strategy, data processing approach, and remote UPI training simulator were developed primarily by the author, but also in collaboration with Gresham. The remote UPI and spin modeling efforts were primarily completed by Gresham; formulation of the experiment design and model development strategies was done collaboratively with the author. Gresham performed all aircraft development and integration efforts, as well as all laboratory and flight-test experiments. The content in Section 2.1, Section 2.4, and Section 2.7 was jointly written with Gresham for a publication led by the author [22]. Additionally, work described in this chapter was enabled by research support from many previous and current students in the Nonlinear System Laboratory at Virginia Tech including Jeremy Hopwood, Jean-Michel Fahmi, Mekonen Halefom, Hunter McClelland, Javier González-Rocha, Chris Gahan, Wade Foster, Patrick Corrigan, and Taylor Ransford. The research in this chapter was advised by Craig Woolsey who offered many helpful suggestions throughout the research process and manuscript preparation. The author gratefully acknowledges and appreciates these efforts which made the research described in this chapter possible.

Chapter 3

Aero-Propulsive Modeling for Propeller Aircraft

This chapter describes methods to identify an integrated propulsion-airframe aerodynamic model and a decoupled propulsion model for fixed-wing aircraft with propellers using flight data. Propulsion aerodynamics and airframe aerodynamics for propeller aircraft are usually modeled separately, which fails to describe unavoidable interaction effects and propeller performance deviations when integrated on an aircraft. Two novel flight-test system identification approaches are presented to develop flight dynamics models with improved characterization of propeller aerodynamics compared to conventional methods. Orthogonal phase-optimized multisine inputs are applied to both the control surfaces and propulsion system to generate data with high-quality information content for model identification. Propulsion explanatory variables derived from propeller aerodynamics theory combined with traditional aircraft modeling variables yield accurate aero-propulsive modeling results and provide propeller performance estimates which are compared to isolated propeller wind-tunnel data. An assessment of model adequacy using flight maneuvers withheld from model identification indicates that the models have good prediction capability. The chapter describes application of these methods to a small unmanned aircraft, but the methods are generalizable to many propeller-driven aircraft. This work has been published as a conference paper [23] and a journal article [24].

The chapter is organized as follows: Section 3.1 presents the motivation for this research. Propeller aerodynamics background information informing the modeling approach is described in Section 3.2. Section 3.3 describes the flight-test experiment design. The integrated and decoupled aero-propulsive modeling methodologies are developed in Section 3.4. Sections 3.5-3.6 provide sample modeling results for each respective modeling method.

3.1 Research Motivation

Fixed-wing aircraft flight dynamics simulations generally consist of a bare airframe aerodynamic model and a separate propulsion model. Bare airframe aerodynamic models are commonly developed using CFD, wind-tunnel testing, and/or flight testing either without propulsors or with propulsors operating at a constant throttle setting. The propulsive forces

and moments are generally characterized using analytical techniques, CFD, or ground testing. The separate airframe aerodynamic model and propulsion model are then combined to predict the applied forces and moments exerted on the aircraft. This assumes that the airframe and propulsion system do not interact or have any influence on one another. For many jet transport aircraft in a cruise configuration, the engine intake and exhaust have limited interactions with the airframe; however, assuming that there are no propulsion-airframe interactions present for propeller-driven aircraft lacks physical justification. Tractor propellers, mounted on the front of the aircraft, will produce slipstreams that flow directly over the airframe; pusher propellers, mounted on the rear of the aircraft, operate in the airframe wake. In many cases, the propeller-induced flowfield also interacts with control surfaces compounding aero-propulsive interactions. This means that there are uncharacterized propulsion-airframe interaction effects, as well as unaccounted for propeller performance deviations due to the presence of the airframe, in classical model build-up strategies using a separate propulsion and airframe aerodynamic model.

Although propeller aerodynamics are often experimentally characterized using ground testing (e.g., see References [114–116]), several previous works have proposed methods for deriving propeller models using flight data. Flight-test thrust estimation techniques used for aircraft performance analysis are described in Reference [117]. Force sensors were used in References [118–125] to measure thrust directly in flight. References [126, 127] used state estimation filters to identify thrust model parameters in simulated flight. Reference [10] used a system identification approach to identify dimensional throttle control derivatives using flight data for an aircraft with distributed electric fans. A flight-based system identification approach for eVTOL aircraft proposed in Reference [32] uses individual propeller rotational speeds as explanatory variables to identify models for all dimensional body-axis force and moment components (see Chapter 9). Previous research for multirotor aircraft has also characterized propeller-driven vehicles through both time-domain and frequency-domain system identification methods using flight data [7, 9, 75, 128–136].

Developing a combined propulsion and airframe aerodynamic model is a preferable approach when simulation accuracy is given more importance than bare-airframe aerodynamic characterization [19]. Wind-tunnel studies have developed combined propulsion and airframe aerodynamic, or aero-propulsive, models for distributed propulsion eVTOL aircraft with significant propulsion-airframe interactions [28, 30, 137] (see Chapter 6 and Chapter 8). Other wind-tunnel research has studied aero-propulsive interaction effects for fixed-wing aircraft with distributed electric fans mounted on the wing [138, 139]. Reference [88] proposed methods for modeling the combined effects of propulsion and airframe aerodynamics for a jet fighter aircraft in flight; the engine rotational speed was included as an explanatory variable in a dimensional x-axis force model and throttle setting was varied using step inputs commanded by the pilot. Reference [106] described a method for modeling combined propulsion and airframe aerodynamics for a propeller-driven aircraft in a dimensional x-axis force model using advance ratio as an explanatory variable. Reference [140] used throttle step inputs to decorrelate propulsion effects from other modeling variables and proposed defin-

ing the propeller advance ratio as a flight condition variable when identifying local linear aerodynamic models.

This work combines aircraft system identification methods and propeller aerodynamics principles to develop methods for aero-propulsive modeling of fixed-wing aircraft with propellers using flight data. The modeling objectives are to characterize aero-propulsive interaction effects, investigate installed propeller performance differences, and develop an accurate flight dynamics simulation for the studied aircraft. Two novel aero-propulsive modeling approaches are presented, each with different advantages and scenarios where one approach may be preferred. The first approach develops an integrated propulsion and airframe aerodynamic model. The second approach develops a decoupled propulsion model characterizing installed propeller performance to accompany a previously identified airframe aerodynamic model. Both methods develop mathematical models from experimental flight data using aircraft system identification techniques [19, 20].

3.2 Propeller Aerodynamics Background

This section provides a theoretical background on axial propeller aerodynamics and propeller aerodynamics at nonzero incidence angles. Understanding of this background information is essential for postulating the aero-propulsive modeling strategies developed in this chapter, as well as interpreting the presented results.

3.2.1 Axial Propeller Aerodynamics

Well-established methods exist for predicting propeller performance analytically and empirically. Theoretical techniques include momentum theory, blade element methods, and vortex theories [141]. Experimental techniques typically consist of developing data tables or functional representations from wind-tunnel or thrust stand data. For propellers operating in airflow normal to the propeller disk, the propeller produces a net thrust force and a net aerodynamic torque acting along the axis of rotation [142]. The individual propeller blades can be thought of as rotating wings which each produce a lift force perpendicular to the relative flow direction and a drag force parallel to the relative flow direction [73]. The summed lift forces produced by the propeller blades is the propeller thrust T. The summed drag forces result in a net moment about the propeller shaft opposite to the direction of rotation, which is the propeller aerodynamic torque Q.

Propeller performance data are generally presented in the form of the thrust coefficient,

$$C_T = \frac{T}{\rho n^2 D^4} \tag{3.1}$$

and torque coefficient,

$$C_Q = \frac{Q}{\rho n^2 D^5} \tag{3.2}$$

(or equivalently by power coefficient $C_P = 2\pi C_Q$). The thrust and torque coefficients can be shown through dimensional analysis to be a function of advance ratio, propeller blade Reynolds number, and propeller tip Mach number for a given fixed-pitch propeller design [142, 143]. For propellers with variable-pitch hubs, thrust and torque also vary with blade pitch angle. Because propeller similitude relations to scale propeller aerodynamics are limited [144], due to differences in boundary layer characteristics [145], propeller characteristics must be tested at full-scale to properly capture all pertinent aerodynamic effects. This provides additional motivation for the flight-test-based propeller characterization techniques presented in this work to be used for large aircraft because full-scale propeller wind-tunnel testing is cost prohibitive.

Advance ratio, which relates to the linear distance traveled by the propeller in one revolution, is defined as:

$$J = \frac{V}{nD} \tag{3.3}$$

Advance ratio generally has the largest effect on fixed-pitch propeller aerodynamics, and accordingly, thrust and torque coefficient representations are commonly expressed as only a function of advance ratio. Representing propeller aerodynamics only as a function of advance ratio for a fixed blade pitch angle requires that airflow is parallel to the propeller axis of rotation, as well as the assumptions that viscous and compressibility effects are negligible [142].

Reynolds number is a dimensionless quantity which corresponds to the ratio of inertial to viscous forces acting on a body. For large aircraft propellers, the propeller blade Reynolds number effects are minimal and can generally be neglected. For small propellers, the Reynolds number is lower, indicating that the viscous forces become important. This effect is manifested as a thicker boundary layer, which is more likely to result in flow separated from the propeller surface [145] and results in propeller performance degrading at lower Reynolds number [114, 115]. Following the definition given in Reference [115], the propeller blade Reynolds number Re is

$$Re = \frac{\rho V_p c}{\mu} \tag{3.4}$$

where c is the propeller chord at 75% blade length, μ is the dynamic viscosity, and $V_p = 0.75\pi nD$ is the propeller blade linear speed at 75% blade length. Mach number is the ratio of flow speed to the speed of sound a, which physically represents the ratio of inertial forces to forces related to compressibility of the fluid [145]. The propeller tip Mach number, which quantifies the averaged compressibility effects, is defined as [146]:

$$M_{\text{tip}} = \frac{\pi nD}{a} \tag{3.5}$$

For the normal operating range of the propellers used in this chapter, the propeller blade Reynolds number is high enough and the tip Mach number is low enough such that their effects are negligible.

3.2.2 Propeller Aerodynamics at Nonzero Incidence Angle

When the airflow relative to a propeller is not parallel to the axis of rotation, the propeller will produce auxiliary forces and moments other than the axial thrust and torque [142]. In this condition, periodic variation in propeller blade local angle of attack results in a non-uniform load distribution on the propeller disk. Thus, in a general case of arbitrary flow direction relative to the propeller disk, propeller forces and moments will also be dependent on the orientation of the propeller axis of rotation relative to the freestream velocity, in addition to advance ratio, propeller blade pitch angle, propeller blade Reynolds number, tip Mach number, and the propeller design. This angle between the freestream airflow and propeller rotation axis is referred to in this work as the propeller incidence angle, i_p, shown in Figure 3.1. The value of i_p is zero when airflow is normal to the propeller disk, opposing the direction of axial thrust.

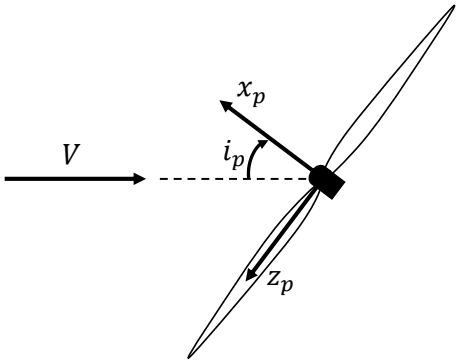

Figure 3.1: Propeller incidence angle definition and coordinate system.

One additional auxiliary force and one additional auxiliary moment are predicted theoretically from the periodic lift and drag imbalance on the individual propeller blades [73, 142]. For example, consider a front mounted propeller on a fixed-wing aircraft in level, forward flight at positive angle of attack, where it is assumed that the propeller axis of rotation coincides with the body x-axis of the aircraft. The propeller blades moving downward will produce more lift than the propeller blades moving upward because the downward moving blade is experiencing a higher angle of attack and relative airspeed. Consequently, the net center of thrust force is offset from the propeller axis of rotation, favoring the side of downward blade movement. When the net thrust force is transferred to the center of the propeller, a net yawing moment is observed acting to rotate the downward moving propeller blades into the oncoming airflow. This effect is often referred to as the P-factor. The individual

propeller blade drag forces are also larger on the side of downward movement, again due to the greater relative angle of attack and airspeed, resulting in a net normal force directed upward for the current example. Thus, a propeller on an airplane at positive angle of attack will produce a normal force and a yawing moment in addition to the conventional axial thrust and torque. Following similar reasoning, the example propeller in sideslip will instead produce a side force and a pitching moment as the auxiliary force and moment.

An analytical treatment of airplane propeller aerodynamics at low angle of attack presented in Reference [73] agrees with the qualitative conclusions obtained from the preceding example. For a propeller operating at a small nonzero angle of attack and zero sideslip, the normal force and yawing moment are shown to be linearly proportional to the propeller incidence angle; pitching moment and side force coefficients are theoretically zero. It is also shown that for low incidence angle conditions, small perturbations in incidence angle have no effect on axial thrust and torque.

The propeller side force T_y, normal force T_z, pitching moment Q_y, and yawing moment Q_z can be nondimensionalized in a manner similar to the thrust T_x and torque Q_x [73]. The propeller normal force coefficient C_{T_z}, side force coefficient C_{T_y}, pitching moment coefficient C_{Q_y}, and yawing moment coefficients C_{Q_z}, are defined as:

$$C_{T_y} = \frac{T_y}{\rho n^2 D^4},\ C_{T_z} = \frac{T_z}{\rho n^2 D^4},\ C_{Q_y} = \frac{Q_y}{\rho n^2 D^5},\ C_{Q_z} = \frac{Q_z}{\rho n^2 D^5} \tag{3.6}$$

The propeller force and moment sign convention follows the right-handed propeller coordinate system shown in Figure 3.1, where the y-axis is pointed into the page.

Several works have employed methods for theoretically and computationally capturing propeller aerodynamics at incidence [73, 147–155], however, experimental techniques provide the most accuracy in revealing the highly complex and nonlinear behavior of high incidence angle propeller aerodynamics. Early experiments described in References [156, 157] were conducted for propellers with varying incidence angle as well as flow speed, blade angle, and rotational speed. These works showed similar trends in propeller force and moment variation with incidence angle and demonstrated the effectiveness of using the normal component of advance ratio, $J \cos i_p$, for describing propeller aerodynamics at incidence. Reference [158] extended this work by studying the high incidence angle aerodynamics of isolated propellers as well as propeller-wing interactions, noting aerodynamic differences due to the presence of the wing.

The increased interest in efficient jet propulsion subsequent to the above work resulted in propeller aerodynamics research becoming dormant for several decades, until recently when increased interest in electrically-powered UAVs, distributed electric propulsion, and eVTOL designs arose in the aerospace community. In Reference [159], wind-tunnel testing of a subscale propeller at incidence angles ranging from 0 to 180 deg with flow speeds up to 29.5 ft/s was conducted. Normal force magnitude was found to be smaller than axial thrust but still significant at nonzero incidence angles; side force was found to be

negligible for all incidence angles. Off-axis pitching and yawing moments were found to be comparable in magnitude to the aerodynamic torque along the axis of rotation at high incidence angles. Notably, this pitching moment result is not predicted by the propeller theory described in Reference [73] showing the limitations of the analytical treatment of propellers at incidence. The significant pitching moment at high incidence angles can be attributed to non-uniform airflow through the front and rear portions of the propeller relative to the airflow, which leads to a tendency for the propeller to pitch upward at near 90 deg incidence angles [159]. Reference [160] followed this work by testing the same propeller and performed additional testing on multiple 3D printed propeller blades. The measured propeller force and moment coefficients showed reasonable agreement between the two testing efforts. Related research efforts conducted by the author that focus on characterization of high incidence angle propeller aerodynamics using wind-tunnel data are described in References [36–38] and will be discussed further in Chapter 6.

3.2.3 Research Propeller

The primary research platform used for this research was the CZ-150 aircraft introduced in Section 2.1.2 and displayed in Figure 2.3. As mentioned previously, the CZ-150 has a single electric motor mounted on the front of the fuselage which drives an Aero-Naut CAM carbon folding, fixed-pitch, two-bladed, 16-inch diameter, 8-inch pitch (16x8-inch) clockwise rotating propeller, as viewed from behind. The assembled propeller is shown in Figure 3.2. References [116, 161] provide performance data for this propeller configuration acquired in wind-tunnel testing. The wind-tunnel data collected at a propeller rotational speed of 5000 rpm are displayed in Figure 3.3 and provide a basis of comparison for the results obtained in this work. A quadratic polynomial fit to the wind-tunnel data is also shown in each plot, which provides an excellent approximation of C_T and C_Q as a function of J.

Figure 3.2: CZ-150 Aero-Naut CAM carbon two-bladed 16x8-inch propeller.

3.3 Experiment Design

Orthogonal phase-optimized multisine inputs [19, 82–85], described in Section 2.3.2, are the excitation input type used for this work. For this study, individual multisine signals were

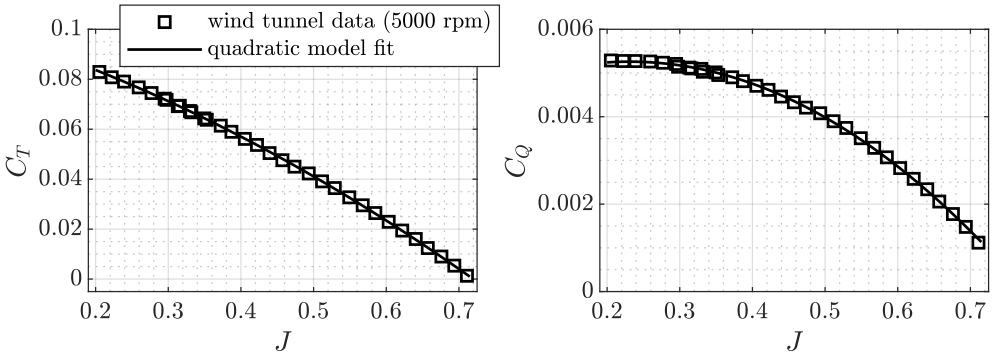

Figure 3.3: Aero-Naut CAM carbon two-bladed 16x8-inch propeller wind-tunnel data [116, 161] and polynomial fit.

generated for the throttle, elevator, aileron, and rudder commands (η_t, η_e, η_a, and η_r, respectively). Several harmonic components were assigned to each control surface and propulsor multisine signal, where the frequency range was set in accordance with frequencies where the rigid-body dynamic response was expected to manifest. Preliminary estimates of the dynamic modes for the CZ-150 aircraft were available from initial exploratory flight testing and informed the experiment design. A maneuver with a 40 second fundamental period T was designed using a frequency range of 0.05 Hz to 1.825 Hz. Each control surface command was assigned 19 harmonic components spread throughout the full excitation frequency range. The throttle harmonic components were focused into lower frequencies to adhere to the lower bandwidth of the propulsion system. Preliminary ground testing indicated that the propulsor rotational speed dynamic response for the CZ-150 aircraft reflected the character of a first-order dynamic system with a break frequency of approximately 0.7 Hz. Accordingly, the 15 harmonic components assigned to the throttle signal were designed to be 0.675 Hz and below. Although higher frequency components would need to be included to characterize the motor dynamics, this effort concentrated on aero-propulsive model identification. Focusing the propulsion frequencies below the break frequency of the motor dynamics improved the aero-propulsive modeling results compared to an alternative input design with a larger range of propulsion frequency components. The input spectra of the multisine signal designed for each control effector are shown in Figure 3.4a.

The optimized multisine input signals used for system identification are shown in Figure 3.4b. The displayed signals are shown in a normalized form with a maximum absolute value of one. This reflects how the signals were injected into the flight controller, where a gain was subsequently applied to each input signal to obtain a good signal-to-noise ratio for model identification. System identification flight testing was conducted using the approach described in Section 2.4. The airplane was flown manually by the pilot without the feedback control system operating. After trimming the aircraft, the pilot enabled system identification inputs using a switch on the RC transmitter. The pilot had the ability to adjust the amplitude of the control surface excitation inputs between 0% to 100% of the maximum

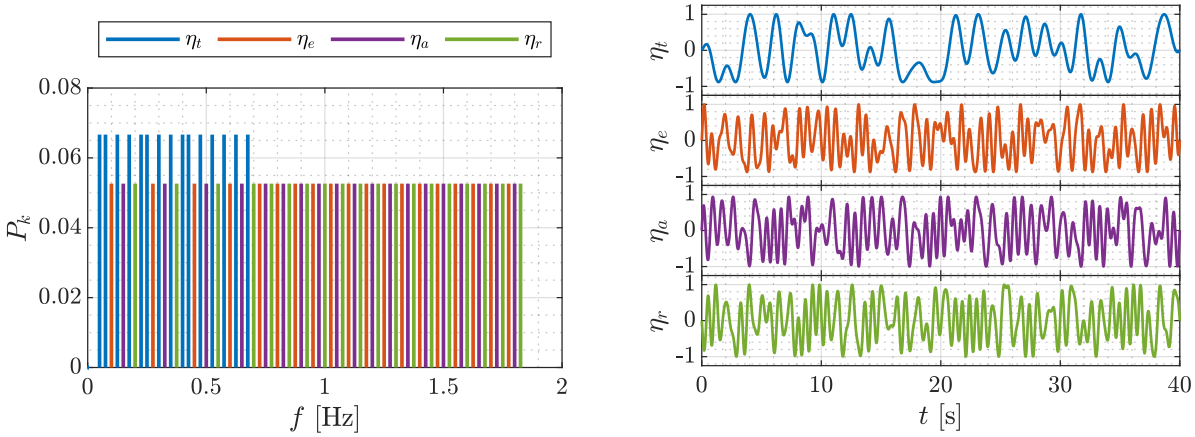

(a) Input spectra for each control effector

(b) Multisine signals for each control effector

Figure 3.4: Orthogonal phase-optimized multisine excitation input design.

values in real-time. The pilot also had the ability to adjust the amplitude of the throttle excitation inputs at discrete values of 0%, ±10%, or ±20%, which keeps excitation inputs near the trim thrust setting and avoids throttle command saturation. Data gathered using these experimental techniques around the nominal trimmed, steady, level flight condition for the aircraft provide rich information content for model identification using the methods described in the following section.

3.4 Aero-Propulsive Modeling Approaches

Two novel approaches for aero-propulsive model development for propeller-driven, fixed-wing aircraft were investigated. Both approaches involve developing models from flight-test data gathered using the multisine maneuver described in Section 3.3. The first approach develops an integrated aero-propulsive model. The second approach identifies a decoupled propulsion model to accompany a bare airframe aerodynamic model. Each method is developed in the following subsections.

For each aero-propulsive model development approach, the primary model structure determination methods was the MOF modeling algorithm [19, 102] described in Section 2.6.2.1. Both PSE and R^2 were used as a cutoff threshold for candidate model terms to include in the final model structure. After the orthogonal regressors were ranked by their ability to reduce the MSFE, the cutoff for model term addition was chosen to be either the candidate model term that minimized the PSE or the last term to increase R^2 by 0.5%, whichever resulted in fewer model terms. As a final step, the MOF results were manually assessed using stepwise regression procedures [19, 103], described in Section 2.6.2.2, to assess whether to include or exclude fringe model terms. After determining the model terms to include in

the model structure, the final parameter values were estimated using least-squares regression with ordinary time-domain regressors (see Section 2.6.1.1).

3.4.1 Approach I: Integrated Aero-Propulsive Modeling

The first approach applied in this work, referred to as "Approach I," is to identify a model describing a combined representation of propulsion aerodynamics and airframe aerodynamics, as well as their interactions. Identification of an integrated aero-propulsive model requires gathering flight data with simultaneous excitation of all control surfaces and the propulsion system in a single maneuver in order to characterize all possible interactions. Accordingly, the multiple-input multisine maneuver described in Section 3.3 and shown in Figure 3.4 was executed to acquire modeling data. The CZ-150 flight data used for model identification are shown in Figure 3.5, where it can be seen that the multi-axis input strategy efficiently excites all aircraft dynamics in a single maneuver around the reference flight condition of $V = 70$ ft/s, $\alpha = 1$ deg, and $J = 0.5$. Although the input command for the propulsion system is the throttle signal η_t, the advance ratio J is the more important quantity to describe propeller aerodynamics. The throttle input is more closely related to the propulsor rotational speed n, but as can be seen in Figure 3.5c, the signals n and η_t are not in perfect proportion because propulsor rotational speed also depends on airspeed V. The multi-axis maneuver results in decorrelated velocity and propulsor rotational speed with good coverage throughout the variable space, which also leads to good coverage of advance ratio.

The response variables, or dependent variables, are defined as the aircraft nondimensional force and moment coefficients in the body axes [see Equation (2.13)]. The body-axis force coefficients are calculated from flight data as shown in Equation (2.16), except without the thrust T being specified separately (i.e., $C_X = \frac{ma_x}{\bar{q}S}$). The body-axis moment coefficients are calculated using the aircraft rotational dynamics equations [Equations (2.10)-(2.12)] accounting for the transient torque and gyroscopic effects from the propulsion system rotation aligned with the body x-axis:

$$C_l = \frac{1}{\bar{q}Sb}\left[I_x\dot{p} - I_{xz}\dot{r} + (I_z - I_y)qr - I_{xz}pq + \dot{h}_x\right] \tag{3.7}$$

$$C_m = \frac{1}{\bar{q}S\bar{c}}\left[I_y\dot{q} + (I_x - I_z)pr + I_{xz}(p^2 - r^2) + rh_x\right] \tag{3.8}$$

$$C_n = \frac{1}{\bar{q}Sb}\left[I_z\dot{r} - I_{xz}\dot{p} + (I_y - I_x)pq + I_{xz}qr - qh_x\right] \tag{3.9}$$

The angular momentum of a single propulsor with its axis of rotation along the body x-axis is

$$h_x = I_p\Omega \tag{3.10}$$

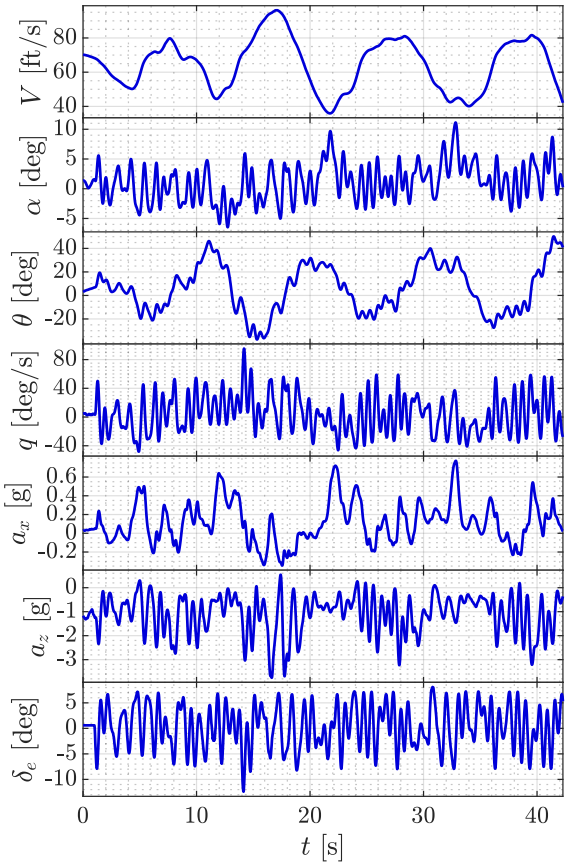

(a) Longitudinal data

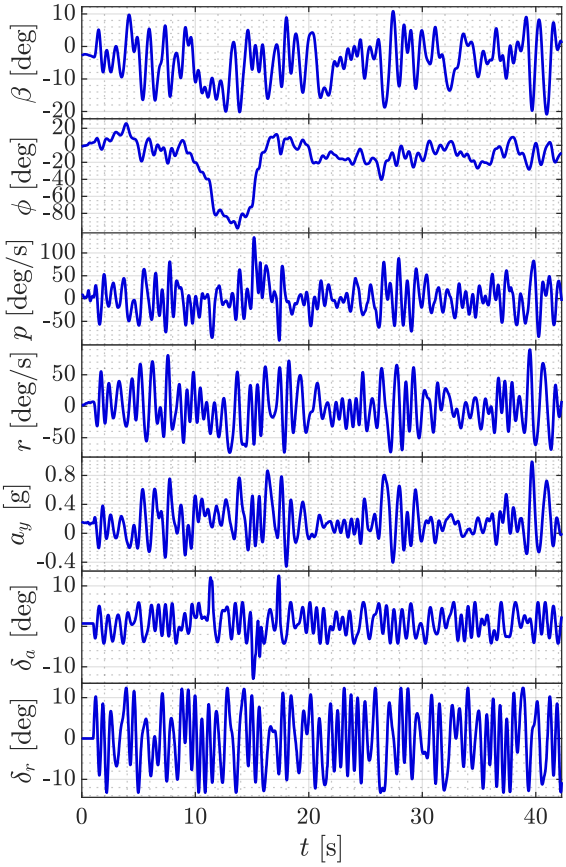

(b) Lateral-directional data

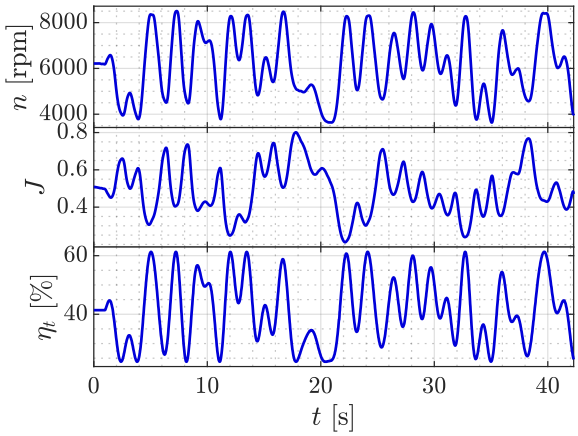

(c) Propulsion data

Figure 3.5: Multiple-input multisine flight maneuver used for model identification.

where I_p is the moment of inertia of the rotating portion of the propulsor and $\Omega = 2\pi n$ is the rotation rate in radians per second, with clockwise rotation being positive as viewed

from behind. It is important to include the propulsor transient torque effects as shown in Equation (3.7) if the propulsion system is dynamically excited while maneuvering. Similarly, when using a single propeller while maneuvering, gyroscopic effects should be included as shown in Equations (3.8)-(3.9). The CZ-150 aircraft studied in this work has a single propeller that is dynamically excited during the system identification maneuver, requiring use of these equations.

The explanatory variables used to develop a functional representation of the body-axis force and moment coefficients include angle of attack α in radians; angle of sideslip β in radians; dimensionless angular rates, $\hat{p}$, $\hat{q}$, $\hat{r}$ [Equation (2.20)]; dimensionless angle of attack rate $\hat{\dot{\alpha}}$ [Equation (2.21)]; and control surface deflection angles, δ_e, δ_a, δ_r, in radians. Although $\hat{q}$ and $\hat{\dot{\alpha}}$ can be highly correlated in standard flight maneuvers, the frequency range included in the multisine input signals excited both the phugoid and short period mode, which sufficiently decorrelates the signals for modeling [162]. A cross plot of q and $\dot{\alpha}$, as well as $\hat{q}$ and $\hat{\dot{\alpha}}$, for the maneuver used for modeling (Figure 3.5) is shown in Figure 3.6. The corresponding pairwise correlation coefficient r between $\hat{q}$ and $\hat{\dot{\alpha}}$ is 0.571. This correlation coefficient value is well below the typical 0.9 correlation coefficient guideline to avoid data collinearity problems [19, 20], demonstrating that the $\hat{q}$ and $\hat{\dot{\alpha}}$ signals are sufficiently decorrelated for accurate model identification.

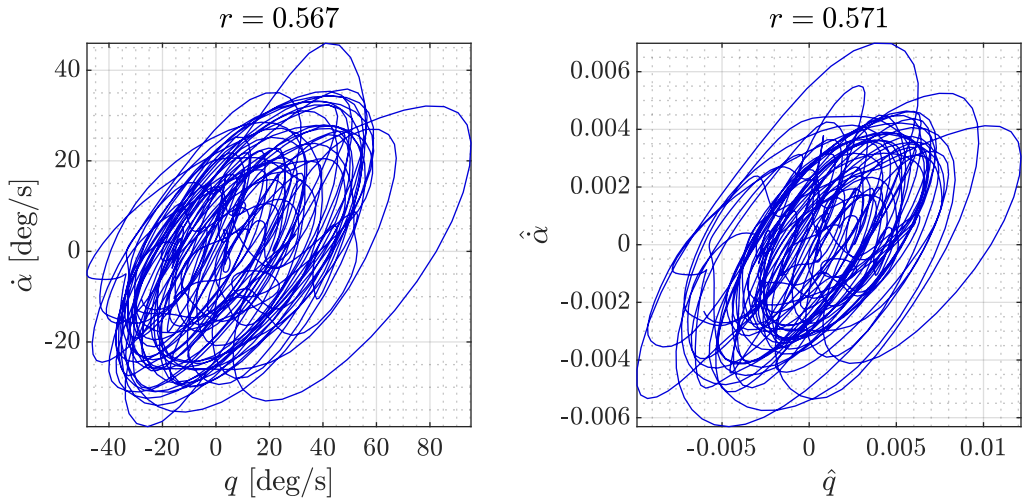

Figure 3.6: Cross plot of q and $\dot{\alpha}$ signals for the maneuver shown in Figure 3.5.

For this work, the longitudinal coefficients (C_X, C_Z, C_m) are expressed as functions of longitudinal state and control variables $(\alpha, \hat{\dot{\alpha}}, \hat{q}, \delta_e)$ and lateral-directional coefficients (C_Y, C_l, C_n) are expressed as functions of lateral-directional state and control variables $(\beta, \hat{p}, \hat{r}, \delta_a, \delta_r)$. This approach is consistent with past work in aircraft system identification [19, 71]. The one exception is that β is also included as an explanatory variable in C_X to model the drag due to sideslip.

Additional explanatory variables are needed to characterize propulsion and propulsion-

airframe interaction effects. The propeller rotational speed n could be used as an explanatory variable, but the variable does not have a widely-used dimensionless form compatible with using the body-axis force and moment coefficients as the response variables. As mentioned previously, advance ratio J is commonly used to parameterize propeller aerodynamics using the propeller thrust coefficient C_T and torque coefficient C_Q as the response variables; however, parameterizing propulsion effects with a polynomial expansion of advance ratio when using the aircraft force and moment coefficients as response variables is not physically consistent. The force and moment coefficients are normalized by freestream dynamic pressure $\bar{q}$, rather than ρn^2 [cf. Equations (3.1)-(3.2)], which is proportional to the dynamic pressure experienced by the individual propeller blades. Geometric constants used for normalization of the airframe and propeller response variables are also different, but these are constant for a particular aircraft, rather than dynamically changing quantities.

To derive a more physically-justified dimensionless variable to characterize the primary propulsion effect on the aircraft force and moment coefficients, consider a model for the propeller thrust coefficient that is quadratic in advance ratio:

$$C_T = C_{T_o} + C_{T_J} J + C_{T_{J^2}} J^2 = C_{T_o} + C_{T_J} \left(\frac{V}{nD} \right) + C_{T_{J^2}} \left(\frac{V}{nD} \right)^2 \tag{3.11}$$

A quadratic model is often a good approximation of C_T as a function of J, as was shown in Figure 3.3. Converting this model to dimensional thrust T using the definition of thrust coefficient [Equation (3.1)] yields:

$$\begin{aligned} T &= \rho n^2 D^4 \left[C_{T_o} + C_{T_J} \left(\frac{V}{nD} \right) + C_{T_{J^2}} \left(\frac{V}{nD} \right)^2 \right] \\ &= \rho D^2 \left(C_{T_o} D^2 n^2 + C_{T_J} D n V + C_{T_{J^2}} V^2 \right) \end{aligned} \tag{3.12}$$

For the thrust force oriented along the body x-axis, the propulsion component of the body x-axis force coefficient C_{X_P} [cf. Equation (2.13)] can be written as:

$$C_{X_P} = \frac{T}{\frac{1}{2}\rho V^2 S} = \frac{2D^2}{S} \left[C_{T_o} \left(\frac{nD}{V} \right)^2 + C_{T_J} \left(\frac{nD}{V} \right) + C_{T_{J^2}} \right] \tag{3.13}$$

The quantity nD/V is the inverse of advance ratio. For notational convenience, this quantity is defined as:

$$\mathcal{J} = \frac{nD}{V} \tag{3.14}$$

Absorbing the constant terms into the model parameters, the propulsion component of the x-axis force coefficient can be written as:

$$C_{X_P} = C_{X_{P_{\mathcal{J}^2}}} \mathcal{J}^2 + C_{X_{P_{\mathcal{J}}}} \mathcal{J} + C_{X_{P_o}} \tag{3.15}$$

A similar derivation can be performed for torque coefficient parameters.

Following the results of this analysis, $\mathcal{J}$ is defined to be the primary explanatory variable for the propulsion system. This variable is defined as an explanatory variable for all force and moment coefficients for generality, although, the MOF modeling process will omit the variable if it does not contribute to improving the model. The variable aids in describing the thrust and torque influences, as well as propulsion-airframe interaction effects which are related to the dynamic pressure within the propeller slipstream. For example, a control surface behind a propeller would have interaction effects that theoretically scale with the slipstream dynamic pressure,

$$\bar{q}_{ss} = \frac{1}{2}\rho V^2 + \frac{T}{A} \tag{3.16}$$

which is the theoretical dynamic pressure located behind a propeller derived from momentum theory [158, 163]. The slipstream dynamic pressure consists of the sum of freestream dynamic pressure $\bar{q} = \frac{1}{2}\rho V^2$ and propeller disk loading T/A, where $A = \frac{\pi}{4}D^2$ is the propeller disk area. It follows that including $\mathcal{J}$ in a multivariate polynomial expansion with the other explanatory variables defined above enables characterization of thrust-related interaction effects. Note that since $\mathcal{J}$ is always biased above zero for an aircraft operating in forward flight, the variable must be centered on a reference value for this approach to decorrelate nonlinear regressors and align with the assumptions of a multivariate Taylor series expansion taken from a single reference point [19]. Centered $\mathcal{J}$ is defined as,

$$\mathcal{J}_c = \mathcal{J} - \mathcal{J}_o \tag{3.17}$$

where $\mathcal{J}_o = 2$ is the centering reference value for the CZ-150 aircraft corresponding to a nominal value for steady, level flight.

As discussed in Section 3.2.2, propellers will produce an off-axis force and moment component when operating at incidence relative to the oncoming airflow. Assuming that the propeller axis of rotation is parallel to the body x-axis, the propeller incidence angle i_p, shown in Figure 3.7, is computed from the body-axis velocity components:

$$i_p = \cos^{-1}\left(\frac{u}{\sqrt{u^2+v^2+w^2}}\right) \tag{3.18}$$

The incidence angle can be conceptualized as a combination of the local angle of attack and local angle of sideslip, or the total angle of attack, for the propeller, which determines the propeller aerodynamic forces and moments due to assumed axial symmetry. An additional flow angle must be defined to determine the acting direction for the auxiliary force and moment component. This quantity, defined here as ξ_p, is the angle specifying the local velocity projection onto the propeller disk plane, or the y–z plane. Figure 3.8 shows a schematic of the definition of ξ_p, which is calculated as:

$$\xi_p = \tan^{-1}\left(\frac{v}{w}\right) \tag{3.19}$$

This airflow angle description has been used to model propellers at incidence in previous work [37]; a similar representation is used for axially symmetric atmospheric re-entry vehicles [164].

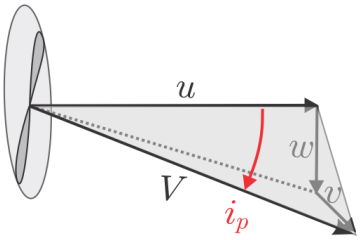

Figure 3.7: Definition of incidence angle, i_p, for a propeller aligned with the body x-axis.

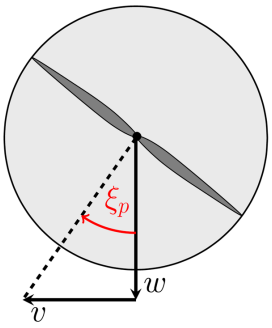

Figure 3.8: Definition of ξ_p on a propeller disk schematic.

As mentioned in Section 3.2.2, Reference [73] shows that the off-axis force and moment component are linearly proportional to the propeller incidence angle i_p. Also, recall that for low incidence angle conditions, Reference [73] shows that incidence angle has no effect on axial thrust and torque. These theoretical predictions of propeller behavior at incidence are also supported by experimental data presented in References [36, 157]. Accordingly, propeller incidence angle effects were only considered for y-axis and z-axis force and moment components. Also, for a propeller aircraft operating at arbitrary angle of attack and angle of sideslip (e.g., see Figure 3.5), the acting direction of the off-axis force and moment component will be dependent on ξ_p. To characterize these effects in the body-axis forces and moment coefficients, additional propulsion explanatory variables are defined as,

$$i_z = i_p \cos \xi_p \tag{3.20}$$

$$i_y = i_p \sin \xi_p \tag{3.21}$$

where i_z is used as an explanatory variable for C_Z and C_n, and i_y is used as an explanatory variable for C_Y and C_m.

Furthermore, for the aircraft used in this work, the moment of inertia of the rotating portion of the propulsion system I_p was not known prior to flight testing. Therefore, I_p had to be estimated in flight, as Reference [165] suggested could be accomplished using a maneuver with significant propulsor rotational speed excitation. The parameter I_p occurs in C_l, C_m, and C_n [c.f. Equations (3.7)-(3.10)] and I_p is the same value in each equation. The most accurate I_p estimates were found to be obtained from the C_n equation so I_p was estimated with the C_n model using $\frac{q\Omega}{\bar{q}Sb}$ as an additional regressor [c.f. Equation (3.9)]. The I_p parameter was then fixed to compute C_l and C_m using Equations (3.7)-(3.8). Note that estimating I_p in the C_n equation only works well if both the propulsor speed and pitch rate are well-excited, as is the case when using the multiple-input excitation strategy explained in Section 3.3.

In summary, the propulsion specific explanatory variables are $\mathcal{J}_c$ for all body-axis force and moment coefficients, i_z for C_Z and C_n, and i_y for C_Y and C_m, with the parameter I_p

estimated with C_n. A nonlinear multivariate polynomial model is identified for each force and moment coefficient as a function of the conventional system identification explanatory variables defined above and the derived propulsion modeling variables.

Using Approach I for model development is advantageous because a model characterizing an integrated representation of propulsion and airframe aerodynamics provides the best model formulation for accurate flight simulations [19]. The model form avoids making assumptions about the validity of superposition of propulsion and airframe aerodynamics, and allows characterization of the propeller performance as integrated on the flight vehicle, as opposed to using information from isolated propeller ground testing or analytical calculations. As discussed previously, the common assumption that propulsion and airframe aerodynamics are decoupled for propeller aircraft is flawed and the proposed integrated aero-propulsive modeling approach resolves this typical modeling deficiency for propeller-driven fixed-wing aircraft. However, as a consequence of the integrated model formulation, the independent aerodynamic contributions of the propulsion and airframe aerodynamics are not separable, which means that an independent estimate of propeller thrust is not available. Also, the model would no longer be valid in the event of a propulsion failure. An alternative method allowing separate characterization of propeller performance is discussed next.

3.4.2 Approach II: Decoupled Propulsion Modeling

The second modeling approach, referred to as "Approach II," seeks to develop a decoupled model for the propulsion system using flight data to accompany a separately identified aerodynamic model for the airframe. This work focused on identification of the thrust parameters, but the methods could also be extended to model torque parameters. For the CZ-150 aircraft, the propeller aerodynamic torque effects were determined to be much smaller than the other C_l influences in the model structure identification process, so the propeller aerodynamic torque effects could be safely neglected for this study.

The first step is to identify a bare airframe aerodynamic model. Here, the bare airframe model is estimated using flight data collected in a glide (without the propulsion system operating) using a multisine maneuver with the input signals shown in Figure 3.4 only operating on the control surfaces. The throttle command is fixed to 0%, which results in the propeller spinning in a minimum drag windmill state while modeling data for the bare airframe are collected. A nonlinear multivariate polynomial model for the airframe is then identified for each force and moment coefficient as a function of angle of attack, angle of sideslip, dimensionless angle of attack rate, dimensionless angular rates, and control surface deflection angles.

After developing a model for the bare airframe, a maneuver with the multisine inputs shown in Figure 4.1 active on all control surfaces and the propulsion system is used to identify a decoupled propulsion model. Despite the objective for this step being to only characterize the propeller aerodynamics, it was found to be beneficial to also inject excitation inputs into

the control surface commands during the maneuver, rather than just using an excitation input on the propulsion system. As mentioned previously, this excitation strategy allows gathering data with decorrelated coverage of airspeed and propulsor rotational speed resulting in good advance ratio coverage. For identifying the thrust model, the C_X bare airframe model structure is held fixed and used to predict the C_X contributions from the airframe. The thrust model is then estimated using $C_{X_P} = C_X - C_{X_A}$ as the response variable, where C_{X_A} is the bare airframe model prediction. In this framework, the installed thrust losses are included in the propulsion model and are the only modeled aero-propulsive interaction effect. Following the above developments [see Equations (3.15) and (3.17)], the regressors in the thrust model are $\mathcal{J}_c$ and $\mathcal{J}_c^2$ as well as a vector of ones to estimate the propulsion bias parameter $C_{X_{P_o}}$. The final aero-propulsive model then consists of the superimposed bare airframe and propulsion C_X aerodynamics,

$$C_X = C_{X_A} + C_{X_P} \tag{3.22}$$

and the bare airframe aerodynamic model for the other force and moment coefficients.

Approach II is useful for developing a separate propulsion model to complement a pre-existing bare airframe aerodynamic model developed using computational methods, wind-tunnel testing, and/or flight testing. Defining a separate airframe and propulsion model is also how many flight dynamics simulations are configured, so having a decoupled propulsion model may allow more straightforward implementation into an existing simulation framework compared to the integrated aero-propulsive modeling method (Approach I). Conventionally, isolated testing or analysis is used to develop the propulsion model, but the performance is generally different when the propulsion system is integrated on a flight vehicle. This method provides a direct thrust estimate identified from flight data, which also characterizes the performance differences due to the presence of the airframe. The method, however, requires assuming that all propulsion-airframe interactions can be accounted for as thrust production deviations.

3.5 Results for Approach I: Integrated Aero-Propulsive Modeling

Following the integrated aero-propulsive modeling approach described in Section 3.4.1 (Approach I), the model for each force and moment coefficient was developed using the CZ-150 flight data shown in Figure 3.5. The candidate regressors modeling a significant portion of the variation in the response variable were included in the final integrated aero-propulsive model structure, in accordance with the model structure determination strategy discussed in Section 3.4. The model structure for each force and moment coefficient was determined to be:

$$C_X = C_{X_\alpha}\alpha + C_{X_{\hat{\dot{\alpha}}}}\hat{\dot{\alpha}} + C_{X_{\alpha^2}}\alpha^2 + C_{X_{\beta^2}}\beta^2 + C_{X_{\mathcal{J}_c}}\mathcal{J}_c + C_{X_{\mathcal{J}_c^2}}\mathcal{J}_c^2 + C_{X_o} \tag{3.23}$$

$$C_Y = C_{Y_\beta}\beta + C_{Y_p}\hat{p} + C_{Y_{\delta_a}}\delta_a + C_{Y_{\delta_r}}\delta_r + C_{Y_{\mathcal{J}_c}}\mathcal{J}_c + C_{Y_{i_y}}i_y + C_{Y_{(\mathcal{J}_c\delta_r)}}(\mathcal{J}_c\delta_r) + C_{Y_o} \tag{3.24}$$

$$C_Z = C_{Z_\alpha}\alpha + C_{Z_q}\hat{q} + C_{Z_{\dot{\alpha}}}\hat{\dot{\alpha}} + C_{Z_{\mathcal{J}_c}}\mathcal{J}_c + C_{Z_o} \tag{3.25}$$

$$C_l = C_{l_\beta}\beta + C_{l_p}\hat{p} + C_{l_r}\hat{r} + C_{l_{\delta_a}}\delta_a + C_{l_{\delta_r}}\delta_r + C_{l_{(\mathcal{J}_c\delta_a)}}(\mathcal{J}_c\delta_a) + C_{l_o} \tag{3.26}$$

$$C_m = C_{m_\alpha}\alpha + C_{m_q}\hat{q} + C_{m_{\delta_e}}\delta_e + C_{m_{\dot{\alpha}}}\hat{\dot{\alpha}} + C_{m_{\alpha^2}}\alpha^2 + C_{m_{(\mathcal{J}_c\delta_e)}}(\mathcal{J}_c\delta_e) + C_{m_o} \tag{3.27}$$

$$C_n = C_{n_\beta}\beta + C_{n_r}\hat{r} + C_{n_{\delta_a}}\delta_a + C_{n_{\delta_r}}\delta_r + C_{n_{(\mathcal{J}_c\delta_r)}}(\mathcal{J}_c\delta_r) + C_{n_o} \tag{3.28}$$

After identifying the model structure, least-squares regression was used to determine the final estimates of the model parameters. The parameter estimates $\hat{\theta}$, parameter standard errors accounting for colored residuals $s(\hat{\theta})$ [19, 99], the percent error calculated as $\left[s(\hat{\theta})/|\hat{\theta}|\right] \times 100$, and R^2 value for each body-axis force and moment coefficient model equation are given in Tables 3.2-3.7 at the end of this chapter. The parameter estimates have reasonably low standard error values and each model has a sufficiently high R^2 value, given the high susceptibility to atmospheric disturbances for small aircraft and low-cost instrumentation system used for this study. The model fit to the force and moment coefficient data used for modeling is shown in Figure 3.9. The models shows good agreement with the measured data for all responses. The best model fit is observed for C_X, which has an R^2 value of 99.6%, indicating that the primary propulsive influences are very well characterized.

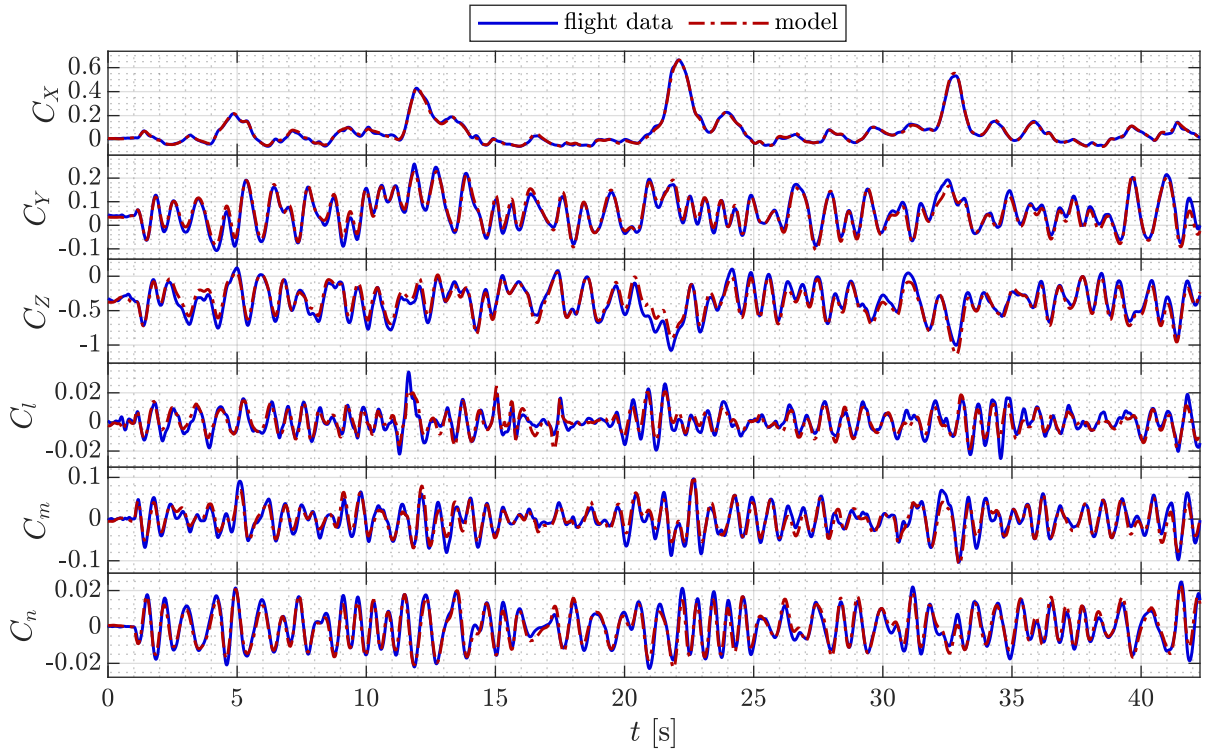

Figure 3.9: Comparison of modeling data and model fit for Approach I.

An alternative modeling approach could be postulated to include advance ratio J [Equation (3.3)] as the dimensionless explanatory variable for modeling aero-propulsive effects, as opposed to $\mathcal{J}$ [Equation (3.14)]. However, as shown previously in Equations (3.11)-(3.15), $\mathcal{J}$ is the more physically consistent variable to include in a multivariate polynomial expansion model for the aircraft force and moment coefficients. This theoretical reasoning was empirically investigated by comparing modeling results using $\mathcal{J}$ and J as modeling variables. Figure 3.10 shows the C_X modeling flight data compared to the model fit using $\mathcal{J}_c$ as an explanatory variable and the model fit using centered J ($J_c = J - J_o$ where $J_o = 0.5$) as an explanatory variable. The figure also compares the absolute modeling residuals and shows the respective R^2 and NRMSE values [Equation (2.86)]. The structure for each model is identical to Equation (3.23), with the exception that J_c replaces $\mathcal{J}_c$ for the model using J_c. The model using $\mathcal{J}_c$ is observed to have a significantly better model fit, a higher R^2 value, and an NRMSE value 3.8 times lower compared to the model using J_c. This demonstrates the benefit of using $\mathcal{J}$ as a propulsion modeling variable when using the aircraft force and moment coefficients as response variables. This approach is effective because propulsion and airframe aerodynamics scale differently and use different expressions for nondimensionalization. The $\mathcal{J}$ variable is used to model propulsion effects in the standard aircraft force and moment coefficients in a form consistent with the correct normalization for propeller aerodynamics. Using J directly in the aircraft force and moment coefficients is akin to using the incorrect nondimensionalization of propulsion effects, which is why degraded modeling performance is observed in Figure 3.10.

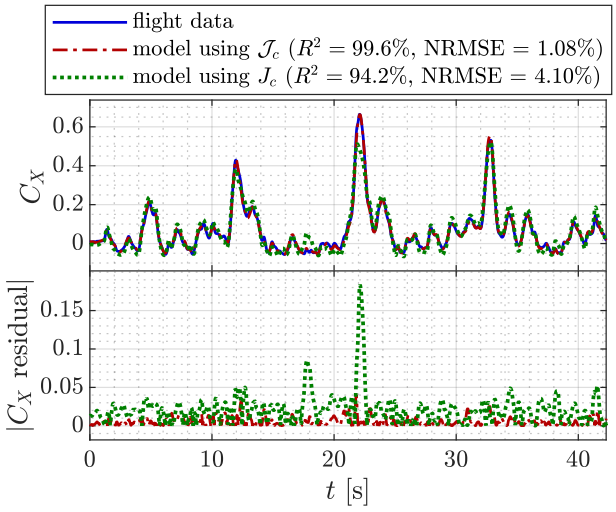

Figure 3.10: Comparison of C_X models using $\mathcal{J}_c$ and J_c as explanatory variables.

Regression methods minimize the summation of squared differences between the modeled and measured response, so assessment of the modeling fit alone does not provide information about the model predictive capability. Assessment of model performance using validation data not used for modeling provides a more reliable estimate of model prediction accuracy.

As mentioned in Section 2.6.3, model validation is also best accomplished using flight data with input waveforms differing from the modeling data. For this work, automated throttle, elevator, aileron, and rudder 3-2-1-1 maneuvers were collected as validation data to assess model performance. These concatenated flight maneuvers are shown in Figure 3.11 along with the model predictions for each of the force and moment coefficients. Overall good model predictive capability is observed, indicating that a quality model has been identified to predict aero-propulsive characteristics driving the aircraft flight dynamic behavior around the nominal reference flight condition. The modeling and validation NRMSE values computed for the response data shown in Figure 3.9 and Figure 3.11, respectively, are compared in Table 3.1. Observing that the modeling and validation NRMSE values are low and similar in value for each response provides further confidence that model development was successful.

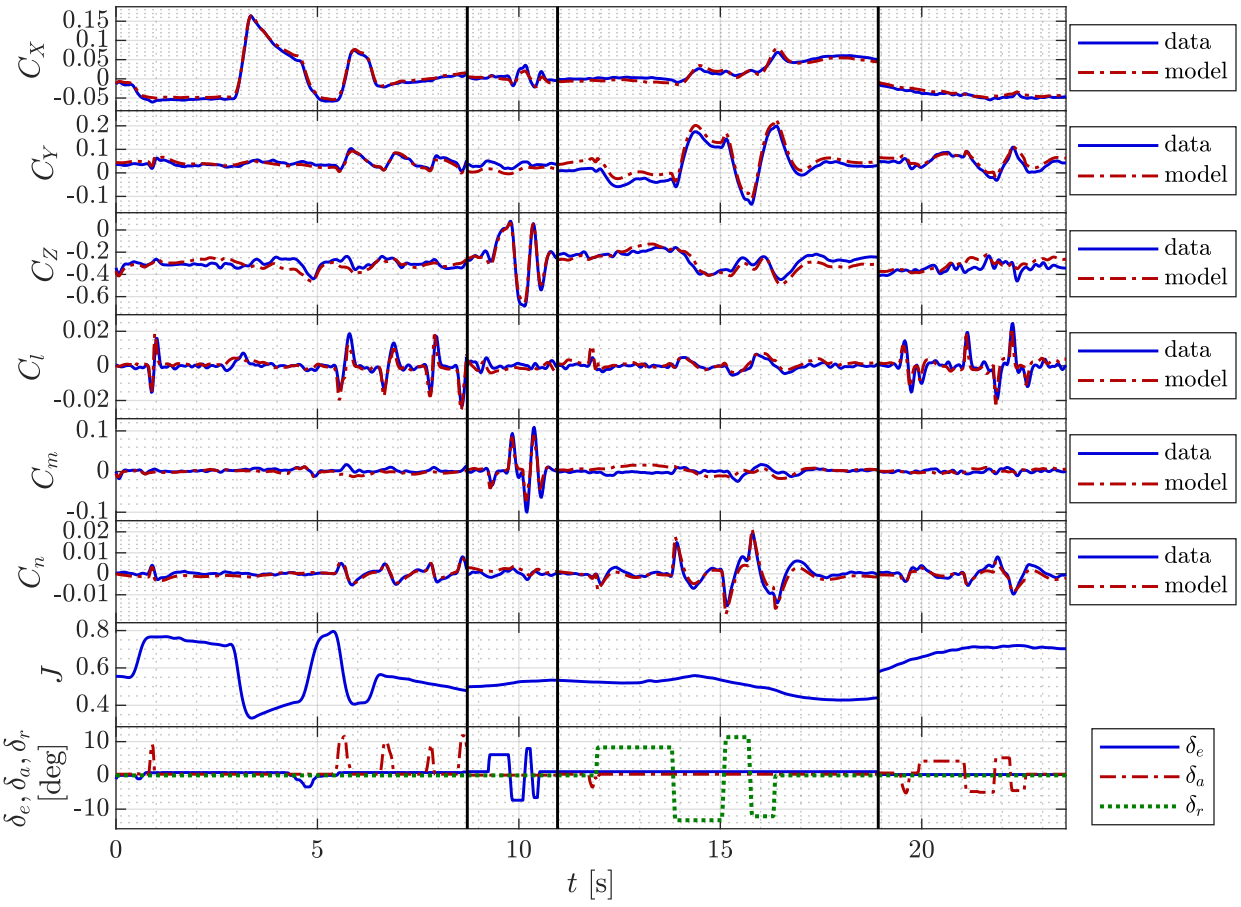

Figure 3.11: Comparison of 3-2-1-1 validation maneuver flight data and model prediction for Approach I.

A few characteristics about the identified aero-propulsive model are highlighted. Excluding the terms with the propulsion variable $\mathcal{J}_c$, the models are mostly linear; the nonlinear model terms are α^2 and β^2 appearing for C_X, which models quadratic drag variation, as well as an α^2 term for C_m. The $\hat{\dot{\alpha}}$ modeling variable is included to aid in modeling unsteady

Table 3.1: Comparison of modeling and validation NRMSE values for Approach I

Metric	C_X	C_Y	C_Z	C_l	C_m	C_n
Modeling NRMSE [%]	1.08	4.09	5.85	5.88	5.85	5.73
Validation NRMSE [%]	0.84	5.11	3.59	4.56	4.22	3.29

aerodynamic phenomena, and was found to be significant in the C_X, C_Z, and C_m models. The propulsion explanatory variable $\mathcal{J}_c$ is included in all longitudinal and lateral-directional responses in the form of isolated effect terms and/or interaction terms (e.g., $\mathcal{J}_c\delta_e$). Also, a propulsion explanatory variable modeling propeller incidence angle effects, i_y, appears in the C_Y model. The i_y and i_z influences for C_Z, C_m, and C_n were found to be too small in the model structure determination process to warrant inclusion in the C_Z, C_m, and C_n models. This is partially because the propeller axis of rotation on the CZ-150 aircraft is canted to help counteract asymmetric effects related to the aircraft having only one propeller. However, i_y and i_z effects should still be considered in the model structure determination process because their influence may be significant for other aircraft and flight conditions. The propulsion effects are expected to be dominant for C_X, but the appearance of propulsion-related model terms in all other responses indicates that the propulsion system has a significant effect on the vehicle aerodynamics beyond generating thrust. Clearly, propulsion and propulsion-airframe interactions are important to consider in the model equations.

The appearance of the $\mathcal{J}\delta_e$, $\mathcal{J}\delta_a$, and $\mathcal{J}\delta_r$ model terms indicate that the propeller slipstream interacts with each control surface. Propulsion-elevator and propulsion-rudder interactions are expected for the CZ-150 aircraft configuration with a nose-mounted propeller. Momentum theory predicts that the slipstream of an isolated propeller will accelerate and contract downstream of the propeller [163]. For the CZ-150, the theoretical propeller slipstream predicted by momentum theory interacts with the fuselage, tail, tail-mounted control surfaces, and inboard portion of the wing. A propulsion-aileron interaction is more difficult to conceptualize in view of momentum theory predictions of propeller slipstream behavior. However, considering the empirical slipstream diffusion and expansion for isolated propellers [166], as well as the large fuselage blockage area behind the CZ-150 propeller (see Figure 3.12), a slipstream expansion resulting in aileron interactions becomes more physically plausible (see Figure 3.13).

3.6 Results for Approach II: Decoupled Propulsion Modeling

As described in Section 3.4.2 (Approach II), the process to identify a decoupled propulsion model from flight data starts with identifying a bare airframe aerodynamic model. Only the C_X model equation is considered here for thrust model identification. Following the model

Figure 3.12: CZ-150 front view.

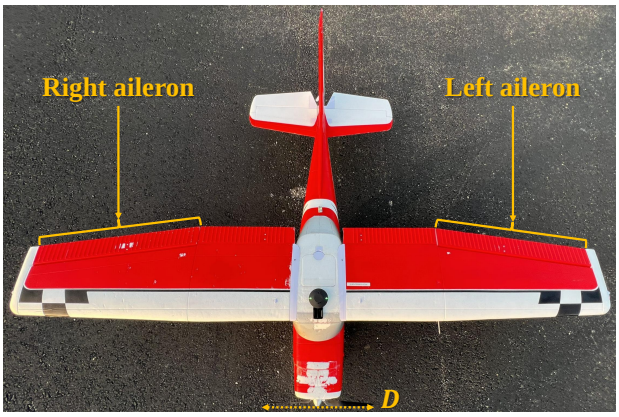

Figure 3.13: CZ-150 overhead view.

structure determination strategy discussed in Section 3.4, the bare airframe model structure for C_X was determined to be:

$$C_{X_A} = C_{X_\alpha}\alpha + C_{X_{\hat{\alpha}}}\hat{\alpha} + C_{X_{\alpha^2}}\alpha^2 + C_{X_{\beta^2}}\beta^2 + C_{X_{A_o}} \tag{3.29}$$

The C_{X_A} model structure is identical to the C_X model structure identified in Approach I [Equation (3.23)] when the propulsion terms are removed. The model fit to flight data collected using a control surface multisine maneuver with the throttle command held at 0% is shown in Figure 3.14a. The model fit is reasonable considering that a bare airframe C_X model is generally more difficult to accurately estimate using flight data and has a smaller influence on aircraft dynamics, compared to the other force and moment coefficients.

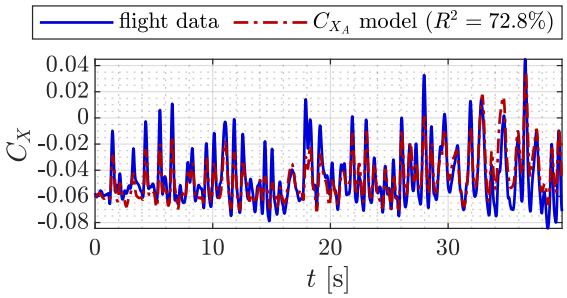

(a) Bare airframe modeling maneuver (step 1)

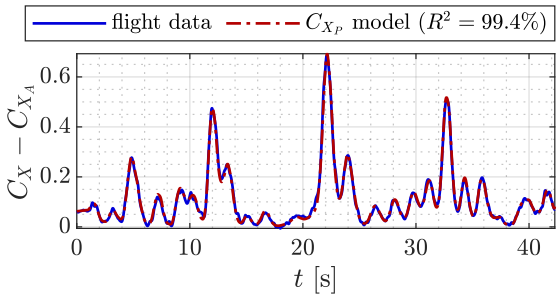

(b) Propulsion modeling maneuver (step 2)

Figure 3.14: C_X model fit for Approach II.

After estimation of the bare airframe model, the propulsion model was estimated with the model structure of Equation (3.15) using centered regressors:

$$C_{X_P} = C_{X_{P_{\mathcal{J}_c^2}}}\mathcal{J}_c^2 + C_{X_{P_{\mathcal{J}_c}}}\mathcal{J}_c + C_{X_{P_o}} \tag{3.30}$$

The data shown in Figure 3.5 were used for modeling, where the response variable was the calculated C_X with the bare airframe aerodynamic model prediction subtracted (C_{X_P} =

$C_X - C_{X_A}$). The model fit to the flight data used for modeling is shown in Figure 3.14b. The visual model fit is very good and the R^2 value of 99.4% is very high, indicating that most of the variation of the response about its mean value is characterized by the C_{X_P} model.

The final C_X model structure is the sum of the identified bare airframe model and propulsion model:

$$\begin{aligned} C_X &= C_{X_A} + C_{X_P} \\ &= \left(C_{X_\alpha}\alpha + C_{X_{\dot{\alpha}}}\hat{\dot{\alpha}} + C_{X_{\alpha^2}}\alpha^2 + C_{X_{\beta^2}}\beta^2 + C_{X_{A_o}}\right) + \left(C_{X_{P_{\mathcal{J}_c^2}}}\mathcal{J}_c^2 + C_{X_{P_{\mathcal{J}_c}}}\mathcal{J}_c + C_{X_{P_o}}\right) \end{aligned} \tag{3.31}$$

The model structure is identical to Equation (3.23), except that the bias terms $C_{X_{A_o}}$ and $C_{X_{P_o}}$ are accounted for as separate model parameters. This is possible because the $C_{X_{A_o}}$ term resulting from the bare airframe model is fixed for identifying the propulsion model, which allows $C_{X_{P_o}}$ to be independently estimated. Decoupling these bias parameters allows the model to make a direct prediction of the thrust produced by the propeller. The C_{X_A} and C_{X_P} model parameter estimates and parameter standard errors are shown in Table 3.8 at the end of this chapter. The standard errors for the model parameters are small, indicating that an accurate model has been identified. The uncertainty in the propulsion model parameters, accounting for colored residuals, is 2.5% or lower, indicating that the parameters are estimated very accurately.

The combined, flight-derived C_X model response compared to the powered-airframe C_X calculated from the flight data used for modeling is shown in Figure 3.15. A model composed of the C_{X_A} parameters identified from flight data combined with the quadratic thrust model developed from available isolated propeller wind-tunnel data [116, 161] (see Figure 3.3) is also shown for comparison. The combined, flight-derived C_X model response shows an excellent match to the C_X flight data, indicating that the C_X propulsion and airframe aerodynamics have been well characterized. The model response using the thrust model derived from wind-tunnel data is seen to overpredict C_X, particularly at higher C_X values, which corresponds to lower advance ratio values (see Figure 3.5c). The NRMSE value for the model developed using only flight data is 5.4 times lower than the model using the wind-tunnel data to predict the propulsion aerodynamics.

Figure 3.16 shows the wind-tunnel data and quadratic model fit that were shown previously in Figure 3.3, as well as a curve showing the flight-derived propulsion model prediction of C_T variation with J. The flight-derived model shows reasonable agreement with the independently obtained wind-tunnel data set, assuming that the data and model are from the same system; however, the wind-tunnel data are for the propeller in isolation, whereas the flight-derived model includes performance losses attributed to the presence of the airframe. The plot shows that the flight-derived model predicts a lower thrust value across most of the advance ratio range tested, particularly at lower advance ratio, and suggests that the flight-derived model is able to describe performance losses not accounted for in the wind-tunnel data. The overall takeaway from Figures 3.15-3.16 is that the propulsion model identified

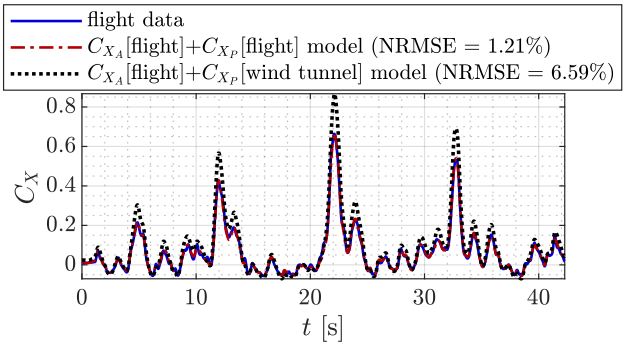

Figure 3.15: Combined C_X model fit for Approach II.

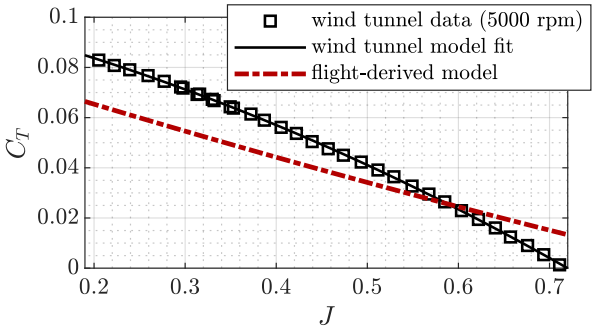

Figure 3.16: Comparison of the identified thrust model to isolated propeller wind-tunnel data [116, 161].

from flight data provides a better overall prediction of the propulsion aerodynamics in flight. The wind-tunnel-derived predictions generally overestimate thrust because there are significant propulsion performance losses when integrated onto the aircraft. These results show that there are clear advantages to developing a propulsion model using flight data.

A throttle 3-2-1-1 maneuver not used for model identification, shown in Figure 3.17a, was used to test and compare the predictive capability of all modeling approaches shown in this chapter for C_X, where the propulsion effects are most prominent. Figure 3.17b shows C_X flight data compared to model predictions and the absolute validation residuals using:

1. The integrated aero-propulsive model identified using flight data (Approach I)
2. The combined bare airframe model and propulsion model identified using flight data (Approach II)
3. The combined bare airframe model identified using flight data and the propulsion model consisting of a quadratic fit to isolated propeller wind-tunnel data [116, 161]

Approach I provides the best prediction of the validation flight data, the smallest residuals, and the lowest NRMSE value. This result makes sense because Approach I models the airframe and propulsion aerodynamics together, without the assumption that their effects

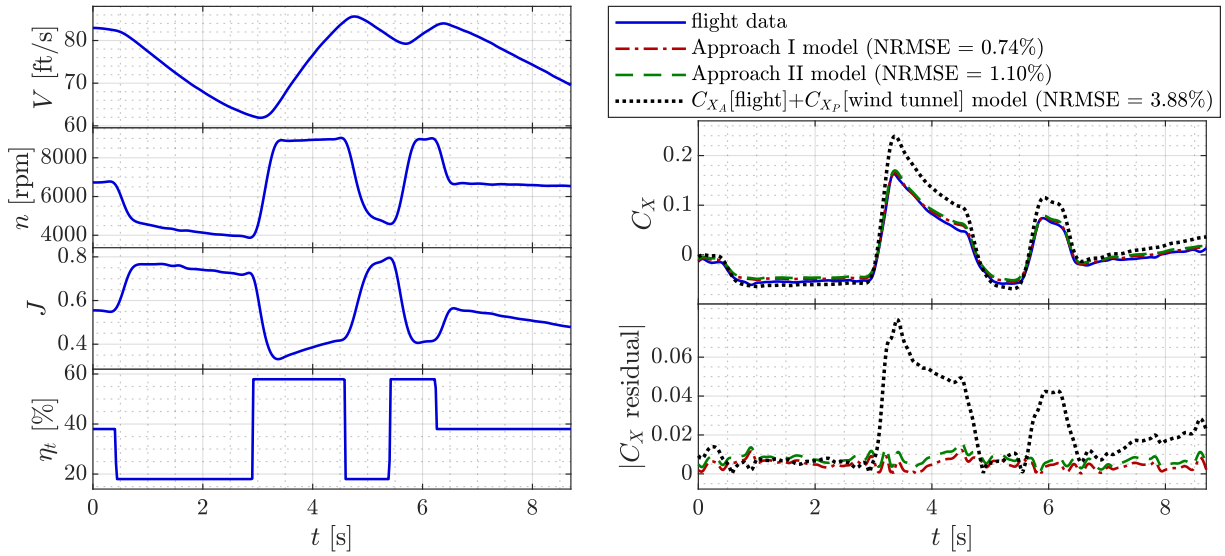

(a) Validation data time history

(b) Model prediction comparison

Figure 3.17: C_X model validation for all approaches.

decouple. Approach II provides the next best prediction of the validation flight data. The assumption that propulsion and airframe aerodynamics can be identified separately, and then combined, is an explanation for the slightly degraded modeling performance compared to Approach I. Although, overall, the prediction capability of Approach I and Approach II is comparable. The worst model prediction capability is observed for the model using the wind-tunnel-derived propulsion model, where the NRMSE value is 5.2 and 3.5 times higher than the NRMSE value for Approach I and Approach II, respectively. The prediction capability is the worst at high C_X values or low J values, which is where the propeller thrust is the highest. This plot shows the importance of characterizing propeller aerodynamics using flight data to model installed performance deviations and, ultimately, develop better predictions of the aircraft behavior in flight.

Additional Results for the MTD and eSPAARO Aircraft Propellers

Figure 3.18 shows flight-derived propulsion model predictions of thrust coefficient variation with advance ratio for the propellers used on the MTD and eSPAARO aircraft introduced in Section 2.1.2, along with available wind-tunnel data [114, 167] and vortex theory data [168]. Similar to the results obtained for the CZ-150 aircraft, the flight-derived model shows reasonable agreement with the independently obtained isolated propeller data and the performance differences are attributed to the presence of the airframe. The flight-derived models include the integrated performance differences, which results in more accurate characterization of the propulsion aerodynamics in flight. Figure 3.18a shows that the flight-derived

MTD propeller model predicts a lower thrust value across most of the advance ratio range tested, indicating that the flight-derived model is able to describe integrated performance losses not accounted for in the wind-tunnel and vortex theory data. In contrast, Figure 3.18b shows that the flight-derived eSPAARO propeller model predicts a slightly greater thrust value across most of the advance ratio range tested, which could be attributed to a favorable fuselage boundary layer ingestion effect [169]. The assortment of results shown in this chapter demonstrate that there are significant advantages to developing a propulsion model using flight data for flight dynamics, controls, and performance analyses.

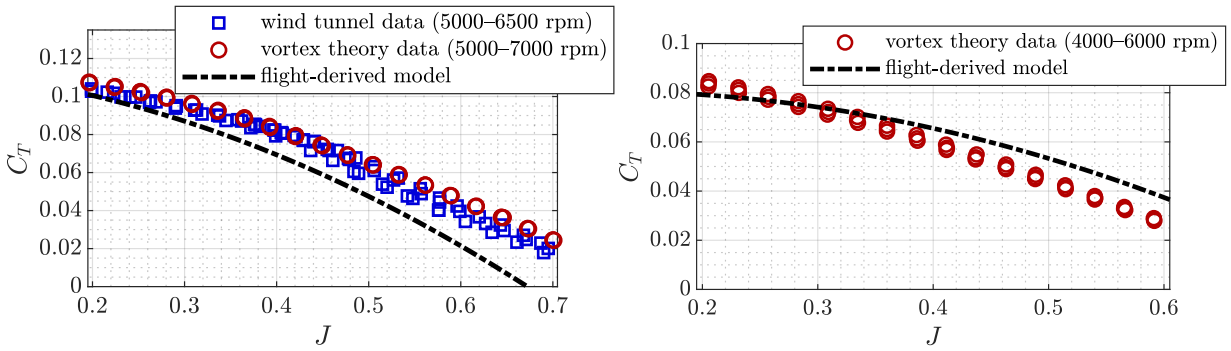

(a) MTD propeller

(b) eSPAARO propeller

Figure 3.18: Comparison of MTD and eSPAARO flight-derived thrust models to isolated propeller wind-tunnel data [114, 167] and vortex theory data [168].

Acknowledgment of Collaborative Research

The research presented in this chapter was primarily conducted by the author, but included important collaborative contributions with other individuals. The experiment design was conceptualized and implemented in collaboration with James Gresham, with the author leading development of the excitation input design strategy. Gresham performed all aircraft development and integration efforts, as well as all laboratory and flight-test experiments. Flight-test support was also provided by Jean-Michel Fahmi and Jeremy Hopwood. The research in this chapter was advised by Craig Woolsey who offered many helpful suggestions throughout the research process and manuscript preparation. The author gratefully acknowledges and appreciates these efforts which made the research described in this chapter possible.

Parameter Estimate Tables

Table 3.2: Approach I C_X parameter estimates ($R^2 = 99.6\%$)

Parameter	$\hat{\theta}$	$s(\hat{\theta})$	% Error
C_{X_α}	+0.188	0.0144	7.7
$C_{X_{\dot{\alpha}}}$	−1.88	0.210	11.1
$C_{X_{\alpha^2}}$	+1.90	0.157	8.3
$C_{X_{\beta^2}}$	+0.282	0.0248	8.8
$C_{X_{\mathcal{J}_c}}$	+0.113	0.00207	1.8
$C_{X_{\mathcal{J}_c^2}}$	+0.0416	0.00100	2.4
C_{X_o}	+0.00678	0.000833	12.3

Table 3.3: Approach I C_Y parameter estimates ($R^2 = 95.4\%$)

Parameter	$\hat{\theta}$	$s(\hat{\theta})$	% Error
C_{Y_β}	−0.654	0.0171	2.6
C_{Y_p}	−0.233	0.0809	34.8
$C_{Y_{\delta_a}}$	−0.182	0.0346	19.1
$C_{Y_{\delta_r}}$	+0.114	0.00867	7.6
$C_{Y_{\mathcal{J}_c}}$	+0.00762	0.00251	33.0
$C_{Y_{i_y}}$	+0.110	0.0131	11.9
$C_{Y_{(\mathcal{J}_c\delta_r)}}$	+0.0776	0.0113	14.6
C_{Y_o}	+0.0139	0.00378	27.3

Table 3.4: Approach I C_Z parameter estimates ($R^2 = 90.1\%$)

Parameter	$\hat{\theta}$	$s(\hat{\theta})$	% Error
C_{Z_α}	−2.99	0.319	10.7
C_{Z_q}	−24.7	5.12	20.8
$C_{Z_{\dot{\alpha}}}$	+31.1	4.60	14.8
$C_{Z_{\mathcal{J}_c}}$	−0.0459	0.0171	37.3
C_{Z_o}	−0.290	0.0169	5.8

Table 3.5: Approach I C_l parameter estimates ($R^2 = 80.6\%$)

Parameter	$\hat{\theta}$	$s(\hat{\theta})$	% Error
C_{l_β}	−0.0446	0.00295	6.6
C_{l_p}	−0.333	0.0202	6.1
C_{l_r}	+0.118	0.00845	7.2
$C_{l_{\delta_a}}$	−0.196	0.00997	5.1
$C_{l_{\delta_r}}$	+0.00527	0.00202	38.2
$C_{l_{(\mathcal{J}_c\delta_a)}}$	−0.0441	0.00627	14.2
C_{l_o}	−0.000194	0.000342	176

Table 3.6: Approach I C_m parameter estimates ($R^2 = 86.5\%$)

Parameter	$\hat{\theta}$	$s(\hat{\theta})$	% Error
C_{m_α}	−0.277	0.0275	10.0
C_{m_q}	−7.10	0.461	6.5
$C_{m_{\delta_e}}$	−0.469	0.0295	6.3
$C_{m_{\dot{\alpha}}}$	+2.70	0.731	27.0
$C_{m_{\alpha^2}}$	−0.673	0.234	34.8
$C_{m_{(\mathcal{J}_c\delta_e)}}$	−0.137	0.0172	12.6
C_{m_o}	+0.0112	0.00130	11.6

Table 3.7: Approach I C_n parameter estimates ($R^2 = 91.9\%$)

Parameter	$\hat{\theta}$	$s(\hat{\theta})$	% Error
C_{n_β}	+0.0452	0.00207	4.6
C_{n_r}	−0.0983	0.00919	9.3
$C_{n_{\delta_a}}$	+0.0341	0.00340	10.0
$C_{n_{\delta_r}}$	−0.0544	0.00253	4.7
$C_{n_{(\mathcal{J}_c\delta_r)}}$	−0.0210	0.00277	13.2
C_{n_o}	+0.00251	0.000316	12.6
I_p, slug·ft^2	+0.000718	0.000127	17.6

Table 3.8: Approach II C_{X_A} and C_{X_P} parameter estimates

Parameter	$\hat{\theta}$	$s(\hat{\theta})$	% Error
C_{X_α}	+0.193	0.0269	13.9
$C_{X_{\dot{\alpha}}}$	−1.52	0.274	18.0
$C_{X_{\alpha^2}}$	+1.24	0.140	11.3
$C_{X_{\beta^2}}$	+0.190	0.0328	17.3
$C_{X_{A_o}}$	−0.0565	0.00281	5.0
$C_{X_{P_{\mathcal{J}_c^2}}}$	+0.0427	0.00108	2.5
$C_{X_{P_{\mathcal{J}_c}}}$	+0.114	0.00229	2.0
$C_{X_{P_o}}$	+0.0664	0.000671	1.0

Chapter 4

Nonlinear Dynamic Model Identification with Unknown Mass Properties

Development of a nonlinear dynamic model for fixed-wing aircraft generally requires accurate, labor-intensive mass properties estimation. This chapter describes a method to identify a nonlinear dynamic model for fixed-wing aircraft using flight data without requiring knowledge of the aircraft mass or moments of inertia. The standard nonlinear rigid-body aircraft equations of motion are reformulated and the nondimensional force and moment coefficients are redefined to be agnostic to vehicle mass properties. Flight experiments for system identification of a small, unmanned, fixed-wing aircraft are conducted using orthogonal phase-optimized multisine inputs applied simultaneously to the aircraft control surfaces. A nonlinear aerodynamic model is then identified for both the proposed mass-agnostic modeling framework and a standard nonlinear modeling approach requiring mass properties information. The identified mass-agnostic nonlinear dynamic model and the traditional nonlinear dynamic model are shown to each provide a good fit to the modeling data and have good prediction capability of flight data not used for model identification in comparative flight simulations. The chapter describes application of the modeling method to a small unmanned aircraft, but the method is generalizable to many aircraft configurations. The mass-agnostic dynamic modeling method will be particularly useful for modern electric aircraft that have limited mass properties changes over the course of a flight, where the identified model can be used for numerous controls and flight simulation applications. This work has been published as a conference paper [25] and a journal engineering note [26].

The chapter is organized as follows: Section 4.1 describes the motivation for this research. Section 4.2 provides an overview of the flight-test experiment design. The dynamic modeling approach is formulated in Section 4.3. Section 4.4 presents modeling results and provides a direct comparison to standard modeling methods.

4.1 Research Motivation

One standard approach for aircraft system identification is estimation of dimensional aerodynamic parameters in transfer function or state space models [19–21]. This approach does not require knowledge of aircraft mass properties, but the linear models are only valid for a small region around the reference flight condition where the model was identified. Also, for small, inexpensive aircraft, the excitation amplitudes needed to obtain a sufficient signal-to-noise ratio for model identification may necessitate the use of nonlinear models. An alternative approach is to develop a model by identifying parameters in a linear or nonlinear aerodynamic model within the nonlinear rigid-body aircraft equations of motion [19, 20], which was the approach discussed in Section 2.2. The resulting model accommodates characterization of more complex, nonlinear aerodynamics over a larger range of flight conditions, but the typical formulation used in previous work requires knowledge of aircraft mass properties, including the overall mass and inertia tensor elements.

Numerous approaches exist for determining the aircraft mass properties needed for aircraft system identification. Vehicle mass properties can be determined from computerized aircraft representations [170–174] or empirical ground tests [175–187]. Measuring the mass of an aircraft in ground testing is generally straightforward; however, accurately estimating aircraft inertia tensor elements is more difficult, time consuming, and expensive. Traditionally, the inertia tensor for flight-test aircraft is determined during ground testing with a pendulum or spinning apparatus. Ground-test methods generally require suspending the aircraft and initiating dynamic swinging or spinning motion. This process can cause damage to the aircraft, necessitates engineering analysis, and adds scheduling requirements for high-demand flight-test assets. The mass properties must also be adjusted when making modifications to the aircraft, either by performing new empirical ground testing or by carefully bookkeeping the modified mass distribution. Mass properties bookkeeping becomes especially burdensome for aircraft that collect flight-test data in many configurations. For example, unmanned aircraft used for combat or package delivery applications may have numerous sensor, payload, external store, and fuel loading combinations, each with different mass properties. Recent flight-test research demonstrated an alternative approach for determining moments of inertia using a specialized flight-test technique for fixed-wing aircraft [165]. Regardless of the method used for estimation of mass properties, significant engineering effort and expertise are needed to precisely estimate the aircraft moments of inertia, and inaccurate inertia estimates corrupt estimation of nondimensional aerodynamic parameters [188, 189].

In this chapter, a method is proposed for nonlinear dynamic model identification for aircraft using flight testing that does not require knowledge of the vehicle mass and inertia tensor. The modeling framework assumes a constant unity mass, a constant identity inertia tensor, and neglects the inertial coupling and gyroscopic precession terms in the rotational dynamics equations, but still allows identification of a nonlinear aerodynamic model. The approach is effectively a combination of the two standard modeling approaches discussed above. The mass properties are subsumed into the model parameters similar to the first ap-

proach using dimensional derivatives, and the nondimensionalization and ability to include nonlinear regressors emulate the second approach, which allows characterization of nonlinear aerodynamic phenomena without requiring knowledge of the aircraft mass properties. The modeling results for the new, mass-agnostic approach are directly compared to and show excellent agreement with a standard nonlinear dynamic modeling approach using known mass properties for large amplitude flight maneuvers. The proposed mass-agnostic modeling technique is useful for rapid, nonlinear dynamic model development for a variety of aircraft, and can be used for applications such as flight simulation, flight control system design, handling qualities assessment, model-based wind estimation, and fault tolerance. Model development in this chapter is performed post-flight for a small, fixed-wing, unmanned aircraft using the equation-error method in the frequency domain; the approach, however, can be readily implemented in real-time applications and is expected to be applicable to numerous aircraft scales and configurations. One downside to the proposed approach is that the identified nondimensional aerodynamic parameters have less physical meaning compared to traditional stability and control derivatives and, accordingly, are not comparable to wind-tunnel or computational aerodynamic predictions. Also, flight testing and model identification need to be repeated when there are substantial changes in aircraft mass properties. However, for flight dynamics models identified solely from flight data with negligible changes in mass properties, the method provides a rapid dynamic modeling capability for a variety of applications and obviates the need to determine the aircraft mass properties. The method is particularly useful for modern electric aircraft that have constant mass properties but can also be used for aircraft that burn fuel or release payload by performing model identification at different loading conditions.

The CZ-150 aircraft, described in Section 2.1.2 and pictured in Figure 2.3, was used as the research platform for this research. The aircraft mass and moments of inertia were determined in ground testing [56] and are listed in Table 2.1. Although the dynamic modeling method demonstrated in this chapter does not require mass properties, these known aircraft properties allowed comparison to the standard approach for nonlinear aircraft model development.

4.2 Experiment Design

Flight-test experiments for model identification were conducted using orthogonal phase-optimized multisine inputs [19, 82–85], described in Section 2.3.2, applied to the aircraft control surfaces. The modeling objective for this work was to identify a bare airframe dynamic model for the CZ-150 aircraft. To meet this objective, flight data used for model identification were collected in a glide without the propulsion system operating and, consequently, the propeller operating in a minimum drag windmill state. As discussed in Chapter 3 and Reference [24], individual multisine signals were generated for the CZ-150 aircraft for the throttle, elevator, aileron, and rudder commands for aero-propulsive model development. The same

multisine design was used for model development for this work, but with the propulsion system amplitude set to zero for bare airframe aerodynamic characterization. Figure 4.1a shows the input spectra of the multisine signal designed for each control surface. The increased separation between lower frequency components is a result of using the aero-propulsive modeling multisine design (see Section 3.3) with the propulsion excitation disabled. Figure 4.1b shows the optimized multisine input signals normalized to have a maximum absolute value of one. The amplitude of each input signal was adjusted to obtain a good signal-to-noise ratio for model identification using the flight data collection approach described in Section 2.4. To conduct a system identification maneuver, the pilot disabled feedback stabilization, trimmed the aircraft in a level glide, enabled the multisine input excitations using a switch on the RC transmitter, and made minor corrections if the aircraft started to significantly deviate from the original trimmed flight condition.

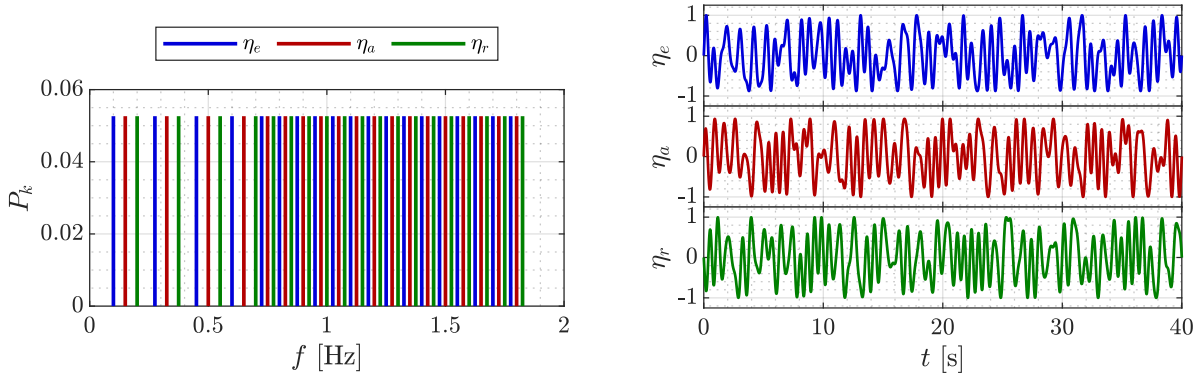

(a) Input spectra for each control effector

(b) Multisine signals for each control effector

Figure 4.1: Orthogonal phase-optimized multisine excitation input design.

4.3 Modeling Approach

Two approaches for fixed-wing aircraft model development were investigated. The first approach represents a standard flight-test approach for nonlinear flight dynamics model development for aircraft with known mass properties (see Section 2.2). The second approach is a new, alternative formulation for nonlinear flight dynamics model development which does not require knowledge of the aircraft mass properties. Both approaches involve developing models from flight-test data gathered using the multiple-axis multisine maneuver described in Section 4.2. Figure 4.2 shows the CZ-150 flight data used for model identification, where it can be seen that all aircraft dynamics are excited in a single maneuver around the reference flight condition of $V = 65$ ft/s and $\alpha = 0$ deg. The amplitude of the control surface excitations and the consequent variation of state variables are large compared to values that would be seen for larger aircraft in standard system identification experiments. Large

amplitude excitations are needed to obtain a sufficient signal-to-noise ratio for modeling small aircraft with low-cost instrumentation systems. A nonlinear model formulation is required for identification because the magnitude of variation of the aircraft states violates the small perturbation assumptions required for using a linearized flight dynamics model.

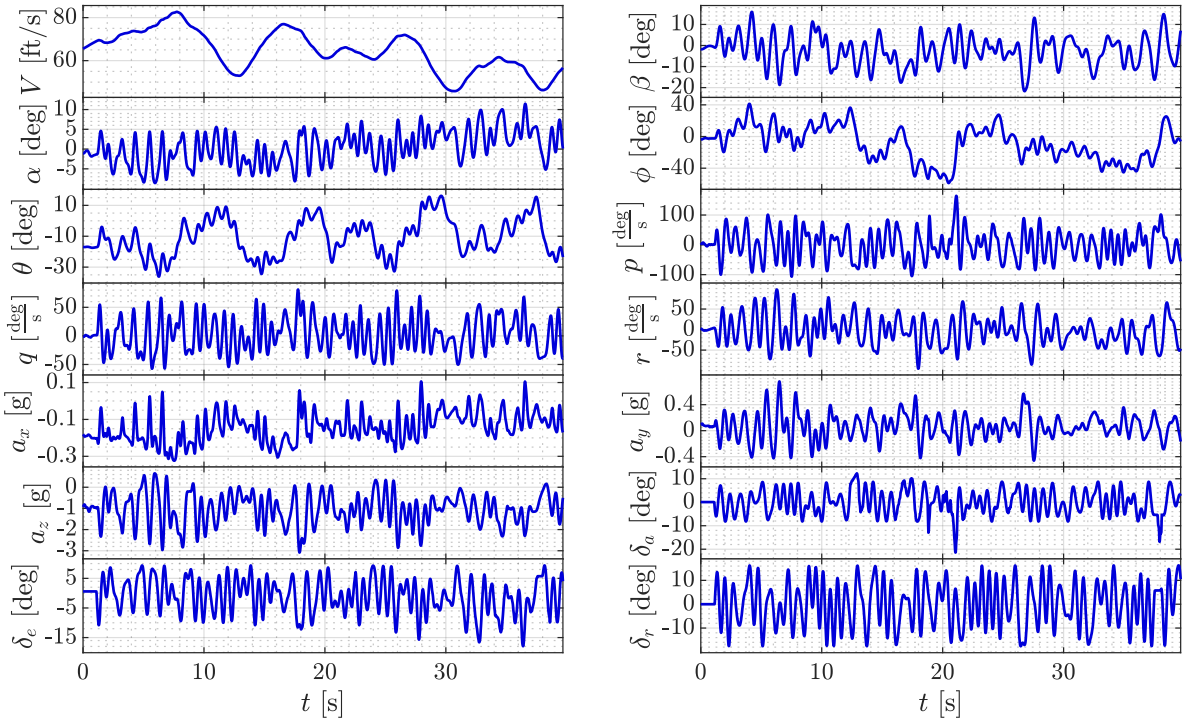

Figure 4.2: Multiple-input multisine flight maneuver used for model identification.

The equation-error method formulated in the frequency domain [19, 70, 100], described in Section 2.6.1.2, was used for model identification in each approach. The Fourier transform frequencies were set between $f_{\min} = 0.05$ Hz and $f_{\max} = 1.85$ Hz with a conservatively-fine frequency resolution of $\Delta f = 0.001$ Hz. Although the frequency-domain equation-error method was selected to be applied in this chapter for its practical advantages noted in Section 2.6.1.2, the modeling approach demonstrated in this chapter can also be readily implemented using time-domain model identification techniques (e.g., see Sections 2.6.1.1 and 2.6.1.3). MOF modeling [19, 102], described in Section 2.6.2.1, was the primary model structure determination method. The method was applied in its frequency-domain formulation discussed in Section 2.6.2.3, which still allows nonlinear model terms to be considered for the model structure [100, 107, 108]. Both PSE and R^2 were used as a cutoff threshold for candidate model terms to include in the final model structure. After the orthogonal regressors were ranked by their ability to reduce the MSFE, the cutoff for model term addition was chosen to be either the candidate model term that minimized the PSE or the last term to increase R^2 by 0.5%, whichever resulted in fewer model terms. As a final step, the MOF results were manually assessed using manual stepwise regression procedures [19, 103], described in Section 2.6.2.2,

to determine whether to include or exclude model terms near the cutoff threshold. After determining the model structure for each response, the final parameter values were estimated using ordinary least-squares regression with the complex regressor and response data (see Section 2.6.1.2).

4.3.1 Standard Modeling Approach

As described in Section 2.2, a standard approach for nonlinear flight dynamics model development is to identify unknown aerodynamic parameters within the aircraft translational dynamics equations [Equations (2.7)-(2.9)] and rotational dynamics equations [Equations (2.10)-(2.12)]. Propulsion forces and moments were not included in the translational and rotational dynamics equations for this study because the flight data used were collected at idle power with a low propeller rotational speed. The effects from the propulsion system could, however, be readily incorporated and identified alongside the aerodynamic parameters, for example, by using techniques described in Chapter 3 (Reference [24]). The response variables are the aircraft nondimensional body-axis force and moment coefficients [Equation (2.13)] which are calculated from flight data using Equation (2.16) with $T = 0$ and Equations (2.17)-(2.19). The explanatory variables used to develop a functional representation of the body-axis force and moment coefficients include angle of attack α in radians; angle of sideslip β in radians; dimensionless angular rates, $\hat{p}$, $\hat{q}$, $\hat{r}$ [Equation (2.20)]; dimensionless angle of attack rate $\dot{\hat{\alpha}}$ [Equation (2.21)]; and control surface deflection angles, δ_e, δ_a, δ_r, in radians. As mentioned in Section 3.4.1, the multisine input signals were designed to excite both the phugoid and short period mode, which sufficiently decorrelates the $\hat{q}$ and $\dot{\hat{\alpha}}$ signals for modeling [162]. For this study, the longitudinal coefficients (C_X, C_Z, C_m) were expressed as functions of longitudinal state and control variables $(\alpha, \dot{\hat{\alpha}}, \hat{q}, \delta_e)$ and lateral-directional coefficients (C_Y, C_l, C_n) were expressed as functions of lateral-directional state and control variables $(\beta, \hat{p}, \hat{r}, \delta_a, \delta_r)$. One exception to this convention was that β is also included as an explanatory variable in C_X to model the drag due to sideslip.

4.3.2 Alternative Modeling Approach

The primary new contribution of this chapter is an investigation of modifications to the standard modeling approach discussed in the previous section to enable nonlinear dynamic model development *without* mass properties knowledge. The proposed modifications are in the definition of the response variables and the equations of motion used for flight simulation. The explanatory variable definitions remain the same as discussed in Section 4.3.1 and the same model identification methods are applied with the redefined response variables.

The first set of modifications to the standard modeling approach is to assume a constant unity mass ($m = 1$ mass unit), which affects equations used to calculate the body-axis force coefficients and the translational dynamics equations. The body-axis force coefficients

calculated from the measured flight data [Equation (2.16) with $T = 0$ because the propulsion system was set to idle for this investigation] are redefined as:

$$K_X = \frac{a_x}{\bar{q}S}, \quad K_Y = \frac{a_y}{\bar{q}S}, \quad K_Z = \frac{a_z}{\bar{q}S} \tag{4.1}$$

The translational dynamics equations [Equations (2.7)-(2.9), including the definitions of X, Y, and Z from Equation (2.13) and with $T = 0$] with the new mass-agnostic force coefficient variables (K_X, K_Y, K_Z) become:

$$\dot{u} = rv - qw - g\sin\theta + \bar{q}SK_X \tag{4.2}$$

$$\dot{v} = pw - ru + g\cos\theta\sin\phi + \bar{q}SK_Y \tag{4.3}$$

$$\dot{w} = qu - pv + g\cos\theta\cos\phi + \bar{q}SK_Z \tag{4.4}$$

Although the physical interpretation of the nondimensional aerodynamic force parameters changes and the aircraft is assumed to have a constant mass, this set of modifications does not result in any dynamic simplification of the nonlinear translational dynamics equations and the framework supports identification of nonlinear aerodynamic model parameters. Because the form of Equation (4.1) and Equations (4.2)-(4.4) emulates the form of Equation (2.16) and Equations (2.7)-(2.9) [with $T = 0$ and using Equation (2.13)], respectively, the traditional and mass-agnostic force coefficients are directly related by aircraft mass:

$$K_X = \frac{C_X}{m}, \quad K_Y = \frac{C_Y}{m}, \quad K_Z = \frac{C_Z}{m} \tag{4.5}$$

This highlights that the mass-agnostic force coefficients can be interpreted as translational acceleration coefficients or traditional force coefficients per unit mass.

The second set of modifications to the standard modeling approach involves the rotational dynamics equations [Equations (2.10)-(2.12)]. The simplifying assumptions are as follows:

1. The roll, pitch, and yaw moments of inertia are constant and have a value of unity ($I_x = I_y = I_z = 1$ inertia unit).
2. The inertial coupling terms involving the product of inertia I_{xz} are negligible.
3. The gyroscopic precession terms (i.e., the remaining nonlinear angular rate terms) are negligible.

Note that the constant multipliers for the neglected terms are either the product of inertia I_{xz} or the difference between two body-axis moments of inertia (I_x, I_y, and I_z). Consequently, for the ignored terms to have a negligible effect, either the inertia multipliers must be small, or the squared and cross angular rates must be small. With these assumptions, the body-axis moment coefficients calculated from the measured flight data [Equations (2.17)-(2.19)] become:

$$K_l = \frac{\dot{p}}{\bar{q}Sb}, \quad K_m = \frac{\dot{q}}{\bar{q}S\bar{c}}, \quad K_n = \frac{\dot{r}}{\bar{q}Sb} \tag{4.6}$$

Accordingly, the rotational dynamics equations [Equations (2.10)-(2.12) with the definitions of L, M, and N from Equation (2.13)] including the inertia-agnostic moment coefficient variables become:

$$\dot{p} = \bar{q}SbK_l, \quad \dot{q} = \bar{q}S\bar{c}K_m, \quad \dot{r} = \bar{q}SbK_n \tag{4.7}$$

Although the physical interpretation of the nondimensional aerodynamic moment parameters changes and the aircraft is assumed to have a constant inertia tensor, this set of modifications does not require knowledge of the aircraft moments of inertia and the framework supports identification of nonlinear aerodynamic model parameters. One consequence, however, is the simplification of the rotational dynamics equations, where the gyroscopic precession terms and inertial coupling terms [190] are neglected. Because the form of Equation (4.6) and Equation (4.7) is simplified compared to Equation (2.17)-(2.19) and Equation (2.10)-(2.12) [with Equation (2.13)], respectively, the traditional and inertia-agnostic moment coefficients are not directly related, but can be approximately compared by:

$$K_l \sim \frac{C_l}{I_x}, \quad K_m \sim \frac{C_m}{I_y}, \quad K_n \sim \frac{C_n}{I_z} \tag{4.8}$$

This shows that the inertia-agnostic moment coefficients can be interpreted as rotational acceleration coefficients or an approximation of the traditional moment coefficients per unit inertia.

The redefined mass-agnostic force coefficients (K_X, K_Y, K_Z) and inertia-agnostic moment coefficients (K_l, K_m, K_n) are the response variables used for the proposed alternative dynamic modeling approach. Note that the terminology of "mass-agnostic" and "inertia-agnostic" pertains to the fact that the calculation of the redefined force and moment coefficients does not require the mass properties to be specified; however, the mass properties are consequently absorbed into the redefined force and moment coefficients, meaning that the values of estimated parameters will change if the mass properties change.

To investigate the impact of the dynamic simplifications made to form the inertia-agnostic moment coefficient calculations [Equation (4.6)], the contributions of each term in the standard moment coefficient equations [Equations (2.17)-(2.19)] were assessed for the flight data used for modeling shown in Figure 4.2. Figure 4.3 shows the time history of each term in the standard moment coefficient equations compared to the total C_l, C_m, and C_n. Clearly, the $\frac{I_x\dot{p}}{\bar{q}Sb}$, $\frac{I_y\dot{q}}{\bar{q}S\bar{c}}$, and $\frac{I_z\dot{r}}{\bar{q}Sb}$ terms are the dominant contributions to C_l, C_m, and C_n, respectively. These dominant terms also directly correspond to K_l, K_m, and K_n scaled by mass properties [cf. Equation (4.6)]. Table 4.1 shows the percent of total C_l, C_m, and C_n variation described by each term in the standard moment coefficient equations, where the dominant terms are seen to describe at least 98% of the total moment coefficient response. Even for the aggressive, large-amplitude multisine maneuver shown in Figure 4.2, this analysis suggests that performing modeling and flight simulations using the simplified, inertia-agnostic moment coefficients K_l, K_m, and K_n will have a small impact on the results. This claim will be investigated further with the presentation of modeling results shown in the next section.

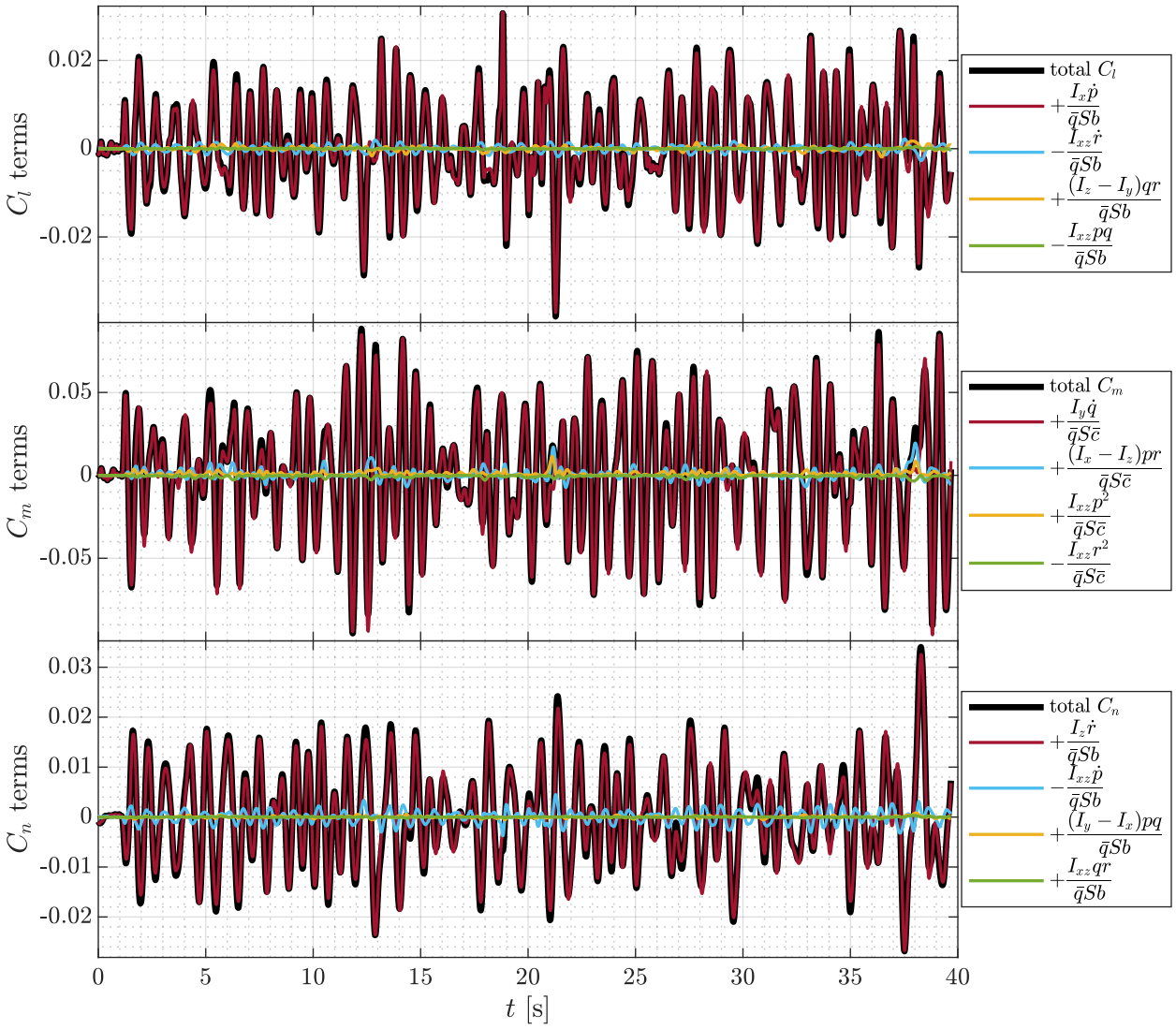

Figure 4.3: Time history of each term in the standard moment coefficient equations for the flight data shown in Figure 4.2.

Table 4.1: Percent of total C_l, C_m, and C_n variation described by each term in the moment coefficient equations

C_l term	% of C_l	C_m term	% of C_m	C_n term	% of C_n
$+\frac{I_x\dot{p}}{\bar{q}Sb}$	99.3	$+\frac{I_y\dot{q}}{\bar{q}S\bar{c}}$	98.9	$+\frac{I_z\dot{r}}{\bar{q}Sb}$	98.3
$-\frac{I_{xz}\dot{r}}{\bar{q}Sb}$	0.478	$+\frac{(I_x-I_z)pr}{\bar{q}S\bar{c}}$	0.989	$-\frac{I_{xz}\dot{p}}{\bar{q}Sb}$	1.61
$+\frac{(I_z-I_y)qr}{\bar{q}Sb}$	0.178	$+\frac{I_{xz}p^2}{\bar{q}S\bar{c}}$	0.105	$+\frac{(I_y-I_x)pq}{\bar{q}Sb}$	0.038
$-\frac{I_{xz}pq}{\bar{q}Sb}$	0.007	$-\frac{I_{xz}r^2}{\bar{q}S\bar{c}}$	0.037	$+\frac{I_{xz}qr}{\bar{q}Sb}$	0.005

It is expected that most operational flight maneuvers will exhibit similar character to the analysis shown in Figure 4.3 and Table 4.1 with $\frac{I_x\dot{p}}{\bar{q}Sb}$, $\frac{I_y\dot{q}}{\bar{q}S\bar{c}}$, and $\frac{I_z\dot{r}}{\bar{q}Sb}$ being the dominant contributors to the moment coefficients. Accordingly, the mass-agnostic modeling approach should yield good predictions for most flight maneuvers. However, certain maneuvers exhibiting large simultaneous angular rates, such as descending or climbing turns, will amplify the importance of neglected terms in Equations (2.17)-(2.19) and, thus, the mass-agnostic modeling approach would be expected to have degraded prediction capability.

An intermediate practical scenario to the above discussion is when estimates of aircraft mass and moments of inertia are available, but are not known accurately. For example, the rough order of magnitude of the aircraft mass and moments of inertia might be known from a rudimentary computerized aircraft representation or deduced from similar aircraft with known mass properties. If this is the case, a variant of the mass-agnostic modeling approach can be applied with the approximate mass, m_e, and approximate body-axis moments of inertia, I_{x_e}, I_{y_e}, and I_{z_e}. The body-axis force and moment coefficients can be redefined as

$$K_{X_e} = m_e K_X = \frac{m_e a_x}{\bar{q}S} \sim C_X, \quad K_{Y_e} = m_e K_Y = \frac{m_e a_y}{\bar{q}S} \sim C_Y, \quad K_{Z_e} = m_e K_Z = \frac{m_e a_z}{\bar{q}S} \sim C_Z \tag{4.9}$$

$$K_{l_e} = I_{x_e} K_l = \frac{I_{x_e}\dot{p}}{\bar{q}Sb} \sim C_l, \quad K_{m_e} = I_{y_e} K_m = \frac{I_{y_e}\dot{q}}{\bar{q}S\bar{c}} \sim C_m, \quad K_{n_e} = I_{z_e} K_n = \frac{I_{z_e}\dot{r}}{\bar{q}Sb} \sim C_n \tag{4.10}$$

where the approximated aircraft mass properties scale the mass-agnostic force and moment coefficients. This approximate scaling gives more physical meaning to the parameter estimates because they more closely reflect traditional stability and control derivatives, but the model simplifications are the same as the mass-agnostic modeling approach.

4.4 Results

This section compares the flight-test system identification results for the standard aircraft dynamic modeling approach with mass properties information to the proposed aircraft dynamic modeling approach that does not require knowledge of the mass properties. For simplicity in notation and discussion, the standard approach will be referred to as the "$C_{(\cdot)}$ model" and the new mass-agnostic approach will be referred to as the "$K_{(\cdot)}$ model" (where "$(\cdot)$" is used to represent the X, Y, Z, l, m, and n subscripts), in accordance with the force and moment coefficient definitions given in Equations (2.16)-(2.19), Equation (4.1), and Equation (4.6).

The aerodynamic model structure for each body-axis force and moment coefficient was determined using the CZ-150 flight data with multisine inputs active on the control surfaces, shown in Figure 4.2. Following the model structure identification approach outlined in Section 4.3 (with additional supporting details provided in Section 2.6.2), the final model

structure for each response variable was composed of candidate regressors describing a significant amount of the variation in the response. The model structure for each force and moment coefficient for the $C_{(\cdot)}$ model was determined to be:

$$C_X = C_{X_\alpha}\alpha + C_{X_{\dot\alpha}}\hat{\dot\alpha} + C_{X_{\alpha^2}}\alpha^2 + C_{X_{\beta^2}}\beta^2 + C_{X_o} \tag{4.11}$$

$$C_Y = C_{Y_\beta}\beta + C_{Y_p}\hat{p} + C_{Y_r}\hat{r} + C_{Y_{\delta_a}}\delta_a + C_{Y_{\delta_r}}\delta_r + C_{Y_o} \tag{4.12}$$

$$C_Z = C_{Z_\alpha}\alpha + C_{Z_q}\hat{q} + C_{Z_{\dot\alpha}}\hat{\dot\alpha} + C_{Z_o} \tag{4.13}$$

$$C_l = C_{l_\beta}\beta + C_{l_p}\hat{p} + C_{l_r}\hat{r} + C_{l_{\delta_a}}\delta_a + C_{l_o} \tag{4.14}$$

$$C_m = C_{m_\alpha}\alpha + C_{m_q}\hat{q} + C_{m_{\delta_e}}\delta_e + C_{m_{\dot\alpha}}\hat{\dot\alpha} + C_{m_{\alpha^2}}\alpha^2 + C_{m_o} \tag{4.15}$$

$$C_n = C_{n_\beta}\beta + C_{n_r}\hat{r} + C_{n_{\delta_a}}\delta_a + C_{n_{\delta_r}}\delta_r + C_{n_o} \tag{4.16}$$

The aerodynamic model structure for the $K_{(\cdot)}$ model is identical, where "C" in Equations (4.11)-(4.16) is simply replaced by "K". However, the parameter estimates and their interpretation in each model are different.

After determining the model structure, complex least-squares regression was used to determine the final estimates of the model parameters for each modeling approach. For each scalar parameter, the parameter estimate $\hat\theta$, parameter standard error $s(\hat\theta)$, and parameter percent error (calculated as $100 \times \left[s(\hat\theta)/|\hat\theta|\right]$) within the body-axis force and moment coefficient model equations are given in Tables 4.3-4.14 at the end of this chapter. The parameter estimates have reasonably low standard error and percent error values, given the low-cost instrumentation system used for this study and the high susceptibility of small aircraft to atmospheric disturbance. Table 4.15 shows the $K_{(\cdot)}$ parameter estimates and standard errors scaled by aircraft mass properties according to Equation (4.5) and Equation (4.8), as well as the scaled $K_{(\cdot)}$ parameter percent errors relative to the corresponding $C_{(\cdot)}$ parameter estimates. The $C_{(\cdot)}$ force coefficient parameters and standard errors are identical to the $K_{(\cdot)}$ force coefficient parameters and standard errors multiplied by a factor of m, as would be expected by the developments presented in Section 4.3.2, where no dynamic simplifications were made to the translational dynamics model. Conversely, for the moment coefficients, the $C_{(\cdot)}$ and scaled $K_{(\cdot)}$ parameter estimates and parameter standard errors are different values as an artifact of the dynamic simplifications made in the rotational dynamics equations discussed in Section 4.3.2. However, the respective $C_{(\cdot)}$ and scaled $K_{(\cdot)}$ moment coefficient parameter estimates and standard errors are observed to be similar in value, and the percent errors of the scaled $K_{(\cdot)}$ moment coefficient parameters relative to the $C_{(\cdot)}$ parameters are generally low.

The model fits to the force and moment coefficients in the frequency domain for the $C_{(\cdot)}$ and $K_{(\cdot)}$ models are shown in Figure 4.4. All response variables, except for C_X and K_X, are observed to have an excellent model fit. The R^2 metric shown on the plot for each response is high, indicating that most of the variation of the response variable about its

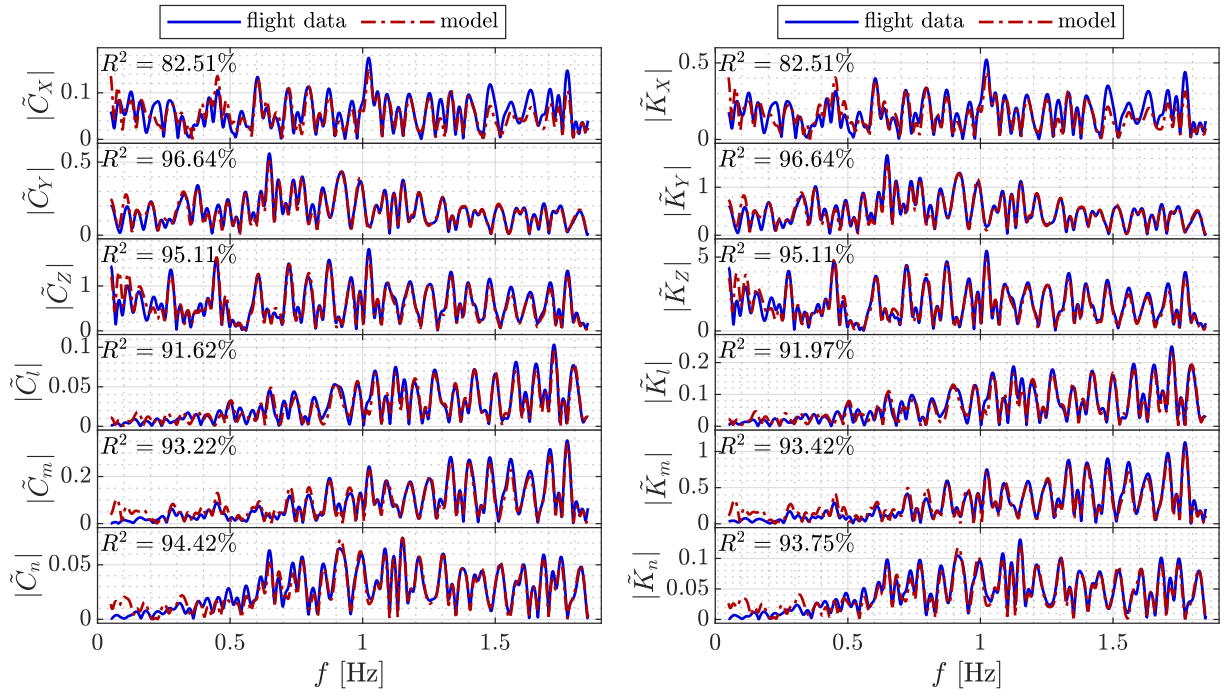

(a) $C_{(\cdot)}$ model (b) $K_{(\cdot)}$ model

Figure 4.4: Comparison of the response data and model fit in the frequency domain.

mean is characterized by the model. The model fits for C_X and K_X are still satisfactory, with an R^2 value of 82.5%, but not as good compared to the other responses because of the limited excitation along the body x-axis. A bare airframe C_X model also has a smaller influence on aircraft dynamics and is typically more difficult to accurately estimate using flight data [88]. Although the response magnitudes are different, the respective $C_{(\cdot)}$ and $K_{(\cdot)}$ force coefficient R^2 values are identical because no dynamic simplifications were made to the translational dynamics model. Conversely, the respective R^2 values for the $C_{(\cdot)}$ and $K_{(\cdot)}$ moment coefficient models are not identical, but the values are observed to be within 0.67%, as a consequence of the simplifications made in the rotational dynamics equations for the $K_{(\cdot)}$ model. Figure 4.5 shows the corresponding time-domain model fits compared to the force and moment coefficients computed from the flight data, as well as the time-domain R^2 value for each response. The model predictions for each response in the time domain reflect the fit quality observed in the frequency domain and show that the model is able to describe a large amount of the variation in each response. Figure 4.6 shows the time-domain modeling residuals corresponding to Figure 4.5 with the mass-agnostic modeling residuals scaled according to Equation (4.5) and Equation (4.8). The three signals shown on each subplot are the standard modeling approach residuals $(C_{(\cdot)} - \hat{C}_{(\cdot)})$, the scaled mass-agnostic modeling approach residuals $[\kappa_{(\cdot)}(K_{(\cdot)} - \hat{K}_{(\cdot)})]$, and the difference between the standard nondimensional response data and the scaled mass-agnostic modeling approach predictions $(C_{(\cdot)} - \kappa_{(\cdot)}\hat{K}_{(\cdot)})$, where the respective scale factor for each response is represented

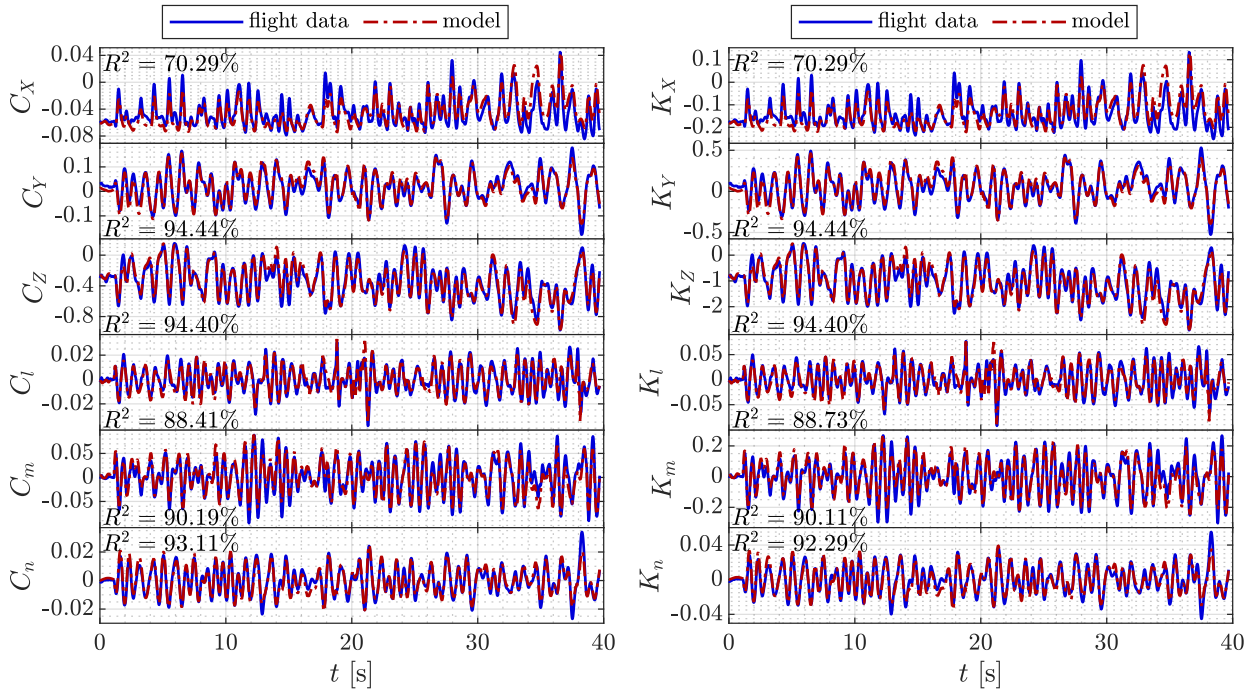

(a) $C_{(\cdot)}$ model (b) $K_{(\cdot)}$ model

Figure 4.5: Comparison of the response data and model fit in the time domain.

by $\kappa_{(\cdot)}$. The modeling residual magnitude and character are observed to be similar for each case shown in Figure 4.6.

After identification of the $C_{(\cdot)}$ and $K_{(\cdot)}$ models, flight simulations were performed to directly compare the performance of the two models to measured flight data and to evaluate the accuracy of using the identified models for applications requiring flight simulation. This simulation analysis was performed using multiple flight maneuvers:

1. the multisine maneuver used for model identification,
2. a validation multisine maneuver with a different distribution of harmonic components assigned to each control effector than was used for model identification, and
3. single-axis multistep maneuvers that were not used for model identification.

The control surface deflections and initial conditions of each flight maneuver were used as simulation inputs. The equations of motion for each approach (see Section 4.3) were integrated to obtain the outputs predicted by the model, which are directly comparable to the measured outputs from the flight data. Because C_X, C_Z, and C_m each included an $\hat{\alpha}$ model term, the equations were manipulated for numerical integration as discussed in Section 2.2.3. The bias parameters were reestimated using the output-error method for each maneuver, as is standard practice [19], but the other model parameters were held constant to the values shown in Tables 4.3-4.14.

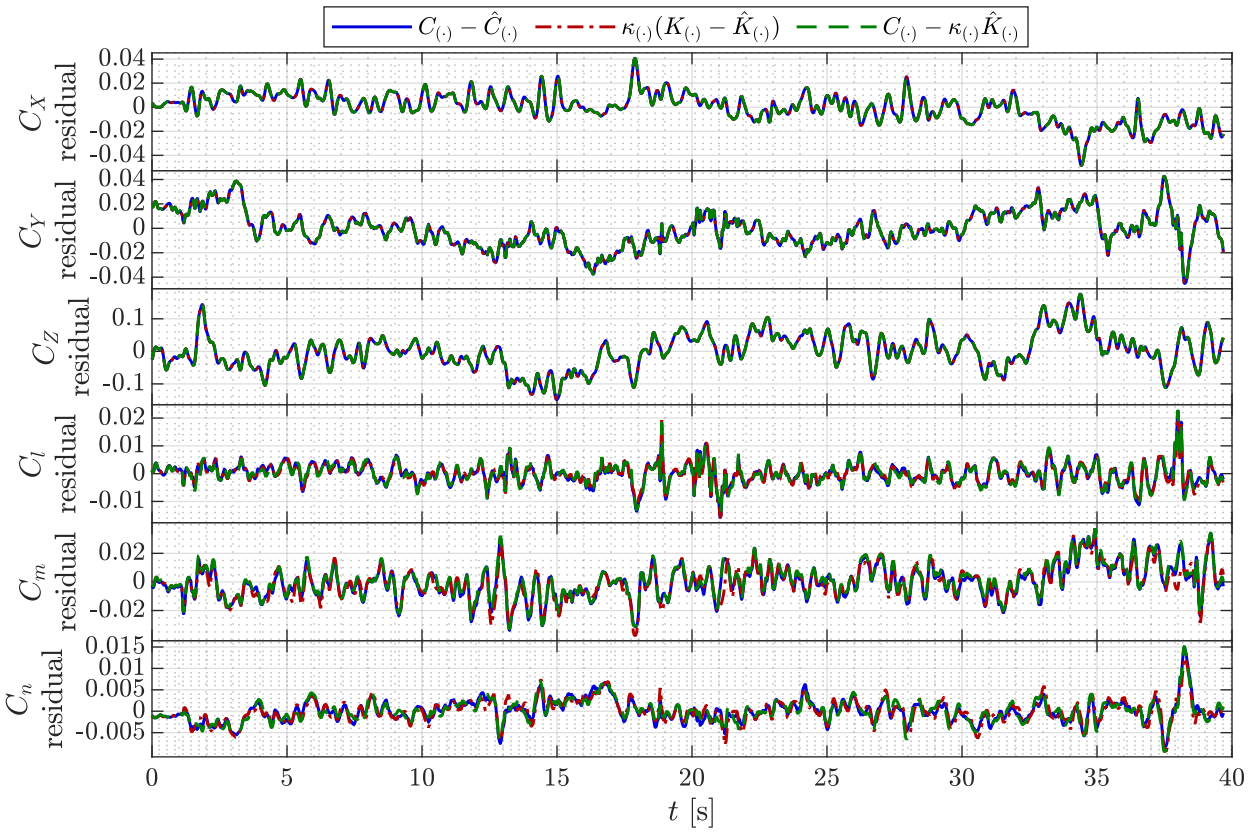

Figure 4.6: Comparison of time-domain modeling residuals.

Figure 4.7 shows simulation results for the multisine maneuver that was used to identify the model parameters. Figure 4.8 shows simulation results for the validation multisine maneuver. The output prediction capability for the modeling and validation multisine maneuvers can be quantitatively characterized and directly compared using the NRMSE metric [Equation (2.86)]. The modeling and validation NRMSE values for each model computed using the output data shown in Figure 4.7 and Figure 4.8, respectively, are compared in Table 4.2. Observing that the modeling and validation NRMSE values are generally low and similar in value for each response provides confidence that both models have good prediction capability. The visual $C_{(\cdot)}$ model response and $K_{(\cdot)}$ model response shown in Figures 4.7-4.8 are also very similar and the model predictions well-emulate the output flight data. Furthermore, the simulation results for an elevator doublet, rudder doublet, and aileron 1-2-1 maneuver are shown in Figure 4.9, where the output responses of the $C_{(\cdot)}$ and $K_{(\cdot)}$ models are very similar, and a good match is observed to the flight data. The visual offset between the a_x flight data and model predictions is attributed to the lack of excitation along the body x-axis for the multistep maneuvers, which results in a low signal-to-noise ratio and, thus, magnifies the difference between the data and model predictions.

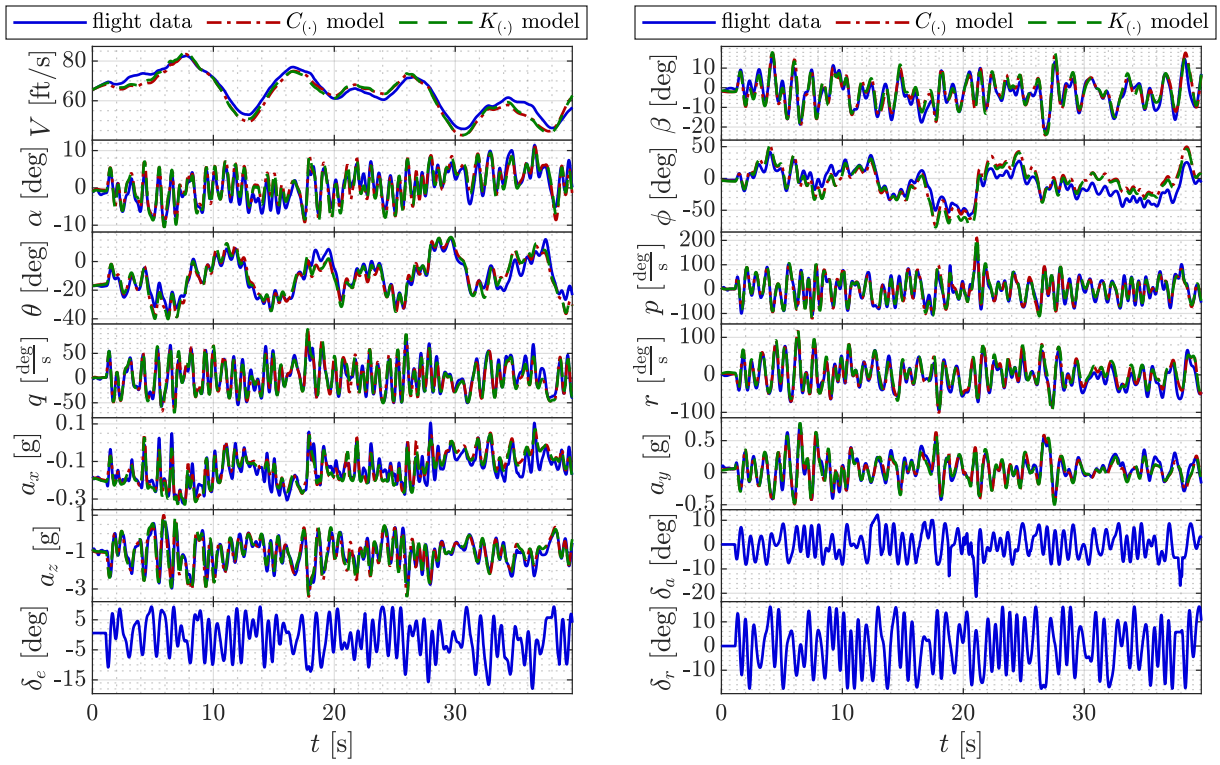

Figure 4.7: Comparison of $C_{(\cdot)}$ and $K_{(\cdot)}$ model simulation results for the model identification maneuver.

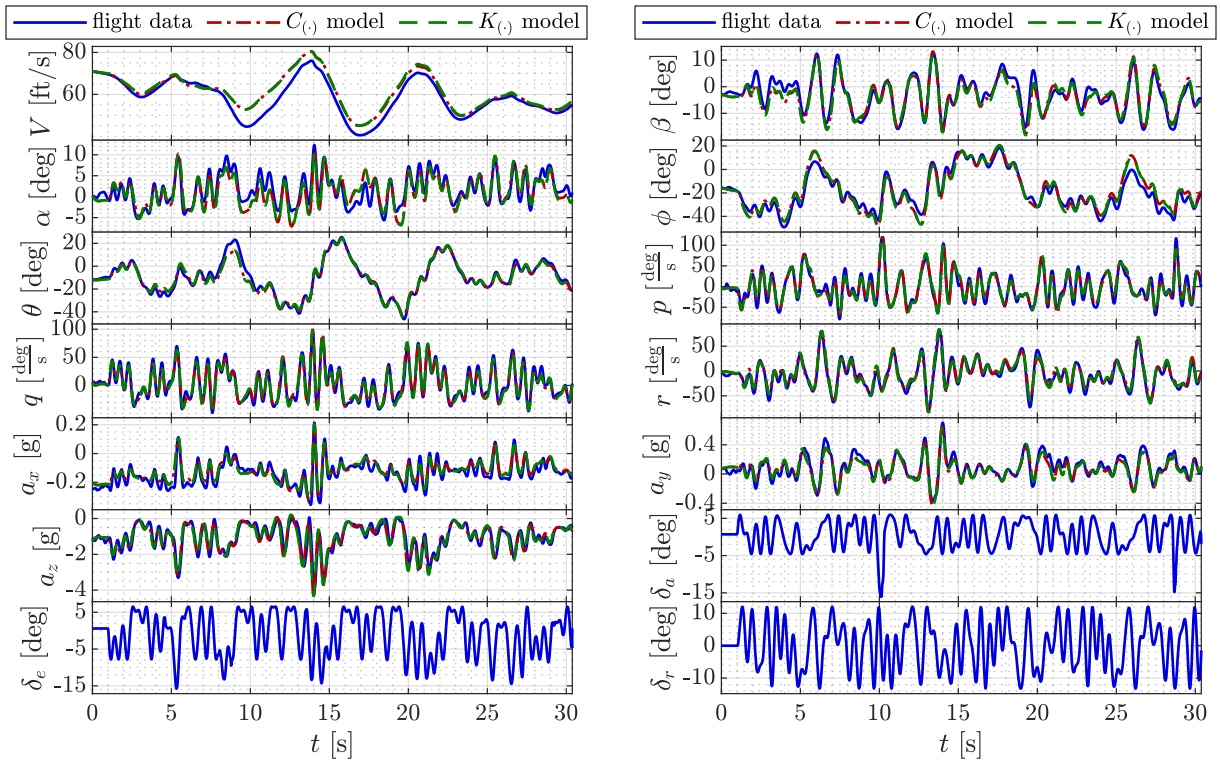

Figure 4.8: Comparison of $C_{(\cdot)}$ and $K_{(\cdot)}$ model simulation results for a validation multisine maneuver.

Table 4.2: Comparison of multisine maneuver output modeling and validation NRMSE values for the $C_{(\cdot)}$ and $K_{(\cdot)}$ models (expressed as a percentage)

	V	α	β	p	q	r	ϕ	θ	a_x	a_y	a_z
Modeling NRMSE, $C_{(\cdot)}$ model	7.8	8.4	7.2	4.3	5.9	5.9	13.0	7.9	8.6	4.7	8.0
Modeling NRMSE, $K_{(\cdot)}$ model	7.4	8.0	7.0	4.2	5.9	6.5	12.3	7.9	8.1	4.6	8.2
Validation NRMSE, $C_{(\cdot)}$ model	10.4	9.1	5.6	3.0	4.1	3.1	4.6	5.2	7.3	4.3	7.3
Validation NRMSE, $K_{(\cdot)}$ model	10.8	9.1	5.7	2.9	4.3	3.2	4.5	5.3	7.1	4.1	7.5

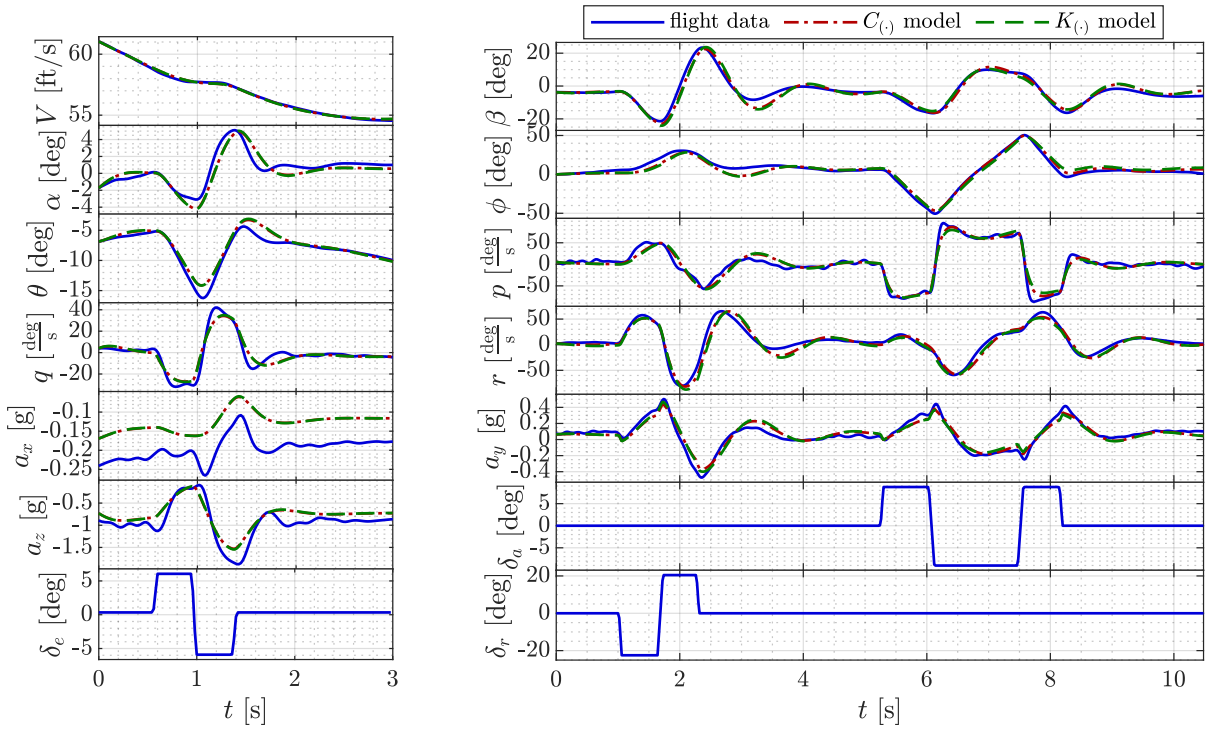

(a) Elevator doublet maneuver

(b) Rudder doublet and aileron 1-2-1 maneuver

Figure 4.9: Comparison of $C_{(\cdot)}$ and $K_{(\cdot)}$ model simulation results for validation multistep maneuvers.

Acknowledgment of Collaborative Research

The research presented in this chapter was primarily conducted by the author, but included important collaborative contributions from other individuals. The experiment design was conceptualized and implemented in collaboration with James Gresham, with the author leading development of the excitation input design. Gresham performed all aircraft development and integration efforts, as well as all laboratory and flight-test experiments. Flight-test support was also provided by Jean-Michel Fahmi and Jeremy Hopwood. The research in this chapter was advised by Craig Woolsey who offered many helpful suggestions throughout the research process and manuscript preparation. The author gratefully acknowledges and appreciates these efforts which made the research described in this chapter possible.

Parameter Estimate Tables

Table 4.3: Standard C_X parameter estimates ($R^2 = 82.51\%$)

Parameter	$\hat{\theta}$	$s(\hat{\theta})$	% Error
C_{X_α}	$+0.240$	0.0114	4.7
$C_{X_{\dot{\alpha}}}$	-1.54	0.229	14.9
$C_{X_{\alpha^2}}$	$+1.26$	0.123	9.8
$C_{X_{\beta^2}}$	$+0.188$	0.0311	16.5
C_{X_o}	-0.0569	0.00331	5.8

Table 4.4: Mass-agnostic K_X parameter estimates ($R^2 = 82.51\%$)

Parameter	$\hat{\theta}$	$s(\hat{\theta})$	% Error
K_{X_α}	$+0.715$	0.0339	4.7
$K_{X_{\dot{\alpha}}}$	-4.58	0.681	14.9
$K_{X_{\alpha^2}}$	$+3.75$	0.367	9.8
$K_{X_{\beta^2}}$	$+0.560$	0.0925	16.5
K_{X_o}	-0.169	0.00986	5.8

Table 4.5: Standard C_Y parameter estimates ($R^2 = 96.64\%$)

Parameter	$\hat{\theta}$	$s(\hat{\theta})$	% Error
C_{Y_β}	-0.457	0.00826	1.8
C_{Y_p}	-0.283	0.0375	13.2
C_{Y_r}	$+0.360$	0.0338	9.4
$C_{Y_{\delta_a}}$	-0.226	0.0186	8.2
$C_{Y_{\delta_r}}$	$+0.0968$	0.00663	6.9
C_{Y_o}	-0.000340	0.00197	580.2

Table 4.6: Mass-agnostic K_Y parameter estimates ($R^2 = 96.64\%$)

Parameter	$\hat{\theta}$	$s(\hat{\theta})$	% Error
K_{Y_β}	-1.36	0.0246	1.8
K_{Y_p}	-0.844	0.112	13.2
K_{Y_r}	$+1.07$	0.101	9.4
$K_{Y_{\delta_a}}$	-0.674	0.0554	8.2
$K_{Y_{\delta_r}}$	$+0.288$	0.0198	6.9
K_{Y_o}	-0.00101	0.00587	580.2

Table 4.7: Standard C_Z parameter estimates ($R^2 = 95.11\%$)

Parameter	$\hat{\theta}$	$s(\hat{\theta})$	% Error
C_{Z_α}	-2.36	0.119	5.0
C_{Z_q}	-24.5	2.58	10.5
$C_{Z_{\dot{\alpha}}}$	$+27.2$	2.89	10.6
C_{Z_o}	-0.321	0.00832	2.6

Table 4.8: Mass-agnostic K_Z parameter estimates ($R^2 = 95.11\%$)

Parameter	$\hat{\theta}$	$s(\hat{\theta})$	% Error
K_{Z_α}	-7.04	0.354	5.0
K_{Z_q}	-73.1	7.68	10.5
$K_{Z_{\dot{\alpha}}}$	$+80.9$	8.60	10.6
K_{Z_o}	-0.957	0.0248	2.6

Table 4.9: Standard C_l parameter estimates ($R^2 = 91.62\%$)

Parameter	$\hat{\theta}$	$s(\hat{\theta})$	% Error
C_{l_β}	-0.0411	0.00224	5.5
C_{l_p}	-0.290	0.0104	3.6
C_{l_r}	$+0.0978$	0.00821	8.4
$C_{l_{\delta_a}}$	-0.186	0.00516	2.8
C_{l_o}	-0.00166	0.000223	13.4

Table 4.10: Inertia-agnostic K_l parameter estimates ($R^2 = 91.97\%$)

Parameter	$\hat{\theta}$	$s(\hat{\theta})$	% Error
K_{l_β}	-0.0917	0.00533	5.8
K_{l_p}	-0.730	0.0247	3.4
K_{l_r}	$+0.242$	0.0195	8.1
$K_{l_{\delta_a}}$	-0.457	0.0122	2.7
K_{l_o}	-0.00371	0.000500	13.5

Table 4.11: Standard C_m parameter estimates ($R^2 = 93.22\%$)

Parameter	$\hat{\theta}$	$s(\hat{\theta})$	% Error
C_{m_α}	-0.300	0.0232	7.7
C_{m_q}	-6.49	0.521	8.0
$C_{m_{\delta_e}}$	-0.390	0.0173	4.4
$C_{m_{\dot{\alpha}}}$	$+2.41$	0.646	26.8
$C_{m_{\alpha^2}}$	-0.537	0.137	25.5
C_{m_o}	$+0.000866$	0.00199	229.6

Table 4.12: Inertia-agnostic K_m parameter estimates ($R^2 = 93.42\%$)

Parameter	$\hat{\theta}$	$s(\hat{\theta})$	% Error
K_{m_α}	-0.968	0.0719	7.4
K_{m_q}	-19.2	1.61	8.4
$K_{m_{\delta_e}}$	-1.21	0.0534	4.4
$K_{m_{\dot{\alpha}}}$	$+7.46$	2.00	26.8
$K_{m_{\alpha^2}}$	-1.63	0.424	26.1
K_{m_o}	-0.00125	0.00659	527.0

Table 4.13: Standard C_n parameter estimates ($R^2 = 94.42\%$)

Parameter	$\hat{\theta}$	$s(\hat{\theta})$	% Error
C_{n_β}	$+0.0498$	0.00163	3.3
C_{n_r}	-0.107	0.00703	6.6
$C_{n_{\delta_a}}$	$+0.0375$	0.00224	6.0
$C_{n_{\delta_r}}$	-0.0406	0.00140	3.4
C_{n_o}	$+0.00185$	0.000181	9.8

Table 4.14: Inertia-agnostic K_n parameter estimates ($R^2 = 93.75\%$)

Parameter	$\hat{\theta}$	$s(\hat{\theta})$	% Error
K_{n_β}	$+0.0811$	0.00282	3.5
K_{n_r}	-0.151	0.0121	8.0
$K_{n_{\delta_a}}$	$+0.0508$	0.00386	7.6
$K_{n_{\delta_r}}$	-0.0683	0.00241	3.5
K_{n_o}	$+0.00304$	0.000316	10.4

Table 4.15: $K_{(\cdot)}$ parameter estimates scaled by aircraft mass properties

Parameter	$\hat{\theta}$	$s(\hat{\theta})$	% Error (relative to $C_{(\cdot)}$)
mK_{X_α}	$+0.240$	0.0114	0
$mK_{X_{\dot{\alpha}}}$	-1.54	0.229	0
$mK_{X_{\alpha^2}}$	$+1.26$	0.123	0
$mK_{X_{\beta^2}}$	$+0.188$	0.0311	0
mK_{X_o}	-0.0569	0.00331	0
mK_{Y_β}	-0.457	0.00826	0
mK_{Y_p}	-0.283	0.0375	0
mK_{Y_r}	$+0.360$	0.0338	0
$mK_{Y_{\delta_a}}$	-0.226	0.0186	0
$mK_{Y_{\delta_r}}$	$+0.0968$	0.00663	0
mK_{Y_o}	-0.000340	0.00197	0
mK_{Z_α}	-2.36	0.119	0
mK_{Z_q}	-24.5	2.58	0
$mK_{Z_{\dot{\alpha}}}$	$+27.2$	2.89	0
mK_{Z_o}	-0.321	0.00832	0
$I_xK_{l_\beta}$	-0.0369	0.00215	10.1
$I_xK_{l_p}$	-0.294	0.00994	1.4
$I_xK_{l_r}$	$+0.0975$	0.00786	0.3
$I_xK_{l_{\delta_a}}$	-0.184	0.00494	0.8
$I_xK_{l_o}$	-0.00150	0.000202	10.0
$I_yK_{m_\alpha}$	-0.307	0.0228	2.2
$I_yK_{m_q}$	-6.10	0.511	6.1
$I_yK_{m_{\delta_e}}$	-0.384	0.0169	1.5
$I_yK_{m_{\dot{\alpha}}}$	$+2.36$	0.634	1.8
$I_yK_{m_{\alpha^2}}$	-0.516	0.134	3.8
$I_yK_{m_o}$	-0.000396	0.00209	145.8
$I_zK_{n_\beta}$	$+0.0479$	0.00167	3.8
$I_zK_{n_r}$	-0.0890	0.00716	16.7
$I_zK_{n_{\delta_a}}$	$+0.0300$	0.00228	19.9
$I_zK_{n_{\delta_r}}$	-0.0403	0.00142	0.6
$I_zK_{n_o}$	$+0.00179$	0.000187	2.8

Chapter 5

Part I Conclusions

System identification of small unmanned aircraft from flight data is challenging due to physical and programmatic challenges, but arguably presents the best method for accurate flight dynamics model development. Chapter 2 of this dissertation gave an overview of the fixed-wing aircraft system identification approaches recently applied in the Nonlinear Systems Laboratory at Virginia Tech using flight data. System identification has been performed for multiple fixed-wing aircraft, which has led to the development and refinement of a standard set of procedures for nonlinear model development for small, unmanned, fixed-wing aircraft. Flight data collection is performed with a ground-based pilot executing piloted maneuvers or coordinating automatic input excitations using custom-developed flight software. After collection of flight data, several data processing steps specific to the small aircraft operations are executed before performing model identification. Model development is then performed using model structure determination and parameter estimation methods supporting nonlinear dynamic model development. After model validation, the models are used for applications such as model-based wind estimation, flight control system design, or flight simulation. Low-cost unmanned aerial systems continue to be used for numerous applications and the methods described in Chapter 2 provide a common framework to accurately characterize aircraft dynamics and performance to support model-based research progression in other areas. Four specific flight-test system identification research advancements were highlighted, two of which constitute primary contributions of this dissertation: aero-propulsive model development for propeller aircraft and nonlinear dynamic model identification without mass properties.

Aircraft flight dynamics models often assume that airframe and propulsion aerodynamic characteristics are decoupled; however, aircraft with propellers used to generate thrust have significant propulsion-airframe interactions and propulsion integration losses which result in modeling inaccuracies when neglected. Chapter 3 in this dissertation proposed and validated two methods for modeling aero-propulsive characteristics for propeller-driven fixed-wing aircraft using flight data. Both methods have advantages and disadvantages which determine the best approach to pursue for a particular modeling effort.

An efficient flight experiment was designed to enable identification of integrated propulsion and airframe aerodynamics in a single maneuver. Orthogonal phase-optimized multisine input signals were applied to the aircraft control surfaces and the propulsion system simultaneously, which allowed collecting information rich flight data for aero-propulsive charac-

terization. The propulsion multisine signal focused excitation power at lower frequencies so that the input excitations remained within the motor bandwidth. The propulsion and control surface excitation amplitudes could be adjusted by the pilot in real time to ensure that the data have a high signal-to-noise ratio, while also keeping the aircraft near the reference trimmed flight condition. The data collected from the designed multisine maneuver were used to identify models using both proposed modeling approaches.

The first aero-propulsive modeling approach identified an integrated aero-propulsive model using flight data from a propulsion and control surface multisine maneuver. The explanatory variables used for modeling included state and control variables commonly used for aircraft system identification, as well as propulsion variables derived from propeller aerodynamics theory. An alternative parametrization of advance ratio used as an explanatory variable for modeling the nondimensional aircraft force and moment coefficients was demonstrated to significantly improve modeling performance. The model identification results indicated that the airframe and propulsion aerodynamics have significant coupling, demonstrating the importance of considering their effects jointly for propeller aircraft. The modeling and prediction error for every response was observed to be less than 6%. The modeling and prediction error for the C_X model was approximately 1%. The models were also shown to have good qualitative prediction capability for maneuvers with different waveforms than were used for modeling.

The second aero-propulsive modeling approach developed a separate bare airframe and propulsion aerodynamic model using flight data. The novelty of this approach is propulsion model development using flight data, as opposed to using ground testing or computational methods. A bare airframe aerodynamic model was identified using data from a gliding maneuver with multisine signals only operating on the control surfaces. Parameters characterizing the propeller thrust effects within the x-axis force coefficient were then identified using data from a flight maneuver with multisine inputs active on the propulsion system and control surfaces, while holding the bare airframe aerodynamic model parameters fixed. The combined bare airframe and propulsion model was shown to have similar but slightly degraded modeling and predictive performance compared to the model where aero-propulsive effects were characterized together. Nonetheless, both proposed modeling methods identified high-quality models that can be used to perform accurate flight dynamics simulations.

Both the integrated and decoupled aero-propulsive modeling approaches developed using flight data were compared to a model constructed using the bare airframe aerodynamic model identified from flight data and a thrust model developed from isolated propeller wind-tunnel data. The latter conventional modeling strategy significantly overpredicted the thrust in flight, particularly at lower advance ratios. In contrast, the two approaches proposed in Chapter 3 yielded models that were able to predict the airframe-integration losses and accurately represent the propulsive performance in flight. Based on the presented analysis, it is recommended to identify models for both the propulsion and airframe aerodynamics using flight data for propeller aircraft applications requiring accurate flight dynamics models.

Nonlinear aircraft flight dynamics models, including the models described in Chapters 2-3, generally require knowledge of aircraft mass and moments of inertia. Although mass is straightforward to accurately measure, computational and/or empirical determination of moment of inertia tensor elements is labor-intensive and inconvenient to perform. Chapter 4 in this dissertation proposed a nonlinear dynamic modeling approach using flight data which does not require knowledge of the aircraft mass properties. The standard nonlinear aircraft dynamics equations were reformulated and the nondimensional force and moment coefficient definitions were redefined to subsume the aircraft mass properties which obviates the need to specify constant aircraft mass and moment of inertia tensor elements for accurate identification of a general nonlinear aerodynamic model. The aerodynamic model parameters lose physical interpretability, but the resulting dynamic model can still be used for a variety of simulation, estimation, and control applications. Flight testing must be repeated if there is a significant change in mass properties, but only a short flight maneuver is required and model parameters can be rapidly reestimated. The proposed method was evaluated using flight data collected using a small, fixed-wing, unmanned aircraft and the modeling results were compared to a standard nonlinear aircraft flight dynamics model development approach that requires mass properties knowledge. The results indicated that the modeling performance of the new mass-agnostic nonlinear dynamic modeling approach was very similar to the standard nonlinear aircraft dynamic model identification approach. Based on the analysis presented in Chapter 4, the proposed approach is recommended as a nonlinear flight dynamics model development technique for a variety of aircraft without accurate mass properties knowledge.

Part II

System Identification for eVTOL Aircraft

Chapter 6

Aero-Propulsive Modeling for eVTOL Aircraft Using Wind-Tunnel Data

This chapter describes approaches for development of a high-fidelity, integrated propulsion-airframe aerodynamic model for the NASA LA-8 tandem tilt-wing, electric vertical takeoff and landing (eVTOL) aircraft. eVTOL vehicle configurations exhibit aerodynamic characteristics of both fixed-wing and rotary-wing aircraft as well as complex vehicle-specific phenomena, such as propeller-wing interactions and high incidence angle propeller aerodynamics. Consequently, conventional aircraft aerodynamic modeling strategies require modification when applied to eVTOL aircraft. Two novel system identification-based approaches are used to develop an aero-propulsive model for the LA-8 aircraft configuration using wind-tunnel data collected with design of experiments and response surface methodology techniques. The modeling strategies are compared by assessing their predictive performance for validation data acquired separately from the data used to identify the model and are shown to have sufficient predictive capability. Research findings are presented with a discussion of unique eVTOL vehicle aero-propulsive modeling characteristics and practical strategies to inform future aero-propulsive modeling efforts for eVTOL aircraft. This work has been published as a conference paper [27] and a journal article [28].

This chapter, and the remainder of Part II, seeks to provide a thorough development and assessment of new system identification approaches for eVTOL aircraft aero-propulsive modeling. A major objective is to formulate and justify generalized eVTOL aircraft empirical modeling strategies based on vehicle attributes; this includes postulating the definitions of modeling explanatory variables and response variables, designing experiments to enable efficient and accurate characterization of pertinent aerodynamic phenomena, development of approaches to accurately model the aircraft over the full transition flight envelope, and investigation of the aero-propulsive coupling that is ubiquitous for eVTOL vehicles. The motivation for this research was explained in Chapter 1. This chapter is organized as follows: Section 6.1 introduces the LA-8 aircraft and highlights other tilt-wing aircraft modeling efforts. Section 6.2 provides an overview of established aircraft system identification approaches in the context of eVTOL aircraft model development. The wind-tunnel data gathering efforts are described in Section 6.3. Section 6.4 describes pertinent system identification techniques, followed by postulation of vehicle-specific aero-propulsive modeling strategies in Section 6.5. Section 6.6 shows sample modeling results accompanied by discussion of the results.

6.1 LA-8 Aircraft

The Langley Aerodrome No. 8 (LA-8) [191], pictured in a wind tunnel in Figure 6.1 and in a flight test in Figure 6.2, is a subscale, tandem tilt-wing, distributed electric propulsion (DEP) aircraft configuration built as a testbed for eVTOL aircraft technology. The aircraft weighs 63 pounds, the front wingspan is 5.8 ft, and the rear wingspan is 6.2 ft. The LA-8 was developed at NASA Langley Research Center as one of several eVTOL aircraft concepts intended to explore their unique flight characteristics and resolve implementation challenges to help bring similar full-scale vehicles into mainstream operation. The LA-8 project has enabled research in rapid vehicle development [191, 192], computational aerodynamic predictions [193, 194], wind-tunnel testing [46, 195], high incidence angle propeller aerodynamics [36, 37, 196, 197], aero-propulsive modeling [24, 29, 30], flight controls [198], and flight-test strategies [32, 199].

The LA-8 is equipped with 20 control effectors, including: two tilting wings, four elevons, four single-slotted Fowler flaps, two ruddervators, and eight electric motors/propellers. A diagram of the propulsors and control surface definitions is shown in Figure 6.3. The front and rear wing tilt angles are denoted δ_{w_1} and δ_{w_2}. The control surface deflections are denoted δ_{e_1}, δ_{e_2}, δ_{e_3}, δ_{e_4} for elevons; δ_{f_1}, δ_{f_2}, δ_{f_3}, δ_{f_4} for flaps; and δ_{r_1}, δ_{r_2} for ruddervators. Wing, elevon, flap, and ruddervator deflections are defined positive trailing edge downward. Wing angle settings of 0 deg correspond to the horizontal, forward flight position and wing angle settings of 90 deg correspond to the vertical position used near hover. The propulsor rotational speeds are denoted n_1, n_2, ..., n_8. Propellers 1, 3, 6, and 8 rotate clockwise and propellers 2, 4, 5, and 7 rotate counterclockwise, as viewed from the rear. All propellers are 16-inch diameter, 8-inch pitch, fixed-pitch, 3-bladed propellers.

(a) LA-8 front view (b) LA-8 rear view

Figure 6.1: LA-8 mounted in the NASA Langley 12-Foot Low-Speed Tunnel.

Figure 6.2: LA-8 flight test.

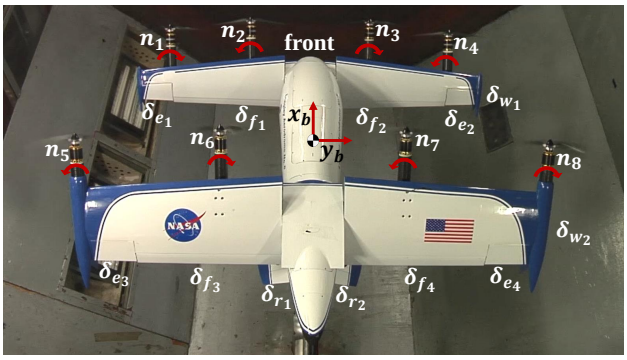

Figure 6.3: LA-8 control effector definitions.

The modeling approaches developed in Part II of this dissertation for eVTOL aircraft are described in the context of and applied to the LA-8 aircraft. Consequently, the subset of eVTOL aircraft of interest in this work are tilt-wing aircraft with wing mounted propellers. The operational advantages resulting from the DEP, tilt-wing design include delayed onset of stall in transition and control surface effectiveness at low airspeed, both due to the propeller slipstreams blowing over a majority of the wing [192]. Efficiency benefits also emerge from the use of DEP technology [200, 201]. The disadvantages of tilt-wing aircraft include sensitivity to wind at low speed due to the upward wing orientation, requiring powerful actuators to rotate the wing, and possible flow separation from the wing in transition [192]. Although the empirical modeling approaches are shown for tilt-wing aircraft, the strategies can be readily applied to many different transitioning eVTOL aircraft, such as tilt-rotor and lift+cruise configurations, with straightforward modifications.

Several previous studies have developed dynamic models for single tilt-wing [202–209] and tandem tilt-wing concepts [210–217]. Many of these efforts develop models using low-to-mid fidelity analytical and/or computational methods with some efforts using wind-tunnel data. The direct predecessor to the LA-8 vehicle studied in this work was a subscale, tilt-wing, tilt-tail, DEP, VTOL aircraft called the GL-10 [218], shown in Figure 6.4. Several different scaled variants of the GL-10 vehicle were developed and tested to enable research in wind-tunnel testing [137, 219], simulation development [218], flight controls [220], and flight testing [221, 222]. The complexity associated with the GL-10 aircraft inspired an ongoing initiative to develop methods to efficiently develop aerodynamic models for arbitrarily complex aerospace vehicles. Several lessons learned from the GL-10 aircraft study informed the development of the aero-propulsive modeling strategies presented in this dissertation.

6.2 Standard Aircraft System Identification Techniques

This section presents an overview of experimental fixed-wing and rotary-wing aircraft modeling techniques, which helps guide the development of the tilt-wing, DEP aircraft mod-

Figure 6.4: GL-10 aircraft.

eling approaches described in Part II of this dissertation.

6.2.1 Fixed-Wing Aircraft Modeling

Fixed-wing aircraft system identification techniques are well-developed for standard problems and have been applied successfully to numerous aircraft configurations [223–226]. Aerodynamic modeling for fixed-wing aircraft is conventionally performed by developing data tables or functional representations of dimensionless aerodynamic force and moment coefficients as a function of aircraft states and controls. For subsonic aircraft, as discussed in Section 2.2, the dimensionless aerodynamic force and moment coefficients are conventionally expressed as a function of angle of attack α; angle of sideslip β; dimensionless angular rates $\hat{p}$, $\hat{q}$, $\hat{r}$; and control surface deflections, such as elevator δ_e, aileron δ_a, and rudder δ_r positions. The dimensionless forces and moments are the response variables; the airflow angles, angular rates, and control surface deflections are the explanatory variables. Models may be developed using computational methods, wind-tunnel testing, or flight testing. Wind-tunnel testing can be used to develop either tabulated or functional representations of the force and moment coefficients through a variety of test techniques [227], which can similarly be applied in a computational setting, whereas flight testing is typically used to develop functional representations of the force and moment coefficients [19, 20]. The dimensionless force and moment coefficients in the aircraft body-axes (C_X, C_Y, C_Z, C_l, C_m, C_n), defined in Equation (2.13), normalize the measured aerodynamic forces and moments by the freestream dynamic pressure and aircraft geometry. The forces are also commonly expressed in the stability-axes for modeling where the lift coefficient C_L [Equation (2.14)] and drag coefficient C_D [Equation (2.15)] replace C_Z and C_X.

Although widely successful for fixed-wing aircraft, the conventional fixed-wing modeling methodology cannot be applied in the same way to modeling eVTOL vehicles. Firstly, nondimensionalization by dynamic pressure $\bar{q} = \frac{1}{2}\rho V^2$ is not valid for vehicles that are propulsion-dominated and experience significant airframe-propulsion interaction. Propeller aerodynamics, for example, scale with the dynamic pressure experienced by the individual

propeller blades, as opposed to freestream dynamic pressure. Due to these aerodynamic scaling differences, testing must be performed at several different airspeed conditions to properly identify the aerodynamics changes across the flight envelope. Another modeling consideration is that eVTOL vehicles will operate at hover which makes modeling in terms of angle of attack α and angle of sideslip β become undefined based on their definitions [see Equations (2.24)-(2.25)]. Airflow angles are also less physically meaningful in the transition regime at low airspeed. Additionally, dimensionless force and moment coefficients are singular in hover due to division by zero dynamic pressure [see Equation (2.13)], and stability frame response variables are meaningless due to their dependence on α.

6.2.2 Rotary-Wing Aircraft Modeling

Rotorcraft system identification follows different conventions from fixed-wing modeling, but is also well defined in the literature for helicopters and tilt-rotor variants [21]. Contrary to fixed-wing aircraft system identification, rotorcraft models generally rely more heavily on computational data or flight-test data because wind-tunnel testing is precluded by difficulties in scaling subscale rotary-wing vehicles and facility limitations [228]. Body-axis force and moment parameters are also generally estimated in their dimensional form due to the differences in scaling between rotor and fuselage aerodynamics. Stability-axes and wind-axes become undefined in hover, so modeling is generally only performed in the body-axes for rotorcraft.

Rotorcraft system identification efforts most often develop linear models at a reference flight condition. These point models are only valid near the flight condition where they are identified and assume that complex rotorcraft aerodynamics can be represented in coupled, linear differential equations. The explanatory variables used for estimation are generally body-axis velocity components u, v, w; angular rates p, q, r; pilot control inputs; and rotor states, such as flapping, lead-lag, inflow, coning, engine dynamics, etc., depending on the design of the vehicle and the desired bandwidth of the developed model. Formulation in terms of body-axis velocity components, as opposed to airflow angles α and β, allows the state variables to be defined in hover and reflects the fact that fuselage angle of attack and angle of sideslip are less physically meaningful for describing rotorcraft aerodynamics. Rotorcraft modeling problems commonly use pilot collective δ_{col}, longitudinal cyclic δ_{lon}, lateral cyclic δ_{lat}, and pedal deflection δ_{ped} because rotor collective and cyclic blade pitch angles are challenging to measure. Models are commonly expressed in the form of a transfer function or state-space model with added time delay parameters to account for unmodeled higher-order dynamics [21].

Similar to fixed-wing aircraft, rotorcraft system identification approaches cannot be applied in the same way to modeling eVTOL vehicles. Firstly, significant airframe-propulsion interactions and rapid aerodynamic variation with flight condition for eVTOL vehicles are not accurately captured using linear rotorcraft modeling techniques, requiring extension to

nonlinear methods. Secondly, pilot control positions are not acceptable for modeling because there is a far greater number of control surfaces and propulsors than pilot inputs. Furthermore, many conventional helicopter rotor states, such as flapping, lead-lag, and coning, are not as relevant to eVTOL vehicles because of smaller and stiffer propeller blades, and measuring or estimating these quantities for each propulsor would be challenging. These additional rotor states are not necessary to capture dominant eVTOL vehicle aerodynamic dependencies due to the smaller-diameter, higher-rigidity distributed propellers and reduced mechanical complexity compared to articulated rotors. For vehicles with fixed-pitch rotors, modeling can be performed using propeller rotational speed measurements, whereas vehicles with variable-pitch rotors will require both rotational speed and blade angle measurements.

6.2.3 Multirotor Aircraft Modeling

Multirotor system identification has become a recent area of research interest with the growing availability and capabilities of electrically-powered UAVs (e.g., see References [7, 9, 75, 128–136]). Multirotor modeling methodologies generally follow closely to rotorcraft system identification techniques, with the exception that certain rotor-specific states become less significant because the rotors generally have a smaller diameter, higher rigidity, and do not use cyclic pitch controls. Airframe-propulsion interactions can account for a significant portion of multirotor aerodynamic forces and moments [229], but are often ignored or lumped into quasi-steady, linear stability derivatives. The aerodynamic characteristics of transitioning eVTOL aircraft configurations are generally a hybrid between multirotor and fixed-wing aircraft, depending on the operational flight mode.

6.3 Wind-Tunnel Testing

The aero-propulsive models presented in this chapter were developed using wind-tunnel data collected at the NASA Langley 12-Foot Low-Speed Tunnel (LST) [230]. The facility is an atmospheric pressure tunnel with a 12-foot width and height octagonal cross-section and 15-foot test section length. Dynamic pressures of up to $\bar{q} = 7$ psf (a freestream velocity of approximately $V = 77$ ft/s at standard sea level conditions) are able to be achieved. The air is pulled through the tunnel by a 6-blade, 15.8-ft diameter fan. The test section longitudinal turbulence intensity is approximately 0.6% for the longitudinal center-line-flow. The 12-Foot LST is primarily used for exploratory aircraft stability and control research with experimental flexibility that enables rapid development of innovative test techniques and characterization of advanced aerospace vehicles. A schematic of the wind tunnel is shown in Figure 6.5.

The LA-8 wind-tunnel tests used for this chapter included an isolated propeller test and a powered-airframe test using the same vehicle that is used for flight testing. Testing at

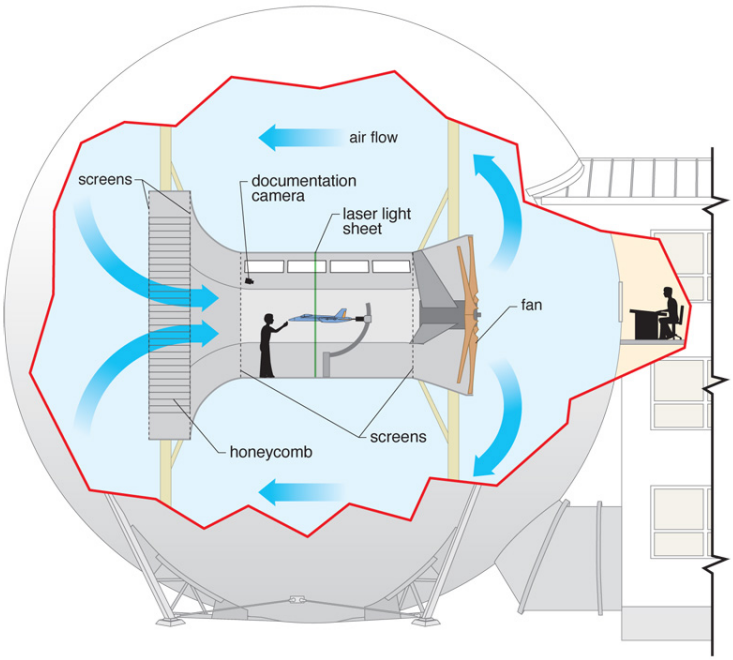

Figure 6.5: Schematic of the NASA Langley Research Center 12-Foot Low-Speed Tunnel.

the flight vehicle full-scale obviates the need to scale using similitude relationships, which are challenging for rotorcraft and typically limit vehicle wind-tunnel testing [144, 228]. An airframe-only test, without propellers, was also performed but not used for model development due to difficulty in superimposing data in the transition flight regime. A buildup aero-propulsive modeling approach was originally considered, including an isolated propulsor model, bare airframe model, and interaction model. However, the blown-wing aerodynamic characteristics, such as delayed stall onset, invalidate the full model buildup approach. An overview of the individual tests used for model development is given next.

6.3.1 Isolated Propeller Testing

Propeller aerodynamics for eVTOL vehicles are complex due to the large range of operational flight conditions, compounded by the presence of many propulsors. An isolated propeller test was conducted to obtain a better understanding of LA-8 propeller behavior in isolation and develop mathematical models for the propeller aerodynamics intended to be used in concert with data from other LA-8 wind-tunnel entries to develop the vehicle aero-propulsive model. The test conditions for the isolated propeller testing included dynamic pressure ranging from 0 to 6 psf (corresponding to a freestream velocity of 0 to 71 ft/s), motor speed ranging from approximately 1500 to 6000 rpm, and angle of incidence relative to the propeller disk ranging from 0 to 180 deg. Combinations of dynamic pressure, motor speed, and incidence angle were tested in a one-factor-at-a-time (OFAT) manner for

both the clockwise and counterclockwise rotating propellers. The collected data cover nearly the full range of expected flight conditions and are used to augment the powered-airframe LA-8 wind-tunnel test described next. The propeller testing methodology and experimental findings are further described in Reference [36]. The test data were subsequently used to develop a propulsion system model that characterizes propeller aerodynamics across the wide range of operational flight conditions expected to be encountered by the LA-8 [37]. Although the OFAT methods employed for this wind-tunnel test were adequate for the intended purpose, the subsequently developed, more efficient and statistically-rigorous experiment design approach for eVTOL aircraft propeller wind-tunnel testing described in Reference [38] is recommended for future eVTOL aircraft propeller testing.

6.3.2 Powered-Airframe Testing

Wind-tunnel tests to capture complex eVTOL vehicle nonlinear aerodynamics and interactions is a challenging undertaking. The LA-8 aircraft, with eight propulsors, ten control surfaces, and two tilting wings, as well as three static flight condition variables, defined by either V, α, β or u, v, w, results in 23 different experimental factors. Due to the large number of factors, traditional static OFAT wind-tunnel testing is not practical for developing models describing the complex nonlinear aerodynamics and vehicle interactions of eVTOL aircraft. Experiments designed using design of experiments (DOE) [231] and response surface methodology (RSM) [232] theory, however, can efficiently scale to a large number of factors allowing wind-tunnel tests to be completed in a reasonable amount of time while supporting identification of interactions between all factors. DOE/RSM-based wind-tunnel tests were used previously to characterize the GL-10 aircraft [137, 219] and is the approach used for the LA-8 powered-airframe testing [46].

DOE/RSM-based testing provides a statistically rigorous experiment design methodology supplying rich information content in a relatively compact data set. The model development process also benefits from properties of *orthogonality*, *randomization*, *replication*, *blocking*, and *sequential testing* [231]. Nearly *orthogonal* experimental factors aid the model structure identification and parameter estimation process by ensuring low candidate regressor correlation. *Randomization* of test points reduces the effects of systematic measurement errors and extraneous factors—errors are reflected in the parameter variance rather than corrupting the parameter estimates. *Replication* of data points provides insight into the measurement facility noise characteristics. *Blocking* minimizes the effects of unmodeled nuisance factors. *Sequential testing* allows efficient data collection to obtain the desired modeling fidelity.

Although DOE/RSM-based testing has several advantages compared to OFAT testing, particularly for eVTOL vehicles, initial exploratory OFAT testing may be needed to help define the ranges of certain factors for testing [46]. Before performing DOE/RSM-based testing, an OFAT test of the LA-8 vehicle was performed to define the nominal flight envelope and find trim points where longitudinal forces were balanced and pitching moment was

zero [195]. Trimming was primarily accomplished by varying motor speeds and wing angles to prevent control surfaces from being near their physical limits. The ranges of factors for the DOE/RSM test were subsequently specified in accordance with the nominal flight envelope, providing improved data density for modeling over the full flight envelope.

Static DOE/RSM wind-tunnel testing for the LA-8 was performed at eight dynamic pressure settings from 0 to 5 psf (freestream airspeed of approximately 0 to 65 ft/s), where the factor ranges at each dynamic pressure reflected the values expected to be seen in flight at that condition. Contrary to subsonic fixed-wing aircraft tests which are typically performed at one dynamic pressure setting, testing was performed at multiple dynamic pressure settings due to the large contributions of both the fixed and rotating components on the vehicle. Fixed-wing aircraft forces and moments are traditionally nondimensionalized by dynamic pressure $\bar{q}$ and aircraft geometric characteristics. Propeller forces and moments are nondimensionalized by air density ρ, rotational speed n squared, and propeller diameter D raised to the power of four or five [see Equations (3.1), (3.2), and (3.6)], while being highly dependent on airspeed in terms of advance ratio [Equation (3.3)]. These differences in aerodynamic scaling suggest testing at a variety of wind-tunnel dynamic pressure settings is required.

The experimental factors specified for DOE testing at each different tunnel dynamic pressure setting were angle of attack α; angle of sideslip β; wing angles δ_{w_1}, δ_{w_2}; elevon deflection angles δ_{e_1}, δ_{e_2}, δ_{e_3}, δ_{e_4}; flap deflection angles δ_{f_1}, δ_{f_2}, δ_{f_3}, δ_{f_4}; ruddervator deflection angles δ_{r_1}, δ_{r_2}; and PWM commands η_1, η_2,..., η_8, resulting in 22 independently varied factors. Although the background information presented in Section 6.2 suggests parameterizing eVTOL aircraft models using body-axis velocity components, the test matrices were specified using α and β for ease of envelope definition and simplified integration into the wind-tunnel test apparatus. The factor ranges for angle of attack, angle of sideslip, and wing angle are shown in Figure 6.6, with derived parameters of z-axis velocity $w = V \sin\alpha \cos\beta$ and y-axis velocity $v = V \sin\beta$ also displayed. The data points show the upper and lower limit for each variable against the tested dynamic pressure setting, and the connecting lines reflect the modeled flight envelope. Although wing angles δ_{w_1} and δ_{w_2} were varied independently during testing, the ranges of values were identical for all testing, so the wing angle is displayed with a generic label δ_w.

After the ranges of factors for each test condition were determined, the powered-airframe wind-tunnel experiment was designed using DOE/RSM techniques. For each experiment at different dynamic pressure settings, a series of five test blocks was designed to acquire the data necessary to identify increasingly complex aero-propulsive models. Block design was accomplished with the aid of Design-Expert®, a commercially available statistical software package [233]. Following the experiment design approach developed in References [47, 48, 137, 234], the test blocks are: (1) a minimum run resolution V face-centered central composite design (FCCCD), (2) a nested minimum run resolution V FCCCD [235], (3) an augmented I-optimal design for quadratic models, (4) another augmented I-optimal design for quadratic models, and (5) a final augmented I-optimal design for quadratic mod-

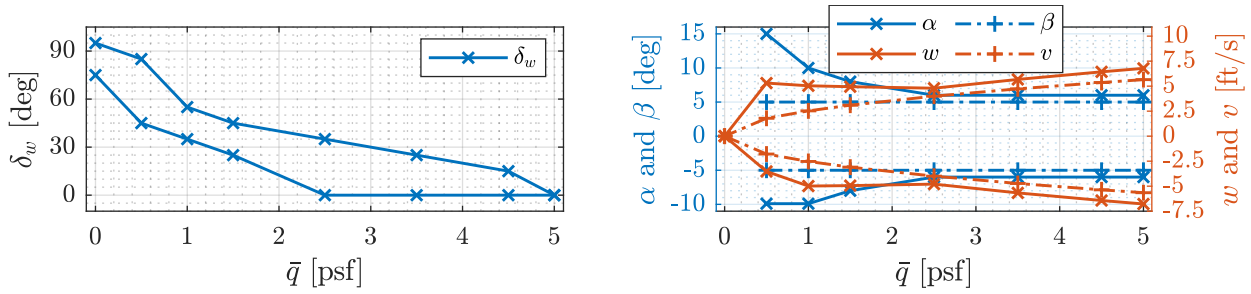

Figure 6.6: LA-8 DOE test state and wing orientation factor ranges against dynamic pressure setting.

els used as validation data. This experiment design will be explained in detail in Chapter 7 (Section 7.3.1). Figure 6.7 shows a two-dimensional slice of the 22-factor space for the LA-8 powered-airframe experiments; Figure 6.7a shows Blocks 1-2 and Figure 6.7b shows Blocks 3-5. Although "Coded Variable 1" and "Coded Variable 2" are shown in the figure, similar plots would be obtained for other test variables and the variables would be converted into engineering units before executing testing.

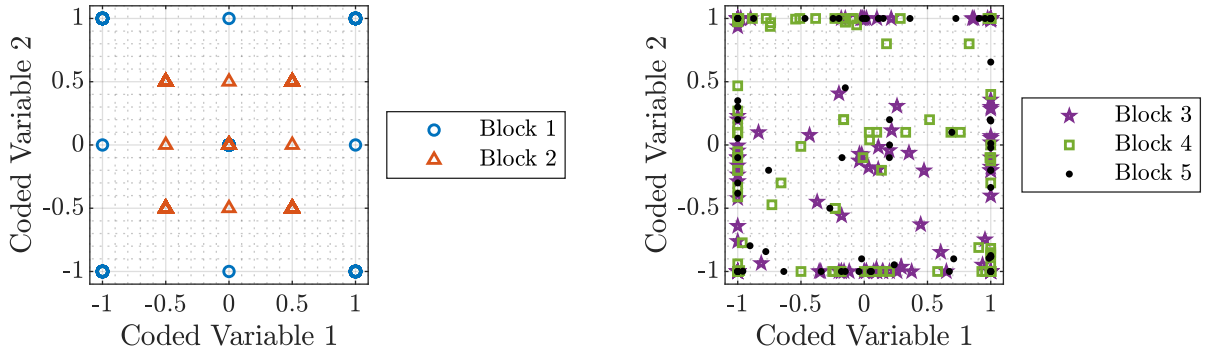

(a) Blocks 1 and 2 (FCCCD and nested FCCCD designs)

(b) Blocks 3, 4, and 5 (I-optimal and validation designs)

Figure 6.7: Two-dimensional slice of the coded factor space for the LA-8 powered-airframe experiments.

6.4 Model Identification

An overview of the methods used for model identification, collinearity analysis, and validation are discussed in the following sections. Although the aircraft system identification research in this chapter and the rest of Part II is different than the work discussed in Part I, the modeling identification techniques were similar to those discussed in Section 2.6 and were

likewise adapted from the SIDPAC software toolbox [19, 50].

6.4.1 Model Structure Determination and Parameter Estimation

Development of an adequate model structure is one of the most challenging aspects of aero-propulsive modeling for eVTOL aircraft. eVTOL vehicles share overlapping characteristics with both fixed-wing and rotary-wing aircraft, as well as complex vehicle-specific phenomena such as high incidence angle propeller aerodynamics, DEP, and propulsion-airframe interactions, which must be represented in the model structure. Consequently, suitable definitions of modeling explanatory and response variables are unclear and the expected model structure is not well defined due to limited previous research in this area. Furthermore, the presence of a larger number of candidate regressors compared to conventional aircraft modeling problems leads to numerical conditioning issues, large data processing times, and a requirement for more user insight. Multiple techniques were investigated to develop the model structure, including stepwise regression [19, 103] and multivariate orthogonal function modeling [19, 102] (see Section 2.6.2). The stepwise regression algorithm from Reference [103], described in Section 2.6.2.2, was used to produce the results presented in this chapter.

The stepwise regression algorithm can be run automatically or manually. Due to the abundance of candidate regressors and large number of model terms needed to describe complex eVTOL aerodynamic phenomena, each model required many iterations to converge to an adequate model structure. For this reason, the stepwise regression algorithm was run automatically until the remaining excluded model terms did not surpass the partial F-statistic cutoff value when added to the model. However, due to the aerodynamic complexity and large number of candidate regressors, the automated algorithm was found to produce models deemed by analysts to require further adjustments to model terms. The automated algorithm was effective in predicting dominant terms that should be included in the model, but was more challenged to determine which borderline terms with similar statistical modeling metrics were worthy of inclusion in the model structure (a task that would be more obvious to a subject matter expert based on physical insight). This results in both model terms excluded from the model that should be included and other model terms included in the final model that should be excluded, based on analyst judgment. For example, if three out of four terms describing the interaction of an elevon with its closest propulsor are included in the model, consideration should be given to adding the fourth elevon-propulsor interaction term. Conversely, if the model includes an interaction term for control effectors far apart on the vehicle lacking physical justification, consideration should be given to removing the term from the model. Most often these borderline model terms are either just above or below the statistical cutoff thresholds. For these reasons, it is useful to add user insight to the modeling process while still utilizing the efficiency gained through automation due to the size of the modeling problem.

To address the desire for modeling efficiency, as well as addition of subject matter expert

user insight when needed, a partially-automated modified stepwise regression (PAMSWR) process was refined and utilized for model development. The automated algorithm is first run to develop a baseline model. After termination of the automatic algorithm, a subject matter expert is given the ability to add insight into the modeling process by adding or removing model terms based on physical vehicle insight and statistical metrics. The PAMSWR approach is particularly useful for eVTOL vehicle modeling because the automated process helps to expedite the model development process, but the manual model adjustment at the end allows for modeling insight from a subject matter expert.

Part of the model structure determination process is to select a pool of candidate regressors to be evaluated for inclusion in the model structure. Due to the large number of LA-8 test factors (22), practical DOE/RSM experiment designs can only support lower-order full polynomial models, such as a quadratic model terms with two-factor interactions terms (Quadratic+2FI). An example of Quadratic+2FI complexity candidate model terms for an arbitrary three-factor study involving explanatory variables of α, β, and δ would be α, β, δ, $\alpha\beta$, $\alpha\delta$, $\beta\delta$, α^2, β^2, and δ^2. From this list of candidate regressors, one can infer that the number of candidate model terms would become large for a study with many factors. For a 22-factor study with Quadratic+2FI complexity, there are 275 candidate model terms.

After determining an adequate model structure, the final parameter values were estimated using ordinary least-squares regression (see Section 2.6.1.1). A characteristic of modeling eVTOL aircraft is the presence of many regressors and associated parameter estimates included in the final models. Thus, even when implemented on modern computers, numerical best practices are emphasized for solving the regression problem. This includes scaling regressor measurements to be the same order of magnitude for performing calculations and using a robust inversion technique to compute $\left(\boldsymbol{X}^T\boldsymbol{X}\right)^{-1}$, such as singular value decomposition. SIDPAC regression codes use robust singular value decomposition matrix inversion by default.

6.4.2 Data Collinearity Assessment

As discussed in Section 2.6.2.4, data collinearity is defined as a correlation between regressors high enough to cause corrupted model identification [19]. Data collinearity will cause difficulty in both model structure determination and parameter estimation because the effects of certain regressors on the response cannot be distinguished. Model structure identification is corrupted by candidate regressor correlation, particularly for the large number of candidate model terms associated with modeling eVTOL aircraft, because an algorithm is more inclined to include model terms that lack physical reality or exclude model terms describing significant aerodynamic phenomena. Parameter estimation algorithms cannot differentiate between highly correlated model terms, resulting in inaccurate parameter estimates and high uncertainties. For these reasons, it is important to develop an experiment design with low correlation among candidate regressors. Note that if a full factorial test matrix was used for

the experiment, all test factors and their interactions would be perfectly orthogonal. The minimum run resolution V factorial and I-optimal test matrix designs used to run a more efficient experiment and a desire for higher-order model terms warrants correlation analysis. Data collinearity should also be assessed after data collection because the designed factor settings may not be perfectly achieved in the experiment and, in this work, some of the explanatory variables differ from test factors, as will be discussed in Sections 6.5.1-6.5.2.

Correlation between two regressors can be assessed using the correlation coefficient r_{ij}, shown in Equation (2.80), where $\boldsymbol{\xi}_i$ and $\boldsymbol{\xi}_j$ represent the two regressor measurement histories. A correlation coefficient value of zero means the signals are uncorrelated, or orthogonal, and an absolute correlation coefficient of one indicates that the signals are completely correlated. A correlation coefficient between regressors with magnitude greater than 0.9 indicates that data collinearity problems may be encountered [19, 20]. The correlation coefficient only quantifies correlation between pairs of regressors, and thus cannot diagnose collinearity among more than two regressors.

Collinearity assessment is useful for confirming a choice of modeling candidate regressors from a given experiment design or data set are sufficiently decorrelated for model identification. Figure 6.8 shows the correlation coefficient values between all Quadratic+2FI candidate regressors for the designed 22-factor test matrix used for LA-8 model development. The pairwise correlation coefficients of each regressor with all other candidate regressors are shown for each regressor index. Correlation among the pure quadratic model terms is the highest at approximately $r_{ij} = 0.7$, but the correlation is still low enough for successful model identification. This figure demonstrates that Quadratic+2FI regressors derived from the experiment test factors are sufficiently decorrelated and provides a basis for comparison to other candidate regressor choices explored in future sections.

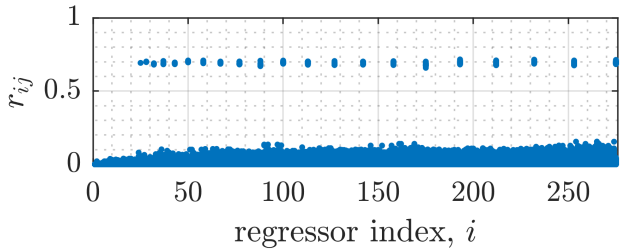

Figure 6.8: Correlation of Quadratic+2FI experimental factor candidate regressors in coded units.

6.4.3 Model Validation

Model validation, discussed previously in Section 2.6.3 in the context of flight-test system identification for fixed-wing aircraft, is an examination of model adequacy using data

withheld from the model development process. Regression methods minimize the summation of squared modeling residuals between modeled and measured response, so inspection of modeling fit metrics and modeling residuals alone does not provide information about the model predictive capability. Assessment of model performance using validation data not used for modeling provides a more reliable estimate of model prediction accuracy. Validation assessment can be performed by comparing the measured response for validation data to the response predicted by the model for the same explanatory variable inputs. Further assessment is performed by analyzing the prediction residuals between the measured and predicted response, $\boldsymbol{e} = \boldsymbol{z} - \hat{\boldsymbol{y}}$. Here, it is useful to compare modeling and prediction residuals because a significant increase in the spread of prediction residuals compared to modeling residuals is a way of diagnosing an improper model. Plots of residuals over a measurement history should appear as white noise with a magnitude below a level deemed acceptable by the analyst for a particular modeling effort. Repeated test points provided an estimate of the measurement error variance and aid in determining an acceptable level of modeling and prediction error; however, acceptable residual character is still somewhat subjective and dependent on factors such as the flight condition, response type, and test facility. Further residual distribution statistics can be computed, such as the RMSE [see Equation (2.84)].

Residuals and their statistical properties can be given further interpretability by normalization. Following the justification given in Section 2.6.3, the error normalization metric used in this work is the range of response variable measurements used to develop the local model, range($\boldsymbol{z}_m$) [Equation (2.85)]. The normalized residual vector is defined as:

$$\boldsymbol{e}^* = \frac{\boldsymbol{z} - \hat{\boldsymbol{y}}}{\text{range}(\boldsymbol{z}_m)} \tag{6.1}$$

The normalized RMSE (NRMSE) was similarly defined in Equation (2.86).

A prediction error metric defined using critical binomial analysis of validation residuals is also useful as a quantitative measure of the model adequacy. For this analysis, each validation data point is considered to either pass or fail relative to a prediction error threshold. Failed trials can indicate model inadequacy or measurement error. The binomial test provides a threshold to determine when the number of failures is statistically significant. For this metric, the prediction error level associated with the number of successful trials being equal to the critical binomial number $\mathcal{B}$ can be used for comparison to a pre-defined level of acceptable modeling error to determine model adequacy. This prediction error threshold is denoted here as e^*_{cv}. For the experiments designed for this work, there were 75 validation points acquired to test the prediction capability of each model. At the 95% confidence level, the binomial test with a 1% inference error has a critical binomial number[1] of $\mathcal{B} = 66$. This can be interpreted as allowing no more than nine validation residuals to exceed the prediction error threshold for an adequate model. The process of computing the 95% prediction error metric interval used for this work is to calculate the normalized prediction residual vector

[1] A method of computing the critical binomial number $\mathcal{B}$ is using the binomial inverse cumulative distribution function in MATLAB®, where the syntax in this case would be `binoinv`$(0.01, 75, 0.95)$.

$\boldsymbol{e}^*$ using Equation (6.1) and then sort the absolute value of $\boldsymbol{e}^*$ in ascending order:

$$\boldsymbol{e}_a^* = \text{sort}\left(|\boldsymbol{e}^*|\right) \tag{6.2}$$

Using the ascending absolute normalized prediction residual vector $\boldsymbol{e}_a^*$, the prediction error metric e_{cv}^* is provided as the $\mathcal{B}$th value of $\boldsymbol{e}_a^*$ vector:

$$e_{cv}^* = \boldsymbol{e}_a^*(\mathcal{B}) \tag{6.3}$$

Further explanation of critical binomial analysis of residuals and justification for using this metric to assess prediction error is given in Reference [236]. This metric has been used in previous aircraft DOE/RSM wind-tunnel testing studies [47, 234, 237].

6.5 Aero-Propulsive Modeling Approaches

Aerodynamic modeling for this effort focuses on developing a polynomial representation of the aero-propulsive forces and moments as a function of vehicle state and control variables. Two approaches were postulated and tested to investigate modeling for eVTOL aircraft. The first approach discussed is a conventional procedure where factors under test, or close variants, are added to a universal candidate regressor pool and the model is identified from the powered-airframe wind-tunnel data. The second approach utilizes identified isolated propeller models to inform full-airframe model identification. The modeling approaches developed herein apply relevant parts from both fixed-wing and rotary-wing modeling methodologies as well as incorporate strategies specific to tilt-wing, DEP aircraft. For this study, the goal was to develop models minimizing prediction error, where a value of 5% or less for e_{cv}^* was considered to be adequate based on analyst judgment and previous aerodynamic modeling studies conducted in the experimental facility used for wind-tunnel testing [234].

Aero-propulsive modeling for tilt-wing, DEP aircraft requires a different approach, compared to conventional fixed-wing and rotary-wing aircraft modeling approaches outlined in Section 6.2. eVTOL vehicles can be considered a fixed-wing/rotary-wing hybrid suggesting that a combination of the two modeling methodologies will facilitate suitable model development. Accordingly, the modeling approaches defined here largely seek to merge appropriate fixed-wing and rotary-wing modeling attributes with certain new strategies to develop a modeling methodology for LA-8 and other similar vehicles. Adopted from rotorcraft modeling, the response variables are defined as the dimensional body-axis aero-propulsive forces and moments X, Y, Z, L, M, and N, as opposed to nondimensional force and moment coefficients C_X, C_Y, C_Z, C_l, C_m, and C_n. Furthermore, the explanatory variables for aerodynamic states are defined in terms of the body-axis velocity components v and w, as opposed to angle of attack α and angle of sideslip β. These choices facilitate a modeling strategy valid from cruise to hover. Adopted from fixed-wing modeling, a generally nonlinear polynomial expansion modeling approach is used to capture the nonlinear aerodynamic effects including airframe-propulsion interactions.

Certain attributes of tilt-wing, DEP aircraft require specific modeling techniques not gleaned from fixed-wing or rotary-wing system identification. Both fixed-wing and rotary-wing modeling approaches also do not translate well to a vehicle with many propulsion elements which individually interact with lifting surfaces and control surfaces. The tilting wings add additional challenges not seen in tilt-rotor designs because the propellers, wings, and wing-fixed control surfaces all change orientation with respect to the modeling frame of reference in the body-axes. Each different combination of wing angle orientation can be interpreted as a vehicle configuration change. One way of handling this complexity is to develop a different aero-propulsive model at each combination of wing angle settings, in addition to flight condition defined by $\bar{q}$ for wind-tunnel testing. This method would be ideal when a transition wing angle schedule has been defined. However, the identified aero-propulsive model may be used to inform the transition wing angle schedule, as is the case for the present vehicle. The presence of two independently tilting wings adds further complication. In this case, developing a new aero-propulsive model at numerous possible combinations of wing angle throughout transition becomes impractical due to the large increase in the number of test points required, and therefore, it is necessary to include wing angles as explanatory variables in the modeling rather than as part of the configuration definition.

6.5.1 Approach I: Modeling Using Only Powered-Aircraft Test Data and Standard Regressor Definitions

The first approach for modeling the LA-8 aircraft, referred to as "Approach I," uses the powered-airframe wind-tunnel test described in Section 6.3.2 for model identification. Models developed from DOE/RSM-based testing conventionally evaluate the factors under test as candidates for explanatory variables. However, due to unique characteristics of eVTOL aircraft, test facility integration limitations, and convenience, analysis was instead performed by redefining certain explanatory variables for modeling. For example, as mentioned in Section 6.3.2, wind-tunnel testing was performed by varying α and β directly for operational convenience. Although testing was performed with experimental factors of α and β, modeling was performed using body-axis velocity components v and w, following rotorcraft system identification convention. Because body-axis velocity components are closely related to airflow angles, this variable change does not affect the ability to identify a model from the data because the regressors retain their low correlation. Similarly, testing was performed by varying motor PWM commands, but modeling was performed using measured propeller rotational speeds. Propeller speed is more relevant to describe propeller aerodynamics and the relationship between PWM command and propeller speed can change significantly due to nuisance factors, such as motor temperature. For this reason, it is essential to acquire a direct measurement of propeller rotational speed for modeling, as opposed to relying on a calibration curve between motor PWM command and propeller speed. Although the PWM command to propeller speed relationship does not follow a linear trend, particularly at inci-

dence [37], low regressor correlation was still sufficiently maintained, making this approach justifiable. Figure 6.9 shows the correlation coefficient metric for Quadratic+2FI candidate regressors computed for the centered explanatory variables specified in this section. The correlation for equivalent levels of model complexity is only slightly higher than the correlation between commanded experimental factors shown in Figure 6.8. This suggests validity in the proposed modeling approach.

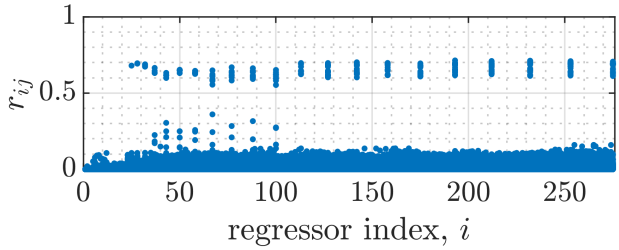

Figure 6.9: Correlation of Approach I Quadratic+2FI candidate regressors.

It is important to perform modeling with explanatory variables expressed in coded units, or in engineering units with the explanatory variables centered on a reference value, to maintain low correlation among candidate regressors. The correlation coefficients among candidate regressors in engineering units assembled from centered explanatory variables are identical to the correlation coefficients among regressors in coded units, if the centering reference value for each explanatory variable is the midpoint between the minimum and maximal value. Both explanatory variable formulations align with the assumptions of a multivariate Taylor series expansion taken from a single reference point. Although models defined in coded units are suitable for model predictions and simulation, models in engineering units are generally desired because of their physical meaning relating to stability and control derivatives. For this reason, the LA-8 aero-propulsive models were developed using explanatory variables in engineering units centered on the respective mean value of each explanatory variable.

To summarize, the modeling explanatory variables for this approach were defined to be the centered body-axis velocity components v, w in ft/s; propeller speed $n_1, n_2, ..., n_8$ in revolutions per second; wing angle $\delta_{w_1}, \delta_{w_2}$ in radians; elevon deflection $\delta_{e_1}, \delta_{e_2}, \delta_{e_3}, \delta_{e_4}$ in radians; flap deflection $\delta_{f_1}, \delta_{f_2}, \delta_{f_3}, \delta_{f_4}$ in radians; and ruddervator deflection $\delta_{r_1}, \delta_{r_2}$ in radians. The response variables are defined as the dimensional aero-propulsive forces X, Y, Z in lbf and moments L, M, N in ft·lbf acting on the aircraft in body-fixed axes. An independent model was developed at each dynamic pressure condition tested.

One advantage of modeling Approach I is its generality, where the only limitation in describing the vehicle static aero-propulsive characteristics is the adequacy of modeling with the particular selection of candidate regressors. Additionally, this approach avoids assumptions of model superposition validity (i.e. combining aerodynamic models for different aircraft components, such as propellers and wings) because all model parameters are estimates from

a comprehensive data set where all states and controls are varied. The final models are also in a compact form allowing easy use for a variety of applications. A second modeling approach, described next, strives to add additional fidelity and simulation advantages utilizing supplementary propeller wind-tunnel testing to develop the aero-propulsive model.

6.5.2 Approach II: Modeling Using a Combination of Isolated Propulsion and Powered-Airframe Testing

An alternative modeling approach, referred to as "Approach II," is to combine isolated propeller models with full-airframe models. Isolated propeller aerodynamics across an eVTOL aircraft flight envelope are highly complex and, at incidence, produce significant off-axis forces and moments in addition to axial thrust and torque. For example, in Reference [37], 31 model terms are identified to characterize the forces and moments produced by a single isolated propeller for airflow incidence angles ranging between 0 to 60 deg. Consequently, the complexity of propeller aerodynamics for many different propulsors increases the difficulty of identifying all necessary model terms from a powered-airframe test alone, suggesting possible merit for pursuing a hybrid propeller and full-airframe modeling approach.

The LA-8 propeller aerodynamic model was developed using the isolated propeller test summarized in Section 6.3.1 and described in detail in Reference [36]. A functional representation of the thrust and torque components in a propeller-fixed axis system were identified using the dimensionless thrust and torque coefficients [see Equations (3.1), (3.2), and (3.6)] as the response variables. The propeller modeling explanatory variables were the normal component of advance ratio,

$$J_x = \frac{V \cos i_p}{nD} \tag{6.4}$$

the edgewise (tangential) component of advance ratio,

$$J_z = \frac{V \sin i_p}{nD} \tag{6.5}$$

and the propeller blade Reynolds number defined in Equation (3.4). Recall that i_p is the propeller incidence angle relative to the oncoming airflow that was shown in Figure 3.1. The variables J_x and J_z are similar to an advance ratio representation used for rotorcraft [145, 146] and have been used in other work characterizing propellers operating at high incidence angles [38, 238]. The LA-8 propeller aerodynamic model development is described in further detail in Reference [37].

Using the aerodynamic model developed for the isolated propellers, the aerodynamic conditions at the eight vehicle propeller disk centers were used to estimate forces and moments produced by each of the propellers in the powered-airframe wind-tunnel data. Each calculated kth propeller forces and moments were transferred from the propeller center in the propeller-fixed frame to the aircraft modeling reference location in the body-fixed frame, as

shown in Reference [37]. The kth propeller forces and moments transferred to the modeling reference location in the body-fixed frame are denoted $T^b_{x_k}$, $T^b_{y_k}$, $T^b_{z_k}$, $Q^b_{x_k}$, $Q^b_{y_k}$, and $Q^b_{z_k}$. The estimated propeller forces and moments for each of the eight propellers were then subtracted from the measured forces and moments to compute an estimate for the non-propulsive forces and moments experienced by the aircraft, denoted $\hat{X}$, $\hat{Y}$, $\hat{Z}$, $\hat{L}$, $\hat{M}$, and $\hat{N}$, as follows:

$$\begin{aligned} \hat{X} &= X - \sum_{k=1}^{8} T^b_{x_k},\ \hat{Y} = Y - \sum_{k=1}^{8} T^b_{y_k},\ \hat{Z} = Z - \sum_{k=1}^{8} T^b_{z_k}, \\ \hat{L} &= L - \sum_{k=1}^{8} Q^b_{x_k},\ \hat{M} = M - \sum_{k=1}^{8} Q^b_{y_k},\ \hat{N} = N - \sum_{k=1}^{8} Q^b_{z_k} \end{aligned} \tag{6.6}$$

These forces and moments with propulsion contributions removed, with respective units of lbf and ft·lbf, are defined as the response variables for modeling Approach II.

Similar to Approach I, the centered explanatory variables used for modeling included body-axis velocity components v, w in ft/s; wing angle $\delta_{w_1}, \delta_{w_2}$ in radians; elevon deflection $\delta_{e_1}, \delta_{e_2}, \delta_{e_3}, \delta_{e_4}$ in radians; flap deflection $\delta_{f_1}, \delta_{f_2}, \delta_{f_3}, \delta_{f_4}$ in radians; and ruddervator deflection $\delta_{r_1}, \delta_{r_2}$ in radians. To model propulsion-airframe interactions and correct for the fact that the presence of the vehicle will have some effect on the forces and moments produced by the propellers, it is important to include a propulsion explanatory variable, even though the main propulsion effects are described by the propeller models. One choice is to use propeller speed $n_1, n_2, ..., n_8$ in revolutions per second, as was the method used in Approach I. An alternative approach is to use the estimated axial thrust for each propeller $T^p_{x_k}$ as an explanatory variable (referred to henceforth as T_k for simplicity). The primary propulsion-airframe interactions for blown wing aircraft are theoretically proportional to the slipstream dynamic pressure. Slipstream dynamic pressure, introduced in Equation (3.16), is the theoretical dynamic pressure located behind a propeller derived from momentum theory [158, 163]. For the kth propeller:

$$\bar{q}_{ss_k} = \frac{1}{2}\rho V^2 + \frac{T_k}{A} \tag{6.7}$$

As mentioned previously in Section 3.4.1, slipstream dynamic pressure consists of the sum of freestream dynamic pressure $\bar{q} = \frac{1}{2}\rho V^2$ and propeller disk loading T_k/A, where $A = \frac{\pi}{4}D^2$ is the propeller disk area. A visualization of the propeller slipstreams present on the LA-8 vehicle is given in Figure 6.10. The slipstream dynamic pressure is an important quantity because it relates to the control authority of control surfaces and wings interacting with the propeller slipstream. Because a new model is developed at each dynamic pressure for this study and propeller area is a constant, axial thrust for each propeller is the only quantity governing these interactions, and thus, $T_1, T_2, ..., T_8$ in lbf are selected as the propulsor explanatory variables for this approach. Following the logic presented in Section 6.5.1, including these quantities as explanatory variables centered on a reference value is permissible because the correlation between modeling terms remains low, as shown in Figure 6.11.

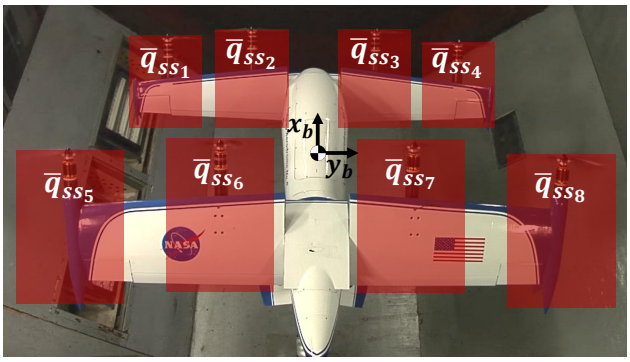

Figure 6.10: Visualization of the propulsor slipstreams on LA-8.

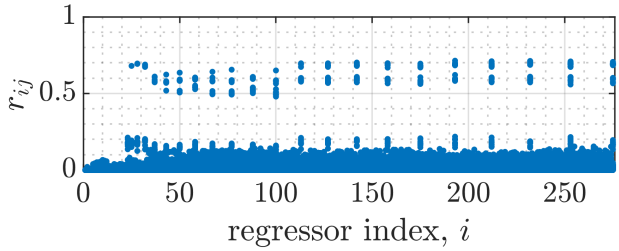

Figure 6.11: Correlation of Approach II Quadratic+2FI candidate regressors.

Modeling Approach II offers multiple additional advantages compared to Approach I. Firstly, Approach II allows for correction of propeller flow conditions when the vehicle model is implemented into a dynamic simulation with nonzero angular velocity [37]. This attribute is important for modeling dynamic aerodynamic effects alongside the static models developed in this study. Angular velocity was not varied during the testing so its effect is not in the models presented in this chapter, but could be modeled using supplemental dynamic testing. Approach II also offers some meaningful extrapolation capability because the primary propulsion forces and moments are modeled in their dimensionless form. Additionally, utilization of individual propeller models facilitates modeling additional vehicle complexity unable to be described by the candidate regressor pool defined for modeling from the powered-airframe test alone. Disadvantages of Approach II include the additional resources needed to perform supplementary propeller testing and the assumption that superposition of propeller models with full-airframe models is acceptable.

The explanatory variables and response variables defined for each specific approach are summarized in Table 6.1. Note that u is not included as an explanatory variable, but its effect is implicitly described by the set of aero-propulsive models identified at different dynamic pressure settings. The following section presents modeling results for these two LA-8 modeling approaches.

Table 6.1: Summary of explanatory variables and response variables for the developed modeling approaches

Approach I	
Explanatory Variables	$v, w, n_1, n_2, n_3, n_4, n_5, n_6, n_7, n_8, \delta_{w_1}, \delta_{w_2}, \delta_{e_1}, \delta_{e_2}, \delta_{e_3}, \delta_{e_4}, \delta_{f_1}, \delta_{f_2}, \delta_{f_3}, \delta_{f_4}, \delta_{r_1}, \delta_{r_2}$
Response Variables	X, Y, Z, L, M, N
Approach II	
Explanatory Variables	$v, w, T_1, T_2, T_3, T_4, T_5, T_6, T_7, T_8, \delta_{w_1}, \delta_{w_2}, \delta_{e_1}, \delta_{e_2}, \delta_{e_3}, \delta_{e_4}, \delta_{f_1}, \delta_{f_2}, \delta_{f_3}, \delta_{f_4}, \delta_{r_1}, \delta_{r_2}$
Response Variables	$\hat{X}, \hat{Y}, \hat{Z}, \hat{L}, \hat{M}, \hat{N}$

6.6 Results

This section presents sample results for the aero-propulsive models identified for the LA-8 aircraft. The two aero-propulsive modeling approaches described in the previous section were used to develop models at the eight different dynamic pressures tested. The results presented here only consider the models identified at $\bar{q} = 3.5$ psf. For vehicle simulation, local models at several dynamic pressure (or airspeed) settings throughout the flight envelope are needed and require a blending methodology to be used for continuous simulation.

6.6.1 Model Identification Results

As described in Section 6.4, the modeling process was facilitated using the PAMSWR procedure and least-squares regression. The final model terms, parameter estimates, and standard errors for the identified models at $\bar{q} = 3.5$ psf for each dimensional body-axis force and moment using modeling Approach I are given in Table 6.7 and Table 6.8, at the end of this chapter. Similar results for the modeling Approach II full-airframe models for each dimensional body-axis force and moment with estimated propulsion effects removed are given in Table 6.9 and Table 6.10. Sample clockwise propeller models used for Approach II are given in Reference [37]. The ranges of validity for each explanatory variable in the identified models at $\bar{q} = 3.5$ psf are given in Table 6.2.

A few interesting characteristics about identified model terms are highlighted. One clear feature is that the number of parameters in the models is far greater than many conventional aircraft modeling problems. Another observation is that significant propulsor-wing angle interaction is reflected in every model equation. Control surface-wing and control surface-propulsion interactions are also clearly represented. Control surface-wing and control surface-propulsion interactions are reflected in x-axis force, rolling moment, and yawing moment, but it is apparent that control surface interactions have limited contributions for pitching

Table 6.2: Ranges of validity for the LA-8 aero-propulsive models developed at $\bar{q} = 3.5$ psf ($V = 54.3$ ft/s)

Factor(s)	Units	Minimum	Maximum
v	ft/s	-4.73	$+4.73$
w	ft/s	-5.67	$+5.67$
$n_1, n_2, ..., n_8$	rpm	2770	6120
$T_1, T_2, ..., T_8$	lbf	-0.22	$+5.94$
$\delta_{w_1}, \delta_{w_2}$	deg	0	$+25$
$\delta_{e_1}, \delta_{e_2}, \delta_{e_3}, \delta_{e_4}$	deg	-25	$+25$
$\delta_{f_1}, \delta_{f_2}, \delta_{f_3}, \delta_{f_4}$	deg	0	$+20$
$\delta_{r_1}, \delta_{r_2}$	deg	-30	$+30$

moment. Control surfaces appear to only have significant interactions with the wings they are affixed to or with the corresponding propulsor(s) displayed graphically in Figure 6.10. Comparing the two modeling approaches, the interaction terms are similar, but Approach II has fewer propulsion terms because most of the isolated propeller aerodynamics are captured by the separate propulsion model. The presence of a large number of strong interaction effects in the model suggests that a linearized form of the aero-propulsive model will have only a small region of validity.

Another characteristic to note is that the models contain significant lateral-directional asymmetries that are not apparent from the LA-8 vehicle configuration. This is a result of manufacturing differences between the clockwise and counterclockwise propellers, which resulted in a significant difference in thrust production between the propeller variants [36]. Because the propulsion-only and propulsion-airframe interaction effects are significant, this propulsion asymmetry is manifested in many model terms. Consequently, lateral-directional forces and moments have nonzero values for symmetric control inputs, and trim solutions require asymmetric control surface deflections and/or propulsor speeds.

Modeling performance statistics, including R^2, PSE, RMSE for modeling data (RMSE_m), and NRMSE for modeling data (NRMSE_m) are given in Table 6.3 for Approach I and Table 6.4 for Approach II. It should be noted that R^2 and PSE for Approach II are calculated using the modeling fit to its unique response variables, $\hat{X}$, $\hat{Y}$, $\hat{Z}$, $\hat{L}$, $\hat{M}$, and $\hat{N}$, defined in Section 6.5.2. Accordingly, direct comparison between Approach I and Approach II cannot be made based on these model fit metrics because a substantial part of the response variations are already described by the isolated propeller models, which is not reflected in these metrics. The RMSE_m and NRMSE_m metrics in Table 6.4 are calculated using the modeling fit to the total forces and moments to facilitate a fairer comparison to the results of Approach I. To aid interpretation of results, Table 6.3 and Table 6.4 also list the number of model terms n_p (excluding the number of model terms in the propeller model used for Approach II); the range of total force and moments in the estimation data, range($\boldsymbol{z}_m$); the maximum absolute total force or moment value in the estimation data, max($|\boldsymbol{z}_m|$); and the standard

deviation of the measured response for replicate data points ν_m, which gives an estimate of the measurement error in testing. Modeling metrics indicate a good fit to the data for both approaches, with comparable metrics reflecting similar values. However, modeling metrics are not always consistent with actual model prediction capability. Prediction error metrics are considered a superior measure of modeling success for prediction (see Section 6.4.3) and are discussed in the next section.

Table 6.3: Approach I modeling metrics at $\bar{q} = 3.5$ psf

Metric	X	Y	Z	L	M	N
R^2	99.3	97.1	98.1	93.3	97.5	98.5
PSE	4.42	0.519	28.3	17.5	54.6	8.76
$\sqrt{\text{PSE}}$	2.10	0.720	5.32	4.18	7.39	2.96
RMSE_m	0.665	0.449	2.94	3.14	4.49	1.33
n_p	52	37	37	43	35	48
$\text{range}(\boldsymbol{z}_m)$	59.1	14.3	116	109	186	78.0
$\max(\lvert\boldsymbol{z}_m\rvert)$	43.9	7.26	108	56.0	96.7	45.7
ν_m	0.196	0.221	0.601	1.00	0.980	0.159
NRMSE_m [%]	1.12	3.14	2.54	2.87	2.41	1.71

Table 6.4: Approach II modeling metrics at $\bar{q} = 3.5$ psf

Metric	X	Y	Z	L	M	N
R^2	98.7	96.0	96.7	86.8	95.2	94.5
PSE	2.71	0.426	25.1	14.7	43.9	3.18
$\sqrt{\text{PSE}}$	1.65	0.653	5.01	3.83	6.62	1.78
RMSE_m	0.713	0.466	3.33	3.29	4.89	1.27
n_p	47	31	35	39	33	45
$\text{range}(\boldsymbol{z}_m)$	59.1	14.3	116	109	186	78.0
$\max(\lvert\boldsymbol{z}_m\rvert)$	43.9	7.26	108	56.0	96.7	45.7
ν_m	0.196	0.221	0.601	1.00	0.980	0.159
NRMSE_m [%]	1.21	3.27	2.88	3.01	2.63	1.62

6.6.2 Model Validation

A test of model prediction capability using data not considered for model estimation is the best way to evaluate modeling success for this study because the objective is to minimize prediction error. Recall from Section 6.3.2 that the validation data are I-optimal test points designed to augment the data used for modeling to optimally reduce prediction error, but are not used to fit the models. Consequently, these validation test points provide

a rigorous prediction test for the designed model complexity. Table 6.5 and Table 6.6 list prediction metrics computed by comparing the modeled response to measured validation response data. The prediction error metrics listed are the RMSE for prediction data (RMSE_v), NRMSE for prediction data (NRMSE_v), and critical binomial analysis of residuals prediction error metric (e^*_{cv}). The RMSE_v and NRMSE_v metrics are useful because they facilitate direct comparison to the equivalent metrics for modeling data. Observing that modeling RMSE metrics hold similar values or are only slightly less than the equivalent validation RMSE metrics, the modeling RMSE metrics are an accurate representation of prediction performance suggesting that modeling was successful. Additionally, RMSE_v can be compared to the $\sqrt{\text{PSE}}$ to quantify how well the model prediction capability can be inferred from the modeling data alone. The $\sqrt{\text{PSE}}$ value is close to the RMSE_v for all responses, and $\sqrt{\text{PSE}}$ generally over-predicts the true prediction error. This is expected because the PSE is a conservative estimate of the prediction error which has the tendency to over-predict the true prediction error for validation data [19]. The critical binomial analysis of residuals prediction error metric e^*_{cv} quantifies the level of error in the models by defining a 95% prediction error metric interval. Seeing that all e^*_{cv} values are roughly 5% or less indicates good models have been identified, given the experimental facility used for wind-tunnel data collection [234].

Table 6.5: Approach I validation metrics at $\bar{q} = 3.5$ psf

Metric	X	Y	Z	L	M	N
RMSE_v	0.796	0.503	3.37	4.19	5.21	2.00
NRMSE_v [%]	1.35	3.52	2.92	3.84	2.79	2.57
e^*_{cv} [%]	1.89	5.39	4.16	5.62	4.16	3.75

Table 6.6: Approach II validation metrics at $\bar{q} = 3.5$ psf

Metric	X	Y	Z	L	M	N
RMSE_v	0.909	0.542	3.48	4.51	5.28	1.78
NRMSE_v [%]	1.54	3.79	3.01	4.13	2.83	2.28
e^*_{cv} [%]	2.47	6.00	4.58	7.03	4.02	2.53

Figure 6.12 shows a comparison of validation metrics for modeling Approach I and Approach II. The metrics displayed are the critical binomial analysis of residuals prediction error metric e^*_{cv} and normalized root mean square error for validation data NRMSE_v. For Approach II, the calculated model predictions are for the total dimensional forces and moments which requires use of both the identified propeller models and full-airframe models. Overall, the prediction error levels and trends are similar between the two different modeling approaches. Future studies are expected to further investigate the utility of the two modeling approaches.

For further model response analysis, Figure 6.13 shows a history of normalized modeling residuals e^*_m and normalized validation residuals e^*_v, as well as the critical binomial analysis

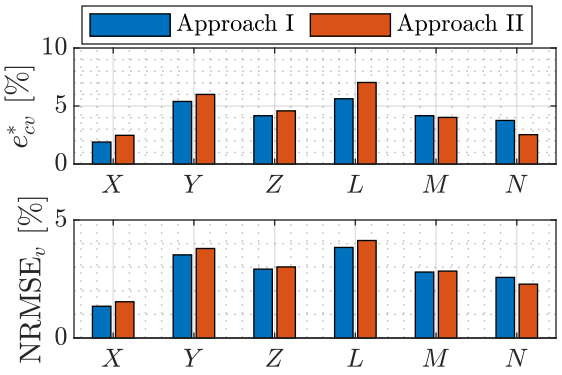

Figure 6.12: Comparison of model validation metrics for both modeling approaches at $\bar{q} = 3.5$ psf.

of residuals prediction error metric bounds, $\pm e^*_{cv}$. The residuals appear to be mostly white noise indicating that the dominant, deterministic aero-propulsive effects are reflected in the identified models. The modeling and prediction residuals also appear to have similar magnitude, supporting the claim that a good predictive model has been identified.

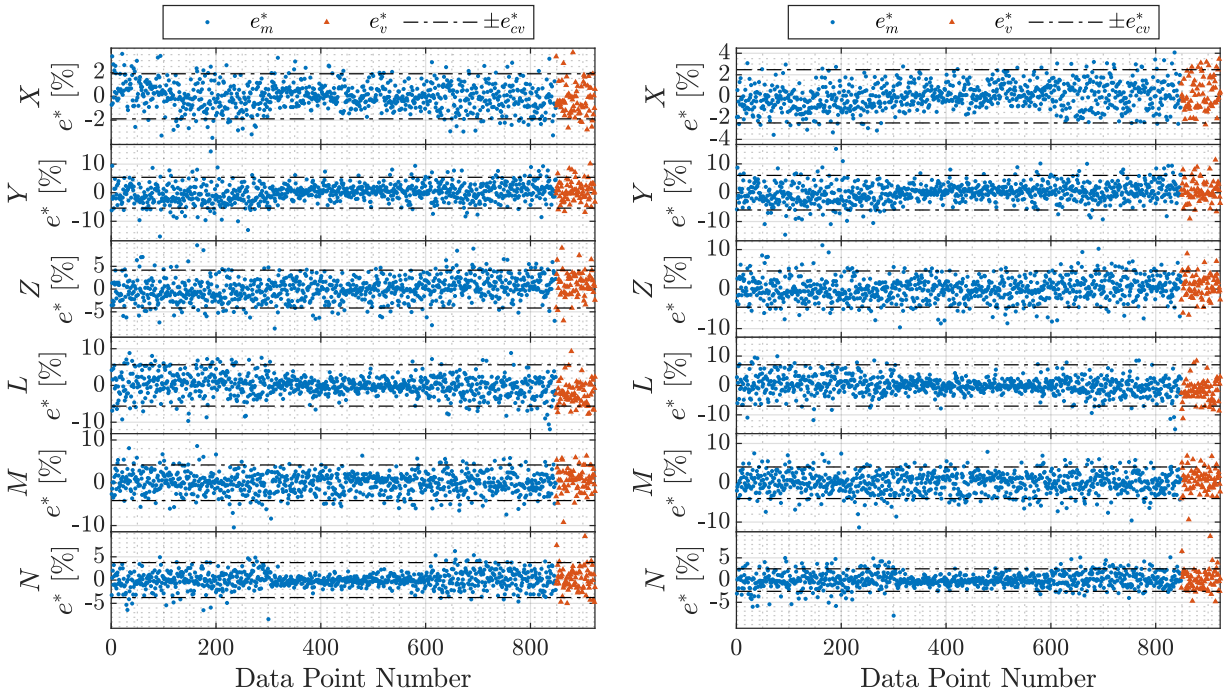

(a) Results for modeling Approach I

(b) Results for modeling Approach II

Figure 6.13: Normalized modeling and prediction residuals at $\bar{q} = 3.5$ psf.

6.6.3 Discussion

When using the models developed in this work, certain attributes should be considered. Firstly, the presented models only contain information about the static aerodynamics and are based on a quasi-steady assumption, where aerodynamics at the current point in time are only dependent on the current states and controls. Identification of dynamic aerodynamic coefficients dependent on vehicle angular rates (and possibly the history of the explanatory variables) will be needed to improve model predictive capability in dynamic maneuvering. Additionally, the experiment design used in this work produces models only capturing two-factor interaction effects; a higher number of factor interactions may need to be included in the model for a vehicle of this complexity. However, experimentation to make these terms identifiable is a challenging task. Also, due to the dimensionality in the models, extrapolation to different flight conditions is not recommended. Finally, lateral-directional asymmetries in the models reflecting physical differences between the vehicle propellers will require attention for trimming and controls.

Acknowledgment of Collaborative Research

The research presented in this chapter was primarily conducted by the author, but included important collaborative contributions with other individuals. The experiment design for the powered-airframe LA-8 DOE/RSM wind-tunnel experiment was developed by Patrick Murphy, who also provided significant technical mentorship on DOE/RSM techniques and offered many helpful suggestions during manuscript preparation. Wind-tunnel test support was provided by Ronald Busan, David Hatke, Earl Harris, Sue Grafton, and Wes O'Neal. LA-8 photography support was provided by Lee Pollard. LA-8 vehicle support and insight was provided by David North, Gregory Howland, Steven Geuther, and Robert McSwain. Discussions about the GL-10 aircraft with Paul Rothhaar, Ronald Busan, Patrick Murphy, Barton Bacon, and Kasey Ackerman assisted postulation of model development approaches. Conversations with Jacob Cook and John Foster also helped to formulate the modeling approaches. Eugene Morelli provided technical guidance on the system identification approach and offered many helpful suggestions during manuscript preparation. The author gratefully acknowledges and appreciates these contributions which made the research described in this chapter possible.

Parameter Estimate Tables

Table 6.7: Approach I aero-propulsive models for X, Z, and M at $\bar{q} = 3.5$ psf

Term	$\hat{\theta} \pm s(\hat{\theta})$	Term	$\hat{\theta} \pm s(\hat{\theta})$	Term	$\hat{\theta} \pm s(\hat{\theta})$
X_w	$+3.60\times10^{-1} \pm 5.88\times10^{-3}$	Z_w	$-2.17\times10^{0} \pm 2.44\times10^{-2}$	M_w	$-2.27\times10^{-1} \pm 3.72\times10^{-2}$
X_{n_1}	$+1.09\times10^{-1} \pm 1.18\times10^{-3}$	Z_{n_1}	$-8.26\times10^{-2} \pm 4.88\times10^{-3}$	M_{n_1}	$+1.91\times10^{-1} \pm 7.48\times10^{-3}$
X_{n_2}	$+8.33\times10^{-2} \pm 1.36\times10^{-3}$	Z_{n_2}	$-1.09\times10^{-1} \pm 5.08\times10^{-3}$	M_{n_2}	$+2.73\times10^{-1} \pm 7.78\times10^{-3}$
X_{n_3}	$+8.76\times10^{-2} \pm 1.15\times10^{-3}$	Z_{n_3}	$-1.30\times10^{-1} \pm 4.60\times10^{-3}$	M_{n_3}	$+2.96\times10^{-1} \pm 7.05\times10^{-3}$
X_{n_4}	$+1.02\times10^{-1} \pm 1.26\times10^{-3}$	Z_{n_4}	$-8.18\times10^{-2} \pm 4.84\times10^{-3}$	M_{n_4}	$+1.97\times10^{-1} \pm 7.41\times10^{-3}$
X_{n_5}	$+9.98\times10^{-2} \pm 1.71\times10^{-3}$	Z_{n_5}	$-5.66\times10^{-2} \pm 6.21\times10^{-3}$	M_{n_5}	$-1.56\times10^{-1} \pm 9.51\times10^{-3}$
X_{n_6}	$+8.37\times10^{-2} \pm 1.38\times10^{-3}$	Z_{n_6}	$-1.22\times10^{-1} \pm 5.39\times10^{-3}$	M_{n_6}	$-1.86\times10^{-1} \pm 8.25\times10^{-3}$
X_{n_7}	$+7.57\times10^{-2} \pm 1.46\times10^{-3}$	Z_{n_7}	$-1.10\times10^{-1} \pm 5.69\times10^{-3}$	M_{n_7}	$-1.92\times10^{-1} \pm 8.72\times10^{-3}$
X_{n_8}	$+1.06\times10^{-1} \pm 1.47\times10^{-3}$	Z_{n_8}	$-6.23\times10^{-2} \pm 5.64\times10^{-3}$	M_{n_8}	$-1.53\times10^{-1} \pm 8.64\times10^{-3}$
$X_{\delta w_1}$	$-1.57\times10^{1} \pm 1.76\times10^{-1}$	$Z_{\delta w_1}$	$-4.34\times10^{1} \pm 6.37\times10^{-1}$	$M_{\delta w_1}$	$+8.14\times10^{1} \pm 9.76\times10^{-1}$
$X_{\delta w_2}$	$-2.37\times10^{1} \pm 1.66\times10^{-1}$	$Z_{\delta w_2}$	$-9.13\times10^{1} \pm 6.50\times10^{-1}$	$M_{\delta w_2}$	$-1.21\times10^{2} \pm 9.94\times10^{-1}$
$X_{\delta e_1}$	$-4.54\times10^{-1} \pm 7.33\times10^{-2}$	$Z_{\delta e_1}$	$-1.54\times10^{0} \pm 3.16\times10^{-1}$	$M_{\delta e_1}$	$+2.45\times10^{0} \pm 4.83\times10^{-1}$
$X_{\delta e_2}$	$-4.78\times10^{-1} \pm 7.35\times10^{-2}$	$Z_{\delta e_2}$	$-2.35\times10^{0} \pm 3.16\times10^{-1}$	$M_{\delta e_2}$	$+2.67\times10^{0} \pm 4.84\times10^{-1}$
$X_{\delta e_3}$	$-4.54\times10^{-1} \pm 7.33\times10^{-2}$	$Z_{\delta e_3}$	$-1.59\times10^{0} \pm 3.16\times10^{-1}$	$M_{\delta e_3}$	$-2.71\times10^{0} \pm 4.84\times10^{-1}$
$X_{\delta e_4}$	$-9.52\times10^{-1} \pm 7.36\times10^{-2}$	$Z_{\delta e_4}$	$-3.79\times10^{0} \pm 3.17\times10^{-1}$	$M_{\delta e_4}$	$-6.71\times10^{0} \pm 4.85\times10^{-1}$
$X_{\delta f_1}$	$-2.56\times10^{0} \pm 1.86\times10^{-1}$	$Z_{\delta f_1}$	$-6.85\times10^{0} \pm 7.98\times10^{-1}$	$M_{\delta f_1}$	$+1.28\times10^{1} \pm 1.22\times10^{0}$
$X_{\delta f_2}$	$-2.57\times10^{0} \pm 1.84\times10^{-1}$	$Z_{\delta f_2}$	$-6.84\times10^{0} \pm 7.91\times10^{-1}$	$M_{\delta f_2}$	$+9.54\times10^{0} \pm 1.21\times10^{0}$
$X_{\delta f_3}$	$-3.59\times10^{0} \pm 1.84\times10^{-1}$	$Z_{\delta f_3}$	$-1.32\times10^{1} \pm 7.93\times10^{-1}$	$M_{\delta f_3}$	$-2.14\times10^{1} \pm 1.22\times10^{0}$
$X_{\delta f_4}$	$-3.55\times10^{0} \pm 1.83\times10^{-1}$	$Z_{\delta f_4}$	$-1.22\times10^{1} \pm 7.87\times10^{-1}$	$M_{\delta f_4}$	$-1.74\times10^{1} \pm 1.21\times10^{0}$
X_{w^2}	$+2.32\times10^{-2} \pm 2.91\times10^{-3}$	$Z_{\delta r_1}$	$-1.42\times10^{0} \pm 2.63\times10^{-1}$	$M_{\delta r_1}$	$-2.25\times10^{0} \pm 4.04\times10^{-1}$
$X_{n_1^2}$	$+9.07\times10^{-4} \pm 1.24\times10^{-4}$	$Z_{\delta r_2}$	$-1.91\times10^{0} \pm 2.65\times10^{-1}$	$M_{\delta r_2}$	$-2.66\times10^{0} \pm 4.06\times10^{-1}$
$X_{n_2^2}$	$+5.26\times10^{-5} \pm 1.29\times10^{-4}$	Z_{w^2}	$+5.28\times10^{-2} \pm 1.12\times10^{-2}$	$M_{w\delta w_1}$	$-4.55\times10^{0} \pm 1.92\times10^{-1}$
$X_{n_3^2}$	$+7.35\times10^{-4} \pm 1.12\times10^{-4}$	$Z_{w\delta w_1}$	$+2.80\times10^{0} \pm 1.25\times10^{-1}$	$M_{n_1\delta w_1}$	$+3.91\times10^{-1} \pm 3.90\times10^{-2}$
$X_{n_4^2}$	$+3.75\times10^{-4} \pm 1.21\times10^{-4}$	$Z_{n_1\delta w_1}$	$-2.36\times10^{-1} \pm 2.55\times10^{-2}$	$M_{n_2\delta w_1}$	$+4.42\times10^{-1} \pm 4.05\times10^{-2}$
$X_{n_5^2}$	$+3.09\times10^{-4} \pm 1.80\times10^{-4}$	$Z_{n_2\delta w_1}$	$-2.97\times10^{-1} \pm 2.65\times10^{-2}$	$M_{n_3\delta w_1}$	$+4.60\times10^{-1} \pm 3.67\times10^{-2}$
$X_{n_6^2}$	$+3.82\times10^{-4} \pm 1.49\times10^{-4}$	$Z_{n_3\delta w_1}$	$-3.30\times10^{-1} \pm 2.41\times10^{-2}$	$M_{n_4\delta w_1}$	$+3.49\times10^{-1} \pm 3.88\times10^{-2}$
$X_{n_7^2}$	$+3.60\times10^{-4} \pm 1.57\times10^{-4}$	$Z_{n_4\delta w_1}$	$-2.35\times10^{-1} \pm 2.53\times10^{-2}$	$M_{\delta w_1^2}$	$-1.87\times10^{2} \pm 1.09\times10^{1}$
$X_{n_8^2}$	$+8.69\times10^{-5} \pm 1.58\times10^{-4}$	$Z_{\delta w_1^2}$	$+9.62\times10^{1} \pm 7.89\times10^{0}$	$M_{w\delta w_2}$	$+4.86\times10^{0} \pm 1.94\times10^{-1}$
$X_{w\delta w_1}$	$+1.59\times10^{-1} \pm 2.95\times10^{-2}$	$Z_{w\delta w_2}$	$+3.90\times10^{0} \pm 1.27\times10^{-1}$	$M_{n_5\delta w_2}$	$-1.42\times10^{-1} \pm 4.90\times10^{-2}$
$X_{n_1\delta w_1}$	$-4.27\times10^{-2} \pm 6.37\times10^{-3}$	$Z_{n_5\delta w_2}$	$-1.05\times10^{-1} \pm 3.20\times10^{-2}$	$M_{n_6\delta w_2}$	$-5.64\times10^{-1} \pm 4.33\times10^{-2}$
$X_{n_2\delta w_1}$	$-1.12\times10^{-1} \pm 6.93\times10^{-3}$	$Z_{n_6\delta w_2}$	$-4.29\times10^{-1} \pm 2.83\times10^{-2}$	$M_{n_7\delta w_2}$	$-5.10\times10^{-1} \pm 4.47\times10^{-2}$
$X_{n_3\delta w_1}$	$-1.12\times10^{-1} \pm 6.07\times10^{-3}$	$Z_{n_7\delta w_2}$	$-3.94\times10^{-1} \pm 2.92\times10^{-2}$	$M_{n_8\delta w_2}$	$-1.77\times10^{-1} \pm 4.54\times10^{-2}$
$X_{n_4\delta w_1}$	$-6.23\times10^{-2} \pm 6.41\times10^{-3}$	$Z_{n_8\delta w_2}$	$-1.23\times10^{-1} \pm 2.97\times10^{-2}$	$M_{\delta w_1\delta w_2}$	$-3.95\times10^{1} \pm 5.01\times10^{0}$
$X_{\delta w_1^2}$	$-3.37\times10^{1} \pm 2.06\times10^{0}$	$Z_{\delta w_2^2}$	$+1.60\times10^{2} \pm 7.73\times10^{0}$	$M_{\delta w_2^2}$	$+1.95\times10^{2} \pm 1.10\times10^{1}$
$X_{n_5\delta w_2}$	$-6.14\times10^{-2} \pm 8.21\times10^{-3}$	$Z_{n_1\delta e_1}$	$-4.15\times10^{-2} \pm 1.26\times10^{-2}$	M_o	$-6.75\times10^{0} \pm 2.83\times10^{-1}$
$X_{n_6\delta w_2}$	$-1.35\times10^{-1} \pm 7.02\times10^{-3}$	$Z_{n_4\delta e_2}$	$-5.31\times10^{-2} \pm 1.25\times10^{-2}$		
$X_{n_7\delta w_2}$	$-1.47\times10^{-1} \pm 7.34\times10^{-3}$	Z_o	$-6.70\times10^{1} \pm 1.89\times10^{-1}$		
$X_{n_8\delta w_2}$	$-6.40\times10^{-2} \pm 7.63\times10^{-3}$				
$X_{\delta w_2^2}$	$-4.35\times10^{1} \pm 2.04\times10^{0}$				
$X_{\delta w_1\delta e_1}$	$-2.05\times10^{0} \pm 3.82\times10^{-1}$				
$X_{\delta w_1\delta e_2}$	$-2.62\times10^{0} \pm 3.81\times10^{-1}$				
$X_{\delta w_2\delta e_3}$	$-1.59\times10^{0} \pm 3.87\times10^{-1}$				
$X_{\delta w_2\delta e_4}$	$-2.72\times10^{0} \pm 3.83\times10^{-1}$				
$X_{n_2\delta f_1}$	$-3.42\times10^{-2} \pm 7.70\times10^{-3}$				
$X_{\delta w_1\delta f_1}$	$-7.26\times10^{0} \pm 9.73\times10^{-1}$				
$X_{n_3\delta f_2}$	$-2.27\times10^{-2} \pm 6.94\times10^{-3}$				
$X_{\delta w_1\delta f_2}$	$-6.42\times10^{0} \pm 9.67\times10^{-1}$				
$X_{n_6\delta f_3}$	$-4.90\times10^{-2} \pm 8.07\times10^{-3}$				
$X_{\delta w_2\delta f_3}$	$-8.36\times10^{0} \pm 9.64\times10^{-1}$				
$X_{n_7\delta f_4}$	$-5.42\times10^{-2} \pm 8.45\times10^{-3}$				
$X_{\delta w_2\delta f_4}$	$-1.14\times10^{1} \pm 9.54\times10^{-1}$				
X_o	$+6.26\times10^{0} \pm 4.70\times10^{-2}$				

Table 6.8: Approach I aero-propulsive models for Y, L, and N at $\bar{q} = 3.5$ psf

Term	$\hat{\theta} \pm s(\hat{\theta})$	Term	$\hat{\theta} \pm s(\hat{\theta})$	Term	$\hat{\theta} \pm s(\hat{\theta})$
Y_v	$-6.30\times10^{-1} \pm 4.40\times10^{-3}$	L_v	$-5.44\times10^{-1} \pm 3.10\times10^{-2}$	N_v	$+1.50\times10^{-1} \pm 1.33\times10^{-2}$
Y_{n_1}	$-5.29\times10^{-3} \pm 7.49\times10^{-4}$	L_{n_1}	$+1.50\times10^{-1} \pm 5.28\times10^{-3}$	N_{n_1}	$+2.36\times10^{-1} \pm 2.25\times10^{-3}$
Y_{n_2}	$-1.86\times10^{-2} \pm 7.79\times10^{-4}$	L_{n_2}	$+1.18\times10^{-1} \pm 5.49\times10^{-3}$	N_{n_2}	$+6.13\times10^{-2} \pm 2.35\times10^{-3}$
Y_{n_3}	$+1.98\times10^{-2} \pm 7.06\times10^{-4}$	L_{n_3}	$-1.28\times10^{-1} \pm 4.98\times10^{-3}$	N_{n_3}	$-6.99\times10^{-2} \pm 2.12\times10^{-3}$
Y_{n_4}	$+6.86\times10^{-5} \pm 7.43\times10^{-4}$	L_{n_4}	$-1.51\times10^{-1} \pm 5.24\times10^{-3}$	N_{n_4}	$-2.21\times10^{-1} \pm 2.23\times10^{-3}$
Y_{n_5}	$+1.00\times10^{-2} \pm 9.54\times10^{-4}$	L_{n_5}	$+1.61\times10^{-1} \pm 6.73\times10^{-3}$	N_{n_5}	$+2.83\times10^{-1} \pm 2.85\times10^{-3}$
Y_{n_6}	$-2.67\times10^{-3} \pm 8.27\times10^{-4}$	L_{n_6}	$+1.37\times10^{-1} \pm 5.87\times10^{-3}$	N_{n_6}	$+8.71\times10^{-2} \pm 2.49\times10^{-3}$
Y_{n_7}	$+6.03\times10^{-4} \pm 8.75\times10^{-4}$	L_{n_7}	$-1.34\times10^{-1} \pm 6.14\times10^{-3}$	N_{n_7}	$-7.51\times10^{-2} \pm 2.61\times10^{-3}$
Y_{n_8}	$-1.22\times10^{-2} \pm 8.70\times10^{-4}$	L_{n_8}	$-1.72\times10^{-1} \pm 6.10\times10^{-3}$	N_{n_8}	$-2.97\times10^{-1} \pm 2.60\times10^{-3}$
$Y_{\delta e_1}$	$-4.37\times10^{-2} \pm 4.84\times10^{-2}$	$L_{\delta e_1}$	$+4.35\times10^{0} \pm 3.42\times10^{-1}$	$N_{\delta e_1}$	$-2.28\times10^{0} \pm 1.46\times10^{-1}$
$Y_{\delta e_2}$	$-9.44\times10^{-2} \pm 4.86\times10^{-2}$	$L_{\delta e_2}$	$-3.90\times10^{0} \pm 3.42\times10^{-1}$	$N_{\delta e_2}$	$+2.10\times10^{0} \pm 1.47\times10^{-1}$
$Y_{\delta e_3}$	$-1.58\times10^{-1} \pm 4.85\times10^{-2}$	$L_{\delta e_3}$	$+3.05\times10^{0} \pm 3.42\times10^{-1}$	$N_{\delta e_3}$	$-4.90\times10^{-1} \pm 1.46\times10^{-1}$
$Y_{\delta e_4}$	$+3.03\times10^{-1} \pm 4.87\times10^{-2}$	$L_{\delta e_4}$	$-8.18\times10^{0} \pm 3.44\times10^{-1}$	$N_{\delta e_4}$	$+1.44\times10^{0} \pm 1.46\times10^{-1}$
$Y_{\delta f_1}$	$-1.18\times10^{0} \pm 1.23\times10^{-1}$	$L_{\delta f_1}$	$+7.12\times10^{0} \pm 8.68\times10^{-1}$	$N_{\delta f_1}$	$-4.26\times10^{0} \pm 3.69\times10^{-1}$
$Y_{\delta f_2}$	$+1.06\times10^{0} \pm 1.22\times10^{-1}$	$L_{\delta f_2}$	$-7.89\times10^{0} \pm 8.57\times10^{-1}$	$N_{\delta f_2}$	$+3.76\times10^{0} \pm 3.66\times10^{-1}$
$Y_{\delta f_3}$	$+1.62\times10^{0} \pm 1.22\times10^{-1}$	$L_{\delta f_3}$	$+1.65\times10^{1} \pm 8.62\times10^{-1}$	$N_{\delta f_3}$	$-7.10\times10^{0} \pm 3.66\times10^{-1}$
$Y_{\delta f_4}$	$-1.71\times10^{0} \pm 1.21\times10^{-1}$	$L_{\delta f_4}$	$-1.41\times10^{1} \pm 8.56\times10^{-1}$	$N_{\delta f_4}$	$+6.22\times10^{0} \pm 3.64\times10^{-1}$
$Y_{\delta r_1}$	$-1.67\times10^{0} \pm 4.05\times10^{-2}$	$L_{\delta w_1}$	$-8.53\times10^{-1} \pm 6.90\times10^{-1}$	$N_{\delta r_1}$	$+2.87\times10^{0} \pm 1.22\times10^{-1}$
$Y_{\delta r_2}$	$+1.61\times10^{0} \pm 4.06\times10^{-2}$	$L_{\delta w_2}$	$+3.43\times10^{0} \pm 7.03\times10^{-1}$	$N_{\delta r_2}$	$-2.81\times10^{0} \pm 1.22\times10^{-1}$
$Y_{\delta w_1}$	$+8.60\times10^{-2} \pm 9.78\times10^{-2}$	L_w	$+4.35\times10^{-2} \pm 2.63\times10^{-2}$	$N_{\delta w_1}$	$+1.87\times10^{0} \pm 2.93\times10^{-1}$
$Y_{\delta w_2}$	$+1.82\times10^{-1} \pm 9.97\times10^{-2}$	$L_{n_1\delta e_1}$	$+6.86\times10^{-2} \pm 1.37\times10^{-2}$	$N_{\delta w_2}$	$+2.63\times10^{-1} \pm 2.97\times10^{-1}$
Y_w	$+1.61\times10^{-2} \pm 3.74\times10^{-3}$	$L_{n_4\delta e_2}$	$-6.92\times10^{-2} \pm 1.36\times10^{-2}$	$N_{n_1\delta e_1}$	$-3.74\times10^{-2} \pm 5.86\times10^{-3}$
$Y_{n_2\delta r_1}$	$-9.69\times10^{-3} \pm 1.67\times10^{-3}$	$L_{n_5\delta e_3}$	$+9.12\times10^{-2} \pm 1.74\times10^{-2}$	$N_{n_4\delta e_2}$	$+4.09\times10^{-2} \pm 5.81\times10^{-3}$
$Y_{n_3\delta r_2}$	$+9.91\times10^{-3} \pm 1.54\times10^{-3}$	$L_{n_8\delta e_4}$	$-8.85\times10^{-2} \pm 1.60\times10^{-2}$	$N_{n_5\delta e_3}$	$-1.66\times10^{-2} \pm 7.50\times10^{-3}$
$Y_{v\delta w_1}$	$-1.01\times10^{-1} \pm 2.29\times10^{-2}$	$L_{n_6\delta f_3}$	$+1.32\times10^{-1} \pm 3.75\times10^{-2}$	$N_{n_8\delta e_4}$	$+2.89\times10^{-2} \pm 6.80\times10^{-3}$
$Y_{n_1\delta w_1}$	$-1.94\times10^{-2} \pm 3.94\times10^{-3}$	$L_{n_7\delta f_4}$	$-1.46\times10^{-1} \pm 3.97\times10^{-2}$	$N_{n_2\delta f_1}$	$-8.06\times10^{-2} \pm 1.53\times10^{-2}$
$Y_{n_2\delta w_1}$	$-9.28\times10^{-3} \pm 4.07\times10^{-3}$	$L_{n_1\delta w_1}$	$+4.80\times10^{-1} \pm 2.75\times10^{-2}$	$N_{n_3\delta f_2}$	$+4.73\times10^{-2} \pm 1.38\times10^{-2}$
$Y_{n_3\delta w_1}$	$+1.64\times10^{-2} \pm 3.68\times10^{-3}$	$L_{n_2\delta w_1}$	$+3.88\times10^{-1} \pm 2.87\times10^{-2}$	$N_{n_6\delta f_3}$	$-6.99\times10^{-2} \pm 1.60\times10^{-2}$
$Y_{n_4\delta w_1}$	$+2.20\times10^{-2} \pm 3.90\times10^{-3}$	$L_{n_3\delta w_1}$	$-3.64\times10^{-1} \pm 2.62\times10^{-2}$	$N_{n_7\delta f_4}$	$+1.03\times10^{-1} \pm 1.69\times10^{-2}$
$Y_{v\delta w_2}$	$-1.74\times10^{-1} \pm 2.31\times10^{-2}$	$L_{n_4\delta w_1}$	$-4.44\times10^{-1} \pm 2.73\times10^{-2}$	$N_{v\delta w_1}$	$+5.54\times10^{-1} \pm 6.88\times10^{-2}$
$Y_{n_5\delta w_2}$	$+2.54\times10^{-3} \pm 4.91\times10^{-3}$	$L_{n_1\delta w_2}$	$+1.06\times10^{-1} \pm 2.77\times10^{-2}$	$N_{n_1\delta w_1}$	$-2.18\times10^{-1} \pm 1.17\times10^{-2}$
$Y_{n_6\delta w_2}$	$+2.45\times10^{-2} \pm 4.35\times10^{-3}$	$L_{n_2\delta w_2}$	$+1.35\times10^{-1} \pm 2.84\times10^{-2}$	$N_{n_2\delta w_1}$	$-1.70\times10^{-1} \pm 1.22\times10^{-2}$
$Y_{n_7\delta w_2}$	$-2.92\times10^{-2} \pm 4.49\times10^{-3}$	$L_{n_3\delta w_2}$	$-1.45\times10^{-1} \pm 2.59\times10^{-2}$	$N_{n_3\delta w_1}$	$+2.12\times10^{-1} \pm 1.12\times10^{-2}$
$Y_{n_8\delta w_2}$	$-1.24\times10^{-2} \pm 4.56\times10^{-3}$	$L_{n_4\delta w_2}$	$-9.99\times10^{-2} \pm 2.71\times10^{-2}$	$N_{n_4\delta w_1}$	$+2.58\times10^{-1} \pm 1.17\times10^{-2}$
$Y_{\delta w_2^2}$	$-5.25\times10^{0} \pm 8.17\times10^{-1}$	$L_{n_5\delta w_2}$	$+4.29\times10^{-1} \pm 3.47\times10^{-2}$	$N_{\delta e_1\delta w_1}$	$-5.02\times10^{0} \pm 7.61\times10^{-1}$
Y_{vw}	$+3.77\times10^{-3} \pm 8.83\times10^{-4}$	$L_{n_6\delta w_2}$	$+5.05\times10^{-1} \pm 3.06\times10^{-2}$	$N_{\delta e_2\delta w_1}$	$+3.92\times10^{0} \pm 7.67\times10^{-1}$
Y_o	$+2.66\times10^{-1} \pm 2.66\times10^{-2}$	$L_{n_7\delta w_2}$	$-5.02\times10^{-1} \pm 3.17\times10^{-2}$	$N_{\delta f_1\delta w_1}$	$-1.10\times10^{1} \pm 1.94\times10^{0}$
		$L_{n_8\delta w_2}$	$-3.72\times10^{-1} \pm 3.20\times10^{-2}$	$N_{\delta f_2\delta w_1}$	$+6.15\times10^{0} \pm 1.93\times10^{0}$
		$L_{\delta e_3\delta w_2}$	$-9.22\times10^{0} \pm 1.79\times10^{0}$	$N_{v\delta w_2}$	$+1.08\times10^{0} \pm 6.91\times10^{-2}$
		$L_{\delta e_4\delta w_2}$	$+1.22\times10^{1} \pm 1.81\times10^{0}$	$N_{n_5\delta w_2}$	$-1.84\times10^{-1} \pm 1.48\times10^{-2}$
		$L_{\delta w_2^2}$	$+4.16\times10^{1} \pm 5.73\times10^{0}$	$N_{n_6\delta w_2}$	$-1.93\times10^{-1} \pm 1.30\times10^{-2}$
		L_{vw}	$-3.88\times10^{-2} \pm 6.24\times10^{-3}$	$N_{n_7\delta w_2}$	$+1.75\times10^{-1} \pm 1.37\times10^{-2}$
		L_o	$-4.59\times10^{0} \pm 1.87\times10^{-1}$	$N_{n_8\delta w_2}$	$+1.60\times10^{-1} \pm 1.37\times10^{-2}$
				$N_{\delta e_3\delta w_2}$	$-3.81\times10^{0} \pm 7.73\times10^{-1}$
				$N_{\delta e_4\delta w_2}$	$+6.35\times10^{0} \pm 7.71\times10^{-1}$
				$N_{\delta f_3\delta w_2}$	$-1.29\times10^{1} \pm 1.92\times10^{0}$
				$N_{\delta f_4\delta w_2}$	$+1.04\times10^{1} \pm 1.90\times10^{0}$
				N_o	$-4.62\times10^{-1} \pm 4.82\times10^{-2}$

Table 6.9: Approach II aero-propulsive models for $\hat{X}$, $\hat{Z}$, and $\hat{M}$ at $\bar{q} = 3.5$ psf

Term	$\hat{\theta} \pm s(\hat{\theta})$	Term	$\hat{\theta} \pm s(\hat{\theta})$	Term	$\hat{\theta} \pm s(\hat{\theta})$
$\hat{X}_{w}$	$+2.62\times10^{-1} \pm 5.93\times10^{-3}$	$\hat{Z}_{w}$	$-1.83\times10^{0} \pm 2.73\times10^{-2}$	$\hat{M}_{w}$	$-4.11\times10^{-1} \pm 4.04\times10^{-2}$
$\hat{X}_{\delta w_1}$	$-1.57\times10^{1} \pm 1.57\times10^{-1}$	$\hat{Z}_{\delta w_1}$	$-2.38\times10^{1} \pm 7.23\times10^{-1}$	$\hat{M}_{\delta w_1}$	$+4.68\times10^{1} \pm 1.07\times10^{0}$
$\hat{X}_{\delta w_2}$	$-2.44\times10^{1} \pm 1.60\times10^{-1}$	$\hat{Z}_{\delta w_2}$	$-7.43\times10^{1} \pm 7.30\times10^{-1}$	$\hat{M}_{\delta w_2}$	$-9.69\times10^{1} \pm 1.08\times10^{0}$
$\hat{X}_{\delta e_1}$	$-4.47\times10^{-1} \pm 7.83\times10^{-2}$	$\hat{Z}_{\delta e_1}$	$-1.43\times10^{0} \pm 3.58\times10^{-1}$	$\hat{M}_{\delta e_1}$	$+2.49\times10^{0} \pm 5.26\times10^{-1}$
$\hat{X}_{\delta e_2}$	$-4.67\times10^{-1} \pm 7.82\times10^{-2}$	$\hat{Z}_{\delta e_2}$	$-2.23\times10^{0} \pm 3.57\times10^{-1}$	$\hat{M}_{\delta e_2}$	$+2.67\times10^{0} \pm 5.27\times10^{-1}$
$\hat{X}_{\delta e_3}$	$-4.05\times10^{-1} \pm 7.77\times10^{-2}$	$\hat{Z}_{\delta e_3}$	$-1.67\times10^{0} \pm 3.56\times10^{-1}$	$\hat{M}_{\delta e_3}$	$-2.51\times10^{0} \pm 5.27\times10^{-1}$
$\hat{X}_{\delta e_4}$	$-9.23\times10^{-1} \pm 7.81\times10^{-2}$	$\hat{Z}_{\delta e_4}$	$-3.62\times10^{0} \pm 3.57\times10^{-1}$	$\hat{M}_{\delta e_4}$	$-6.72\times10^{0} \pm 5.29\times10^{-1}$
$\hat{X}_{\delta f_1}$	$-2.43\times10^{0} \pm 1.97\times10^{-1}$	$\hat{Z}_{\delta f_1}$	$-6.84\times10^{0} \pm 8.95\times10^{-1}$	$\hat{M}_{\delta f_1}$	$+1.24\times10^{1} \pm 1.33\times10^{0}$
$\hat{X}_{\delta f_2}$	$-2.47\times10^{0} \pm 1.96\times10^{-1}$	$\hat{Z}_{\delta f_2}$	$-6.83\times10^{0} \pm 8.93\times10^{-1}$	$\hat{M}_{\delta f_2}$	$+9.65\times10^{0} \pm 1.32\times10^{0}$
$\hat{X}_{\delta f_3}$	$-3.53\times10^{0} \pm 1.96\times10^{-1}$	$\hat{Z}_{\delta f_3}$	$-1.35\times10^{1} \pm 8.90\times10^{-1}$	$\hat{M}_{\delta f_3}$	$-2.14\times10^{1} \pm 1.32\times10^{0}$
$\hat{X}_{\delta f_4}$	$-3.47\times10^{0} \pm 1.94\times10^{-1}$	$\hat{Z}_{\delta f_4}$	$-1.24\times10^{1} \pm 8.87\times10^{-1}$	$\hat{M}_{\delta f_4}$	$-1.77\times10^{1} \pm 1.31\times10^{0}$
$\hat{X}_{T_1}$	$-1.61\times10^{-1} \pm 8.57\times10^{-3}$	$\hat{Z}_{\delta r_1}$	$-1.39\times10^{0} \pm 2.97\times10^{-1}$	$\hat{M}_{\delta r_1}$	$-2.35\times10^{0} \pm 4.39\times10^{-1}$
$\hat{X}_{T_2}$	$-2.84\times10^{-1} \pm 1.03\times10^{-2}$	$\hat{Z}_{\delta r_2}$	$-1.97\times10^{0} \pm 2.98\times10^{-1}$	$\hat{M}_{\delta r_2}$	$-2.68\times10^{0} \pm 4.42\times10^{-1}$
$\hat{X}_{T_3}$	$-3.20\times10^{-1} \pm 8.04\times10^{-3}$	$\hat{Z}_{T_1}$	$-3.65\times10^{-1} \pm 3.93\times10^{-2}$	$\hat{M}_{T_1}$	$+4.28\times10^{-1} \pm 5.83\times10^{-2}$
$\hat{X}_{T_4}$	$-1.45\times10^{-1} \pm 9.37\times10^{-3}$	$\hat{Z}_{T_2}$	$-6.46\times10^{-1} \pm 4.68\times10^{-2}$	$\hat{M}_{T_2}$	$+1.20\times10^{0} \pm 6.92\times10^{-2}$
$\hat{X}_{T_5}$	$-1.44\times10^{-1} \pm 1.24\times10^{-2}$	$\hat{Z}_{T_3}$	$-7.00\times10^{-1} \pm 3.69\times10^{-2}$	$\hat{M}_{T_3}$	$+1.07\times10^{0} \pm 5.46\times10^{-2}$
$\hat{X}_{T_6}$	$-2.91\times10^{-1} \pm 1.05\times10^{-2}$	$\hat{Z}_{T_4}$	$-4.12\times10^{-1} \pm 4.31\times10^{-2}$	$\hat{M}_{T_4}$	$+6.33\times10^{-1} \pm 6.37\times10^{-2}$
$\hat{X}_{T_7}$	$-3.36\times10^{-1} \pm 1.13\times10^{-2}$	$\hat{Z}_{T_5}$	$-2.23\times10^{-1} \pm 5.67\times10^{-2}$	$\hat{M}_{T_5}$	$-3.75\times10^{-1} \pm 8.40\times10^{-2}$
$\hat{X}_{T_8}$	$-1.55\times10^{-1} \pm 1.05\times10^{-2}$	$\hat{Z}_{T_6}$	$-7.33\times10^{-1} \pm 4.79\times10^{-2}$	$\hat{M}_{T_6}$	$-9.06\times10^{-1} \pm 7.07\times10^{-2}$
$\hat{X}_{\delta w_1^2}$	$-4.17\times10^{1} \pm 1.77\times10^{0}$	$\hat{Z}_{T_7}$	$-6.75\times10^{-1} \pm 5.21\times10^{-2}$	$\hat{M}_{T_7}$	$-9.96\times10^{-1} \pm 7.70\times10^{-2}$
$\hat{X}_{w\delta w_2}$	$-1.61\times10^{-1} \pm 3.11\times10^{-2}$	$\hat{Z}_{T_8}$	$-2.41\times10^{-1} \pm 4.82\times10^{-2}$	$\hat{M}_{T_8}$	$-2.56\times10^{-1} \pm 7.13\times10^{-2}$
$\hat{X}_{\delta w_2^2}$	$-5.16\times10^{1} \pm 1.78\times10^{0}$	$\hat{Z}_{w^2}$	$+9.37\times10^{-2} \pm 1.26\times10^{-2}$	$\hat{M}_{w\delta w_1}$	$-5.74\times10^{0} \pm 2.08\times10^{-1}$
$\hat{X}_{\delta w_1 \delta e_1}$	$-2.10\times10^{0} \pm 4.04\times10^{-1}$	$\hat{Z}_{w\delta w_1}$	$+3.38\times10^{0} \pm 1.40\times10^{-1}$	$\hat{M}_{\delta w_1^2}$	$-2.43\times10^{2} \pm 1.21\times10^{1}$
$\hat{X}_{\delta w_1 \delta e_2}$	$-2.64\times10^{0} \pm 4.02\times10^{-1}$	$\hat{Z}_{\delta w_1^2}$	$+1.40\times10^{2} \pm 8.95\times10^{0}$	$\hat{M}_{w\delta w_2}$	$+5.84\times10^{0} \pm 2.11\times10^{-1}$
$\hat{X}_{\delta w_2 \delta e_3}$	$-1.61\times10^{0} \pm 4.10\times10^{-1}$	$\hat{Z}_{w\delta w_2}$	$+4.42\times10^{0} \pm 1.42\times10^{-1}$	$\hat{M}_{\delta w_1 \delta w_2}$	$-4.35\times10^{1} \pm 5.46\times10^{0}$
$\hat{X}_{\delta w_2 \delta e_4}$	$-3.10\times10^{0} \pm 4.06\times10^{-1}$	$\hat{Z}_{\delta w_2^2}$	$+2.06\times10^{2} \pm 8.76\times10^{0}$	$\hat{M}_{\delta w_2^2}$	$+2.04\times10^{2} \pm 1.22\times10^{1}$
$\hat{X}_{\delta w_1 \delta f_1}$	$-5.86\times10^{0} \pm 1.03\times10^{0}$	$\hat{Z}_{\delta w_1 T_1}$	$-5.03\times10^{-1} \pm 2.02\times10^{-1}$	$\hat{M}_{\delta w_1 T_1}$	$+1.33\times10^{0} \pm 2.99\times10^{-1}$
$\hat{X}_{\delta w_1 \delta f_2}$	$-5.26\times10^{0} \pm 1.02\times10^{0}$	$\hat{Z}_{\delta e_1 T_1}$	$-2.49\times10^{-1} \pm 1.00\times10^{-1}$	$\hat{M}_{\delta w_1 T_2}$	$+2.34\times10^{0} \pm 3.59\times10^{-1}$
$\hat{X}_{\delta w_2 \delta f_3}$	$-9.32\times10^{0} \pm 1.02\times10^{0}$	$\hat{Z}_{\delta w_1 T_2}$	$-1.29\times10^{0} \pm 2.43\times10^{-1}$	$\hat{M}_{\delta w_1 T_3}$	$+1.98\times10^{0} \pm 2.78\times10^{-1}$
$\hat{X}_{\delta w_2 \delta f_4}$	$-1.03\times10^{1} \pm 1.01\times10^{0}$	$\hat{Z}_{\delta w_1 T_3}$	$-1.24\times10^{0} \pm 1.89\times10^{-1}$	$\hat{M}_{\delta w_1 T_4}$	$+1.36\times10^{0} \pm 3.33\times10^{-1}$
$\hat{X}_{\delta w_1 T_1}$	$-8.70\times10^{-2} \pm 4.37\times10^{-2}$	$\hat{Z}_{\delta w_1 T_4}$	$-8.21\times10^{-1} \pm 2.25\times10^{-1}$	$\hat{M}_{\delta w_2 T_6}$	$-2.62\times10^{0} \pm 3.66\times10^{-1}$
$\hat{X}_{\delta e_1 T_1}$	$-1.12\times10^{-1} \pm 2.19\times10^{-2}$	$\hat{Z}_{\delta e_2 T_4}$	$-4.36\times10^{-1} \pm 1.12\times10^{-1}$	$\hat{M}_{\delta w_2 T_7}$	$-2.41\times10^{0} \pm 3.94\times10^{-1}$
$\hat{X}_{\delta w_1 T_2}$	$-5.07\times10^{-1} \pm 5.31\times10^{-2}$	$\hat{Z}_{\delta w_2 T_6}$	$-2.03\times10^{0} \pm 2.48\times10^{-1}$	$\hat{M}_{o}$	$-1.03\times10^{1} \pm 3.33\times10^{-1}$
$\hat{X}_{\delta f_1 T_2}$	$-2.71\times10^{-1} \pm 6.68\times10^{-2}$	$\hat{Z}_{\delta w_2 T_7}$	$-2.05\times10^{0} \pm 2.67\times10^{-1}$		
$\hat{X}_{\delta w_1 T_3}$	$-5.44\times10^{-1} \pm 4.14\times10^{-2}$	$\hat{Z}_{o}$	$-6.41\times10^{1} \pm 2.31\times10^{-1}$		
$\hat{X}_{\delta f_2 T_3}$	$-1.77\times10^{-1} \pm 5.17\times10^{-2}$				
$\hat{X}_{\delta w_1 T_4}$	$-2.01\times10^{-1} \pm 4.88\times10^{-2}$				
$\hat{X}_{\delta e_2 T_4}$	$-1.08\times10^{-1} \pm 2.45\times10^{-2}$				
$\hat{X}_{\delta w_2 T_5}$	$-1.30\times10^{-1} \pm 6.37\times10^{-2}$				
$\hat{X}_{\delta e_3 T_5}$	$-8.65\times10^{-2} \pm 3.21\times10^{-2}$				
$\hat{X}_{\delta w_2 T_6}$	$-8.24\times10^{-1} \pm 5.38\times10^{-2}$				
$\hat{X}_{\delta f_3 T_6}$	$-3.33\times10^{-1} \pm 6.61\times10^{-2}$				
$\hat{X}_{\delta w_2 T_7}$	$-8.49\times10^{-1} \pm 5.89\times10^{-2}$				
$\hat{X}_{\delta f_4 T_7}$	$-4.33\times10^{-1} \pm 7.28\times10^{-2}$				
$\hat{X}_{\delta w_2 T_8}$	$-1.38\times10^{-1} \pm 5.47\times10^{-2}$				
$\hat{X}_{\delta e_4 T_8}$	$-7.64\times10^{-2} \pm 2.71\times10^{-2}$				
$\hat{X}_{o}$	$-9.89\times10^{0} \pm 4.88\times10^{-2}$				

Table 6.10: Approach II aero-propulsive models for $\hat{Y}$, $\hat{L}$, and $\hat{N}$ at $\bar{q} = 3.5$ psf

Term	$\hat{\theta} \pm s(\hat{\theta})$	Term	$\hat{\theta} \pm s(\hat{\theta})$	Term	$\hat{\theta} \pm s(\hat{\theta})$
$\hat{Y}_v$	$-5.26\times10^{-1} \pm 4.55\times10^{-3}$	$\hat{L}_v$	$-5.12\times10^{-1} \pm 3.23\times10^{-2}$	$\hat{N}_v$	$+2.72\times10^{-1} \pm 1.26\times10^{-2}$
$\hat{Y}_{\delta e_3}$	$-1.81\times10^{-1} \pm 5.01\times10^{-2}$	$\hat{L}_{\delta e_1}$	$+4.27\times10^{0} \pm 3.59\times10^{-1}$	$\hat{N}_{\delta e_1}$	$-2.10\times10^{0} \pm 1.39\times10^{-1}$
$\hat{Y}_{\delta e_4}$	$+3.08\times10^{-1} \pm 5.04\times10^{-2}$	$\hat{L}_{\delta e_2}$	$-3.80\times10^{0} \pm 3.58\times10^{-1}$	$\hat{N}_{\delta e_2}$	$+2.10\times10^{0} \pm 1.40\times10^{-1}$
$\hat{Y}_{\delta f_1}$	$-1.26\times10^{0} \pm 1.26\times10^{-1}$	$\hat{L}_{\delta e_3}$	$+2.92\times10^{0} \pm 3.57\times10^{-1}$	$\hat{N}_{\delta e_3}$	$-3.95\times10^{-1} \pm 1.39\times10^{-1}$
$\hat{Y}_{\delta f_2}$	$+1.11\times10^{0} \pm 1.26\times10^{-1}$	$\hat{L}_{\delta e_4}$	$-8.02\times10^{0} \pm 3.60\times10^{-1}$	$\hat{N}_{\delta e_4}$	$+1.44\times10^{0} \pm 1.39\times10^{-1}$
$\hat{Y}_{\delta f_3}$	$+1.59\times10^{0} \pm 1.26\times10^{-1}$	$\hat{L}_{\delta f_1}$	$+7.25\times10^{0} \pm 8.99\times10^{-1}$	$\hat{N}_{\delta f_1}$	$-3.86\times10^{0} \pm 3.50\times10^{-1}$
$\hat{Y}_{\delta f_4}$	$-1.68\times10^{0} \pm 1.25\times10^{-1}$	$\hat{L}_{\delta f_2}$	$-7.81\times10^{0} \pm 8.94\times10^{-1}$	$\hat{N}_{\delta f_2}$	$+3.82\times10^{0} \pm 3.50\times10^{-1}$
$\hat{Y}_{\delta r_1}$	$-1.66\times10^{0} \pm 4.21\times10^{-2}$	$\hat{L}_{\delta f_3}$	$+1.66\times10^{1} \pm 9.01\times10^{-1}$	$\hat{N}_{\delta f_3}$	$-7.08\times10^{0} \pm 3.47\times10^{-1}$
$\hat{Y}_{\delta r_2}$	$+1.60\times10^{0} \pm 4.23\times10^{-2}$	$\hat{L}_{\delta f_4}$	$-1.39\times10^{1} \pm 8.96\times10^{-1}$	$\hat{N}_{\delta f_4}$	$+6.04\times10^{0} \pm 3.47\times10^{-1}$
$\hat{Y}_{\delta w_1}$	$+1.66\times10^{-1} \pm 1.02\times10^{-1}$	$\hat{L}_{\delta w_1}$	$-1.04\times10^{0} \pm 7.23\times10^{-1}$	$\hat{N}_{\delta r_1}$	$+2.83\times10^{0} \pm 1.15\times10^{-1}$
$\hat{Y}_{\delta w_2}$	$+2.42\times10^{-1} \pm 1.03\times10^{-1}$	$\hat{L}_{\delta w_2}$	$+4.86\times10^{0} \pm 7.36\times10^{-1}$	$\hat{N}_{\delta r_2}$	$-2.84\times10^{0} \pm 1.16\times10^{-1}$
$\hat{Y}_w$	$+1.86\times10^{-2} \pm 3.85\times10^{-3}$	$\hat{L}_w$	$+3.36\times10^{-2} \pm 2.73\times10^{-2}$	$\hat{N}_{\delta w_1}$	$+1.28\times10^{0} \pm 2.80\times10^{-1}$
$\hat{Y}_{T_1}$	$-3.65\times10^{-2} \pm 5.51\times10^{-3}$	$\hat{L}_{T_1}$	$+6.78\times10^{-1} \pm 3.91\times10^{-2}$	$\hat{N}_{\delta w_2}$	$-1.66\times10^{-1} \pm 2.81\times10^{-1}$
$\hat{Y}_{T_2}$	$-1.61\times10^{-1} \pm 6.58\times10^{-3}$	$\hat{L}_{T_2}$	$+6.84\times10^{-1} \pm 4.67\times10^{-2}$	$\hat{N}_w$	$-6.10\times10^{-2} \pm 1.06\times10^{-2}$
$\hat{Y}_{T_3}$	$+1.43\times10^{-1} \pm 5.19\times10^{-3}$	$\hat{L}_{T_3}$	$-5.86\times10^{-1} \pm 3.69\times10^{-2}$	$\hat{N}_{T_1}$	$-5.93\times10^{-1} \pm 1.50\times10^{-2}$
$\hat{Y}_{T_4}$	$-4.05\times10^{-3} \pm 6.06\times10^{-3}$	$\hat{L}_{T_4}$	$-8.01\times10^{-1} \pm 4.31\times10^{-2}$	$\hat{N}_{T_2}$	$-4.60\times10^{-1} \pm 1.80\times10^{-2}$
$\hat{Y}_{T_5}$	$+7.71\times10^{-2} \pm 8.00\times10^{-3}$	$\hat{L}_{T_5}$	$+5.91\times10^{-1} \pm 5.68\times10^{-2}$	$\hat{N}_{T_3}$	$+4.49\times10^{-1} \pm 1.41\times10^{-2}$
$\hat{Y}_{T_6}$	$-1.90\times10^{-2} \pm 6.72\times10^{-3}$	$\hat{L}_{T_6}$	$+9.89\times10^{-1} \pm 4.77\times10^{-2}$	$\hat{N}_{T_4}$	$+5.16\times10^{-1} \pm 1.66\times10^{-2}$
$\hat{Y}_{T_7}$	$-1.73\times10^{-3} \pm 7.33\times10^{-3}$	$\hat{L}_{T_7}$	$-9.72\times10^{-1} \pm 5.19\times10^{-2}$	$\hat{N}_{T_5}$	$-6.01\times10^{-1} \pm 2.16\times10^{-2}$
$\hat{Y}_{T_8}$	$-9.40\times10^{-2} \pm 6.80\times10^{-3}$	$\hat{L}_{T_8}$	$-5.47\times10^{-1} \pm 4.82\times10^{-2}$	$\hat{N}_{T_6}$	$-4.92\times10^{-1} \pm 1.83\times10^{-2}$
$\hat{Y}_{v\delta w_2}$	$-1.78\times10^{-1} \pm 2.39\times10^{-2}$	$\hat{L}_{\delta e_3\delta w_2}$	$-1.00\times10^{1} \pm 1.87\times10^{0}$	$\hat{N}_{T_7}$	$+5.47\times10^{-1} \pm 1.98\times10^{-2}$
$\hat{Y}_{\delta w_2^2}$	$-4.67\times10^{0} \pm 9.14\times10^{-1}$	$\hat{L}_{\delta e_4\delta w_2}$	$+1.33\times10^{1} \pm 1.87\times10^{0}$	$\hat{N}_{T_8}$	$+5.97\times10^{-1} \pm 1.85\times10^{-2}$
$\hat{Y}_{\delta w_1 T_1}$	$-1.21\times10^{-1} \pm 2.86\times10^{-2}$	$\hat{L}_{\delta w_2^2}$	$+4.02\times10^{1} \pm 6.46\times10^{0}$	$\hat{N}_{v\delta w_1}$	$+5.36\times10^{-1} \pm 6.53\times10^{-2}$
$\hat{Y}_{\delta r_1 T_2}$	$-7.16\times10^{-2} \pm 1.42\times10^{-2}$	$\hat{L}_{vw}$	$-3.63\times10^{-2} \pm 6.48\times10^{-3}$	$\hat{N}_{\delta e_1\delta w_1}$	$-4.87\times10^{0} \pm 7.21\times10^{-1}$
$\hat{Y}_{\delta w_1 T_2}$	$-1.34\times10^{-1} \pm 3.42\times10^{-2}$	$\hat{L}_{\delta e_1 T_1}$	$+5.02\times10^{-1} \pm 1.01\times10^{-1}$	$\hat{N}_{\delta e_2\delta w_1}$	$+3.87\times10^{0} \pm 7.23\times10^{-1}$
$\hat{Y}_{\delta r_2 T_3}$	$+6.25\times10^{-2} \pm 1.12\times10^{-2}$	$\hat{L}_{\delta w_1 T_1}$	$+1.21\times10^{0} \pm 2.01\times10^{-1}$	$\hat{N}_{v\delta w_2}$	$+1.13\times10^{0} \pm 6.55\times10^{-2}$
$\hat{Y}_{\delta w_1 T_3}$	$+1.57\times10^{-1} \pm 2.66\times10^{-2}$	$\hat{L}_{\delta w_1 T_2}$	$+2.38\times10^{0} \pm 2.44\times10^{-1}$	$\hat{N}_{\delta e_3\delta w_2}$	$-3.15\times10^{0} \pm 7.29\times10^{-1}$
$\hat{Y}_{\delta w_1 T_4}$	$+1.47\times10^{-1} \pm 3.17\times10^{-2}$	$\hat{L}_{\delta w_2 T_2}$	$+1.11\times10^{0} \pm 2.44\times10^{-1}$	$\hat{N}_{\delta e_4\delta w_2}$	$+5.55\times10^{0} \pm 7.26\times10^{-1}$
$\hat{Y}_{\delta w_2 T_6}$	$+2.00\times10^{-1} \pm 3.49\times10^{-2}$	$\hat{L}_{\delta w_1 T_3}$	$-1.56\times10^{0} \pm 1.90\times10^{-1}$	$\hat{N}_{\delta f_3\delta w_2}$	$-1.19\times10^{1} \pm 1.82\times10^{0}$
$\hat{Y}_{\delta w_2 T_7}$	$-2.62\times10^{-1} \pm 3.76\times10^{-2}$	$\hat{L}_{\delta w_2 T_3}$	$-1.10\times10^{0} \pm 1.90\times10^{-1}$	$\hat{N}_{\delta f_4\delta w_2}$	$+9.13\times10^{0} \pm 1.80\times10^{0}$
$\hat{Y}_o$	$+2.44\times10^{-1} \pm 2.93\times10^{-2}$	$\hat{L}_{\delta e_2 T_4}$	$-4.68\times10^{-1} \pm 1.12\times10^{-1}$	$\hat{N}_{\delta e_1 T_1}$	$-2.89\times10^{-1} \pm 3.90\times10^{-2}$
		$\hat{L}_{\delta w_1 T_4}$	$-1.30\times10^{0} \pm 2.24\times10^{-1}$	$\hat{N}_{\delta w_1 T_1}$	$-7.71\times10^{-1} \pm 7.79\times10^{-2}$
		$\hat{L}_{\delta e_3 T_5}$	$+8.39\times10^{-1} \pm 1.46\times10^{-1}$	$\hat{N}_{\delta f_1 T_2}$	$-6.41\times10^{-1} \pm 1.18\times10^{-1}$
		$\hat{L}_{\delta f_3 T_6}$	$+9.71\times10^{-1} \pm 3.04\times10^{-1}$	$\hat{N}_{\delta w_1 T_2}$	$-1.09\times10^{0} \pm 9.47\times10^{-2}$
		$\hat{L}_{\delta w_2 T_6}$	$+2.86\times10^{0} \pm 2.48\times10^{-1}$	$\hat{N}_{\delta f_2 T_3}$	$+3.01\times10^{-1} \pm 9.16\times10^{-2}$
		$\hat{L}_{\delta f_4 T_7}$	$-1.04\times10^{0} \pm 3.34\times10^{-1}$	$\hat{N}_{\delta w_1 T_3}$	$+1.15\times10^{0} \pm 7.38\times10^{-2}$
		$\hat{L}_{\delta w_2 T_7}$	$-3.10\times10^{0} \pm 2.68\times10^{-1}$	$\hat{N}_{\delta e_2 T_4}$	$+3.25\times10^{-1} \pm 4.35\times10^{-2}$
		$\hat{L}_{\delta e_4 T_8}$	$-6.11\times10^{-1} \pm 1.25\times10^{-1}$	$\hat{N}_{\delta w_1 T_4}$	$+1.22\times10^{0} \pm 8.72\times10^{-2}$
		$\hat{L}_o$	$-4.22\times10^{0} \pm 2.07\times10^{-1}$	$\hat{N}_{\delta e_3 T_5}$	$-1.06\times10^{-1} \pm 5.71\times10^{-2}$
				$\hat{N}_{\delta f_3 T_6}$	$-4.98\times10^{-1} \pm 1.18\times10^{-1}$
				$\hat{N}_{\delta w_2 T_6}$	$-1.35\times10^{0} \pm 9.60\times10^{-2}$
				$\hat{N}_{\delta f_4 T_7}$	$+6.55\times10^{-1} \pm 1.29\times10^{-1}$
				$\hat{N}_{\delta w_2 T_7}$	$+1.21\times10^{0} \pm 1.04\times10^{-1}$
				$\hat{N}_{\delta e_4 T_8}$	$+1.72\times10^{-1} \pm 4.84\times10^{-2}$
				$\hat{N}_o$	$+5.19\times10^{-1} \pm 4.49\times10^{-2}$

Chapter 7

Evaluation of Response Surface Experiment Designs for eVTOL Aircraft Aero-Propulsive Modeling

Modern distributed hybrid and electric propulsion aircraft, including vertical, short, and conventional takeoff and landing configurations, exhibit significant aero-propulsive complexity and a large number of interacting test factors. This chapter presents the development and evaluation of experiment designs for aero-propulsive characterization of distributed propulsion aircraft. Five different foundational response surface designs are evaluated to inform the development of two sequential design approaches tailored to complex aircraft aerodynamic characterization experiments. The first approach, which builds on sequential face-centered central composite designs, has been used previously to develop aero-propulsive models for complex aircraft using wind-tunnel testing, including the work described in Chapter 6. The second approach is a new response surface design strategy leveraging a regular I-optimal and nested I-optimal design that was developed for this study. The two sequential design strategies are compared for experiments with a large number of test factors using pre-experiment design evaluation metrics, as well as modeling results obtained from simulated wind-tunnel data for the NASA LA-8 eVTOL aircraft. The design evaluation metrics show that the sequential I-optimal base design has higher statistical power, lower correlation among candidate regressors, lower prediction variance, and more precise parameter estimates. The simulated wind-tunnel experiments conducted using each design reveal that the sequential I-optimal base design has better predictive capability with fewer test points. The experiment design and evaluation procedures are described in detail to inform future aerodynamic characterization experiments for complex aircraft. This work has been published as a conference paper [29].

The chapter is organized as follows: Section 7.1 provides additional motivation for this study and describes the LA-8 wind-tunnel simulation applied in this chapter. Section 7.2 compares five foundational response surface designs using pre-experiment design evaluation metrics. This analysis informs presentation of a new block design approach developed alongside a legacy block design approach in Section 7.3. A comparison of pre-experiment design evaluation metrics for the two sequential design approaches is shown in Section 7.4. An overview of the employed model identification approach is given in Section 7.5, followed by modeling results for simulated wind-tunnel experiments presented in Section 7.6.

7.1 Research Motivation

Traditional aircraft aerodynamic characterization methods generally involve using OFAT experiments, where testing is commonly conducted by sweeping one variable with the other variables held at a constant setting. This approach has been used successfully for many years in aerospace testing and yields suitable results for conventional aerospace vehicles. However, traditional static OFAT testing is not practical for developing models describing the complex nonlinear aerodynamics and interactions present with distributed propulsion aircraft due to the large number of test factors. Fortunately, experiments planned using DOE [231] and RSM [232] theory can efficiently scale to a large number of factors, allowing tests to be completed in a reasonable amount of time while also supporting identification of interaction effects. DOE/RSM-based testing fundamentally provides a statistically-rigorous experiment design approach supplying rich information content in a relatively compact data set. As discussed in Section 6.3.2, the model development process also benefits from additional design properties of orthogonality, randomization, replication, blocking, and sequential testing [231].

As an example of the efficiency gains realized using DOE/RSM techniques, consider a complex aircraft with 22 test factors—the number of factors independently varied in static LA-8 wind-tunnel experiments at each dynamic pressure setting (see Chapter 6). OFAT testing covering all possible combinations of each test factor at three different levels (a low, medium, and high value) requires 31,381,059,609 test points. Alternatively, a minimum run resolution V, face-centered central composite design (CCD) with one center point, which also tests three levels of each factor and allows characterization of interactions among all pairs of test factors as well as quadratic response variation with each test factor, requires only 299 test points. A two-dimensional and three-dimensional slice of the OFAT and face-centered CCD factor space are shown in Figures 7.1a-7.1b. This example comparing the number of test points for a three-level OFAT and CCD test matrix is expanded to between 5 and 30 test factors in Figure 7.1c. Clearly, application of the CCD response surface design has substantially reduced the number of required test points, while still allowing characterization of nonlinear, interactional features.

This chapter presents an assessment of multiple static experiment designs and evaluates their relative utility for application to experiments characterizing complex distributed propulsion aircraft. A new DOE/RSM test matrix design approach is formulated and compared to previous experiment designs [28, 47, 48, 234] using design evaluation metrics and prediction capability assessment from simulated LA-8 wind-tunnel experiments. The sequential experiment designs compared in this chapter were applied to develop an aero-propulsive model for the LA-8 vehicle (see Section 6.1). The experiments were executed in an LA-8 simulation modeling the primary aero-propulsive characteristics of tilt-wing aircraft. The aircraft components included in the model were the fuselage, two tilting wings, inverted v-tail, four elevons, four flaps, two ruddervators, and eight wing-mounted propellers with geometry and placement consistent with the LA-8 vehicle. Other smaller components, such as winglets and propeller support struts, were not included in the model. The semi-empirical

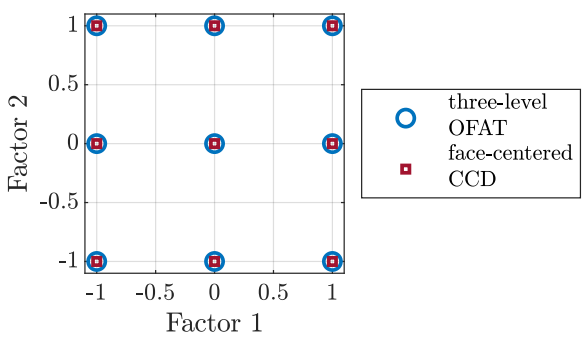

(a) Two-dimensional design space slice

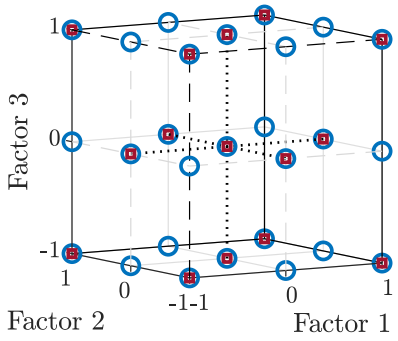

(b) Three-dimensional design space slice

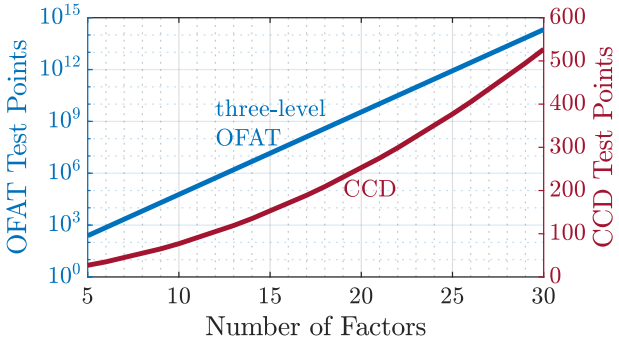

(c) Number of test points

Figure 7.1: Comparison of three-level OFAT and minimum run resolution V, face-centered CCD experiments.

aircraft model utilizes strip-theory-based tilt-wing aerodynamic predictions [207] combined with high-fidelity LA-8 propeller models identified from isolated propeller wind-tunnel testing [37]. For this study, force and moment predictions were corrupted using zero-mean, Gaussian, white noise with measurement noise standard deviations representative of values seen in the LA-8 wind-tunnel tests. The simulation was intended to be representative of LA-8 wind-tunnel test results to inform future wind-tunnel experiments and allow rapid, inexpensive experimentation in a controlled, repeatable test environment. The simulated experiments were executed at a dynamic pressure of $\bar{q} = 3.5$ psf (freestream airspeed of $V = 54.3$ ft/s at standard sea-level conditions), with the test factor ranges shown in Table 7.1. This condition represents a high-speed transition phase of flight for the LA-8 aircraft. Multiple dynamic pressure settings need to be tested to develop a full-envelope aero-propulsive model [28], but these experiments provide a suitable data set for evaluation and comparison of experiment designs.

Table 7.1: LA-8 simulated wind-tunnel experiment test factor ranges at $\bar{q} = 3.5$ psf ($V = 54.3$ ft/s)

Factor(s)	Units	Minimum	Maximum
α	deg	-6	$+6$
β	deg	-5	$+5$
$\delta_{w_1}, \delta_{w_2}$	deg	0	$+25$
$\delta_{e_1}, \delta_{e_2}, \delta_{e_3}, \delta_{e_4}$	deg	-25	$+25$
$\delta_{f_1}, \delta_{f_2}, \delta_{f_3}, \delta_{f_4}$	deg	0	$+20$
$\delta_{r_1}, \delta_{r_2}$	deg	-30	$+30$
$n_1, n_2, ..., n_8$	rpm	3700	6100

7.2 Evaluation of Foundational Response Surface Experiment Designs

Within the body of DOE/RSM theory, there are multiple response surface design types that can yield an adequate model for experiments with a large number of test factors. This section compares five different 22-factor, cuboidal, completely randomized response surface experiment designs supporting identification of a full quadratic design model (all possible linear, pure quadratic, and two-factor interaction model terms). All the experiment designs presented in this chapter were created using Design-Expert® [233]. The designs include: (1) a minimum run resolution V, face-centered central composite design (FCCCD); (2) an *I*-optimal design; (3) an *A*-optimal design; (4) a *D*-optimal design; and (5) a distance-based optimal design. The FCCCD is composed of a two-level fractional factorial design, six center points, and a low and high axial point for each test factor, for a total of 304 test points. Minimum run resolution V fractional factorial designs contain the minimum number of test points to support estimation of linear and two-factor interaction model terms. The axial test points augment the fractional factorial design to allow estimation of pure quadratic model terms. The center points aid in stabilization of the prediction variance within the experimental region and allow estimation of pure error [231]. The other designs considered are *I*-, *A*-, *D*-, and distance-based optimal designs for a full quadratic design model, each with the same number of test points and center points as the FCCCD to allow direct comparisons of the designs. It has also been observed in related research that using the same number of test points as a minimum run resolution V FCCCD for a given number of test factors generally yields good design evaluation metrics for optimal designs. *I*-optimal designs minimize the integrated prediction variance for a predefined model order over the range of factors [231, 232, 239, 240]. Alternatively, *D*- and *A*-optimal designs focus on optimizing the design for precise estimation of model parameters for a predefined model order. *D*-optimal designs minimize the confidence ellipsoid volume of the model parameters and *A*-optimal designs minimize the sum of the variances of model parameters. The distance-based design is a Maximin design, or a design where the minimum distance between design

points is maximized [232], that is modified to ensure that model terms are not aliased [233]. The designs were optimized using 298 free design points and one center point. After design optimization had completed, 5 additional center points were added to the design and the test matrix was re-randomized. This was done because it has been noted that including multiple replicate points in the center of a design during the optimization process can repel the optimized points away from the interior of the design space.

Figure 7.2 shows two-dimensional slices of the 22-factor space for each design. The figure shows that the I- and A-optimal designs cover the broadest number of individual factor settings in two-dimensions, although, the test points are mostly concentrated around the design space boundaries. The D-optimal and distance-based designs are more heavily concentrated around the design boundaries, with very few points in the interior of the displayed factor space. The FCCCD design only tests the low, high, and center value of each test factor. Favoring the design space boundaries can result in significant bias error in the interior of the design space when there are nonlinearities not described by the assumed model [232]. The remainder of this section presents a comparison of the design evaluation metrics of the five candidate base designs. These metrics provide insight into the design quality prior to conducing an experiment. Evaluation of the base designs is then used to justify the choice of a new sequential design aimed at mitigating against bias errors in the interior of the design space.

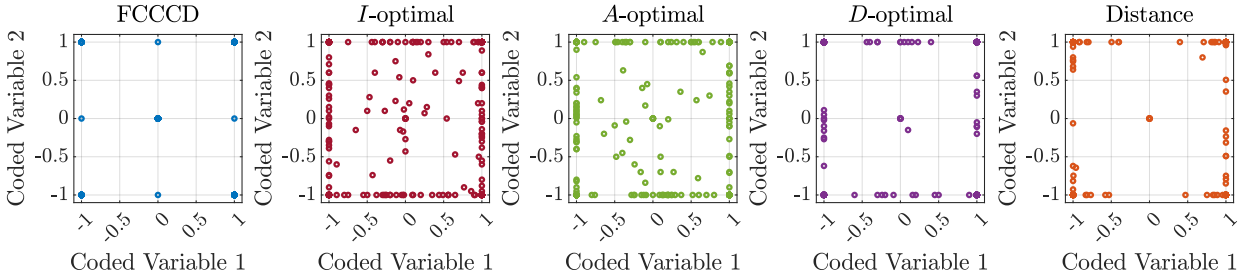

Figure 7.2: Two-dimensional slices of the 22-factor space for each base design.

7.2.1 Statistical Power

Statistical power is the probability of detecting a significant effect in a model [231, 239, 241]. In other words, power is the probability of including a particular model term that is significant to the model. Power is a function of the number of design points, the placement of the design points, the significance level α_p, and the ratio of the effect size δ and noise level σ. A general rule of thumb for experiment design is to strive for statistical power of at least 80% [241].

The lowest power among all the linear (L), interaction (I), and quadratic (Q) model

terms for each base design is shown graphically in Figure 7.3 and numerically in Table 7.2. Figure 7.3a and Table 7.2a show the power for each design with $\alpha_p = 0.05$ and $\delta/\sigma = 2$, which are common values used when assessing power. All designs have nearly 100% power for the linear and interaction model terms. The power for quadratic model terms is just below 80% for the FCCCD and distance-based design, whereas the I-, A-, and D-optimal designs have close to 100% power for quadratic model terms. Figure 7.3b and Table 7.2b show the power for each design with $\alpha_p = 0.0001$ and $\delta/\sigma = 1$, which are much more conservative numbers to use in the power calculation and, accordingly, the power is lower. The FCCCD design has the lowest power for each classification of model terms, followed by the distance-based design. The highest power is generally observed for the I- and A-optimal designs. This suggests that models estimated from the I- and A-optimal designs have a lower probability of failing to include model terms that are significant to the model.

Table 7.2: Base design power comparison (expressed as a percentage)

(a) Power calculation with $\alpha_p = 0.05$ and $\delta/\sigma = 2$

Model Terms	Power for FCCCD	Power for I-optimal design	Power for A-optimal design	Power for D-optimal design	Power for distance design
L	99.999996	100.0000000000	100.0000000000	99.9999999999	99.999999995
I	99.99991	99.9999999997	99.9999999999	99.9999999999	99.9999996
Q	79.8	99.9999999999	99.9999999999	99.8	76.8

(b) Power calculation with $\alpha_p = 0.0001$ and $\delta/\sigma = 1$

Model Terms	Power for FCCCD	Power for I-optimal design	Power for A-optimal design	Power for D-optimal design	Power for distance design
L	27.8	85.7	77.4	69.4	46.0
I	19.6	54.4	57.1	59.1	34.1
Q	0.4	66.2	70.9	4.3	0.4

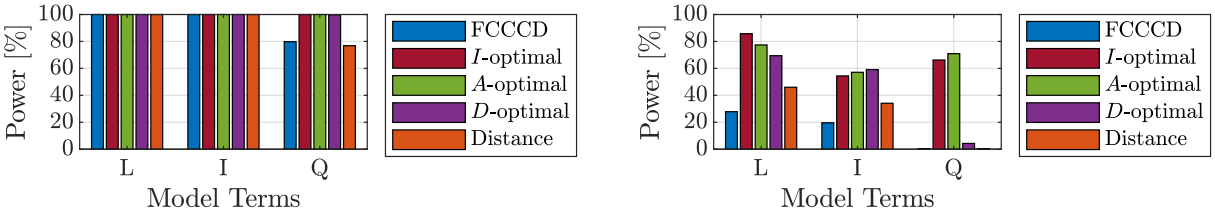

(a) Power calculation with $\alpha_p = 0.05$ and $\delta/\sigma = 2$

(b) Power calculation with $\alpha_p = 0.0001$ and $\delta/\sigma = 1$

Figure 7.3: Base design power comparison.

7.2.2 Correlation Metrics

As discussed previously in Sections 2.6.2.4 and 6.4.2, data collinearity occurs when the correlation between regressors high enough to cause corrupted model identification [19]. Data collinearity will cause difficulty in both model structure determination and parameter estimation, thus, it is important to develop an experiment design with low correlation among candidate regressors.

Correlation between two candidate regressors can be assessed using the pairwise correlation coefficient r_{ij}, defined in Equation (2.80) and discussed in Section 6.4.2, where $\boldsymbol{\xi}_i$ and $\boldsymbol{\xi}_j$ are two regressor measurement histories. Another metric that can be used to assess candidate regressor correlation is the variance inflation factor (VIF). For the regressor $\boldsymbol{\xi}_j$, the respective VIF is

$$\text{VIF}_j = \frac{1}{1 - R_j^2} \tag{7.1}$$

where R_j^2 is the coefficient of determination obtained through creating a regression model of $\boldsymbol{\xi}_j$ as a function of all other regressors. A VIF value greater than 10 suggests that data collinearity may be present [19, 240, 242]. The r_{ij}, VIF_j, and R_j^2 metrics only quantify correlation between pairs of regressors and, thus, cannot diagnose collinearity among more than two regressors [19, 109].

An alternative method that can be used to assess multiple correlation between more than two inputs is analysis of the eigenvalues of $\boldsymbol{X}^T\boldsymbol{X}$, where $\boldsymbol{X}$ is a matrix composed of column vectors of the regressors in the regression model. The inverse of the $\boldsymbol{X}^T\boldsymbol{X}$ matrix is required to compute the ordinary least-squares regression solution [cf. Equation (2.56)]. The ratio of the maximum eigenvalue and minimum eigenvalue

$$\kappa = \lambda_{\text{max}}/\lambda_{\text{min}} \tag{7.2}$$

is the condition number of the $\boldsymbol{X}^T\boldsymbol{X}$ matrix. A value of κ close to one indicates low multiple correlation whereas a large value of κ indicates an ill-conditioned estimation problem due to data collinearity. Values of κ indicating adverse effects from data collinearity range anywhere from 100 to 100,000 depending on the particular data set [19, 20, 109, 242].

The pairwise and multiple correlation metrics for each design evaluated for a full quadratic model are shown in Figures 7.4-7.7. This represents a conservative analysis performed prior to the experiment that assumes all candidate regressors are included in the model. Many candidate model terms considered here for the full quadratic model were expected to be excluded through model structure determination after data collection.

Figure 7.4 shows the maximum absolute pairwise correlation value, $|r_{ij}|$, among pairs of linear regressors (L-L), linear-interaction regressors (L-I), linear-quadratic regressors (L-Q), interaction regressors (I-I), interaction-quadratic regressors (I-Q), and quadratic regressors (Q-Q). The maximum VIF_j and R_j^2 for linear (L), two-factor interaction (I), and quadratic (Q) model terms are shown in Figures 7.5-7.6. Figure 7.7 shows the condition number κ

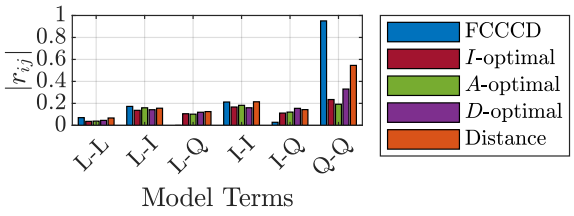

Figure 7.4: Maximum absolute r_{ij} values among candidate regressors in a quadratic model for each base design.

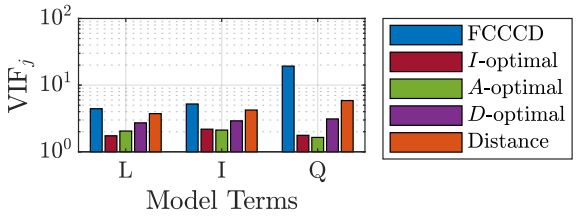

Figure 7.5: Maximum VIF_j for candidate regressors in a quadratic evaluation model for each base design.

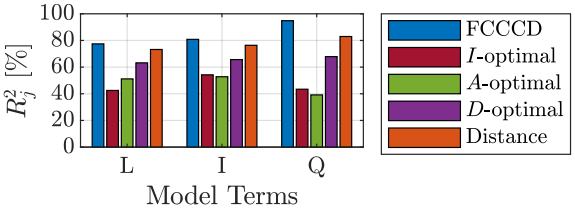

Figure 7.6: Maximum R_j^2 for candidate regressors in a quadratic evaluation model for each base design.

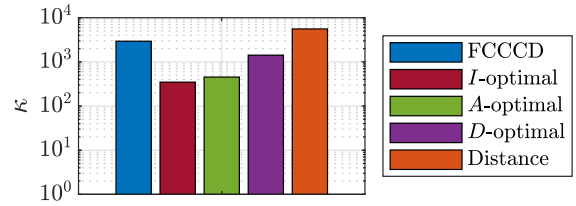

Figure 7.7: Condition number of $\boldsymbol{X}^T\boldsymbol{X}$ in a full quadratic evaluation model for each base design.

of $\boldsymbol{X}^T\boldsymbol{X}$ for a full quadratic model. The overall takeaway from these figures is that the correlation metric values are generally lowest for the I- and A-optimal designs. The correlation metrics are generally highest for the FCCCD and distance-based designs, with the correlation metrics associated with the quadratic model terms being the highest, particularly for the FCCCD, where the pairwise correlation and VIF for the quadratic regressors are above 0.95, and 19, respectively. This analysis supports the recommendation given in Reference [243] against using a face-centered central composite design for a large number of test factors because of the high correlation among the quadratic model terms.

7.2.3 Prediction Variance

Assessment of the prediction variance of a response surface design for a given model structure provides insight into its precision of prediction and allows comparison of different experiment designs. The variance of the predicted response is

$$\text{Var}[\hat{y}(\boldsymbol{x}_0)] = \sigma^2 \boldsymbol{x}_0^T \left(\boldsymbol{X}^T\boldsymbol{X}\right)^{-1} \boldsymbol{x}_0 \tag{7.3}$$

where $\hat{y}(\boldsymbol{x}_0)$ is the predicted response evaluated at the design space location $\boldsymbol{x}_0$ expanded to the form of the model structure, $\boldsymbol{X}$ is a matrix composed of the designed test points in the form of the model structure, and σ^2 is the measurement error variance [232]. From Equation (7.3), the prediction variance is a function of the experiment design, the model

structure, the location in the design space, and the measurement facility error variance. The scaled prediction variance (SPV) and unscaled prediction variance (UPV) removes the dependence on σ^2 and, thus, can be used to compare experiment designs when σ^2 is unknown prior to experimentation. SPV is defined as

$$\text{SPV} = \frac{N \operatorname{Var}[\hat{y}(\boldsymbol{x}_0)]}{\sigma^2} = N \boldsymbol{x}_0^T \left(\boldsymbol{X}^T \boldsymbol{X}\right)^{-1} \boldsymbol{x}_0 \tag{7.4}$$

where the number of test points N penalizes a larger design size [232]. The SPV considers the prediction accuracy as well as the expense of test points when comparing designs. The UPV, defined as

$$\text{UPV} = \frac{\operatorname{Var}[\hat{y}(\boldsymbol{x}_0)]}{\sigma^2} = \boldsymbol{x}_0^T \left(\boldsymbol{X}^T \boldsymbol{X}\right)^{-1} \boldsymbol{x}_0 \tag{7.5}$$

provides an assessment of the prediction precision independent from the size of the experiment design.

Graphical presentation of the distribution of prediction variance throughout the design space is an effective way to assess experiment designs. Fraction of design space (FDS) plots, introduced by Reference [244], depict the prediction variance distribution over the design space in a concise manner, where the prediction variance metrics are plotted against the FDS encompassing a prediction variance less than or equal to a particular value. It is also useful to consider the FDS including a particular model precision, quantified by the confidence interval half-width δ [240, 245, 246]. The model precision δ normalized by the response standard deviation σ plotted against FDS provides further insight into the prediction capability of the model developed from a particular experiment design, prior to conducting the experiment. For this study, a design was deemed to be adequate for fitting a particular model complexity if δ/σ was less than two for greater than 95% of the design space. The prediction variance threshold PV^* used to determine the FDS within a given model precision level is

$$\text{PV}^* = \left(\frac{\delta/\sigma}{t_{\alpha_p/2, N-p}}\right)^2 \tag{7.6}$$

where N is the number of test points, p is the number of parameters in the model, and α_p is the significance level chosen as $\alpha_p = 0.05$.

Figure 7.8 shows the UPV and δ/σ threshold values against FDS for each base experiment design using a quadratic evaluation model order. The average UPV for each design is also shown. The FCCCD and distance-based designs have the highest UPV and δ/σ threshold across the design space; the I- and A-optimal designs have the lowest UPV and δ/σ threshold across the design space. The I-optimal design has the lowest average UPV, which is expected because the design objective for the I-optimal designs is to minimize the average prediction variance across the design space; however, the prediction variance distribution for the A-optimal design is very close to the I-optimal design.

Table 7.3 lists the FDS with $\delta/\sigma \leq 1$, $\delta/\sigma \leq 1.5$, and $\delta/\sigma \leq 2$ for each design using a full quadratic evaluation model. An adequate FDS (FDS ≥ 0.95) for a normalized model

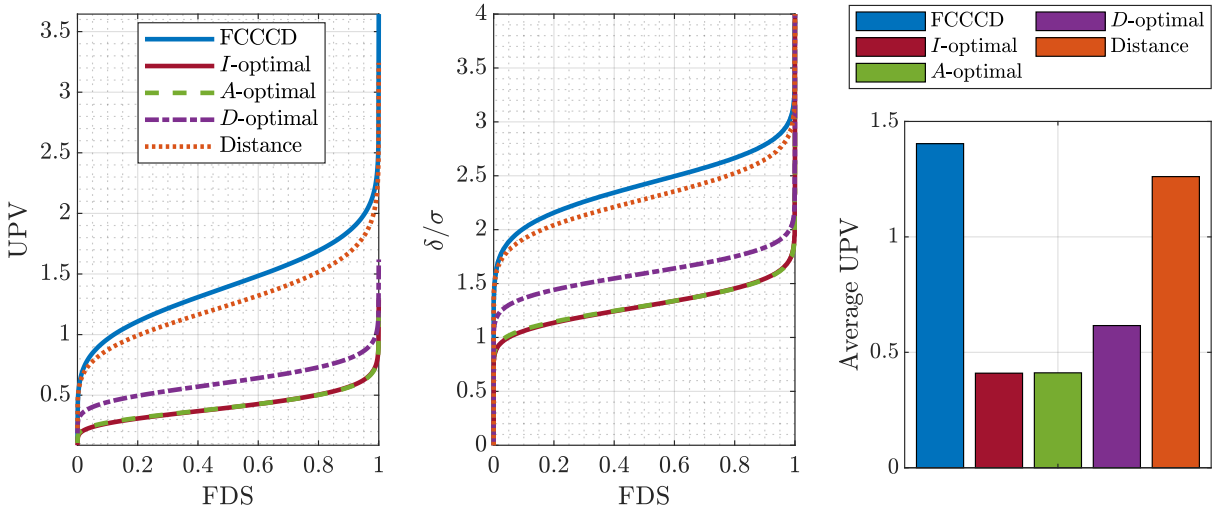

Figure 7.8: Prediction variance plots for a quadratic evaluation model for each base design.

precision $\delta/\sigma \leq 2$ is only obtained for the I-, D-, and A-optimal designs. Evaluation with $\delta/\sigma \leq 1$ and $\delta/\sigma \leq 1.5$ shows that, the I- and A-optimal designs have the highest FDS meeting these δ/σ thresholds.

Table 7.3: Prediction variance threshold FDS values using a quadratic evaluation model for each base design

Design	FDS with $\delta/\sigma \leq 1$	FDS with $\delta/\sigma \leq 1.5$	FDS with $\delta/\sigma \leq 2$
FCCCD	0.000	0.003	0.093
I-optimal	0.048	0.853	0.999
A-optimal	0.037	0.858	0.999
D-optimal	0.000	0.297	0.982
distance-based	0.000	0.003	0.161

7.2.4 Model Parameter Precision

The precision of the estimated model parameters can be assessed using the standard error of individual model parameters or properties of the $(\boldsymbol{X}^T\boldsymbol{X})^{-1}$ matrix. Figure 7.9 shows the highest standard error for linear (L), interaction (I), and quadratic (Q) model terms for each design. The standard errors are normalized by assuming unity measurement noise variance and are denoted SE*. The standard error of the model terms estimated using the FCCCD and distance-based designs are the largest, particularly for the quadratic model terms, as a consequence of the higher correlation associated with the quadratic model terms. The I-

and A-optimal designs generally have the lowest standard error values. Figure 7.10 shows the scaled D-optimality criterion [243]

$$D^* = N \left(\det\left[(\boldsymbol{X}^T\boldsymbol{X})^{-1}\right]\right)^{1/p} \tag{7.7}$$

and the trace of $(\boldsymbol{X}^T\boldsymbol{X})^{-1}$ which reflects the A-optimality [232]. The D-optimal design has the lowest D^* and the A-optimal design has the lowest value of $\mathrm{tr}[(\boldsymbol{X}^T\boldsymbol{X})^{-1}]$, as expected. The FCCCD design has the highest D^* and $\mathrm{tr}[(\boldsymbol{X}^T\boldsymbol{X})^{-1}]$ values.

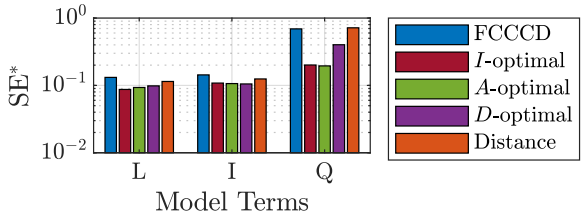

Figure 7.9: Normalized standard error of the model parameters in a full quadratic model for each base design.

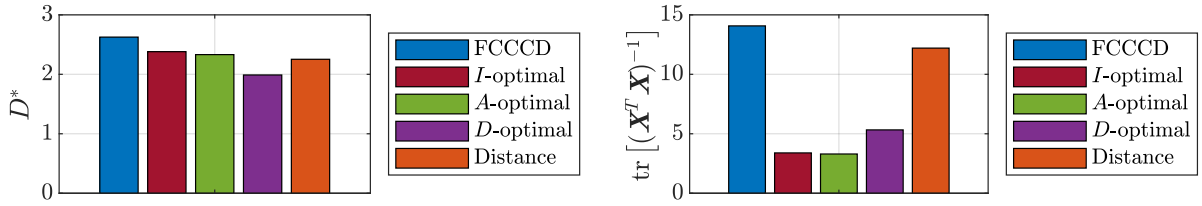

(a) Scaled D-optimality metric

(b) A-optimality metric

Figure 7.10: Overall model parameter precision metrics for a full quadratic evaluation model for each base design.

7.2.5 Discussion

The analysis in the previous subsections has shown that the I- and A-optimal designs generally have the highest statistical power for candidate model terms, the lowest correlation among candidate model terms, the lowest prediction variance across the design space, and the lowest model parameter standard errors. Based on these metrics, the I- and A-optimal designs are expected to yield the most appropriate model structure, provide the most precise estimates of model parameters, and have the best predictive performance. The FCCCD and distance-based designs generally have the worst design evaluation metrics, and the D-optimal design generally has moderate values between the most and least favorable designs. Based on this analysis, the I- and A-optimal designs are recommended for experiments with a large

number of test factors in a cuboidal test region, as is needed to develop an aero-propulsive model for a distributed propulsion aircraft. For this study, the decision was made to proceed with the I-optimal over the A-optimal design because of the slightly better precision of prediction. An I-optimal design will be expanded in the next section to address the scarcity of design points in the interior of the design space.

7.3 Sequential Response Surface Experiment Designs

Two separate sequential, cuboidal, completely randomized, response surface block designs were executed and compared to investigate possible improvement of modeling results and reduction of the number of test points needed for future aircraft characterization experiments. The designs will be referred to as the face-centered base (FCB) design and a I-optimal base (IOB) design. The FCB design has been used previously in wind-tunnel and computational testing for fixed-wing and eVTOL aircraft [28, 39, 47, 48, 137, 234], including the powered-airframe wind-tunnel test described in Chapter 6. The IOB design is a new block design process introduced in this work building on previous work which developed the FCB design. The I-optimal design was selected for this study based on the design evaluation analysis presented in Section 7.2. The block design approach for the FCB and IOB designs are described in the following subsections. For each design, a series of five test blocks was designed to acquire the data necessary to incrementally develop more accurate aero-propulsive models.

7.3.1 Face-Centered Base (FCB) Design

The sequential FCB design blocks for the LA-8 22-factor experiments are as follows [28]:

- **Block 1** is the same minimum run resolution V, face-centered central composite design (FCCCD) described in Section 7.2.
- **Block 2** is a nested FCCCD. The nested FCCCD was originally developed in Reference [235], where it was shown to be an effective design strategy for a 5-factor fixed-wing aircraft aerodynamic characterization experiment. The nested design augments the conventional FCCCD to allow estimation of pure cubic model terms and provides additional information in the interior region of the design space. The nested FCCCD applied for this work emulates the ordinary FCCCD, except that the factorial and axial points are all located at half the distance from the center of the design space. The nested FCCCD is designed separately from the Block 1 FCCCD (i.e., knowledge of the data points within Block 1 do not influence the choice of data points in Block 2).
- **Block 3** is an I-optimal design for a full quadratic design model with the number of model points being five times the number of test factors [137]. Five additional lack-of-fit points, which are selected using the Maximin distance-based criterion, as well as

five additional non-center replicates are also included in the design [243]. Inclusion of five lack-of-fit points and five non-center replicates are the default settings in Design-Expert® for base optimal response surface designs to permit lack-of-fit testing [233]. The *I*-optimal design augments the designs from previous blocks to sequentially improve the model and avoid duplicating previously tested combinations of factor settings. In other words, the previously tested FCCCD and nested FCCCD design points are factored into the optimization algorithm to minimize the prediction variance.

- **Block 4** is another augmented *I*-optimal design for a quadratic design model, which follows the same augmented design procedure from Block 3. With fewer test factors, the design model could be increased to a higher order, for example, including cubic model terms [47, 48].
- **Block 5** is another augmented *I*-optimal design for a quadratic design model, or the highest design model complexity from Blocks 1-4, which is used for model validation. The block contains 75 validation test points, which has been found to provide a good estimate of prediction error while remaining a modest number of test points. No lack-of-fit, replicate, or center points are included. Because the validation data are *I*-optimal test points designed to augment the data used for modeling to optimally reduce prediction error, but are not used to fit the models, the data provide a rigorous prediction test for the designed model complexity. The factor settings for these validation data, however, are dependent on the designs used for model identification and tend to favor the boundaries of the design space.

7.3.2 *I*-Optimal Base (IOB) Design

The sequential IOB design blocks for the LA-8 22-factor experiments are as follows:

- **Block 1** is the same *I*-optimal design for a quadratic design model described in Section 7.2. The design includes the same total number of test points and the same number of center points as the Block 1 FCB design to provide a direct comparison. Lack-of-fit points and non-center replicates are not included in the design.
- **Block 2** is a nested *I*-optimal design for a quadratic design model, which was inspired by the concept of the nested FCCCD proposed in Reference [235]. The nested *I*-optimal emulates the same design process as Block 1, except that the design points are all located at half the distance from the center of the design space. The nested *I*-optimal design was created separately from the Block 1 *I*-optimal design (i.e., knowledge of the Block 1 design does not influence the Block 2 design). The design provides more broad coverage of the interior portion of the design space, which aids in reducing model bias [232].
- **Block 3** is an *I*-optimal design for a quadratic design model with the number of model points being five times the number of experimental factors, following Reference [137].

Five additional lack-of-fit points and five additional non-center replicates are also included in the design, following the Block 3 FCB design approach. The I-optimal design augments the designs from previous blocks to sequentially improve the model and avoid duplicating previously tested combinations of factor settings.

- **Block 4** is another augmented I-optimal design for a quadratic design model following the same augmented design procedure from the previous block, and also following the Block 4 FCB design approach.
- **Block 5** contains 75 additional validation test points selected using a random number generator. This block provides validation data that are agnostic to the model development experiment design and the model complexity it was designed for. Because this block is design agnostic, it will be used to directly compare the IOB design with the FCB design later in the chapter. Note that for the simulated LA-8 wind-tunnel experiments executed for this study, the validation block was increased to 304 test points (the same number of test points as Block 1 and Block 2) selected using a random number generator to provide a greater validation sample size. Increasing the number of validation points for these simulated experiments is justified because of the low computational expense of executing each test point, but acquiring a large number of validation test points would not be practical for an expensive and/or time-consuming experiment.

7.3.3 Block Design Summary

The FCB and IOB designs are summarized in Table 7.4. The designs intentionally have the same number of test points in each block so that the design qualities can be compared directly. The difference between the sets of test blocks is the type of design used in Block 1, Block 2, and Block 5. It is worth noting that the FCCCD designs are available nearly instantaneously, whereas each I-optimal design blocks can take roughly 1-2 hours to create due to the computational expense of the employed coordinate exchange optimization algorithm [232, 239]. Figures 7.11-7.12 show two-dimensional slices of the 22-factor space for each design. Each block is plotted sequentially with points from the previous blocks to show how the higher complexity designs fill the design space. The figure shows that the IOB design covers a broader number of individual factor settings compared to the FCB design. The next section compares the pre-experiment design evaluation metrics for the FCB and IOB designs.

7.4 Sequential Experiment Design Evaluation

This section compares the sequential FCB and IOB experiment design approaches using the pre-experiment design evaluation metrics described in Section 7.2. The designs are

Table 7.4: FCB and IOB test block design summary

(a) FCB design

Block	Design Type	Block Points	Cumulative Points
1	FCCCD	304	304
2	nested FCCCD	304	608
3	I-optimal	120	728
4	I-optimal	120	848
5	I-optimal (validation)	75	923

(b) IOB design

Block	Design Type	Block Points	Cumulative Points
1	I-optimal	304	304
2	nested I-optimal	304	608
3	I-optimal	120	728
4	I-optimal	120	848
5	random (validation)	75	923

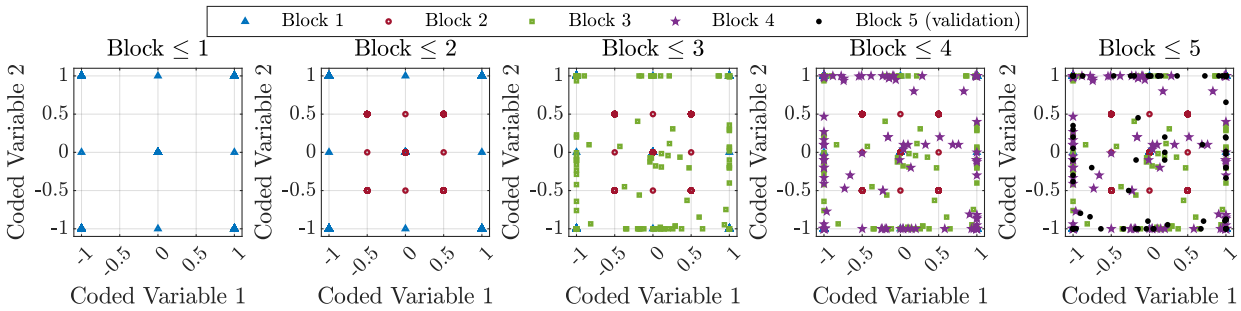

Figure 7.11: Sequential two-dimensional slices of the 22-factor space for each FCB test block.

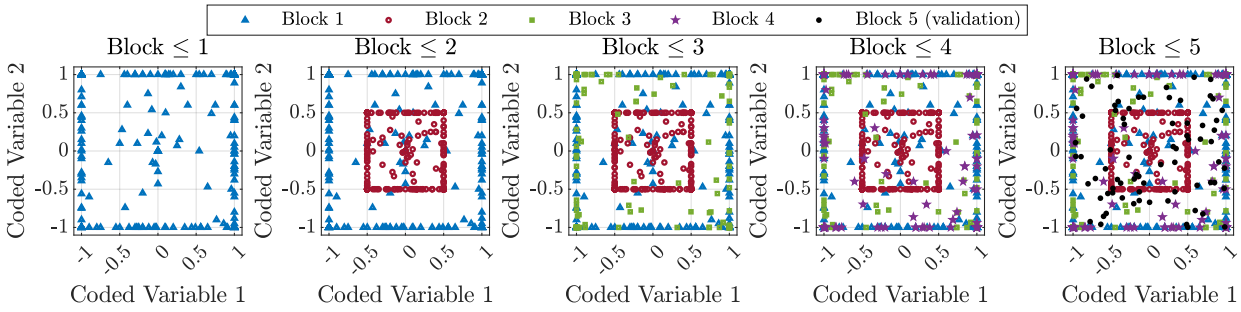

Figure 7.12: Sequential two-dimensional slices of the 22-factor space for each IOB test block.

assessed sequentially at each block, meaning that the analysis for each block includes the design points in the current block and all previous blocks.

7.4.1 Statistical Power

The lowest statistical power among all the linear (L), interaction (I), and quadratic (Q) model terms for each design and block number are shown in Figure 7.13. The power values are also shown numerically in Table 7.14. Figure 7.13a and Table 7.14a show the power for

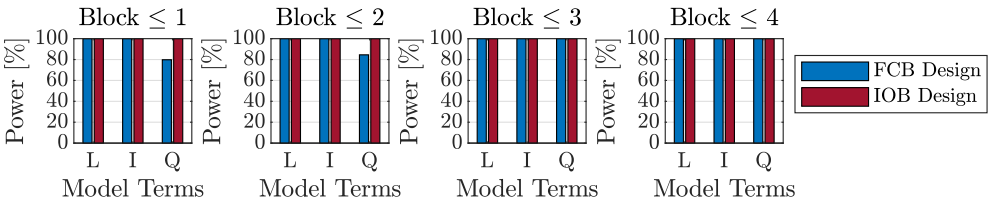

(a) Power calculation with $\alpha_p = 0.05$ and $\delta/\sigma = 2$

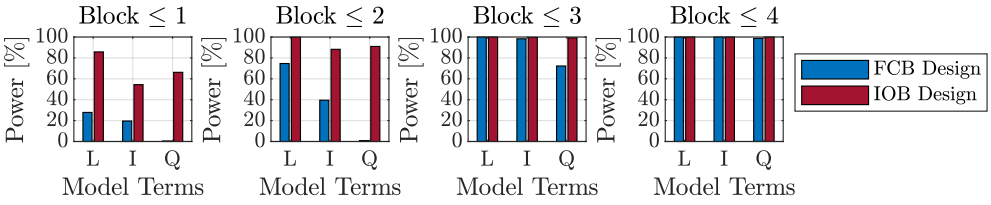

(b) Power calculation with $\alpha_p = 0.0001$ and $\delta/\sigma = 1$

Figure 7.13: FCB and IOB design power comparison.

Figure 7.14: FCB and IOB design power comparison (expressed as a percentage)

(a) Power calculation with $\alpha_p = 0.05$ and $\delta/\sigma = 2$

Block	Model Terms	Power for FCB Design	Power for IOB Design
1	L	99.999996	100.0000000000
1	I	99.99991	99.9999999997
1	Q	79.8	99.9999999999
2	L	99.9999999999	100.0000000000
2	I	99.999996	99.9999999999
2	Q	84.5	100.0000000000
3	L	100.0000000000	100.0000000000
3	I	100.0000000000	100.0000000000
3	Q	99.9999999999	100.0000000000
4	L	100.0000000000	100.0000000000
4	I	100.0000000000	100.0000000000
4	Q	100.0000000000	100.0000000000

(b) Power calculation with $\alpha_p = 0.0001$ and $\delta/\sigma = 1$

Block	Model Terms	Power for FCB Design	Power for IOB Design
1	L	27.8	85.7
1	I	19.6	54.4
1	Q	0.4	66.2
2	L	74.6	99.9
2	I	39.5	88.2
2	Q	0.8	91.0
3	L	99.96	99.9996
3	I	98.3	99.6
3	Q	72.3	99.2
4	L	99.999997	99.9999998
4	I	99.990	99.998
4	Q	98.7	99.98

each design with common values of $\alpha_p = 0.05$ and $\delta/\sigma = 2$. The FCB design has nearly 100% power for the linear and interaction model terms in all blocks. The power for quadratic model terms is near 80% for Blocks 1-2 and near 100% for Blocks 3-4. The IOB design has nearly 100% power for all model terms in all blocks. Figure 7.13b and Table 7.14b show the power for each design with conservative values of $\alpha_p = 0.0001$ and $\delta/\sigma = 1$, resulting in lower power. For Block 1, the lowest power among the groups of model terms is between 54% and 86% for the IOB design and between 0% and 28% for the FCB design. For Block

2, each group of model terms has a power value below 75% for the FCB design, whereas all model terms have a power above 88% for the IOB design. For Block 3, the lowest power for the quadratic model terms is 72.3% for the FCB design, but above 99% for the IOB design; the power for linear and interaction model terms are above 98% for both designs, but the power is higher for the IOB design. For Block 4, all model terms in each design have a high power, but the power for the IOB design is higher. The overall takeaway is that, for the same number of design points, the statistical power for the IOB design is always higher than the FCB design, particularly for the quadratic model terms. This means that for the same significance level, models estimated from the IOB design have a lower probability of failing to include model terms that are significant to the model. The power is also seen to increase as the block number increases, as would be expected when increasing the total number of available data points.

7.4.2 Correlation Metrics

The pairwise and multiple correlation metrics for each design evaluated for a full quadratic model are shown in Figures 7.15-7.18. As mentioned in Section 7.2.2, this is a conservative analysis that assumes all candidate regressors are included in the model and many candidate model terms were expected to be excluded through model structure determination after data collection. The important takeaway from these figures is that the correlation metric values are generally lower for the IOB design compared to the FCB design. For the FCB design, the correlation metrics associated with the quadratic model terms are the highest, particularly for the Block 1 FCCCD and Block 2 nested FCCCD, where the pairwise correlation and VIF for the quadratic regressors are above 0.95, and 19, respectively. The condition number for each FCB design block is also higher compared to the corresponding IOB block, indicating that adverse effects from multiple correlation are greater, particularly for the Block 1 FCCCD and Block 2 nested FCCCD designs. Again, this analysis assumes a full quadratic model; if a subset of the model terms is selected for the model, then the condition number will be reduced.

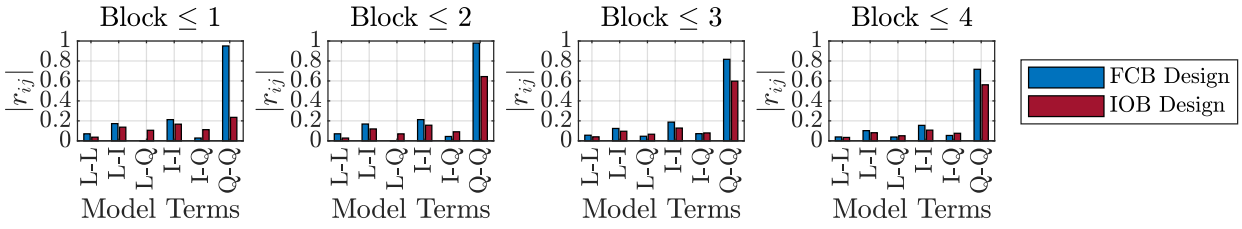

Figure 7.15: Maximum absolute r_{ij} values among candidate regressors in a quadratic model for FCB and IOB designs.

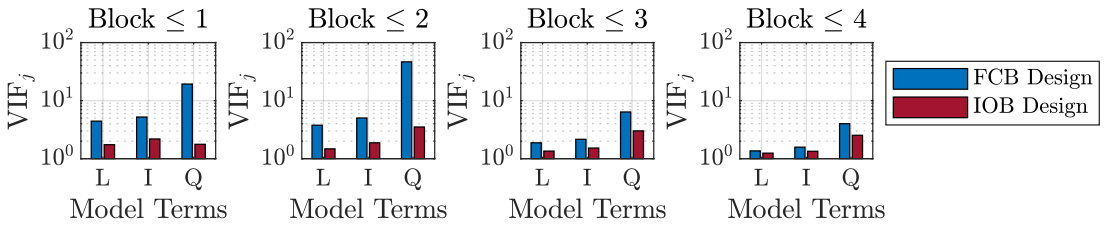

Figure 7.16: Maximum VIF$_j$ for candidate regressors in a quadratic evaluation model for FCB and IOB designs.

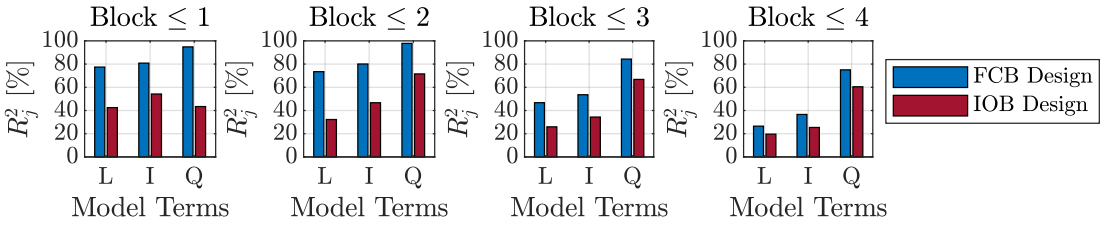

Figure 7.17: Maximum R_j^2 for candidate regressors in a quadratic evaluation model for FCB and IOB designs.

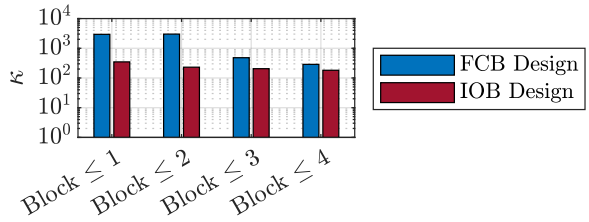

Figure 7.18: Condition number of $\boldsymbol{X}^T\boldsymbol{X}$ in a full quadratic evaluation model for FCB and IOB designs.

7.4.3 Prediction Variance

Figure 7.19 shows the UPV and δ/σ threshold values against FDS, as well as the average UPV, for each experiment design using a quadratic evaluation model order. The UPV and δ/σ threshold curve decreases in value and becomes more uniform (flat) as the block number increases. Block 1 and Block 2 for the FCB design (a FCCCD and nested FCCCD) have a significantly higher UPV across the design space compared to Block 1 and Block 2 for the IOB design (an I-optimal and nested I-optimal design). This is expected because the design objective for the I-optimal designs is to minimize the average prediction variance across the design space. The respective Block 3 and Block 4 designs have a more similar prediction variance distribution and average value because both design approaches employ augmented I-optimal designs for these blocks, but the IOB design blocks still have a lower UPV value across the design space.

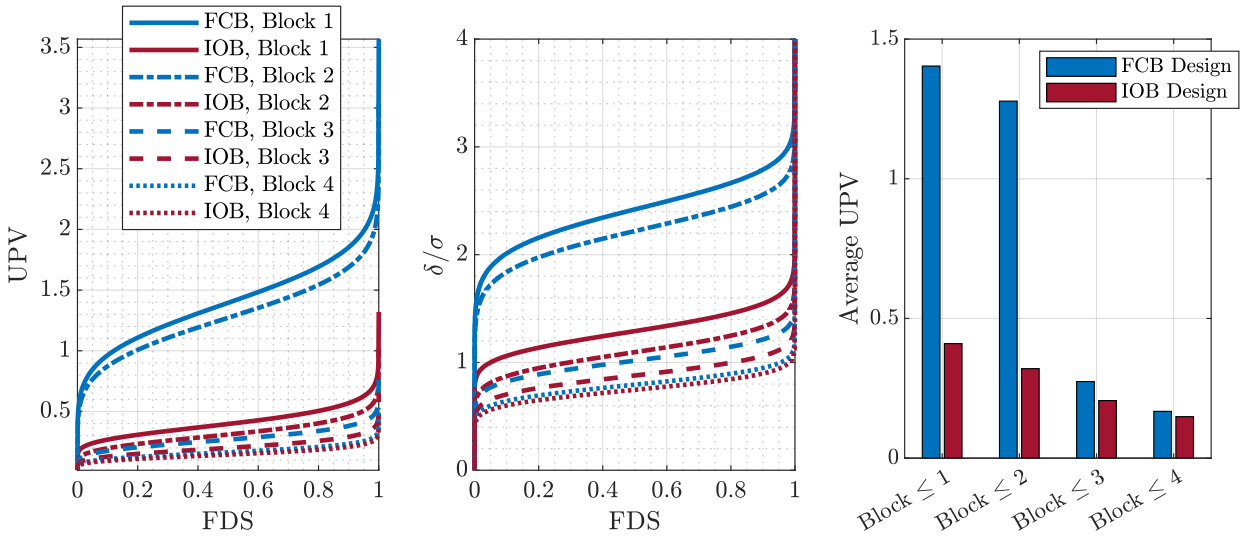

Figure 7.19: Prediction variance plots for a quadratic evaluation model for FCB and IOB designs.

Table 7.5 lists the FDS with $\delta/\sigma \leq 1$ and $\delta/\sigma \leq 2$ for each design using a full quadratic evaluation model. An adequate FDS (FDS ≥ 0.95) for a normalized model precision $\delta/\sigma \leq 2$ is obtained for each IOB block, whereas this threshold is only achieved in Block 3 and Block 4 for the FCB design. Evaluation with $\delta/\sigma \leq 1$ shows that, for each block, a larger FDS meets this more stringent requirement for the IOB design compared to the FCB design.

Table 7.5: Prediction variance threshold FDS values using a quadratic evaluation model for FCB and IOB designs

Block	FCB Design FDS with $\delta/\sigma \leq 1$	IOB Design FDS with $\delta/\sigma \leq 1$	FCB Design FDS with $\delta/\sigma \leq 2$	IOB Design FDS with $\delta/\sigma \leq 2$
1	0.000	0.048	0.093	0.999
2	0.000	0.288	0.222	1.000
3	0.448	0.799	1.000	1.000
4	0.953	0.982	1.000	1.000

7.4.4 Model Parameter Precision

Figure 7.20 shows the highest standard error for each group of model terms for each design and block number. The standard error of the model terms estimated using the FCB design are greater, particularly for the quadratic model terms, as a consequence of the higher correlation associated with the quadratic model terms. Figure 7.21 shows the scaled D-optimality criterion [243] and the trace of $(\boldsymbol{X}^T\boldsymbol{X})^{-1}$ (representing the A-optimality [232]).

For Block 1 and Block 2, the IOB design has lower D- and A-optimality metrics compared to the FCB designs. For Block 3 and Block 4, the D- and A-optimality metrics are similar for each design.

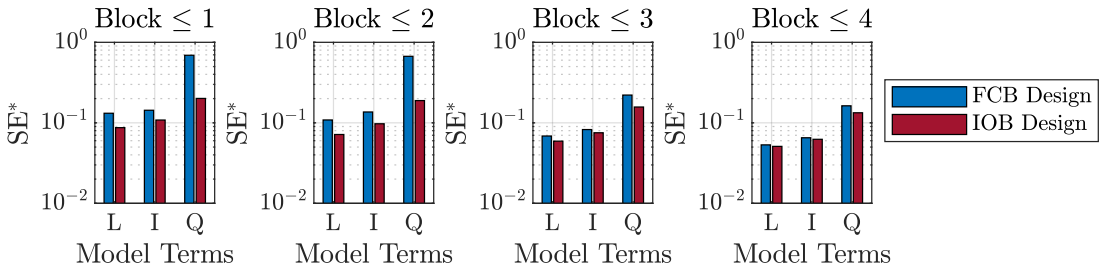

Figure 7.20: Normalized standard error of the model parameters in a full quadratic model for FCB and IOB designs.

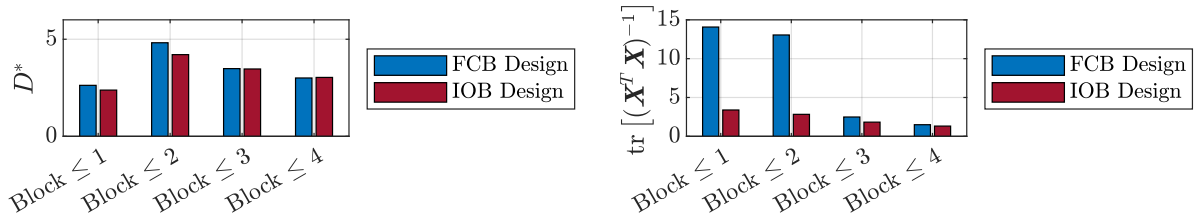

(a) Scaled D-optimality metric

(b) A-optimality metric

Figure 7.21: Overall model parameter precision metrics for a full quadratic evaluation model for FCB and IOB designs.

7.4.5 Discussion

This section presented several pre-experiment design metrics and direct comparisons were made between the FCB and IOB design approaches assuming a full quadratic model structure. The analysis indicated that the IOB design has improved statistical power, correlation among model terms, prediction variance, and precision of estimated model parameters compared to the FCB design. The following sections further investigate the two experiment design approaches by comparing results from simulated LA-8 wind-tunnel experiments.

7.5 Model Identification Approach

Similar to Chapter 6, aero-propulsive modeling for this effort focuses on developing a polynomial representation of the aero-propulsive forces and moments as a function of vehicle

state and control variables. Factors under test, or close variants (as discussed in Chapter 6 and Reference [28]), are defined as explanatory variables, and a model is identified from the data collected using the experiment designs described in Section 7.3. Following the approach described in Section 6.5.1, the modeled responses are the dimensional body-axis aero-propulsive forces X, Y, Z in lbf and moments L, M, N in ft·lbf. The explanatory variables are defined as the body-axis velocity components v, w in ft/s; propeller speeds $n_1, n_2, ..., n_8$ in revolutions per second; wing angles $\delta_{w_1}, \delta_{w_2}$ in radians; elevon deflections $\delta_{e_1}, \delta_{e_2}, \delta_{e_3}, \delta_{e_4}$ in radians; flap deflections $\delta_{f_1}, \delta_{f_2}, \delta_{f_3}, \delta_{f_4}$ in radians; and ruddervator deflections $\delta_{r_1}, \delta_{r_2}$ in radians.

The model structure was developed using the stepwise regression algorithm from Reference [103] (see Section 2.6.2.2) and the model parameters were estimated using ordinary least-squares regression (see Section 2.6.1.1). The stepwise regression algorithm was run automatically until the remaining excluded model terms did not surpass the partial F-statistic cutoff value when added to the model. The significance level α_p is commonly chosen as $\alpha_p = 0.05$, or 95% confidence that a model term is significant; however, this threshold has been noted to admit a large number of model terms that lack physical justification for eVTOL aircraft aero-propulsive modeling problems. For the data analyzed in this chapter, a significance level from $\alpha_p = 0.01$ to $\alpha_p = 0.0001$ (99% confidence to 99.99% confidence, respectively) appeared to be a good choice to obtain a parsimonious model with good prediction capability. After identifying the model structure and parameter estimates, model adequacy was examined by comparing modeling residuals to validation residuals using data withheld from the model development process.

7.6 Modeling Results

Separate aero-propulsive models were identified using the data collected from the FCB and IOB simulated wind-tunnel experiments for each sequential test block. Figure 7.22 shows a comparison of the modeling NRMSE (NRMSE_m) and validation NRMSE (NRMSE_v) for the sequential models developed using the FCB and IOB designs. Histories of normalized modeling residuals and normalized validation residuals, as well as validation NRMSE metric bounds ($\pm 2\,\text{NRMSE}_v$), for each block are shown in Figures 7.23-7.26 at the end of this chapter to compare residual values and verify that the residuals are independent. The y-axis limits for each response across each block and design type are identical to aid in visual comparisons of residual character. Additional omitted residual diagnostic plots were viewed for each design to verify that the residuals were normally distributed and had constant variance.

As can be seen in Figure 7.22, most respective IOB-design NRMSE values calculated using the modeling and validation data for each response are similar and low-valued signifying that a high-quality model has generally been identified at each block; however, for the first IOB design block, the NRMSE_v values for Z and M are notably larger than the

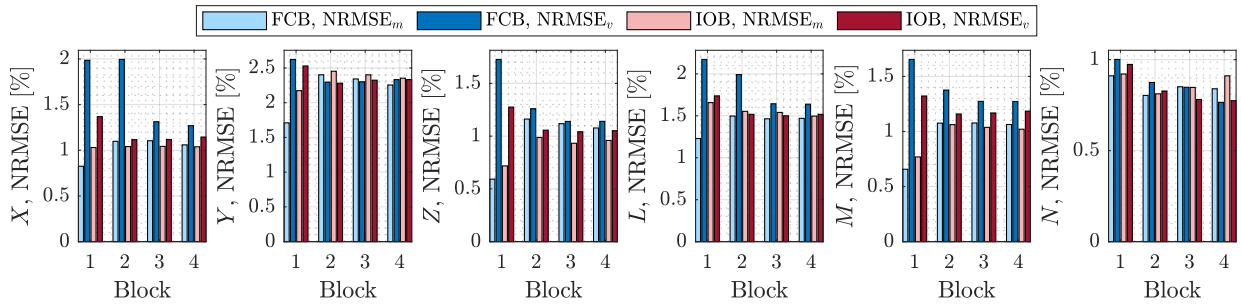

Figure 7.22: Modeling and validation NRMSE for models developed at each test block for LA-8 simulated wind-tunnel experiments.

respective NRMSE$_m$ values suggesting that the Block 1 model for these responses may require improvement to obtain an adequate model. There is a decrease between the NRMSE$_v$ values between Block 1 and Block 2 for all responses indicating that augmentation with the nested I-optimal design has improved the prediction capability. The NRMSE$_v$ values for Block 3 and Block 4 are similar to those obtained for Block 2 indicating that the additional data collected in Block 3 and Block 4 provide little additional benefit in terms of prediction capability. These results suggests that only the first two IOB test blocks need to be executed for this experiment.

For the first FCB design block, the NRMSE$_v$ values for all responses except N are significantly larger than the respective NRMSE$_m$ values suggesting that the model may be deficient, which could be attributed to the sparsity of interior data points. This residual character is also clearly reflected in Figure 7.23a, where the magnitude of normalized validation residuals for most responses is significantly larger than the magnitude of the respective normalized modeling residuals. Although model adequacy reservations were noted for the Block 1 IOB design for some responses, the disparity between the respective modeling and validation NRMSE values is more prominent for the FCB design. Execution of the second FCB block decreases the NRMSE$_v$ for most responses and results in the NRMSE$_v$ values for each response being closer to the respective NRMSE$_m$ values; however, the NRMSE$_v$ values are still notably larger compared to the NRMSE$_m$ values for certain responses. For the Block 3 and Block 4 FCB models, the NRMSE$_m$ and NRMSE$_v$ values for each response are similar in value, providing confidence that model development was successful. The NRMSE$_v$ values obtained for the models identified from the Block 3 and Block 4 FCB designs are also similar in value to the corresponding NRMSE$_v$ values obtained for the Block 3 and Block 4 IOB models, but lower prediction error is still generally obtained for the models identified using the IOB block designs. I-optimal designs are optimized to reduce prediction error for the identified models, so it makes sense that the IOB design blocks result in lower prediction error values. Future studies are recommended to further investigate the utility of the presented response surface experiment design approaches in wind-tunnel experimentation and other complex modeling problems with a large number of test factors.

Acknowledgment of Collaborative Research

The research presented in this chapter was primarily conducted by the author, but included important collaborative contributions with other individuals. The LA-8 face-centered base design strategy was developed by Patrick Murphy. The LA-8 strip theory model used to conduct simulated experiments was developed by Jacob Cook. The author gratefully acknowledges and appreciates these contributions which made the research described in this chapter possible.

Residual Plots

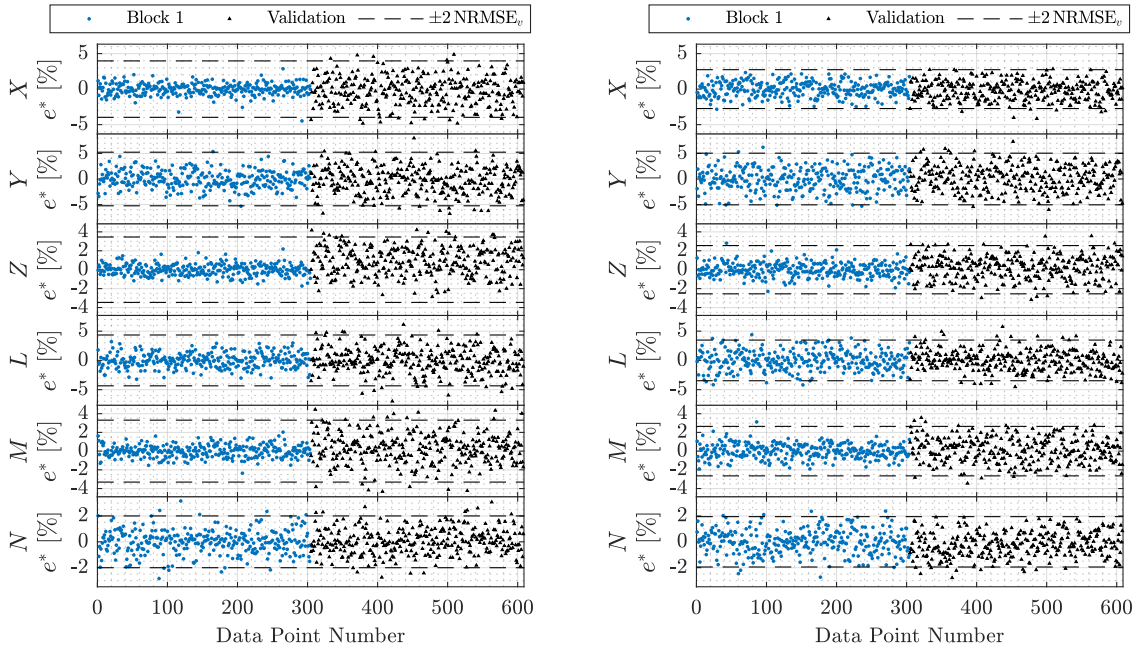

(a) FCB test matrix

(b) IOB test matrix

Figure 7.23: Normalized modeling and prediction residuals (1 modeling block).

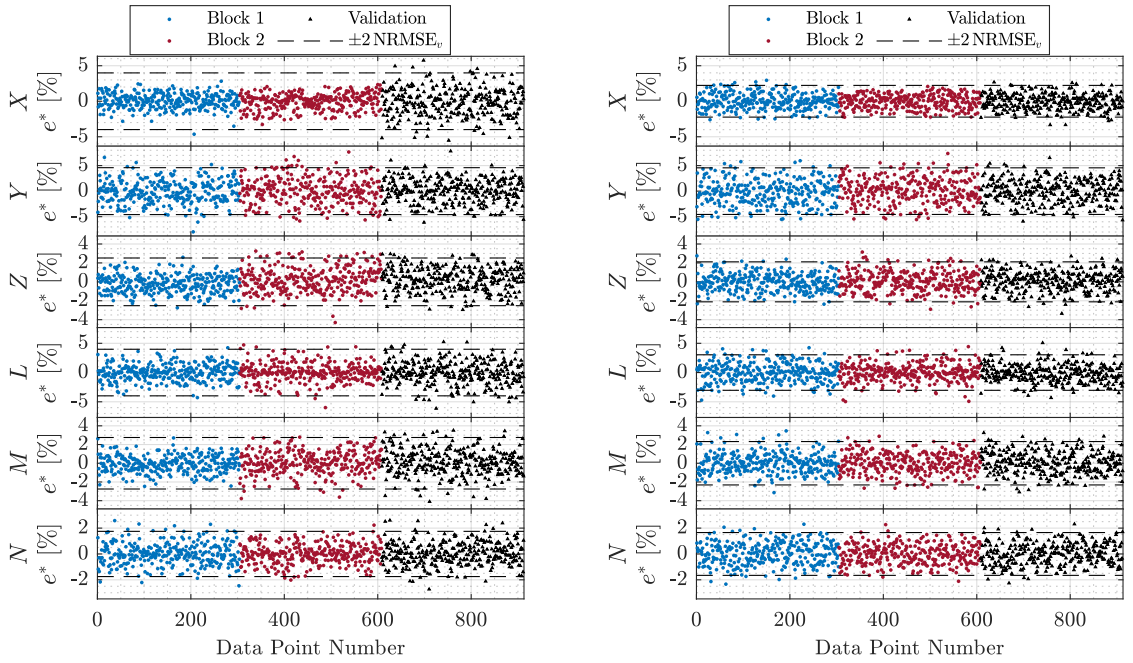

(a) FCB test matrix (b) IOB test matrix

Figure 7.24: Normalized modeling and prediction residuals (2 modeling blocks).

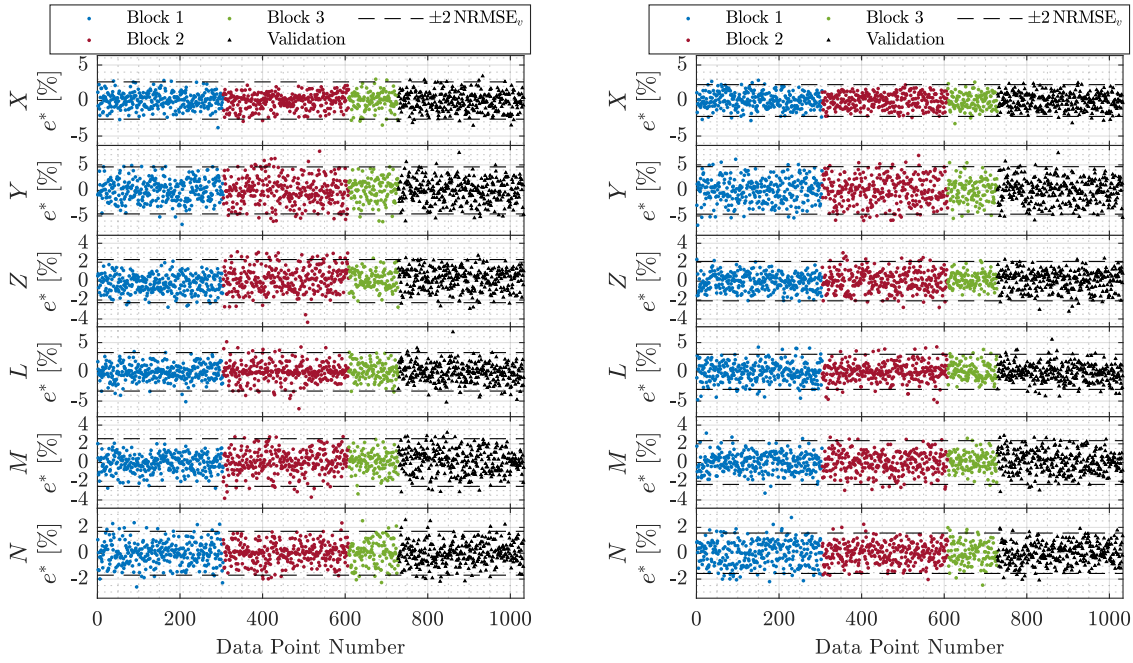

(a) FCB test matrix (b) IOB test matrix

Figure 7.25: Normalized modeling and prediction residuals (3 modeling blocks).

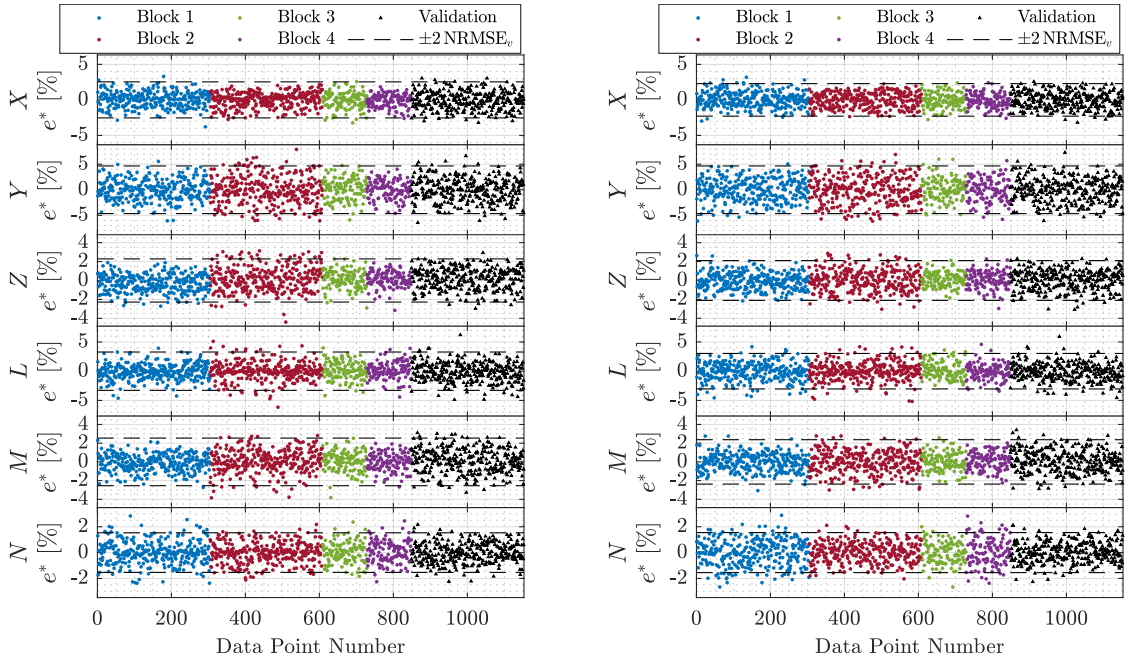

(a) FCB test matrix

(b) IOB test matrix

Figure 7.26: Normalized modeling and prediction residuals (4 modeling blocks).

Chapter 8

Aero-Propulsive Modeling for eVTOL Aircraft Using Wind-Tunnel Testing with Multisine Inputs

This chapter describes an approach for modeling the aero-propulsive characteristics of eVTOL aircraft leveraging wind-tunnel testing with dynamic excitation inputs. As has been emphasized in previous chapters, compared to many conventional aircraft, eVTOL aircraft designs exhibit greater aero-propulsive complexity and many interacting factors requiring development of new testing and aerodynamic modeling strategies. An efficient, hybrid wind-tunnel experiment is designed for the NASA LA-8 eVTOL aircraft using a combination of response surface methods and dynamic programmed test inputs. An I-optimal response surface design is developed for slow moving test variables and orthogonal phase-optimized multisine signals are designed for each control surface and propulsor. Testing is conducted by applying both experiment design methods simultaneously to collect informative wind-tunnel data subsequently used for model identification using a novel, multistep modeling process. The model adequacy is assessed using validation data acquired separately from data used to identify the model and indicates that the models have good predictive capability. The amount of required test time using the techniques described in this chapter is substantially reduced compared to previous static wind-tunnel testing for the LA-8 aircraft, while still providing high-quality models and greater parameterization flexibility. This work has been published as a conference paper [30].

The chapter is organized as follows: Section 8.1 provides motivation and background information for this research. Section 8.2 describes the experiment design methodology, followed by a description of the wind-tunnel test and data processing methods in Section 8.3. The aero-propulsive modeling approach and the model identification strategy are described in Section 8.4. Section 8.5 provides sample modeling results, followed by discussion of the results and modeling approach in Section 8.6.

8.1 Research Motivation

Previous research, including the work described in Chapters 6-7, has investigated methods for efficient eVTOL aircraft aero-propulsive modeling across their wide flight envelopes using static DOE/RSM wind-tunnel testing [28, 46, 137, 219]. Although these methods are much more efficient and statistically rigorous compared to executing a traditional OFAT test, the efficiency can be further improved by using continuously sampled data and techniques gleaned from flight-test system identification. The present work builds on and combines previous research to develop an effective aero-propulsive modeling strategy for eVTOL aircraft using novel wind-tunnel testing that results in substantial test efficiency increases. The distributed propulsion, tilt-wing aircraft modeling approach proposed in Chapter 6 is combined with a more efficient, hybrid wind-tunnel experiment designed using modern response surface methods [231, 232] and multisine PTI excitations [19, 82–85]. This multilayered testing and modeling strategy is similar to previous fixed-wing aircraft modeling research using flight testing [247] and flight simulations [248]. The present work is also inspired by recent NASA Learn-to-Fly Project [249, 250] wind-tunnel testing [237] and flight testing [105, 106, 140] used for modeling fixed-wing aircraft and extends efficient model development strategies to eVTOL aircraft. Reference [237] presents a related wind-tunnel testing and modeling approach leveraging a combination of response surface designs and PTI excitations used for fixed-wing aircraft aerodynamic modeling. The new contributions of this work include a new experiment design methodology and a novel, multistep model identification procedure tailored to the data collection methods, as well as application to a complex eVTOL aircraft with significant aero-propulsive coupling.

8.2 Experiment Design

The factors under test were divided into static factors and dynamic factors for the wind-tunnel experiment design based on the frequency band of typical variations in flight, as well as the capabilities of the wind-tunnel testing apparatus. Static and dynamic test factor experiment designs were developed separately, but the designs were run simultaneously for test execution. The respective experiment design methods forming the hybrid testing strategy are discussed in the following subsections. Note that this study was exploratory in nature with an objective of refining the proposed testing approach to guide future wind-tunnel tests for eVTOL vehicles. Consequently, the wind-tunnel experiment was expected to yield excess data with the goal of determining the data collection requirements enabling development of satisfactory aero-propulsive models in an efficient manner.

8.2.1 Static Experiment Design

The static test factors were angle of attack α, angle of sideslip β, front wing angle δ_{w_1}, and rear wing angle δ_{w_2}. These factors were held at constant settings during data collection due to their slow relative movement and for operational convenience in wind-tunnel testing. Moving the airflow orientation angles and wing angles dynamically changes the tare values and introduces additional dynamic modeling complexity. The factor settings for each of the four static test factors were independently commanded by the wind-tunnel control system at each test point. Although Chapter 6 suggests parameterizing eVTOL aircraft models using body-axis velocity components, the test matrices were specified using α and β for ease of envelope definition and simplified integration into the wind-tunnel test apparatus. The freestream velocity was held at a constant setting for the testing described in this chapter, but would need to be varied to develop an aero-propulsive model valid throughout the operational flight envelope.

A set of five sequential static test blocks was developed using DOE [231] and RSM [232] theory to acquire the data necessary to identify and validate increasingly complex aero-propulsive models. Modeling block design was accomplished with the aid of Design-Expert® [233]. Previous model identification results for the LA-8 aircraft suggested that at least pure quadratic and two-factor interaction model terms are needed to characterize the slow moving test factors (see Chapter 6), but additional model complexity in the form of higher-order model terms was not investigated in that study. The hybrid testing strategy employed in this work allows identification of higher-order models, while still conducting efficient testing.

The static factor settings were chosen using sequential, completely randomized I-optimal response surface designs, which are designs that minimize the average prediction variance for a predefined model order over the range of factor settings [231, 232]. The four blocks used for modeling were I-optimal designs for:

1. a quadratic design model (up to pure quadratic and two-factor interaction model terms),
2. a cubic design model (up to pure cubic terms and all arrangements of cross terms up to a total of third order),
3. a quartic design model (up to pure quartic terms and all arrangements of cross terms up to a total of fourth order), and
4. a quintic design model (up to pure quintic terms and all arrangements of cross terms up to a total of fifth order).

The I-optimal block designs were composed of the minimum number of test points needed to fit a full model of the specified complexity. Three additional center points were also included in each block to allow estimation of pure error and to aid in stabilization of the prediction variance at the center of the experimental region [231]. Each sequential I-optimal design augmented the collective design from previous blocks to sequentially increase the identifiable

model complexity, improve the model prediction, and avoid duplicating previously tested combinations of factor settings. All modeling blocks were executed to investigate the model complexity needed to characterize eVTOL aircraft, but not all blocks were expected to be needed to identify a satisfactory aero-propulsive model.

An additional fifth block consisting of 20 static test points selected using a random number generator was used as validation data withheld from model identification. The choice of randomized test points makes the validation test impartial to the experiment design. This validation block was found to provide a good estimate of prediction error while using a modest number of test points for the present application.

Figure 8.1 shows two-dimensional slices of the factor space for the four static test factors. Each block is plotted sequentially with points from the previous blocks to show how the higher complexity I-optimal designs fill the design space. The randomized validation test points are also shown on each plot. Figure 8.2 shows a four-dimensional representation for all static test factors and all test blocks. Although the factors are displayed in coded units in the figure, the variables would be converted into engineering units for test execution.

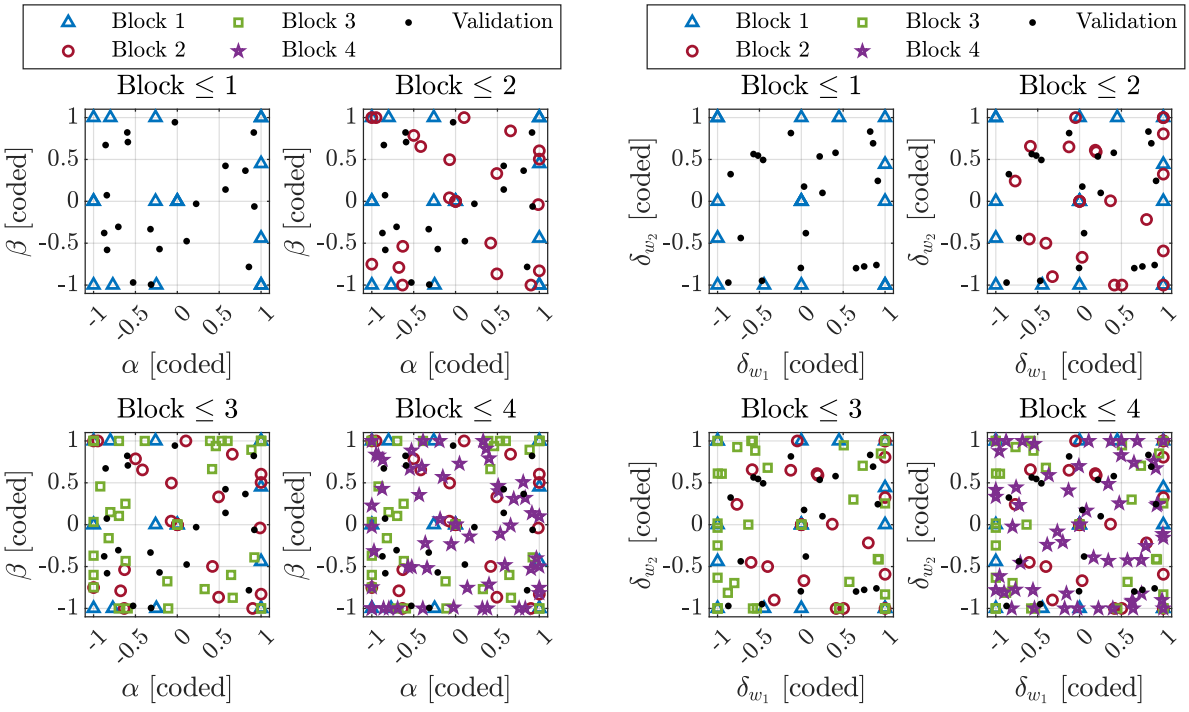

Figure 8.1: Sequential two-dimensional slices of the coded factor space for the static test factors.

As discussed in Section 7.2.3, evaluation of the prediction variance of a response surface design provides insight into its precision of prediction and allows comparison of different designs prior to experimentation. Table 8.1 lists the number of test points for each block,

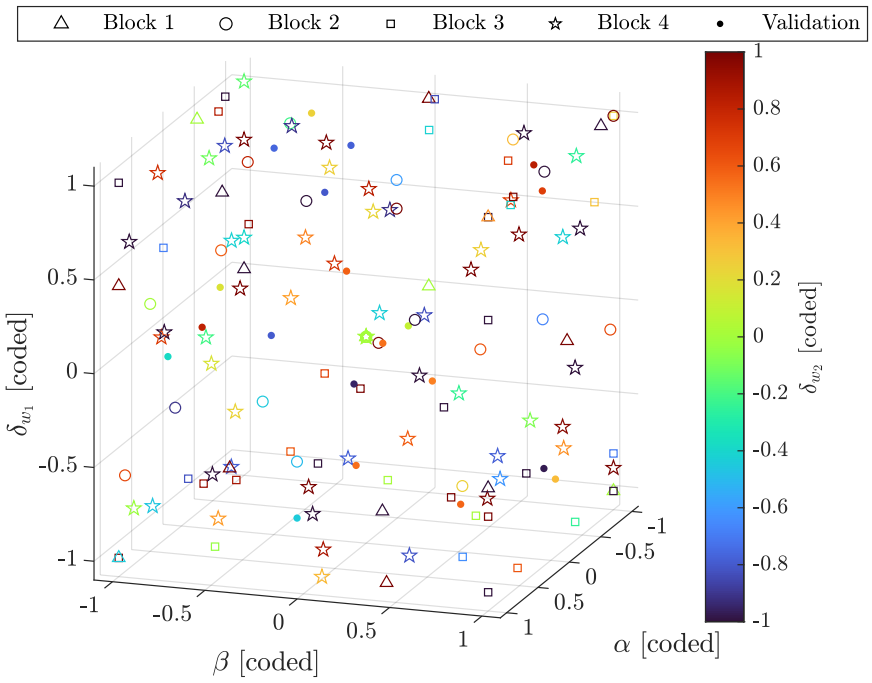

Figure 8.2: Four-dimensional representation of the coded factor space for the static test factors.

as well as the FDS with $\delta/\sigma \leq 2$ for quadratic, cubic, and quartic evaluation models. An adequate FDS (FDS ≥ 0.95) for a normalized model precision $\delta/\sigma \leq 2$ is obtained with a design order one power larger than the evaluation model order. Figures 8.3, 8.4, and 8.5 show the UPV, SPV, and δ/σ threshold values against FDS for a quadratic, cubic, and quartic model evaluation model order, respectively. Each block is analyzed sequentially, meaning that the analysis for each block includes the design points in the current block and all previous blocks. The UPV and δ/σ threshold curve decreases in value and becomes more uniform (flat) as the design order increases. The SPV curves for each block are similar for the quadratic evaluation model. For the cubic and quartic evaluation models, a lower and more uniform SPV is obtained with a design complexity greater than the evaluation model complexity.

Table 8.1: Cumulative experiment design properties for each test block

Block	Design Order	Block Points	Cumulative Points	Quadratic Model FDS with $\delta/\sigma \leq 2$	Cubic Model FDS with $\delta/\sigma \leq 2$	Quartic Model FDS with $\delta/\sigma \leq 2$
1	Quadratic	18	18	0.448	0.000	0.000
2	Cubic	23	41	0.999	0.215	0.000
3	Quartic	38	79	1.000	0.998	0.151
4	Quintic	59	138	1.000	1.000	0.994

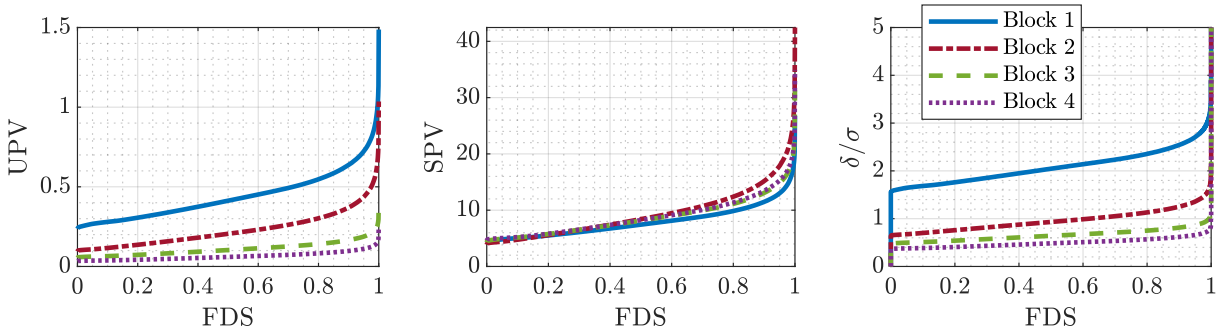

Figure 8.3: FDS plots for a quadratic evaluation model.

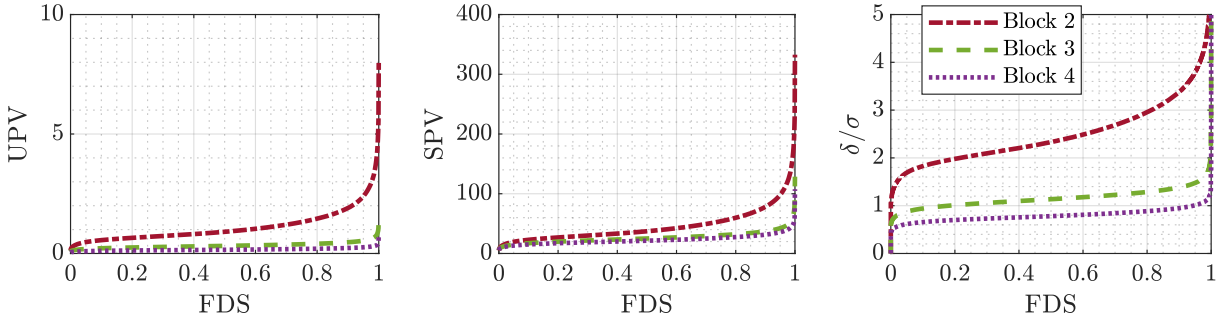

Figure 8.4: FDS plots for a cubic evaluation model.

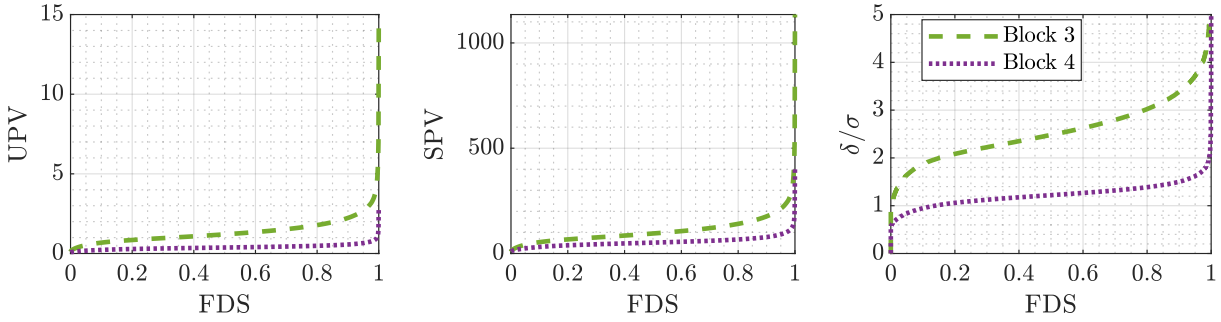

Figure 8.5: FDS plots for a quartic evaluation model.

8.2.2 Dynamic Experiment Design

The ten control surfaces (four elevons, four flaps, and two ruddervators) and eight propulsors present on the LA-8 aircraft were treated as dynamically changing factors at each static test point. Orthogonal phase-optimized multisine inputs [19, 82–85], described in Section 2.3.2, were the excitation input type, or PTI, applied to these control effectors. Multisine inputs have been used successfully in previous aircraft system identification work to simultaneously characterize the effects of many individual control effectors [84, 251–253].

For this study, individual multisine signals were generated for each of the LA-8 control surfaces and propulsors, for a total of 18 different excitation signals. The multisine design process is similar to the process that would be used to create multisine inputs for LA-8 flight experiments, as will be discussed in Chapter 9 (Reference [32]). Several harmonic components were assigned to each control surface and propulsor multisine signal, where the overall frequency range was set to between 0.05 Hz and 1.8 Hz in accordance with frequencies that would be used in flight. The propulsion harmonic components were focused into lower frequencies below 1.2 Hz to adhere to the lower bandwidth of the propulsors [37]. Focusing the propulsor excitation frequencies below this limit avoids over-stressing the motors and prevents the propulsor excitation power from being attenuated by the motor dynamics. Six different sets of multisine input frequency components were considered for the experiment by varying the fundamental period T from 30 seconds to 180 seconds in 30-second increments. A larger fundamental period results in a finer frequency resolution, $\Delta f = 1/T$ Hz, which allows assigning more frequency components to each individual multisine signal. The design with the shortest fundamental period ($T = 30$ seconds) had three harmonic components assigned to each propulsor and control surface signal; the design with the longest fundamental period ($T = 180$ seconds) had 16 harmonic components assigned to each propulsor signal and 18 harmonic components assigned to each control surface signal. Because the starting phase angles for each harmonic component in the non-convex RPF optimization are generally chosen randomly in $(-\pi, +\pi]$, a different set of phase angles optimized for minimum RPF is generally obtained each time a multisine signal is designed. Multisine optimization with randomly chosen starting phase angles was performed 30 times for each different set of frequency components and the design with the shortest time to decrease the maximum absolute pairwise correlation among up to quadratic and two-factor interaction control effector model terms was selected to compare to signals developed with different fundamental periods.

Multisine signals are orthogonal in the time domain at integer multiples of T, which might be interpreted to suggest using a multisine design with a small fundamental period. However, obtaining high-quality modeling results requires low correlation rather than zero correlation [85], meaning that good modeling results can be obtained by using a data collection time shorter than the fundamental period of the multisine signal. Also, using a larger number of frequency components provides more diverse dynamic information, which has been shown to improve modeling results [251]. Following an approach similar to Reference [85], correlation metrics were used as criteria to assess the quality of each multisine design as data collection time progresses.

As explained in Section 7.2.2, correlation between pairs of signals ($\boldsymbol{\xi}_i$ and $\boldsymbol{\xi}_j$) can be assessed using the pairwise correlation coefficient r_{ij} [Equation (2.80)]. The variance inflation factor VIF_j [Equation (7.1)] and R_j^2 metrics (see Section 7.2.2) can also be used to assess pairwise correlation. Multiple correlation between more than two inputs is quantified by the eigenvalues of $\boldsymbol{X}^T\boldsymbol{X}$ and condition number κ of $\boldsymbol{X}^T\boldsymbol{X}$ [Equation (7.2)]. The evolution of correlation metrics over time for four multisine designs with a different fundamental period is

shown in Figure 8.6. A linear and full quadratic model (every possible linear, quadratic, and

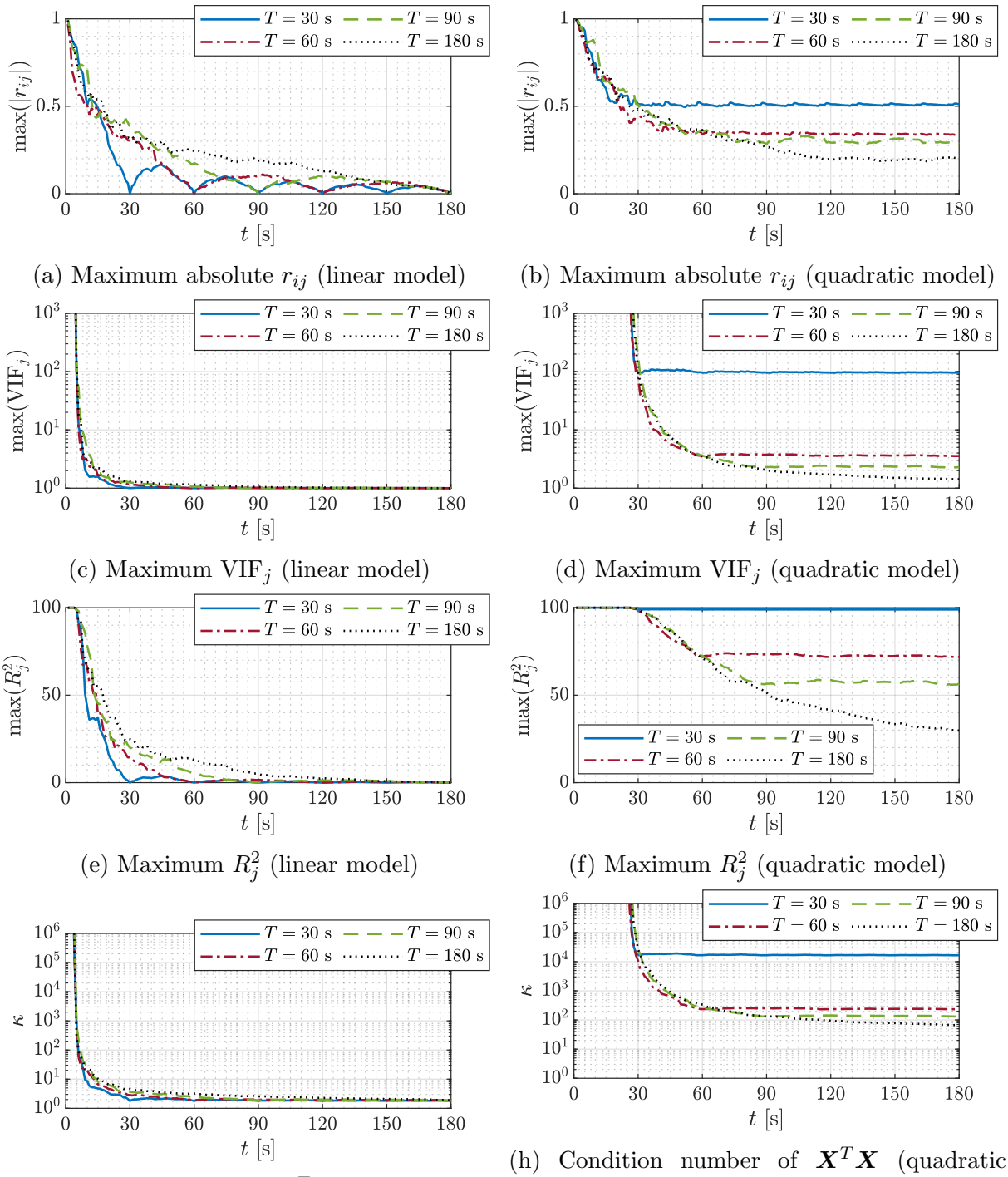

(a) Maximum absolute r_{ij} (linear model)

(b) Maximum absolute r_{ij} (quadratic model)

(c) Maximum VIF_j (linear model)

(d) Maximum VIF_j (quadratic model)

(e) Maximum R_j^2 (linear model)

(f) Maximum R_j^2 (quadratic model)

(g) Condition number of $\boldsymbol{X}^T\boldsymbol{X}$ (linear model)

(h) Condition number of $\boldsymbol{X}^T\boldsymbol{X}$ (quadratic model)

Figure 8.6: Input signal correlation metrics against time.

two-factor interaction model term) for all the control surfaces and propulsors are considered for this analysis. This represents a conservative analysis performed prior to the experiment that assumes all candidate regressors are included in the model. Many candidate model terms considered here, particularly for the full quadratic model, were expected to be excluded through model structure determination after data collection. The PTI excitations were run in a continuous loop for testing, meaning that different set points contained different portions of the full PTI signals. Consequently, the analysis here shows the highest value of each metric for time segments evaluated throughout the full duration of the periodic signal, as opposed to just from the start of the signal at $t = 0$.

Figures 8.6a and 8.6b show the maximum absolute pairwise correlation value, $\max(|r_{ij}|)$, for each multisine design as a function of time for a linear and quadratic evaluation model, respectively. The maximum correlation for each different multisine design shows a similar rate to decrease below 0.5, which is achieved in roughly 10 seconds for the linear model and roughly 25 seconds for the quadratic model. Figure 8.6a shows that the pairwise correlation values are zero at integer multiples of the fundamental period of the respective multisine design for a linear model. For the quadratic model, the correlation pairwise correlation values decrease until passing the fundamental period for the multisine design where the pairwise correlation value remains relatively constant thereafter. Multisine designs with a larger fundamental period ultimately achieve lower correlation among quadratic model regressors. Similar character is observed for the maximum VIF_j and R_j^2 variation with time shown in Figures 8.6c-8.6f. For a linear model, all multisine designs achieve a maximum VIF of less than 10 in roughly 7 seconds. For a quadratic model, the multisine designs with a longer fundamental period achieve a maximum VIF of less than 10 in roughly 40 seconds.

Figures 8.6g-8.6h show the condition number κ of $\boldsymbol{X}^T\boldsymbol{X}$ for each multisine design as a function of time. For the linear model, all multisine designs achieve a condition number of less than 100 in approximately 7 seconds at nearly the same rate and, thereafter, the condition numbers continue to decrease at a slower rate. For the quadratic model, the condition number for each multisine design is seen to decrease until reaching the fundamental period, and a nearly constant condition number is observed thereafter. The multisine designs with longer fundamental periods achieve a condition number less than 1,000 in roughly 40 seconds. Again, this analysis assumes that all candidate regressors are included in the model. If a subset of the model terms is selected for the model, then the condition number is typically reduced.

The overall takeaway from Figure 9.2 is that multisine designs with different fundamental periods reduce correlation metric values at a similar rate up to the respective fundamental period of each design. Also, multisine designs with longer fundamental periods obtain lower correlation metrics over time for a quadratic model. Informed by these time-dependent correlation analysis results and previous research showing the benefits of increased frequency resolution [251], the multisine design with the largest fundamental period ($T = 180$ seconds) was selected to be used for the wind-tunnel experiment.

The input spectra for the final set of orthogonal phase-optimized multisine signals with a fundamental period of $T = 180$ seconds is shown in Figure 8.7. There are 308 total harmonic components, with 16 frequencies assigned to each propulsor and 18 frequencies assigned to each control surface in an alternating manner. The overall frequency range is between $f_{\min} = 0.05$ Hz and $f_{\max} = 1.756$ Hz with a frequency resolution of $\Delta f = 1/T = 0.00556$ Hz. The input spectra plot shows that the propulsor harmonic components are in a lower frequency range, reflecting that the input excitations were designed to be within the bandwidth of the propulsion system. Figure 8.8 shows the first 20 seconds of the input excitation signals normalized to have a maximum absolute value of one. The RPF values for the propulsor inputs were below 1.32 and the RPF values for the control surface inputs were below 1.60. A gain is applied to scale each input signal to a sufficient amplitude to obtain a good signal-to-noise ratio for model identification.

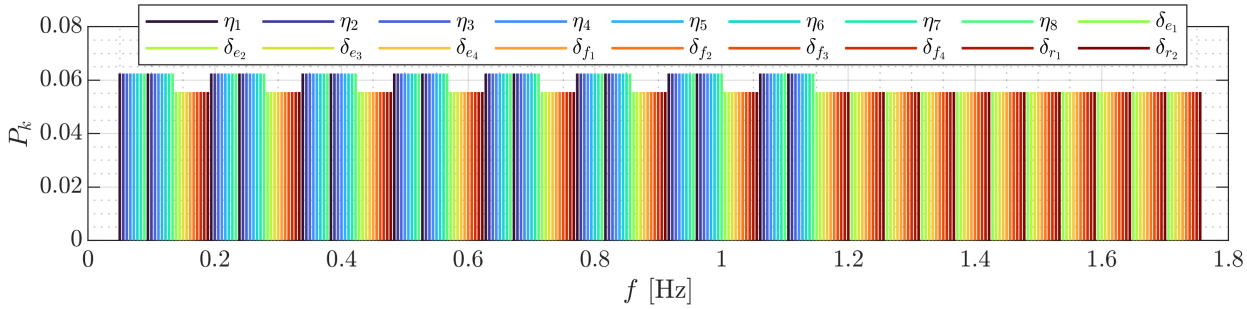

Figure 8.7: Multisine input spectra for the LA-8 control effectors.

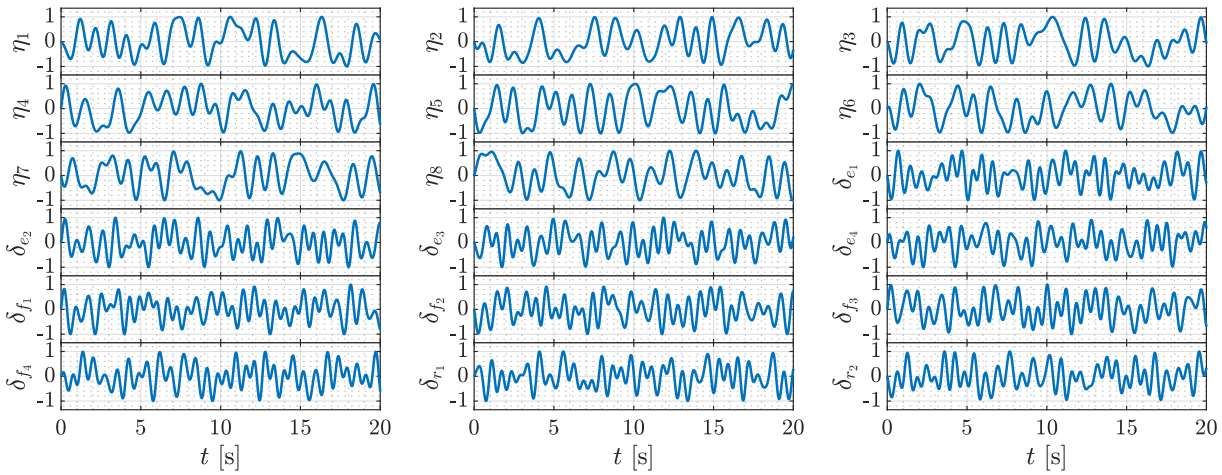

Figure 8.8: Normalized multisine inputs for the LA-8 control effectors.

8.3 Data Collection and Signal Processing

The experiment described in the previous section was executed at the NASA Langley 12-Foot Low-Speed Tunnel [230] (described in Section 6.3). The static test points, consisting of α, β, δ_{w_1}, and δ_{w_2} settings, were run using an automated data collection procedure developed for previous testing using DOE/RSM techniques [46, 219]. The PTI excitations for control surface and propulsor commands were run in a continuous loop while traversing through the static test matrix, but data were only collected at each static test point. Experiments used for this chapter were executed at a dynamic pressure of 3.5 psf (freestream airspeed of 54.3 ft/s at standard sea-level conditions), with the test factor ranges shown in Table 8.2. This condition represents a high-speed transition phase of flight for the LA-8 aircraft. Note that multiple dynamic pressure settings need to be tested to develop a full-envelope aero-propulsive model.

Table 8.2: Test factor ranges at $\bar{q} = 3.5$ psf ($V = 54.3$ ft/s)

Factor(s)	Units	Minimum	Maximum
α	deg	-6	$+6$
β	deg	-5	$+5$
$\delta_{w_1}, \delta_{w_2}$	deg	0	$+25$
$\delta_{e_1}, \delta_{e_2}, \delta_{e_3}, \delta_{e_4}$	deg	-15	$+15$
$\delta_{f_1}, \delta_{f_2}, \delta_{f_3}, \delta_{f_4}$	deg	0	$+20$
$\delta_{r_1}, \delta_{r_2}$	deg	-15	$+15$
$\eta_1, \eta_2, ..., \eta_8$	μs	1400	1500

Data collected for model identification included sting orientation, control surface deflection angles, propulsor rotational speeds, and applied forces and moments. The six force and moment components were measured using a strain gage balance, and a propeller rotational speed measurement was provided by the ESC. Direct control surface position measurements were not available, so a calibration curve was developed for each control surface to convert the desired deflection angles to commanded PWM signal values for testing. Data were collected at a sample rate of 50 Hz for 60 seconds at each static test point, with less overall time expected to be needed for model identification.

The dynamic nature of the data used for this study required multiple signal processing steps to condition the data for model identification. First, the propulsor speed and control surface deflection angle signals were found to have a time lag relative to the force and moment measurements. The time lag was determined by finding the peak of the cross-correlation function between the control surface and propulsor signals and the dominant force or moment component where the control effects manifested. The cross-correlation was computed using data collection runs executed with a reduced number of control effectors being dynamically excited to clarify time lag estimation. After determining the time lag,

time skew corrections were made for the signals used for model identification.

The force and moment signals were also found to contain significant measurement noise and suspected structural modes. An analog sixth-order low-pass Butterworth anti-alias filter with a cutoff frequency of 10 Hz was applied to the balance measurements prior to sampling. Nonetheless, residual frequency content outside of the excitation frequencies was observed in the data. To mitigate these effects, the model identification from the dynamic data was performed using only information content contained in the dynamic excitation frequency range, as will be discussed further in Section 8.4. For time-domain model validation, data were smoothed using a zero phase-shift digital filtering technique using the `filtfilt` function in MATLAB® [90], with a digital sixth-order low-pass Butterworth filter with a cutoff frequency of 3.1 Hz applied both forward and backward in time [94]. The cutoff frequency was selected to preserve lower frequency information associated with the control effector excitation frequencies, but reject most higher frequency noise. The frequency response of the zero phase-shift digital smoother is shown in Figure 8.9 (phase is not shown because it is zero across the frequency range). The linear magnitude at 1.756 Hz (the highest PTI excitation frequency) is greater than 0.999 and −20 dB attenuation is achieved at 3.7 Hz.

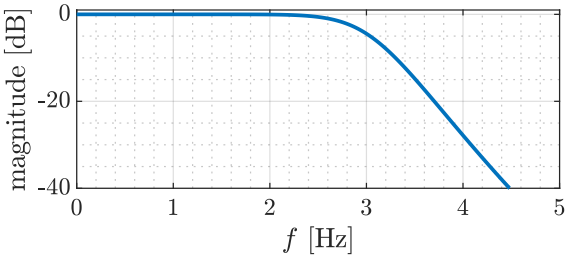

Figure 8.9: Frequency response for the zero phase-shift digital low-pass Butterworth smoother.

Sample measured and smoothed force and moment data in the time and frequency domain are shown in Figures 8.10-8.11. The power spectra shown in Figure 8.11 were computed using Welch's method with the `pwelch` MATLAB® function available in the MathWorks® Signal Processing Toolbox [90]. The power spectra of the original force and moment measurements show evidence of structural modes and measurement noise above the PTI excitation frequencies, which are avoided by only performing model identification using the frequency band corresponding to the control effector excitation frequencies, indicated by the shaded areas on the plot. The figures also show that the smoother suppresses the structural modes and measurement noise above the PTI excitation frequencies while preserving the lower-frequency information attributed to the dynamic excitation inputs.

Furthermore, the reaction torque effects in the rolling and yawing moment signals must be accounted for because the propulsors are being dynamically excited [37]. The combination of aero-propulsive moments and moments due to the angular momentum rate of the propulsors

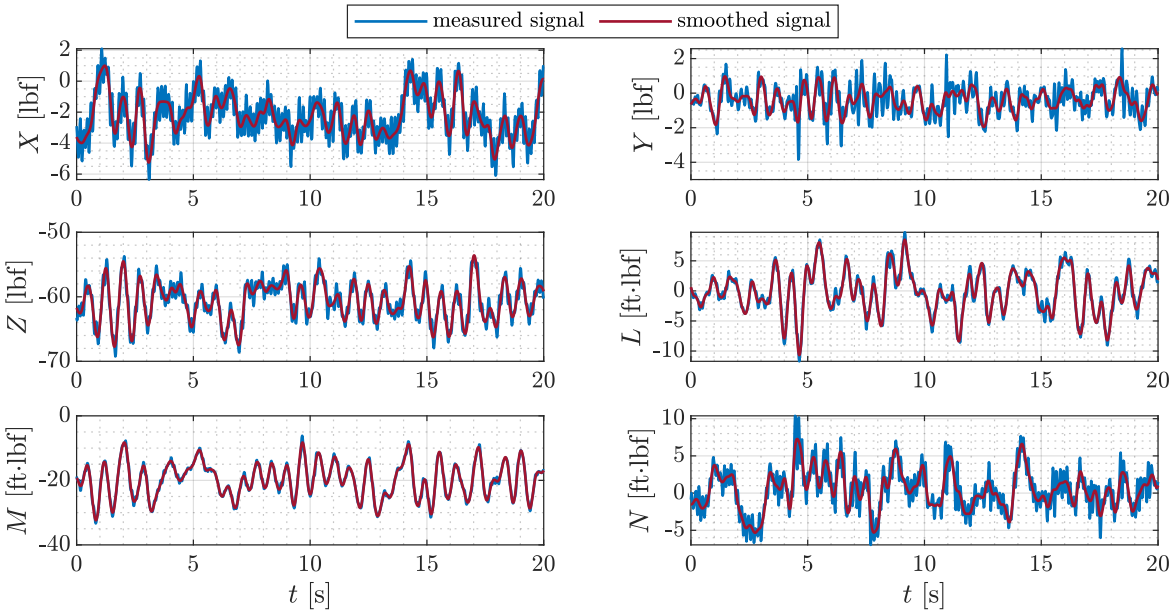

Figure 8.10: Sample balance force and moment measurement histories ($v = w = 0$ ft/s, $\delta_{w_1} = \delta_{w_2} = 12.5$ deg).

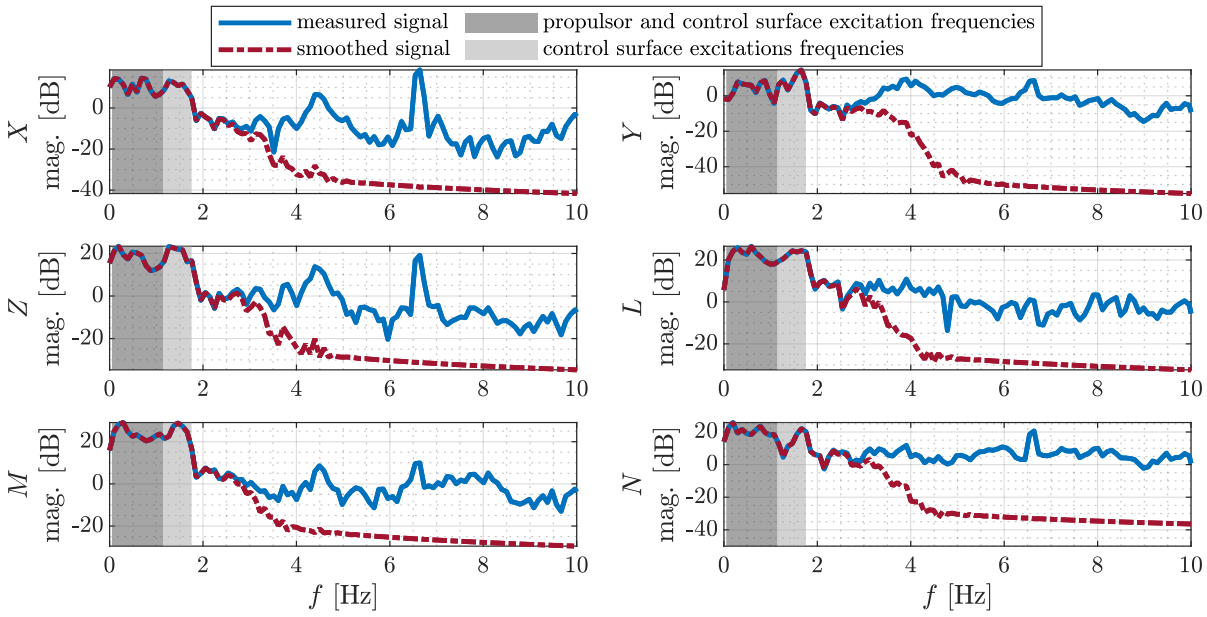

Figure 8.11: Sample balance force and moment measurement power spectra ($v = w = 0$ ft/s, $\delta_{w_1} = \delta_{w_2} = 12.5$ deg).

is measured by the balance. Therefore, to model the aero-propulsive moments, the angular

momentum rate effects must be removed. This is accomplished using the expressions

$$L = L_E + \dot{h}_x = L_E + \sum_{k=1}^{n_p} \dot{h}_{p_k} \cos\delta_{w_k} = L_E + \sum_{k=1}^{n_p} I_{p_k} \dot{\Omega}_{p_k} \cos\delta_{w_k} \tag{8.1}$$

$$N = N_E + \dot{h}_z = N_E + \sum_{k=1}^{n_p} \dot{h}_{p_k}(-\sin\delta_{w_k}) = N_E + \sum_{k=1}^{n_p} I_{p_k} \dot{\Omega}_{p_k}(-\sin\delta_{w_k}) \tag{8.2}$$

where L_E and N_E are the uncorrected balance measurements. The angular momentum of the kth propulsor about its axis of rotation is $h_{p_k} = I_{p_k}\Omega_{p_k}$, where I_{p_k} is the moment of inertia of the rotating portion of the propulsor and $\Omega_{p_k} = 2\pi n_k$ is the rotation rate in radians per second, with clockwise rotation when viewed from behind the rotating propulsor being positive. For use in the above equations, the angular momentum rate for each propulsor is rotated into the aircraft body axes through the corresponding wing angle δ_{w_k}, and then summed to compute the components of net angular momentum rate for all n_p propulsors ($\dot{h}_x$, $\dot{h}_z$). Note that if the vehicle orientation was dynamically changing during data collection, propulsor gyroscopic effects would also need to be taken into account.

8.4 Aero-Propulsive Modeling Approach

Similar to Chapters 6-7, aero-propulsive modeling for this effort focuses on developing a polynomial representation of the aero-propulsive forces and moments as a function of vehicle state and control variables. However, a different model parameterization and identification approach is needed to properly create a model from the wind-tunnel data collected using the techniques described in Sections 8.2-8.3. Following the justification given in Chapter 6, the modeled responses are the dimensional body-axis aero-propulsive forces X, Y, Z in lbf and moments L, M, N in ft·lbf. Likewise, the explanatory variables are defined as the body-axis velocity components v, w in ft/s; propeller speeds $n_1, n_2, ..., n_8$ in revolutions per second; wing angles $\delta_{w_1}, \delta_{w_2}$ in radians; elevon deflections $\delta_{e_1}, \delta_{e_2}, \delta_{e_3}, \delta_{e_4}$ in radians; flap deflections $\delta_{f_1}, \delta_{f_2}, \delta_{f_3}, \delta_{f_4}$ in radians; and ruddervator deflections $\delta_{r_1}, \delta_{r_2}$ in radians. Note that it is important to perform modeling with explanatory variables centered on a reference value to maintain low correlation among candidate regressors in time or spatial domain analysis and to avoid spectral leakage in frequency-domain analysis [100]. For this work, the centering reference values were the explanatory variable mean values in the data used for modeling.

The following subsections provide an overview of the methods used for model structure development, parameter estimation, and model validation. The model identification approach occurs in two stages. First, the continuous time series data at each static test point, or set point, are analyzed using frequency-domain methods to determine the model structure and parameter estimates associated with the dynamically changing explanatory variables (n_1, n_2, ..., n_8, δ_{e_1}, δ_{e_2}, δ_{e_3}, δ_{e_4}, δ_{f_1}, δ_{f_2}, δ_{f_3}, δ_{f_4}, δ_{r_1}, δ_{r_2}) using the aero-propulsive

force and moments (X, Y, Z, L, M, N) as the response variables. Then, in the second step, the parameter estimates for the models identified from the dynamically changing explanatory variables become the responses to be modeled as a function of the static explanatory variables (v, w, δ_{w_1}, δ_{w_2}). Model structure determination and parameter estimation are performed in a weighted least-squares formulation using the parameter uncertainty estimates from the first model identification step. This framework ultimately yields a two-layer model to predict the aero-propulsive force and moments as a function of the static and dynamic explanatory variables, as will be explained further throughout the remainder of the chapter.

To the best knowledge of the author, this chapter (first published in Reference [30]) presents the first development and application of a compound modeling strategy leveraging frequency-domain and weighted least-squares regression methods for model structure determination to combine the static and dynamic data information content for aggregate model identification. Previous work presented in References [247, 248] implemented a similar two-layered aerodynamic modeling approach using time-domain ordinary least-squares regression methods. Reference [140] developed a global aerodynamic model using a tabulated representation of local parameters estimated using the same frequency-domain equation-error method used in this work.

8.4.1 Step I: Frequency-Domain Modeling at Each Set Point

The first step in the modeling process involves analyzing the continuous time series data collected during each individual set point. As mentioned in Section 8.3, the sampled data contained measurement noise and structural dynamics outside of the range of the PTI excitations. Fortunately, as discussed in Section 2.6.1.2, application of frequency-domain estimation techniques allows model identification to be performed only in the frequency band associated with the input excitations, which effectively smooths the modeling data [19, 70, 100]. Model identification was performed using the equation-error method formulated in the frequency domain [19, 100] (see Section 2.6.1.2). For this study, the transform frequency range was selected to match the excitation input design with a fundamental period of $T = 180$ s (see Section 8.2.2). The Fourier transform frequencies were set between $f_{\min} = 0.05$ Hz and $f_{\max} = 1.756$ Hz with a frequency resolution of $\Delta f = 0.00556$ Hz, resulting in $M = 308$ transform frequencies. A parameter sensitivity study indicated that using a finer frequency resolution relative to the input design provided minimal additional parameter estimation accuracy, and it is expected that using a frequency resolution coarser than the input design will degrade parameter estimation accuracy.

MOF modeling [19, 102] applied in the frequency domain [100, 107, 108], described in Sections 2.6.2.1 and 2.6.2.3, was used as the model structure identification technique for this work. After the orthogonal regressors were ranked by their ability to reduce the MSFE, the cutoff for model term addition was chosen to be the candidate model term where the PSE was minimized. For this work, MOF modeling was applied separately to the time series data

collected at each individual set point. Although the model structure determined for each response at each set point was similar, there were some differences due to the experimental nature of the study and having a rough estimate of $\sigma^2_{\max}$. The model structure for each individual response used to identify the final model parameter estimates at each set point was constrained to be the same. The model terms selected for the final model for each response were the terms that the MOF algorithm included in the model for a majority of the set points.

After determining the model structure for each response, the final parameter values were estimated using ordinary least-squares regression with the complex regressor and response data. Then, for each response, the bias parameter estimate was found in the time domain and the bias parameter standard error was estimated accounting for colored residuals [19, 99].

8.4.2 Step II: Weighed Least-Squares Aggregate Modeling

The results from Step I of the model identification yield parameter estimates and uncertainty estimates associated with the dynamic explanatory variables at each set point. Step II of the model identification procedure developed for this work uses the Step I modeling results to develop a response surface model for each parameter identified in Step I as a function of the static explanatory variables held constant at each set point. Contrary to Step I, the explanatory and response variable data for this step are real and have no meaningful time dependence. Also, each response data point has an associated uncertainty estimate accurately determined using the methods implemented in Step I. This suggests using a weighted least-squares framework for identification of the model structure and parameter estimates. The weights are stored in a diagonal matrix $\boldsymbol{W}$ with the diagonal elements being the inverse of the variance associated with each response observation (i.e., the uncertainty estimates obtained using the methods described in Section 8.4.1):

$$\boldsymbol{W} = \begin{bmatrix} w_1 & 0 & \dots & 0 \\ 0 & w_2 & \dots & 0 \\ \vdots & \vdots & \ddots & \vdots \\ 0 & 0 & \dots & w_N \end{bmatrix} = \begin{bmatrix} 1/s_1^2 & 0 & \dots & 0 \\ 0 & 1/s_2^2 & \dots & 0 \\ \vdots & \vdots & \ddots & \vdots \\ 0 & 0 & \dots & 1/s_N^2 \end{bmatrix} \tag{8.3}$$

The MOF modeling algorithm [19, 102] (see Section 2.6.2.1), is again used for model structure determination in Step II of model identification; however, certain modifications are needed to accommodate the fact that the variance estimates associated with each response measurement are known and not constant, which leads to a weighted least-squares estimation problem. First, after generation of the candidate regressors, but before orthogonalization, the candidate regressors and response data for each data point are multiplied by the square root of the diagonal elements of the diagonal weight matrix $\boldsymbol{W}$, or the inverse of the estimated

standard error at each data point, as:

$$\boldsymbol{X}'' = \begin{bmatrix} \sqrt{w_1}\, x_{11} & \sqrt{w_1}\, x_{12} & \dots & \sqrt{w_1}\, x_{1p} \\ \sqrt{w_2}\, x_{21} & \sqrt{w_2}\, x_{22} & \dots & \sqrt{w_2}\, x_{2p} \\ \vdots & \vdots & \ddots & \vdots \\ \sqrt{w_N}\, x_{N1} & \sqrt{w_N}\, x_{N2} & \dots & \sqrt{w_N}\, x_{Np} \end{bmatrix} = \begin{bmatrix} x_{11}/s_1 & x_{12}/s_1 & \dots & x_{1p}/s_1 \\ x_{21}/s_2 & x_{22}/s_2 & \dots & x_{2p}/s_2 \\ \vdots & \vdots & \ddots & \vdots \\ x_{N1}/s_N & x_{N2}/s_N & \dots & x_{Np}/s_N \end{bmatrix} \tag{8.4}$$

$$\boldsymbol{z}'' = \begin{bmatrix} \sqrt{w_1}\, z_1 \\ \sqrt{w_2}\, z_2 \\ \vdots \\ \sqrt{w_N}\, z_N \end{bmatrix} = \begin{bmatrix} z_1/s_1 \\ z_2/s_2 \\ \vdots \\ z_N/s_N \end{bmatrix} \tag{8.5}$$

Recall that the response variable data in this step are the model parameter estimates from the frequency-domain modeling performed at each set point in Step I. Additionally, the PSE expression is reformulated as:

$$\text{PSE} = \frac{1}{N} (\boldsymbol{z} - \hat{\boldsymbol{y}})^T \boldsymbol{W} (\boldsymbol{z} - \hat{\boldsymbol{y}}) + c\frac{p}{N} \tag{8.6}$$

Here, the weight matrix $\boldsymbol{W}$ serves as a model-independent error variance estimate. Due to the scaling by $\boldsymbol{W}$, the response measurement error variance $\hat{\sigma}$ is equal to one. Thus, inclusion of the scale factor $c = c\hat{\sigma}^2 = \sigma^2_{\max}$ is a similar concept to the scale factor used in References [254, 255] when a model-independent measurement error variance estimate was available from wind-tunnel testing. A value of $c = 10$ was found to be a good value to develop models with minimum prediction error.

After determining the model structure for each response, weighted least-squares regression is used to compute the final parameter estimates in ordinary regressor space. Weighted least-squares regression estimates a vector $\boldsymbol{\theta}$ of p unknown model parameters for a given model $\boldsymbol{y} = \boldsymbol{X}\boldsymbol{\theta}$, where $\boldsymbol{y}$ is the length N model response vector and $\boldsymbol{X}$ is a $N \times p$ matrix consisting of column vectors of regressors assumed to be measured without error [19, 20, 242]. The regression equation shown in Equation (2.54) still applies, except that the measurement of the response variable $\boldsymbol{z}$ is corrupted by zero-mean, uncorrelated error $\boldsymbol{\nu}$ with *non-constant* variance. For weighted least-squares parameter estimation, the optimal estimate of the unknown parameters $\boldsymbol{\theta}$ is determined by minimizing the cost function

$$J(\boldsymbol{\theta}) = \frac{1}{2} (\boldsymbol{z} - \boldsymbol{X}\boldsymbol{\theta})^T \boldsymbol{W} (\boldsymbol{z} - \boldsymbol{X}\boldsymbol{\theta}) \tag{8.7}$$

where $\boldsymbol{W}$ is the diagonal matrix given in Equation (8.3) and each diagonal element is the inverse of the variance associated with each response data point which, here, is a parameter estimate from Step I. Consequently, response data with lower uncertainty have an increased influence for computing the least-squares solution. It follows that the solution to compute an optimal estimate of the unknown parameters is

$$\hat{\boldsymbol{\theta}} = \left(\boldsymbol{X}^T \boldsymbol{W} \boldsymbol{X}\right)^{-1} \boldsymbol{X}^T \boldsymbol{W} \boldsymbol{z} \tag{8.8}$$

where $\hat{\boldsymbol{\theta}}$ is a vector of p estimated parameters. The length p vector of standard errors $\boldsymbol{s}(\hat{\boldsymbol{\theta}})$ corresponding to the estimated parameters $\hat{\boldsymbol{\theta}}$ is given as:

$$\boldsymbol{s}(\hat{\boldsymbol{\theta}}) = \sqrt{\text{diag}\left[\left(\boldsymbol{X}^T\boldsymbol{W}\boldsymbol{X}\right)^{-1}\right]} \tag{8.9}$$

An alternative way to compute the weighted least-squares solution is to multiply each normal equation by the square root of the respective diagonal element in $\boldsymbol{W}$ (or the inverse of the measurement standard error) and then use ordinary least-squares regression to compute the parameter estimates. In other words, the same solution is obtained using $\boldsymbol{X}''$ and $\boldsymbol{z}''$ from Equations (8.4)-(8.5) in an ordinary least-squares regression estimator.

8.4.3 Final Model Validation

As discussed previously, model fit metrics and modeling residuals alone do not provide information about the model predictive capability—analysis using validation data withheld from modeling provides a more reliable estimate of model prediction accuracy. Final model validation is performed by comparing the measured response for validation data to the response predicted by the model for the same explanatory variable inputs. Further assessment is performed by analyzing the prediction residuals between the measured and predicted response, normalized residuals [Equation (6.1)], and NRMSE [Equation (2.86)]. For this study, the goal was to develop models minimizing prediction error, where a value of approximately 5% or less for NRMSE was considered to be adequate based on analyst judgment and previous aerodynamic modeling studies conducted in the experimental facility used for wind-tunnel testing.

8.5 Results

This section presents sample results for the aero-propulsive models identified for the LA-8 aircraft. The results presented here only consider models identified at $\bar{q} = 3.5$ psf, which corresponds to an airspeed of 54.3 ft/s at standard sea-level conditions. For eVTOL vehicle simulations, models valid at multiple dynamic pressure (or airspeed) settings throughout the flight envelope are needed [28, 46].

8.5.1 Step I Modeling Results

Following the aero-propulsive modeling approach described in Section 8.4, for Step I, a model structure for each force and moment component was developed using the time series data collected at each set point as a function of the dynamically changing explanatory

variables. The candidate regressors included in the model structure for a majority of the individual set point models were included in a uniform, final aero-propulsive model structure used to identify the local parameter values for each set point. In other words, only regressors modeling a significant portion of the variation in the response variables throughout the majority of the static test variable space were included, in accordance with the model structure determination strategy discussed in Section 8.4.1. The individual set point model structures for each aero-propulsive force and moment component were determined to be:

$$\begin{aligned} X = {} & X_{\delta_{e_1}}\delta_{e_1} + X_{\delta_{e_2}}\delta_{e_2} + X_{\delta_{e_3}}\delta_{e_3} + X_{\delta_{e_4}}\delta_{e_4} + X_{\delta_{f_1}}\delta_{f_1} + X_{\delta_{f_2}}\delta_{f_2} + X_{\delta_{f_3}}\delta_{f_3} \\ & + X_{\delta_{f_4}}\delta_{f_4} + X_{n_1}n_1 + X_{n_2}n_2 + X_{n_3}n_3 + X_{n_4}n_4 + X_{n_5}n_5 + X_{n_6}n_6 + X_{n_7}n_7 \\ & + X_{n_8}n_8 + X_o \end{aligned} \tag{8.10}$$

$$\begin{aligned} Y = {} & Y_{\delta_{f_1}}\delta_{f_1} + Y_{\delta_{f_2}}\delta_{f_2} + Y_{\delta_{f_3}}\delta_{f_3} + Y_{\delta_{f_4}}\delta_{f_4} + Y_{\delta_{r_1}}\delta_{r_1} + Y_{\delta_{r_2}}\delta_{r_2} + Y_{n_1}n_1 + Y_{n_2}n_2 \\ & + Y_{n_3}n_3 + Y_{n_4}n_4 + Y_{n_5}n_5 + Y_{n_6}n_6 + Y_{n_7}n_7 + Y_{n_8}n_8 + Y_o \end{aligned} \tag{8.11}$$

$$\begin{aligned} Z = {} & Z_{\delta_{e_1}}\delta_{e_1} + Z_{\delta_{e_2}}\delta_{e_2} + Z_{\delta_{e_3}}\delta_{e_3} + Z_{\delta_{e_4}}\delta_{e_4} + Z_{\delta_{f_1}}\delta_{f_1} + Z_{\delta_{f_2}}\delta_{f_2} + Z_{\delta_{f_3}}\delta_{f_3} \\ & + Z_{\delta_{f_4}}\delta_{f_4} + Z_{\delta_{r_1}}\delta_{r_1} + Z_{\delta_{r_2}}\delta_{r_2} + Z_{n_1}n_1 + Z_{n_2}n_2 + Z_{n_3}n_3 + Z_{n_4}n_4 + Z_{n_5}n_5 \\ & + Z_{n_6}n_6 + Z_{n_7}n_7 + Z_{n_8}n_8 + Z_o \end{aligned} \tag{8.12}$$

$$\begin{aligned} L = {} & L_{\delta_{e_1}}\delta_{e_1} + L_{\delta_{e_2}}\delta_{e_2} + L_{\delta_{e_3}}\delta_{e_3} + L_{\delta_{e_4}}\delta_{e_4} + L_{\delta_{f_1}}\delta_{f_1} + L_{\delta_{f_2}}\delta_{f_2} + L_{\delta_{f_3}}\delta_{f_3} \\ & + L_{\delta_{f_4}}\delta_{f_4} + L_{n_1}n_1 + L_{n_2}n_2 + L_{n_3}n_3 + L_{n_4}n_4 + L_{n_5}n_5 + L_{n_6}n_6 + L_{n_7}n_7 \\ & + L_{n_8}n_8 + L_o \end{aligned} \tag{8.13}$$

$$\begin{aligned} M = {} & M_{\delta_{e_1}}\delta_{e_1} + M_{\delta_{e_2}}\delta_{e_2} + M_{\delta_{e_3}}\delta_{e_3} + M_{\delta_{e_4}}\delta_{e_4} + M_{\delta_{f_1}}\delta_{f_1} + M_{\delta_{f_2}}\delta_{f_2} + M_{\delta_{f_3}}\delta_{f_3} \\ & + M_{\delta_{f_4}}\delta_{f_4} + M_{\delta_{r_1}}\delta_{r_1} + M_{\delta_{r_2}}\delta_{r_2} + M_{n_1}n_1 + M_{n_2}n_2 + M_{n_3}n_3 + M_{n_4}n_4 \\ & + M_{n_5}n_5 + M_{n_6}n_6 + M_{n_7}n_7 + M_{n_8}n_8 + M_o \end{aligned} \tag{8.14}$$

$$\begin{aligned} N = {} & N_{\delta_{e_1}}\delta_{e_1} + N_{\delta_{e_2}}\delta_{e_2} + N_{\delta_{e_3}}\delta_{e_3} + N_{\delta_{e_4}}\delta_{e_4} + N_{\delta_{f_1}}\delta_{f_1} + N_{\delta_{f_2}}\delta_{f_2} + N_{\delta_{f_3}}\delta_{f_3} \\ & + N_{\delta_{f_4}}\delta_{f_4} + N_{\delta_{r_1}}\delta_{r_1} + N_{\delta_{r_2}}\delta_{r_2} + N_{n_1}n_1 + N_{n_2}n_2 + N_{n_3}n_3 + N_{n_4}n_4 + N_{n_5}n_5 \\ & + N_{n_6}n_6 + N_{n_7}n_7 + N_{n_8}n_8 + N_o \end{aligned} \tag{8.15}$$

Although pure quadratic and two-factor interaction candidate regressors were considered for Step I model structure determination, the final model describing the variation of the force and moment components at each test point is linear in the dynamic explanatory variables. This makes sense because the variables were excited over a relatively small range of values. The method, however, is also capable of modeling nonlinear effects, such as propulsor-control surface interactions, which can be considered for future studies with a greater excitation range. As was found in Chapter 6 (Reference [28]), tilt-wing vehicles exhibit significant nonlinearity with body-axis velocity and wing angle variation, which is captured in the Step II model identification strategy.

Figure 8.12 shows the Z parameter estimates and error bars of $\pm 2s(\hat{\theta})$ computed using

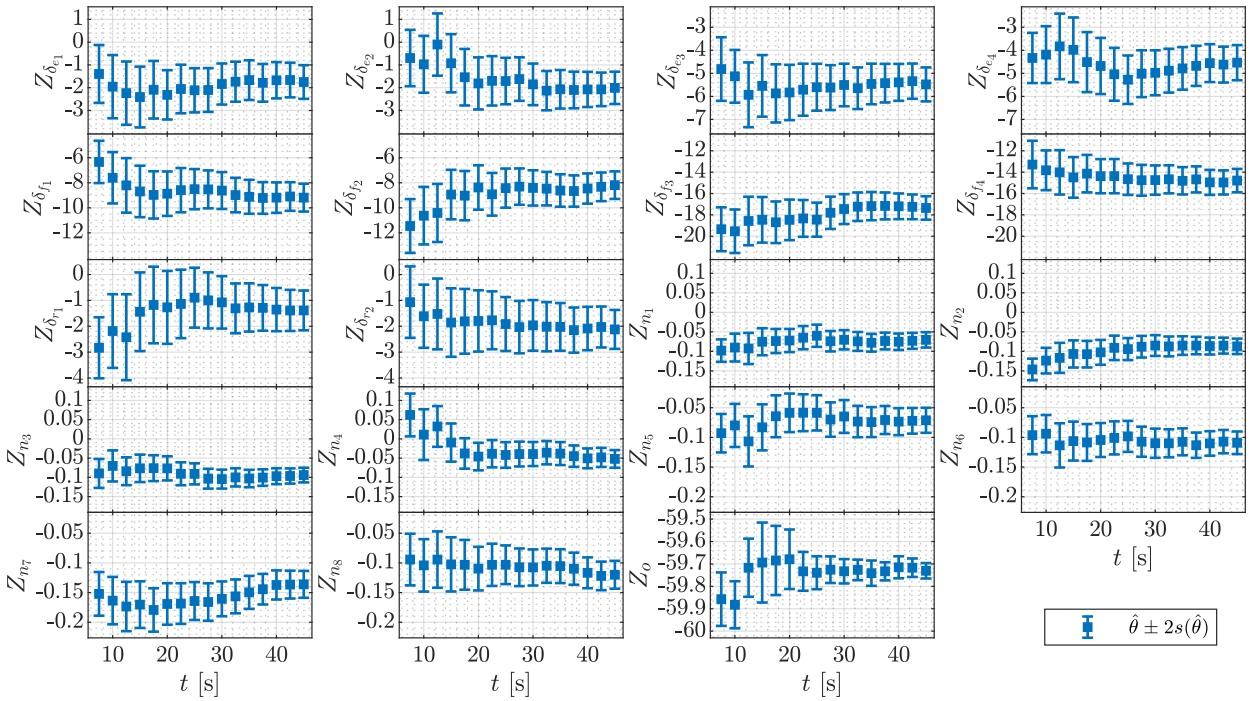

Figure 8.12: Variation of Z parameter estimates with data collection time used for modeling at a sample set point ($v = w = 0$ ft/s, $\delta_{w_1} = \delta_{w_2} = 12.5$ deg).

the parameter estimation techniques described in Section 8.4.1 against the amount of data collection time used for modeling at a sample set point. The parameters appear to converge to reasonably consistent values by the time 40 seconds has elapsed, which was also determined to be a satisfactory data collection time in a simulated flight-test system identification study for the LA-8 aircraft [32] that will be described in Chapter 9. A similar parameter convergence rate was observed for the parameters corresponding to the other aero-propulsive forces and moments, and at different set points. In view of the parameter convergence analysis shown in Figure 8.12, the findings in Reference [32],[1] and with the knowledge that 40 seconds is the amount of time needed to complete two full periods of the lowest frequency sinusoidal component of the multisine signals ($f_{\min} = 0.05$ Hz), 40 seconds was selected as the amount of data collection time to use for modeling at each set point. Although the actual data collection time at each set point was greater than 40 seconds, providing additional information for modeling, a goal of this study was to inform future wind-tunnel testing efforts with practical, efficient data collection strategies. Consequently, modeling was performed with the recommended data collection time of 40 seconds based on the present reasoning, as opposed to using all available data. Note that the parameter estimates shown in Fig-

[1]Note that the work presented in Reference [32] (Chapter 9) was chronologically completed before the work described in this chapter (Reference [30]). This is why Reference [32] is cited as justification for selection of the data collection time before presentation of the work in this dissertation.

ure 8.12 contain asymmetries that are not apparent from the LA-8 vehicle configuration, such as differences in the reflected flap parameter estimates. This is a result of manufacturing differences between the clockwise and counterclockwise propellers, which resulted in a significant difference in thrust production between the propeller variants [36]. Because the propulsion-only and propulsion-airframe interaction effects are significant, this propulsion asymmetry is manifested in many of the model terms (see Chapter 6 and Reference [28]).

Figure 8.13a shows the model fit in the frequency domain using a modeling time of 40 seconds at a sample set point. The corresponding control surface deflection and propulsor rotational speed signals are shown in Figure 8.14. A good model fit is observed for each response. The R^2 metric shown on the subplot for each response is approximately 95% or higher, indicating that most of the variation of the response variable about its mean value is characterized by the model. Figure 8.13b shows the corresponding time-domain model fit compared to the smoothed, measured aero-propulsive forces and moments. The modeled responses are close to the measured responses, indicating that the model is able to describe a large amount of the variation in each response. The modeling performance at other set points was similar.

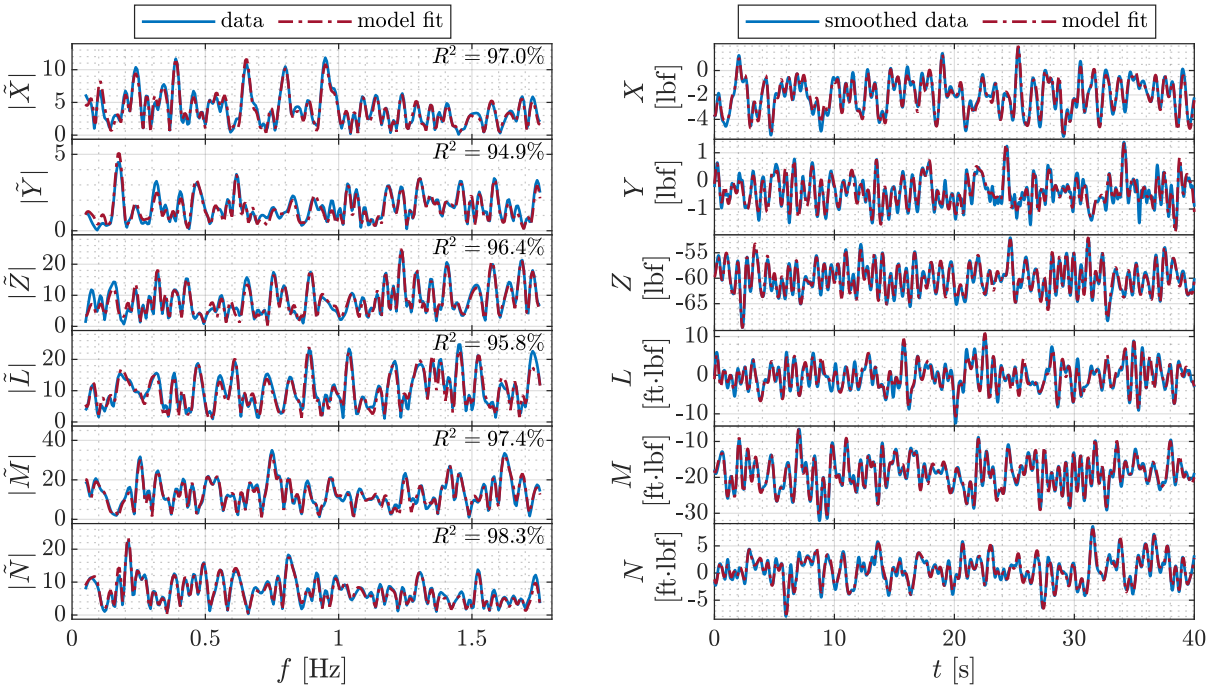

(a) Model fit in the frequency domain

(b) Model fit in the time domain

Figure 8.13: Comparison of response data and model fit at a sample set point ($v = w = 0$ ft/s, $\delta_{w_1} = \delta_{w_2} = 12.5$ deg).

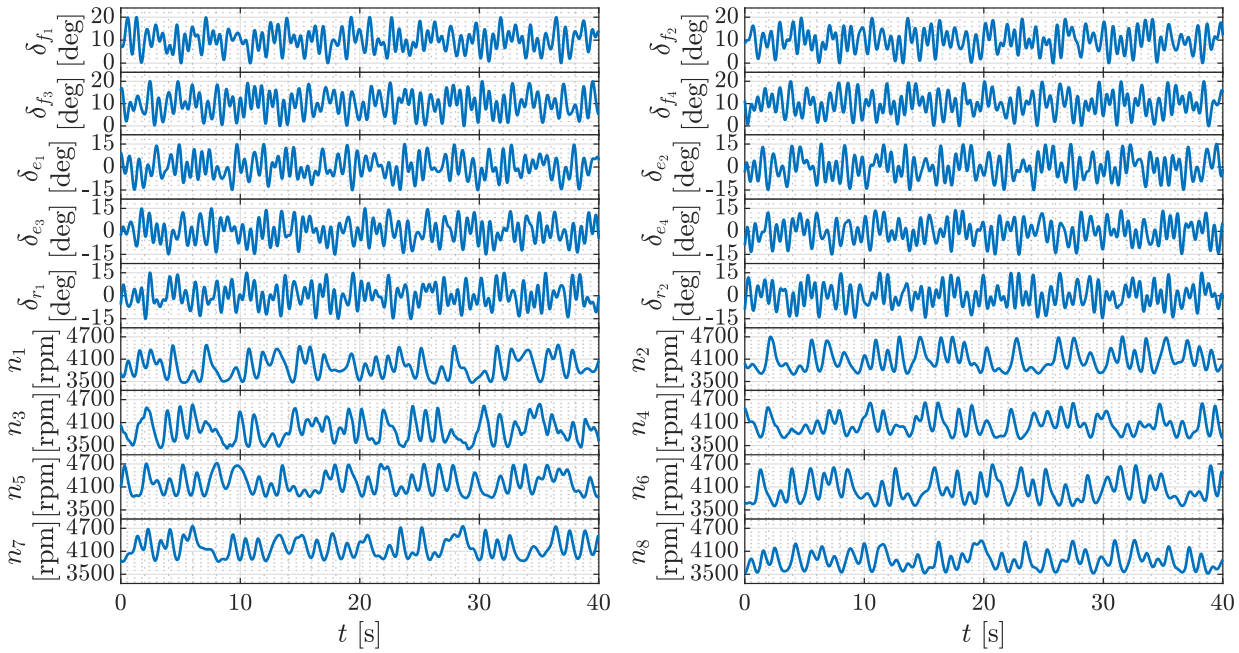

Figure 8.14: Control effector signals at a sample set point ($v = w = 0$ ft/s, $\delta_{w_1} = \delta_{w_2} = 12.5$ deg).

8.5.2 Step II Modeling Results

After identification of the model parameters associated with the dynamic explanatory variables at each set point, models were developed to characterize the variation in those model parameters across the static variable space. As discussed in Section 8.4.2, the parameter estimates associated with the dynamic explanatory variables were treated as the response variables for Step II of the modeling approach. In Step II, the static test variables associated with each set point (v, w, δ_{w_1}, δ_{w_2}) were the explanatory variables. The models for each Step II response variable were developed using weighted least-squares regression techniques because uncertainty estimates for each response variable data point were available from the Step I parameter estimation results.

As an example of a polynomial model structure developed in this modeling stage, the final model structure identified for $Z_{\delta_{f_1}}$ using MOF modeling in a weighted least-squares formulation was:

$$Z_{\delta_{f_1}} = Z_{\delta_{f_1}(w)} w + Z_{\delta_{f_1}(\delta_{w_1})} \delta_{w_1} + Z_{\delta_{f_1}(w\delta_{w_1})} w\delta_{w_1} + Z_{\delta_{f_1}(\delta^2_{w_1})} \delta^2_{w_1} + Z_{\delta_{f_1}(o)} \tag{8.16}$$

The bias parameters (e.g., Z_o) had the largest number of model terms because they characterize the direct effects of the static explanatory variables on the aero-propulsive forces and

moments. For example, a model structure identified for the Z_o model was:

$$Z_o = Z_{o_{(w)}} w + Z_{o_{(v)}} v + Z_{o_{(\delta_{w_1})}} \delta_{w_1} + Z_{o_{(\delta_{w_2})}} \delta_{w_2} + Z_{o_{(w^2)}} w^2 + Z_{o_{(wv)}} wv + Z_{o_{(v^2)}} v^2 + Z_{o_{(w\delta_{w_1})}} w\delta_{w_1} + Z_{o_{(\delta^2_{w_1})}} \delta^2_{w_1} + Z_{o_{(w\delta_{w_2})}} w\delta_{w_2} + Z_{o_{(\delta_{w_1}\delta_{w_2})}} \delta_{w_1}\delta_{w_2} + Z_{o_{(\delta^2_{w_2})}} \delta^2_{w_2} + Z_{o_{(o)}} \quad (8.17)$$

For use of the final model equations to predict the aero-propulsive forces and moments as a function of all static and dynamic explanatory variables, each of the models identified in Step II are used to compute the values of the parameters in Equations (8.10)-(8.15) as a function of the centered static explanatory variables (v, w, δ_{w_1}, δ_{w_2}). Then, the total aero-propulsive forces and moments are computed using the Equations (8.10)-(8.15) polynomial expressions as a function of the centered dynamic explanatory variables (n_1, n_2, ..., n_8, δ_{e_1}, δ_{e_2}, δ_{e_3}, δ_{e_4}, δ_{f_1}, δ_{f_2}, δ_{f_3}, δ_{f_4}, δ_{r_1}, δ_{r_2}).

Several models were developed to explore the utility of using a different number of modeling blocks and different model complexities. The same general modeling approach was used for each model, with the only difference being the data volume associated with the sequential blocks of static test points described in Section 8.2.1. Figure 8.15 shows the modeling NRMSE (NRMSE_m), the validation NRMSE (NRMSE_v), and the cumulative execution time for each block (including the data collection time from all preceding blocks) with a different model complexity determined based on the analysis presented in Section 8.2.1 and with the knowledge that at least quadratic model, or up to pure quadratic and two-factor interaction model terms, are needed to model the LA-8 aircraft over the static explanatory variable range tested for this study (see Chapter 6 and Reference [28]). Consequently, up to a quadratic model is used for Block 1, even though the model evaluation metrics do not meet the FDS criteria explained in Section 8.2.1. Blocks 2-4 are assigned the highest model complexity meeting the FDS criteria for this comparison (see Table 8.1 and the accompanying discussion). The test execution time shown in Figure 8.15b indicates the amount of time needed to complete the data collection with a sample time of 40 seconds per set point, including the

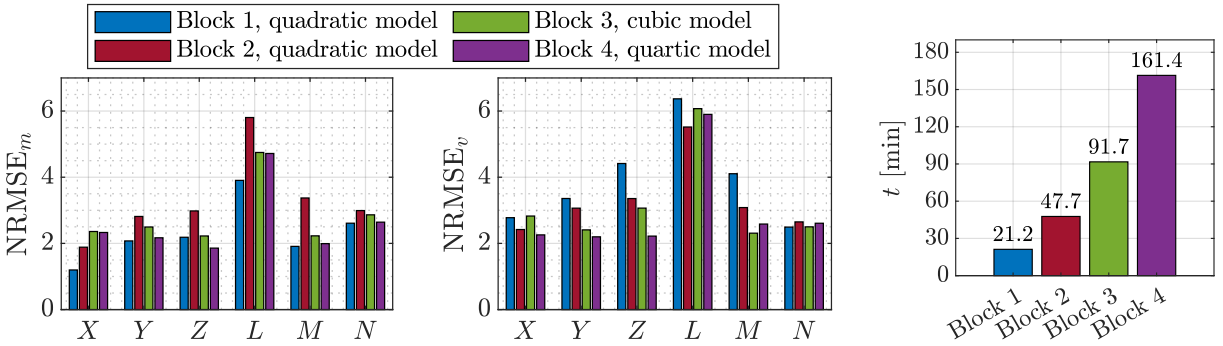

(a) Modeling and validation NRMSE

(b) Cumulative test time

Figure 8.15: Comparison of NRMSE metrics and test time for each modeling block with different model complexity.

amount of time to conduct a static tare run. Block 1 generally has the highest validation NRMSE value for each response; there is also a significant increase in the values of the validation NRMSE compared to the modeling NRMSE for the Block 1 model, suggesting that the model is deficient due to the sparsity of data points. For the X, Y, and Z responses, the Block 4 model has the lowest prediction error. For L and M, the Block 2 and Block 3 models, respectively, have the lowest prediction error. The prediction error for N is similar for each number of modeling blocks. For the Block 2 to 4 models, the respective modeling NRMSE and validation NRMSE for each response have similar values, which provides confidence that model development was successful.

Balancing prediction performance, test execution time, and model parsimony, using data up to Block 2 (a cubic design order) with a quadratic model complexity was selected as the final modeling strategy. Given these results, it is recommended to use a cubic I-optimal experiment design with up to a quadratic polynomial structure for modeling similar aircraft over a similar range of test variables. For the Block 2 quadratic model, the prediction error, quantified by the NRMSE_v metric, is less than 6% for every response, and X, Y, Z, M, and N have NRMSE_v values of approximately 3% or less, indicating that high-quality models have been developed.

Figure 8.16a shows the model fit and model prediction compared to the smoothed, measured aero-propulsive force and moment histories. Figure 8.16b shows the same plot zoomed in on a single validation set point, which better conveys the dynamic prediction capability. The model fits and model predictions are close to the measured responses, indicating that the model is able to describe a large amount of the variation in each response. Figure 8.17 shows a history of normalized modeling residuals and normalized validation residuals. The modeling and prediction residuals have similar magnitudes, supporting the claim that good predictive models have been identified.

8.6 Discussion

The preceding results show that good models have been identified for the LA-8 eVTOL aircraft using the hybrid testing and compound modeling approach developed in this chapter. Furthermore, the final aero-propulsive model at $\bar{q} = 3.5$ psf was developed from a total of 48 minutes of test execution time. If the test technique and modeling approach were to be applied to model the LA-8 transition envelope by executing testing and developing models at several dynamic pressure settings (see Chapter 6 and References [28, 46]), then a global transition model could be developed in a single day of wind-tunnel testing. This approach is significantly faster than previous testing conducted to characterize the LA-8 aircraft using purely static DOE/RSM testing, which was already vastly more efficient compared to using OFAT testing (see Section 7.1). The amount of test time needed for modeling data collection and tare runs for a purely static DOE/RSM wind-tunnel experiment to develop aero-propulsive models at $\bar{q} = 3.5$ psf described in Chapter 6 (Reference [28]) took

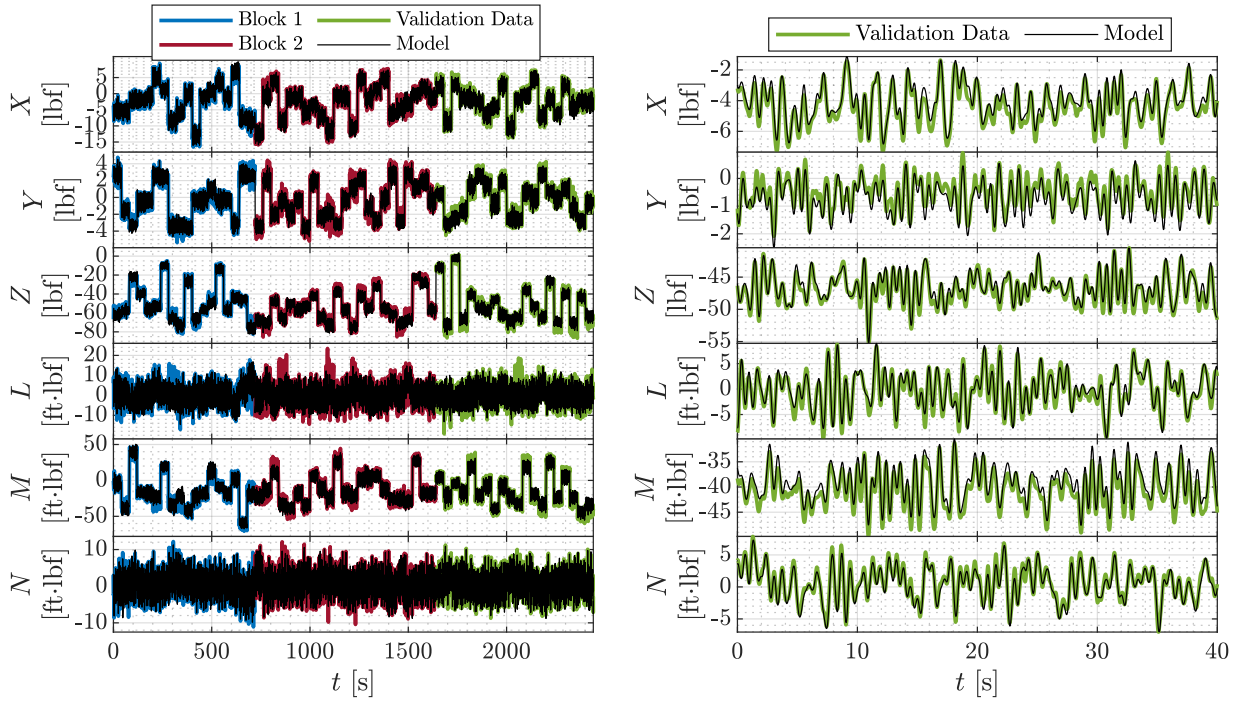

(a) Modeling and validation data (two blocks used for model identification)

(b) Sample validation set point

Figure 8.16: Model fit and model prediction compared to smoothed, measured response data.

approximately 267 minutes (4.45 hours). The hybrid DOE/RSM and PTI wind-tunnel test technique described in this chapter is 5.6 times more efficient in terms of test execution time for the data used to develop the model. Note that the models developed in Chapter 6 (Reference [28]) included additional quadratic and interaction model terms for the control effectors; however, that is largely because of the reduced range of excitation for those variables in this study. The control effector amplitude used for the results presented in this chapter could be increased without requiring additional test time.

In addition to reduced test time, the models developed using the approach presented in this chapter allow characterization of additional important aero-propulsive phenomena for tilt-wing aircraft. The tilting wings add significant modeling challenges not seen in conventional aircraft designs because the propellers, wings, and wing-fixed control surfaces all change orientation with respect to the modeling frame of reference in the body axes. Furthermore, there will also be interactions with the magnitude and orientation of oncoming airflow, suggesting that up to four-factor interactions may be present among the explanatory variables. As was mentioned in Section 6.5, one way of handling this complexity is to develop a different aero-propulsive model at each combination of wing angle settings, treating each different combination of wing angle orientation as a vehicle configuration change. This method would be ideal when a transition wing angle schedule has been defined; however,

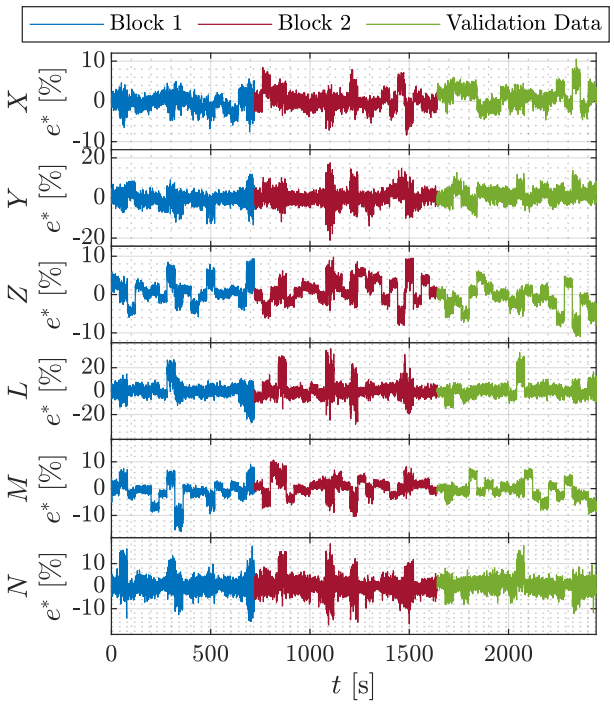

Figure 8.17: Normalized modeling and prediction residuals against time.

this is impractical when the identified aero-propulsive model is used to develop the flight controller and informs the transition wing angle schedule. In Chapter 6 (Reference [28]), the propeller, control surface, wing, and airflow interactions were modeled using only two-factor interaction effects and were limited by the purely static DOE/RSM testing strategy. Alternatively, the experiment design and compound modeling strategy developed in this chapter supports modeling additional interactions among the explanatory variables. This is possible because of the way the model parameters associated with the dynamic test variables are modeled as a function of the static test variables.

As an example of how the compound modeling approach supports characterization of additional complexity, consider Equation (8.16), where $Z_{\delta_{f_1}}$ is modeled as a function of w and δ_{w_1} including variation with a $w\delta_{w_1}$ interaction and a $\delta_{w_1}^2$ quadratic term. Note that these are effectively cubic model terms because of the multiplication of the $Z_{\delta_{f_1}}$ parameter by δ_{f_1}. For a static DOE/RSM experiment supporting up to a quadratic model, the only model terms involving w and δ_{w_1} that could model an interaction with δ_{f_1} are $\delta_{f_1}w$ and $\delta_{f_1}\delta_{w_1}$. Suppose also that a larger range of the dynamic test variables were tested and the interaction term $n_2\delta_{f_1}$ was included in the Step I model. Then, by the same process, the $n_2\delta_{f_1}$ interaction could be modeled as a function of w and δ_{w_1} including nonlinear model terms. This additional parameterization flexibility enabled by the testing and modeling approach described herein provides significant benefits to modeling complex eVTOL aircraft. Furthermore, the range of each static explanatory variable, determined as described in Reference [46], could

be increased to model a larger range of aero-propulsive phenomena. This might require additional design complexity beyond the Block 2 cubic experiment design order, but this increase in static experiment design complexity could be accommodated with only modest increases in the amount of test time (cf. Figure 8.15b) while allowing characterization of a broader range of flight conditions and aero-propulsive complexity using the same model identification framework.

When using the modeling approach developed in this chapter, a few limitations and drawbacks should be considered. First, the models are based on a quasi-steady assumption, where aero-propulsive effects at the current point in time are only dependent on the current states and controls. Second, the data were collected in the wind tunnel with zero vehicle angular velocity, and consequently, no damping terms could be identified. Identification of models dependent on vehicle angular rates (and possibly the history of the explanatory variables) will be needed to improve model predictive capability in dynamic maneuvering. Also, integrating the PTI excitation technique into an existing wind-tunnel test facility typically requires significant time and engineering effort. After the PTI excitation capability is integrated, however, the test efficiency gains are significant. Finally, the compound model identification approach is more complex than ordinary least-squares regression analysis, which is generally used for model development from conventional static DOE/RSM experiments and is readily available in commercial statistical software packages. However, the model identification approach described in this chapter is still tractable to implement using algorithms available in SIDPAC [19, 50] to develop models leveraging the much more efficient hybrid test technique. Ultimately, the ability to develop a higher complexity aero-propulsive model and significantly reduce the amount of required test time can easily justify the steps required to implement the new approach.

Acknowledgment of Collaborative Research

The research presented in this chapter was primarily conducted by the author, but included important collaborative contributions with other individuals. Eugene Morelli provided guidance on the dynamic experiment design for the LA-8 aircraft, helped to formulate the two-layered model identification approach, and offered many helpful technical suggestions on the paper documenting the work in this chapter. Ronald Busan, Wes O'Neal, and David Hatke provided wind-tunnel test support and integrated a new capability into the NASA Langley 12-Foot Low-Speed Tunnel allowing injection of PTI excitations. Additional wind-tunnel testing and LA-8 vehicle support was provided by Gregory Howland, David North, and Steven Geuther. The author gratefully acknowledges and appreciates these contributions which made the research described in this chapter possible.

Chapter 9

Flight-Test System Identification Approach for eVTOL Aircraft

This chapter presents a flight-test system identification method for eVTOL aircraft. Employing the techniques discussed in previous chapters, the approach merges fixed-wing and rotary-wing system identification approaches with new strategies to develop a modeling method for eVTOL vehicles using flight-test data. The eVTOL aircraft system identification approach is demonstrated through application to the NASA LA-8 eVTOL aircraft using a high-fidelity flight dynamics simulation, but can be applied to future aircraft flight-test system identification efforts. Orthogonal phase-optimized multisine inputs are applied to each control surface and propulsor at numerous trimmed flight conditions throughout the flight envelope to collect informative flight data enabling aero-propulsive model identification at each condition. The local model parameters are then blended to create a global model across the nominal flight envelope. The identified models are shown to provide a good fit to modeling data with good prediction capability. The methodology is developed with a discussion of unique eVTOL vehicle aerodynamic characteristics and practical strategies intended to inform future flight-based system identification efforts for eVTOL aircraft. This work has been published as a conference paper [31] and a journal article [32].

The chapter is organized as follows: The motivation for this research is presented in Section 9.1. Section 9.2 provides an overview of the eVTOL aircraft flight dynamics simulation used to perform simulated flight testing. Section 9.3 describes the proposed eVTOL aircraft aero-propulsive modeling framework, followed by a description of the flight-test experiment design techniques needed to collect data for model identification in Section 9.4. Section 9.5 provides sample local and global modeling results.

9.1 Research Motivation

Previous research, including Chapters 6-8 in this dissertation, has investigated methods for efficient, empirical eVTOL aircraft aero-propulsive modeling across their wide flight envelopes using wind-tunnel testing [28–30, 46, 47, 137, 219]. Other related work has applied similar methods to CFD experiments [39, 48]. Based on this work, References [28, 30, 39] justified the use of eVTOL-aircraft-specific modeling procedures.

CFD aerodynamic characterization studies are advantageous because they allow analysis in early design stages, where the aircraft configuration is not yet finalized and vehicle hardware has not yet been developed. Wind-tunnel studies require a test asset, but allow efficient, high-fidelity vehicle characterization in a low-risk test environment. The disadvantages of CFD include necessary simplifying assumptions to make calculations computationally tenable and flowfield models which may not adequately reflect real flight vehicle aerodynamics, particularly for modeling complex flowfields of eVTOL aircraft. One disadvantage of wind-tunnel testing is the presence of sting and wall effects. Also, the general requirement of using subscale models for wind-tunnel testing requires using similitude relationships to scale the results, which are challenging for rotorcraft and typically limit vehicle wind-tunnel testing [144, 228].

A goal of an aircraft aerodynamic model is to accurately describe the aerodynamics in flight, which drive aircraft flight dynamic behavior. Thus, aerodynamic characterization using flight data offers the closest prediction to operational reality. This work builds on the previous chapters in this dissertation to propose a method for flight-based aero-propulsive model development. As discussed in Section 6.2, fixed-wing aircraft and rotorcraft generally follow different modeling conventions, but their system identification techniques are well-developed for standard problems and have been applied successfully to numerous aircraft configurations [19–21, 223–226].

Although eVTOL aircraft share aerodynamic characteristics overlapping with both fixed-wing and rotary-wing aircraft, system identification approaches used for either type of vehicle must be applied differently for modeling eVTOL vehicles. As highlighted previously, eVTOL aircraft aerodynamic modeling is also challenging due to the presence of many control surfaces and propulsors, propulsion-airframe interactions, high incidence angle propulsor aerodynamics, vehicle instability, rapidly changing aerodynamics through transition, and large flight envelopes with complex character that need to be described by a global aero-propulsive model. Recent system identification research for aircraft configurations with related challenges is briefly highlighted to provide context for the present work. Reference [84] describes a procedure for efficient estimation of the effectiveness of 16 different control surfaces on a dynamically-scaled model of a generic commercial transport aircraft using the equation-error method in the frequency domain. Orthogonal phase-optimized multisine signals were applied to each control surface allowing individual control derivatives to be identified simultaneously using the data from a single flight maneuver. A similar strategy was used for system identification of the X-56 aeroelastic technology demonstrator aircraft [252, 256, 257], which has 10 control surfaces on the trailing edge of the wing and two engines. A collection of different multisine signals was designed to excite the control effectors independently and in pairs for efficient model identification using frequency domain modeling methods [253]. Reference [10] describes a system identification effort for an aircraft propelled by eight distributed electric ducted fans (EDFs). Multisine signals were applied to control surfaces and throttle doublets were applied to individual EDFs to identify linear longitudinal and lateral-directional state-space models using a frequency-domain equation-error method. Nu-

merous recent studies have developed models for distributed propulsion multirotor vehicles using both time-domain and frequency-domain system identification techniques and various excitation input types exercised in flight testing [75, 128–136]. System identification for a quadrotor configuration intended for a UAM mission using simulated flight data was described in Reference [258]. Frequency sweeps were applied to each pilot control input to generate data for frequency response and state-space model identification. References [7, 9] injected orthogonal phase-optimized multisine signals to the motor commands on multirotor configurations to identify linear dynamic models. Due to vehicle instabilities, system identification for the X-56 aircraft and multirotor configurations highlighted here was performed with active feedback control.

This work proposes an aircraft system identification process tailored to eVTOL aircraft based on their unique aero-propulsive characteristics and extends global modeling techniques used in previous fixed-wing aircraft research [140]. System identification maneuvers are executed sequentially starting from trimmed flight conditions throughout transition and modeling is performed using the equation-error method in the frequency domain at each reference condition in post-flight analysis. The approach is formulated using simulated flight data, but can be applied to future flight-test system identification efforts for eVTOL aircraft.

9.2 LA-8 Flight Dynamics Simulation

The system identification approach is exercised for the LA-8 tandem tilt-wing eVTOL vehicle in a MATLAB®/Simulink® generalized UAM-class vehicle simulation developed at NASA Langley Research Center [259]. The high-fidelity simulation environment contains both common, aircraft-agnostic simulation components and aircraft-specific model components, which provides a flexible framework for algorithm development for multiple eVTOL vehicle configurations. The vehicle equations of motion, numerical integrators, and the atmospheric model are common to all vehicles. Each vehicle model, which includes the aero-propulsive model, actuator models, inertial properties, and control laws, is implemented in a modular framework to enable simultaneous assessment of multiple vehicles.

Nonlinear vehicle simulations are performed using the kinematic and dynamic aircraft equations of motion developed under a standard set of assumptions [19, 68, 72]. The aircraft is modeled as a six degree-of-freedom rigid body, treating the gyroscopic effects from the rotating portions of the propulsion system as applied external moments. Aircraft moments of inertia and center of gravity are varied through vehicle conversion, as applicable, depending on the specific vehicle. Applied forces (X, Y, Z) and moments (L, M, N) are computed using the vehicle aero-propulsive model, which includes the collective contributions of propulsion and airframe effects as well as their interactions. The translational dynamics equations are the same as those shown previously in Equations (2.7)-(2.9). The rotational dynamics equations, assuming that the vehicle is symmetric about the body x–z plane ($I_{xy} = I_{yz} = 0$)

and augmented to include propulsor gyroscopic effects, are:

$$I_x\dot{p} - I_{xz}\dot{r} = L + (I_y - I_z)qr + I_{xz}pq - (\dot{h}_x + qh_z - rh_y) \tag{9.1}$$

$$I_y\dot{q} = M + (I_z - I_x)pr + I_{xz}(r^2 - p^2) - (\dot{h}_y + rh_x - ph_z) \tag{9.2}$$

$$I_z\dot{r} - I_{xz}\dot{p} = N + (I_x - I_y)pq - I_{xz}qr - (\dot{h}_z + ph_y - qh_x) \tag{9.3}$$

The angular momentum of a single propulsor about its axis of rotation is $h_p = I_p\Omega$, where I_p is the moment of inertia of the rotating portion of the propulsor and $\Omega = 2\pi n$ is the rotation rate in radians per second, with clockwise rotation when viewed from behind the rotating propulsor being positive. For use in the above equations, the angular momentum for each propulsor is rotated into the aircraft body axes and then summed to compute the net angular momentum for all propulsors (h_x, h_y, h_z) [37]. Computing the net rate of change of angular momentum ($\dot{h}_x$, $\dot{h}_y$, $\dot{h}_z$) follows the same process. If the propulsors are operated symmetrically, their angular momentum components cancel; however, asymmetric propulsor operation necessary for system identification causes the propulsion gyroscopic effects to become significant.

The aircraft equations of motion are also augmented with additional states to represent the dynamics associated with control surface actuation and propulsor speed changes. Lag associated with the propulsors is particularly important to consider for controller design because propulsion dynamics can be significantly slower than control surface dynamics, particularly for eVTOL vehicles with fixed-pitch propellers. For this work, propulsor and control surface dynamics were modeled using first-order and second-order dynamics, respectively, representing the lag between a commanded value and an actual value. Expressed as a differential equation, these respectively take the form,

$$\tau\dot{\delta} + \delta = \delta_{\text{cmd}} \tag{9.4}$$

$$\ddot{\delta} + 2\zeta\omega_n\dot{\delta} + \omega_n^2\delta = \omega_n^2\delta_{\text{cmd}} \tag{9.5}$$

where δ is the actual value of a propulsor or control surface variable, δ_{cmd} is the corresponding commanded value, τ is the first-order time constant, ω_n is the natural frequency, and ζ is the damping ratio.

eVTOL aircraft are generally unstable in a significant portion of their flight envelope. Consequently, an active flight control system is required to fly the aircraft or perform simulation studies. Flight control system design for complex eVTOL aircraft is a major challenge for many reasons, including: inherent vehicle instability, strong aerodynamic nonlinearities, interaction effects, and ambiguous control allocation strategies due to the availability of many redundant control effectors. The baseline control framework implemented in the simulation, described in References [198, 260], is referred to as the robust uniform control approach for VTOL aircraft. The approach integrates a robust servomechanism linear quadratic regulator (RSLQR) control framework with control allocation techniques and airspeed-based

gain scheduling to develop a full-envelope flight controller. The controller has been successfully applied to multiple eVTOL aircraft configuration types across their operational flight envelopes [198, 260].

Although atmospheric turbulence models are included within the simulation architecture, for this study, flight simulations were performed in still air, for simplicity. The simulated flight data were corrupted with white, Gaussian measurement noise. The sensor noise levels used for this work emulate values estimated from flight testing of a subscale jet transport aircraft that were implemented in a simulation-based aircraft system identification study [87]. Accurate flight-test noise levels for eVTOL aircraft were not known at the time of this study. It is recognized that the noise levels for an actual eVTOL aircraft flight test may be different than the values used in this chapter. Sensor bias and scale factor errors generally seen in flight data were not considered because these systematic instrumentation errors would be removed using kinematic consistency correction techniques prior to model identification [19].

The LA-8 aero-propulsive model development process using wind-tunnel testing was described in Chapter 6 and Reference [28]. The aero-propulsive model consists of a set of nonlinear response surface equations describing the aero-propulsive forces and moments exerted on the aircraft at several discrete reference airspeed conditions throughout the vehicle flight envelope with a range of wing angle settings corresponding to the trim envelope at each airspeed condition. These point model responses are then blended together to enable continuous simulation from hover through forward flight. Recall that two approaches were used to identify the LA-8 aero-propulsive response surface equations. The first approach used data from a powered-airframe wind-tunnel experiment executed at multiple freestream velocity settings to develop the model (see Section 6.5.1). A second approach sought to produce a higher fidelity model utilizing isolated propulsion data in concert with powered-airframe data to improve characterization of aero-propulsive interaction effects and enhance prediction of propulsion forces and moments (see Section 6.5.2). The latter, more complex model was used to perform flight simulations for this study.

9.3 eVTOL Aircraft Modeling Approach Using Flight Data

As explained in Sections 6.2 and 6.5, aero-propulsive modeling for eVTOL aircraft requires a different approach compared to conventional fixed-wing and rotary-wing aircraft modeling approaches. The modeling approach defined here applies relevant aspects from both fixed-wing and rotary-wing system identification and incorporates strategies specific to eVTOL aircraft. The proposed eVTOL aircraft system identification method focuses on developing a model of the aero-propulsive forces and moments exerted on the aircraft as a function of vehicle state and control variables. The approach is informed by vehicle attributes, as well as experience gained from the work presented in Chapters 6 and 8

(References [28, 30]). Note that the approach in this chapter applies when most or all of the distributed propulsors are operational on the aircraft. Certain vehicles, such as the lift+cruise configuration type [12], disable most propulsion elements when operating in a high-speed forward flight condition. For that aircraft type and flight regime, for example, a fixed-wing system identification approach would be applicable, as was used in Reference [39].

Following the rotorcraft modeling convention, the aero-propulsive models are developed and estimated in a dimensional form. The response variables are defined as the dimensional body-axis applied aero-propulsive forces and moments X, Y, Z, L, M, and N. A generally nonlinear multivariate polynomial modeling approach adopted from fixed-wing applications has been used in previous studies to characterize the nonlinear aero-propulsive effects [28, 39]. Significant airframe-propulsion interactions and rapid aerodynamic variation with flight condition for eVTOL vehicles suggests that a linear aero-propulsive model will have a small region of local validity. For many applications, identification of a nonlinear aero-propulsive model will be required; however, for this chapter, a linear aero-propulsive model structure used with the nonlinear aircraft equations of motion was found to produce adequate modeling results for small perturbations from a reference flight condition. For this reason, a linear aero-propulsive model was used as the local model structure and linear model parameters were identified at numerous flight conditions across the LA-8 flight envelope to develop a nominal model for the purpose of illustrating system identification applied to eVTOL aircraft. This approach is similar to previous work that identified and combined linear models to produce a global model [131, 140]. The method used for this chapter can be readily extended to using nonlinear aero-propulsive models in future studies which, for example, might require two-factor interaction or quadratic model terms.

Although the dimensional forces and moments are defined as the responses to be modeled, these quantities cannot be measured directly in flight and must be inferred from other measurements. The dimensional applied forces are calculated as the vehicle mass multiplied by the body-axis translational accelerometer measurements corrected to the aircraft center of gravity:

$$X = ma_x, \quad Y = ma_y, \quad Z = ma_z \tag{9.6}$$

The applied moments are calculated using the rotational dynamic equations accounting for propulsor gyroscopic effects [cf. Equations (9.1)-(9.3)] as:

$$L = I_x\dot{p} - I_{xz}\dot{r} + (I_z - I_y)qr - I_{xz}pq + \dot{h}_x + qh_z - rh_y \tag{9.7}$$

$$M = I_y\dot{q} + (I_x - I_z)pr + I_{xz}(p^2 - r^2) + \dot{h}_y + rh_x - ph_z \tag{9.8}$$

$$N = I_z\dot{r} - I_{xz}\dot{p} + (I_y - I_x)pq + I_{xz}qr + \dot{h}_z + ph_y - qh_x \tag{9.9}$$

It is important to include propulsor gyroscopic effects in these equations because the propulsors will be dynamically commanded and asymmetrically operated during maneuvers used for system identification. Note that the moments of inertia and center of gravity will change through transition for eVTOL vehicles that rotate components for conversion (e.g., the tilting

wings on the LA-8), and must be bookkept for model identification. Because the nonlinear translational and rotational dynamics equations are used to model the aircraft dynamics, the resulting models can be used to predict vehicle motion at different loading conditions.

The vehicle states defined as explanatory variables for modeling include the body-axis translational velocity components u, v, w in ft/s and angular velocity components p, q, r in rad/s, following the convention used in rotorcraft system identification. The longitudinal force and moment components (X, Z, M) use only the longitudinal states (u, w, q) as explanatory variables, and the lateral-directional force and moment components (Y, L, N) use only the lateral-directional states (v, p, r) as explanatory variables. The vehicle control surface deflection angles in radians are also defined as explanatory variables, as is commonly done for fixed-wing aircraft system identification. To complete the definition of modeling variables, the rotational speeds of each propulsor in revolutions/s are defined as explanatory variables, which applies for modeling vehicles with fixed-pitch propellers. If the vehicle had variable-pitch propellers, the propulsion explanatory variables for each propulsor would be both rotational speed and blade pitch angle. This formulation deviates from fixed-wing aircraft modeling where propulsion aerodynamics are generally not characterized in flight, as well as rotary-wing aircraft modeling which generally includes more rotor states.

For this work, the forward airspeed component u is treated as a flight condition variable, where local models are identified at a set of reference airspeed conditions u_o. Density altitude h, or atmospheric density ρ, could be included as another flight condition variable, but the approach taken here is to develop modeling techniques at a single altitude. Additionally, wing tilt angles for the LA-8 vehicle are treated as flight condition variables scheduled with airspeed, as opposed to being defined as explanatory variables, which assumes an existing wing angle schedule. Including wing tilt angles as explanatory variables would introduce additional complications because the propellers, wings, and wing-fixed control surfaces all change orientation with respect to the body-axes. Also, the assumption that the aircraft is operating as a single rigid body would be violated. The aircraft moments of inertia are computed based on wing angle and are held constant at each reference flight condition.

The flight condition variables, explanatory variables, and response variables defined for the LA-8 aircraft used in this work are summarized in Table 9.1. As mentioned above, a fixed linear aero-propulsive model structure was used for developing a local model for each reference flight condition and several linear models were developed throughout the nominal flight envelope. For example, the local model structure for Z is:

$$\begin{aligned} Z = {} & Z_u u + Z_w w + Z_q q + Z_{\delta_{e_1}} \delta_{e_1} + Z_{\delta_{e_2}} \delta_{e_2} + Z_{\delta_{e_3}} \delta_{e_3} + Z_{\delta_{e_4}} \delta_{e_4} \\ & + Z_{\delta_{f_1}} \delta_{f_1} + Z_{\delta_{f_2}} \delta_{f_2} + Z_{\delta_{f_3}} \delta_{f_3} + Z_{\delta_{f_4}} \delta_{f_4} + Z_{\delta_{r_1}} \delta_{r_1} + Z_{\delta_{r_2}} \delta_{r_2} \\ & + Z_{n_1} n_1 + Z_{n_2} n_2 + Z_{n_3} n_3 + Z_{n_4} n_4 + Z_{n_5} n_5 + Z_{n_6} n_6 + Z_{n_7} n_7 + Z_{n_8} n_8 + Z_o \end{aligned} \tag{9.10}$$

Here, Z_o contains the aerodynamic bias as well as contributions related to the regressor reference values [19]. The model structures for X and M include the same explanatory variables. The model structures for Y, L, and N are similar, with the only difference being

that v, p, and r are included as explanatory variables, as opposed to u, w, and q. The next section discusses an experiment design methodology which ensures the effects of all the explanatory variables on the responses can be adequately characterized.

Table 9.1: Summary of modeling variables for the LA-8 aircraft

Variable Type	Variable Symbol
flight condition variables	$u_o, \delta_{w_1}, \delta_{w_2}, h$
explanatory variables	$u, v, w, p, q, r, \delta_{e_1}, \delta_{e_2}, \delta_{e_3}, \delta_{e_4}, \delta_{f_1}, \delta_{f_2}, \delta_{f_3}, \delta_{f_4}, \delta_{r_1}, \delta_{r_2}, n_1, n_2, n_3, n_4, n_5, n_6, n_7, n_8$
response variables	X, Y, Z, L, M, N

9.4 Flight Experiment Design

A flight experiment must be properly executed to generate informative data from which a useful model can be identified using the approach outlined in the previous section. This includes the flight-test instrumentation and excitation input design strategies, discussed next.

9.4.1 Flight-Test Instrumentation

The instrumentation requirements for eVTOL aircraft system identification largely follow what is used for research-quality fixed-wing and rotary-wing aircraft testing [19–21]. The desired measurements for LA-8 include body-axis translational acceleration, body-axis angular rates, Euler orientation angles, air-data parameters, control surface deflection angles, wing tilt angles, and propulsor rotational speeds. The inertial navigation system should have the built-in capability to provide reconstructed body-axis velocity components through use of a state estimator, such as an extended Kalman filter. This is important for system identification at low airspeed where air data will likely have low signal-to-noise ratios. A sample eVTOL aircraft system identification measurement list for the LA-8 aircraft is summarized in Table 9.2. Note that different eVTOL aircraft configurations might require other measurements, such as propulsor blade pitch angle and propulsor tilt angle.

Additional aircraft configuration data are required prior to flight testing. The vehicle mass and moments of inertia should be accurately measured or estimated for use with the aircraft dynamics equations. The moment of inertia of the rotating portion of each propulsor is also needed to properly account for gyroscopic effects. A preliminary estimate of the aircraft dynamic modes and control bandwidth (particularly propulsion control bandwidth) is useful for excitation input design.

Table 9.2: Sample eVTOL aircraft system identification measurement list for the LA-8 aircraft

Measurement Name	Notes
body-axis translational acceleration (a_x, a_y, a_z)	— —
body-axis angular velocity (p, q, r)	— —
Euler orientation angles (ϕ, θ, ψ)	reconstructed via state estimation
true airspeed (V)	— —
body-axis velocity (u, v, w)	reconstructed via state estimation
airflow angles (α, β)	airflow angles are not reliable at low airspeed
static pressure	used to compute air density and density altitude
ambient temperature	used to compute air density and density altitude
control surface deflection angles	— —
propulsor rotational speeds	— —
wing tilt angles	— —

9.4.2 Input Design

Orthogonal phase-optimized multisine inputs [19, 82–85], described in Section 2.3.2, are the excitation input type used for this work. Individual multisine signals were generated for each of the LA-8 control surfaces and propulsors, for a total of 18 different excitation signals. The overall frequency range was set in accordance with frequencies where the rigid-body dynamics of interest were expected to manifest and the propulsion harmonic components were focused into lower frequencies to adhere to the lower bandwidth of the propulsors [37]. The multisine design process followed similar steps to the process followed in Section 8.2.2 (Reference [30]) for LA-8 wind-tunnel experiments using multisine inputs. The difference in the design process for this chapter is that the design evaluation focuses on the linear control effector model terms, whereas pure quadratic and two-factor interaction model terms among control effectors were also considered in Chapter 8. The same six sets of multisine input designs with different fundamental periods using 30 optimization runs with randomly chosen starting phase angles were evaluated for the input design in this chapter. The best design was determined using the pairwise correlation coefficient r_{ij} [Equation (2.80)] between linear input signals $\boldsymbol{\xi}_i = \boldsymbol{u}_i$ and $\boldsymbol{\xi}_j = \boldsymbol{u}_j$. The multisine design with the quickest time to decrease all pairwise correlation coefficient values to 0.5 or lower was selected to compare to signals developed with different fundamental periods. The relative peak factor for the design with the quickest time to decrease pairwise correlation values to below 0.5 for each fundamental period T is shown in Figure 9.1. A similar RPF is obtained for each control effector signal for different values of T, with a slight general decreasing trend in RPF as T increases. The propulsor signals also generally have a lower RPF value compared to the control surface signals.

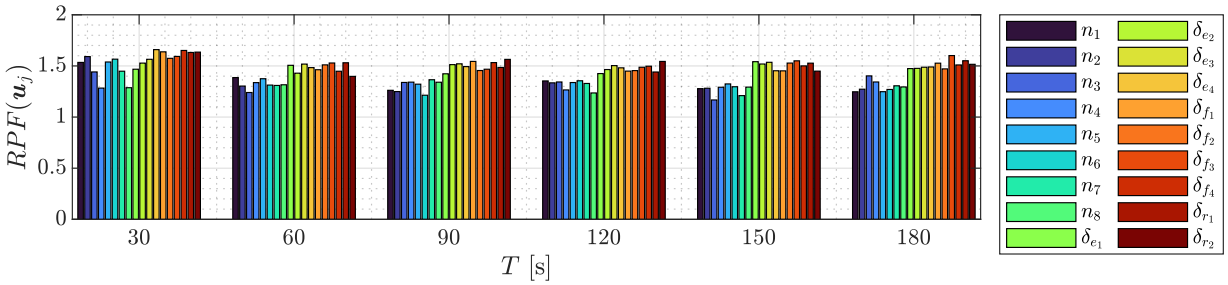

Figure 9.1: Relative peak factor of candidate LA-8 aircraft multisine designs.

Following an approach similar to Reference [85] and Chapter 8 (Reference [30]), input correlation metrics were used as criteria to assess the quality of each multisine design as maneuver time progresses. The progression of correlation metrics over time for each multisine design with a different fundamental period is shown in Figure 9.2. Figure 9.2a shows the

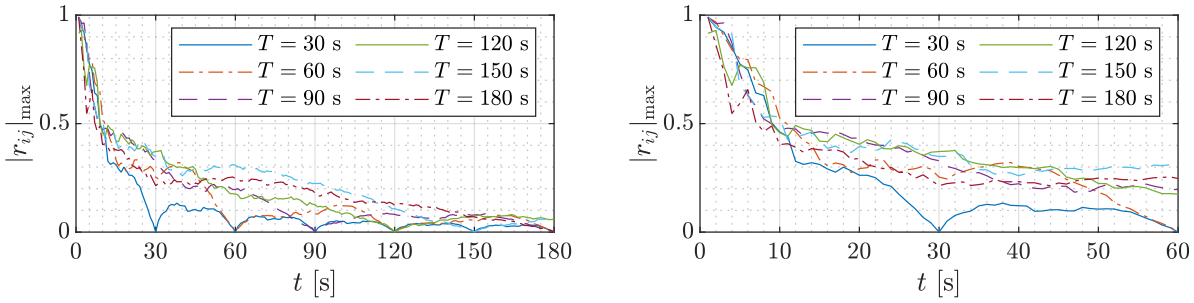

(a) Maximum pairwise correlation coefficient (180 seconds)

(b) Maximum pairwise correlation coefficient (60 seconds)

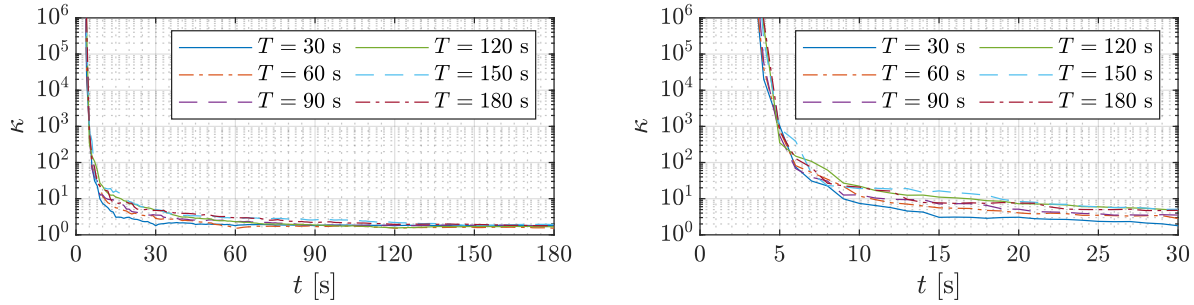

(c) Condition number of $\boldsymbol{U}^T\boldsymbol{U}$ (180 seconds)

(d) Condition number of $\boldsymbol{U}^T\boldsymbol{U}$ (30 seconds)

Figure 9.2: Input signal correlation metrics against time.

maximum absolute pairwise correlation value $|r_{ij}|_{\max}$ for each multisine design as a function of time, with Figure 9.2b displaying the same plot over a shorter time interval. Figure 9.2c shows the condition number κ of $\boldsymbol{U}^T\boldsymbol{U}$ for each multisine design as a function of time, with Figure 9.2d displaying the same plot over a shorter time interval. Here, $\boldsymbol{U}$ is a matrix composed of column vectors of the input signals, $\boldsymbol{U} = [\boldsymbol{u}_1, \boldsymbol{u}_2, ..., \boldsymbol{u}_m]$. The interpretation of

Figure 9.2 is similar to the explanation given Section 8.2.2 for the linear model. Figures 9.2a-9.2b show that the design with the greatest fundamental period ($T = 180$ seconds) generally has the lowest maximum pairwise correlation for the first 10 seconds. After 10 seconds, each design has reasonably close $|r_{ij}|_{\max}$ values until approaching the fundamental period for each design, where the signals converge to zero correlation. As was also observed in Chapter 8, Figure 9.2 shows that multisine designs with different fundamental periods obtain low correlation metrics in a similar maneuver time. In view of these findings and previous research showing the benefits of increased frequency resolution [251], the multisine design with the largest fundamental period ($T = 180$ seconds) was selected to be used for the system identification experiments.

The input spectra for the final set of orthogonal phase-optimized multisine signals with a fundamental period of $T = 180$ seconds were identical to those shown in Figure 8.7. The only frequency-domain difference for this chapter is that the excitations are applied to the rotational speed commands $n_1, n_2, ..., n_8$ as opposed to the throttle PWM commands $\eta_1, \eta_2, ..., \eta_8$. Figure 9.3 shows the first 20 seconds of the input excitation signals normalized to have a maximum absolute value of one. This reflects how the signals are injected into the flight controller, where a gain is applied to scale each input signal to a sufficient amplitude to obtain a good signal-to-noise ratio, while not deviating far from the trimmed flight condition or perturbing the aircraft to an unsafe flight condition. Although the time-domain signals shown in Figure 9.3 and Figure 8.8 are different due a different set of optimized phased angles for each design, the spectral content for each is identical. Note that the maneuver length used for system identification is generally different than the 20-second input signal duration shown for demonstration purposes in Figure 9.3.

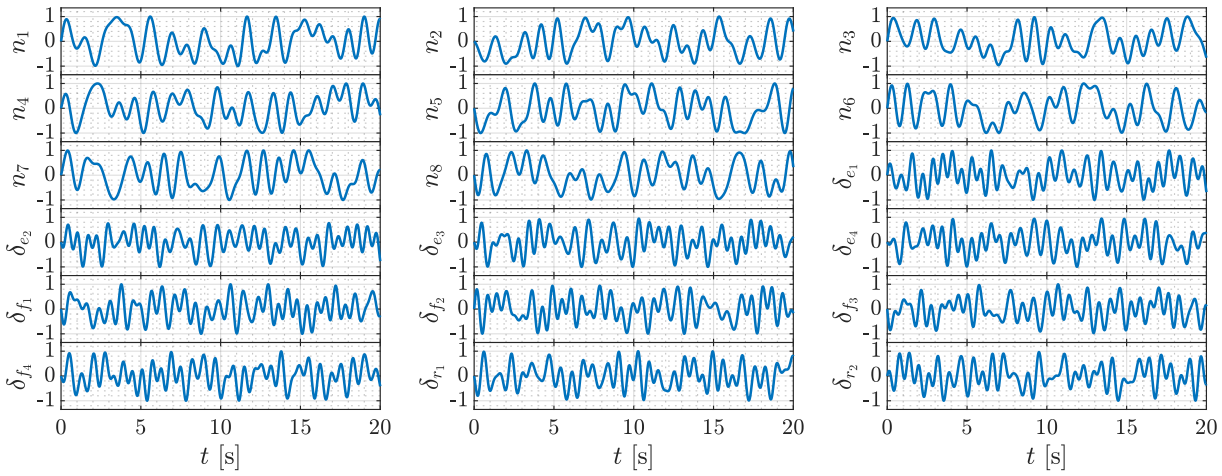

Figure 9.3: LA-8 aircraft normalized multisine inputs used for system identification.

9.4.3 Input Strategy with Feedback Control

eVTOL aircraft dynamics are generally unstable over a large portion of their flight envelopes, which requires the feedback control system to be active when operating at these conditions. Although necessary for safety, flight control systems can create deficiencies in the data information content available for system identification. Control systems act to suppress the natural aircraft motions that system identification maneuvers are designed to excite, distort optimally designed control inputs, and lead to correlation between explanatory variables, making their independent effects more difficult to distinguish. Strategies used for modeling aircraft with feedback control include using *a priori* information to better condition the modeling problem, lowering the feedback gains, and/or injecting the input excitations downstream of the control laws. Using preliminary information can result in biased estimates if the parameters are not a good representation for actual aircraft characteristics. Also, tampering with the control system is generally not advisable from a risk-mitigation standpoint, particularly for unstable aircraft. Hence, the strategy used here for handling the presence of the flight controller is to sum each input excitation signal with the control effector command from the control system just before the commanded actuator position and rate limits [19]. An early demonstration of the effectiveness of direct single control surface excitation for unstable aircraft system identification was shown in Reference [261]. Extending this direct control surface excitation approach to multiple inputs allows characterizing the influence of each control effector on the aircraft open-loop dynamic response simultaneously [19, 82, 83, 85, 251], as well as characterization of control interaction effects [19, 85]. This input excitation framework is depicted in Figure 9.4.

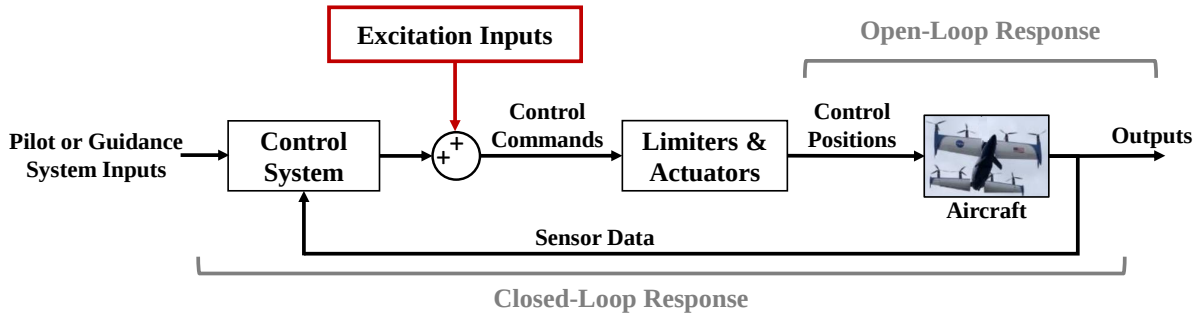

Figure 9.4: Proper application of excitation inputs relative to the control system [19].

9.5 Results

As described in Section 9.3, the modeling approach used for this chapter is to identify several linear aero-propulsive models across the nominal flight envelope for the LA-8 aircraft.

The parameters withing each model equation were estimated using the equation-error method formulated in the frequency domain [19, 100] (see Section 2.6.1.2). The frequency range was selected to match the excitation input design with a fundamental period of $T = 180$ s (see Section 9.4.2), as was also done in Chapter 8; i.e., the Fourier transform frequencies were set between $f_{\min} = 0.05$ Hz and $f_{\max} = 1.756$ Hz with a frequency resolution of $\Delta f = 0.00556$ Hz. After identification of local model parameters, the parameters are blended together to form a global aero-propulsive model. Sample local and global modeling results obtained from simulated LA-8 flight tests are provided in this section.

9.5.1 Local Modeling Results

Simulated LA-8 flight data for a level maneuver at a reference forward airspeed of $u_o = 45$ ft/s and wing angles fixed at $\delta_{w_1} = \delta_{w_2} = 25$ deg with orthogonal phase-optimized multisine inputs active on all control surfaces and propulsors are shown in Figures 9.5-9.6. As mentioned previously, the simulated flight data used for modeling were corrupted with measurement error using noise levels consistent with a previous simulation-based aircraft system identification study [87]. The control effector signal waveform shown in Figure 9.5 is different than the designed signals shown in Figure 8.8 due to distortion from the active flight control system. Even with this distortion, modeling variables are still sufficiently decorrelated for model identification as a result of injecting the excitation inputs as shown in Figure 9.4 [19]. A total maneuver length of 60 seconds was selected by investigating the parameter estimation results and the RMSE [Equation (2.84)] for validation data as a function of maneuver time used for modeling, as will be demonstrated below. All of the following analysis in this subsection uses the simulated flight data shown in Figures 9.5-9.6.

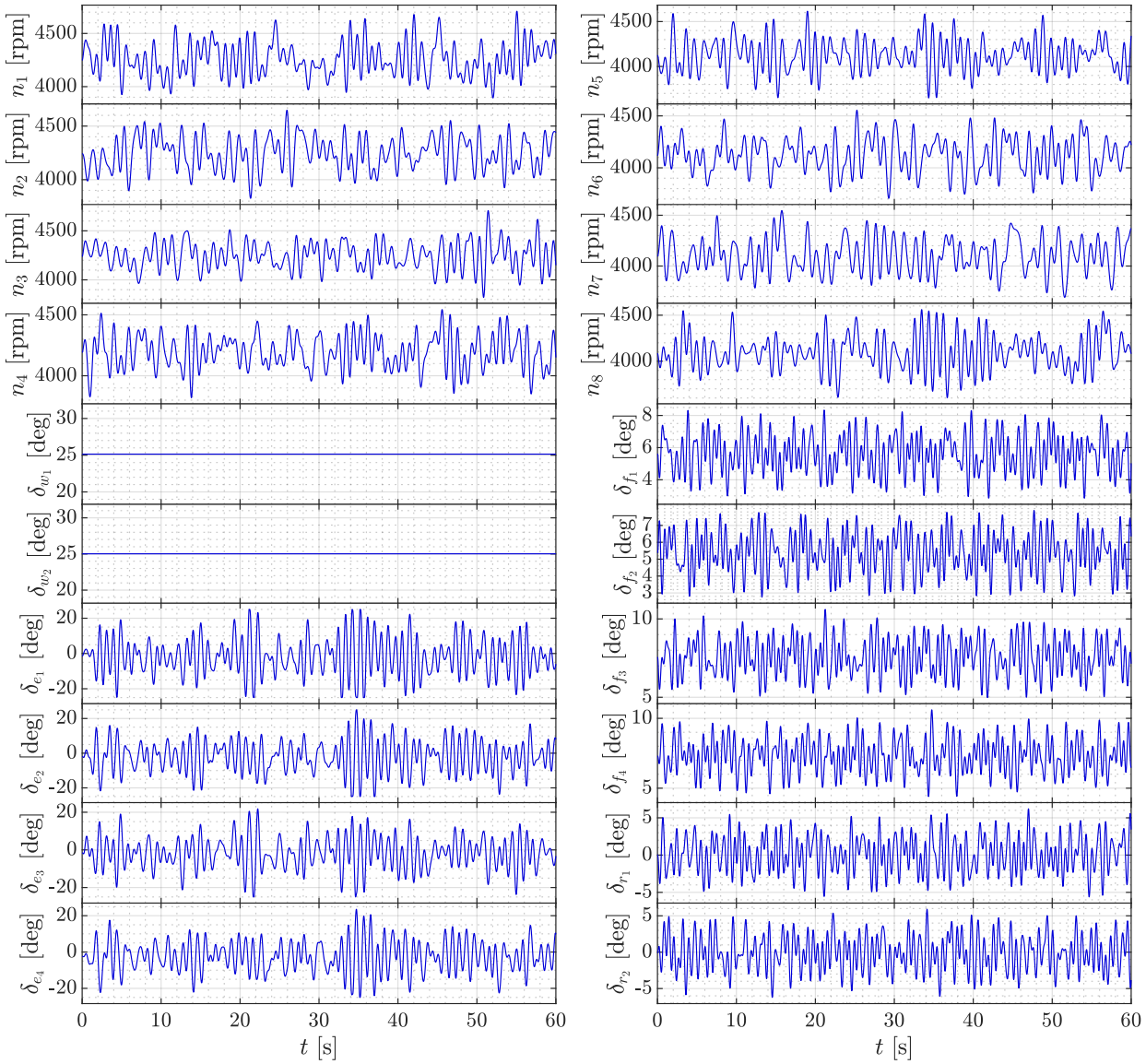

Figure 9.5: Control surface deflection angles and propulsor rotational speeds during a simulated LA-8 system identification maneuver at $u_o = 45$ ft/s.

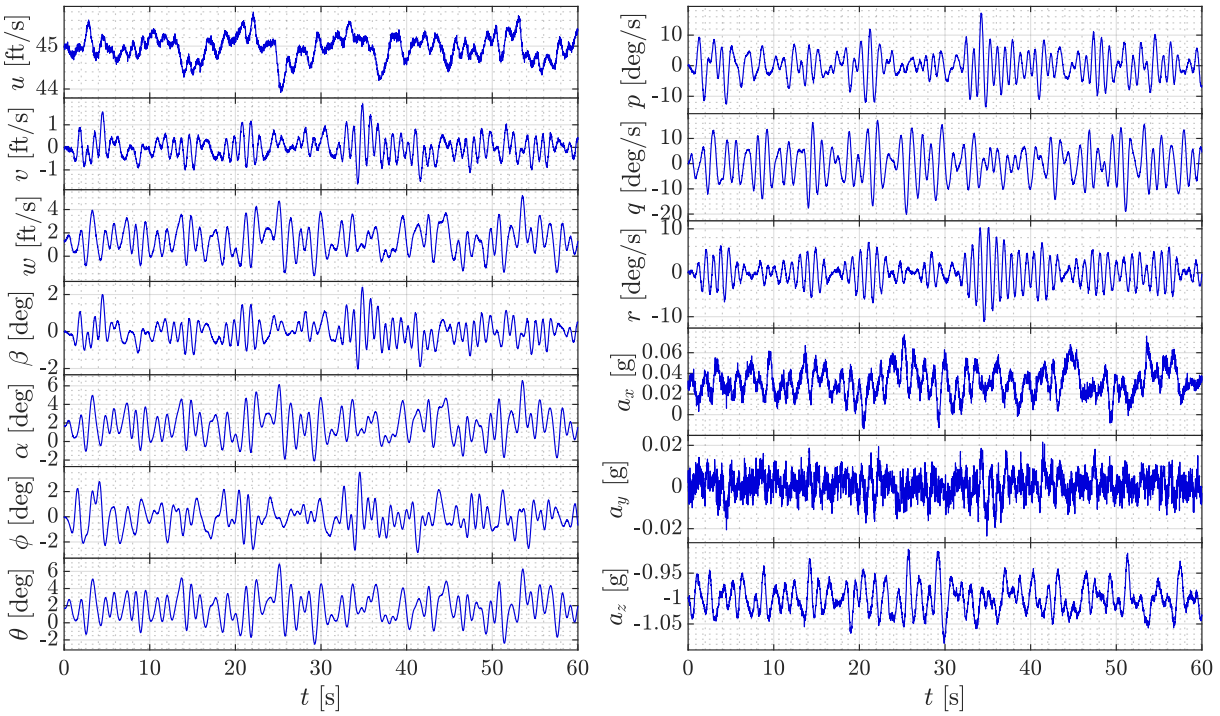

Figure 9.6: Simulated LA-8 flight data at $u_o = 45$ ft/s with multisine inputs active on all control effectors.

Figure 9.7 shows the Z parameter estimates and error bars of $\pm 2s(\hat{\theta})$ computed using complex least-squares regression against the amount of maneuver time used for modeling. Parameter estimates were computed in a batch manner for the various different maneuver lengths used for modeling, as opposed to implementing real-time calculations. The plot also shows the linearized parameters computed directly from the nonlinear LA-8 simulation using central finite differences, for comparison. The parameters appear to converge to reasonably consistent values by the time 40 seconds has elapsed and show good concurrence with the linearized LA-8 simulation parameters. Similar results were obtained for the parameters corresponding to the other aero-propulsive forces and moments and at different flight conditions throughout the LA-8 flight envelope. Note that the parameter estimates contain asymmetries that are not apparent from the LA-8 vehicle configuration. This is a result of manufacturing differences between the clockwise and counterclockwise propellers, which resulted in a significant difference in thrust production between the propeller variants [36]. Because the propulsion-only and propulsion-airframe interaction effects are significant, this propulsion asymmetry is manifested in many control effector model terms (see Chapter 6 and Reference [28]).

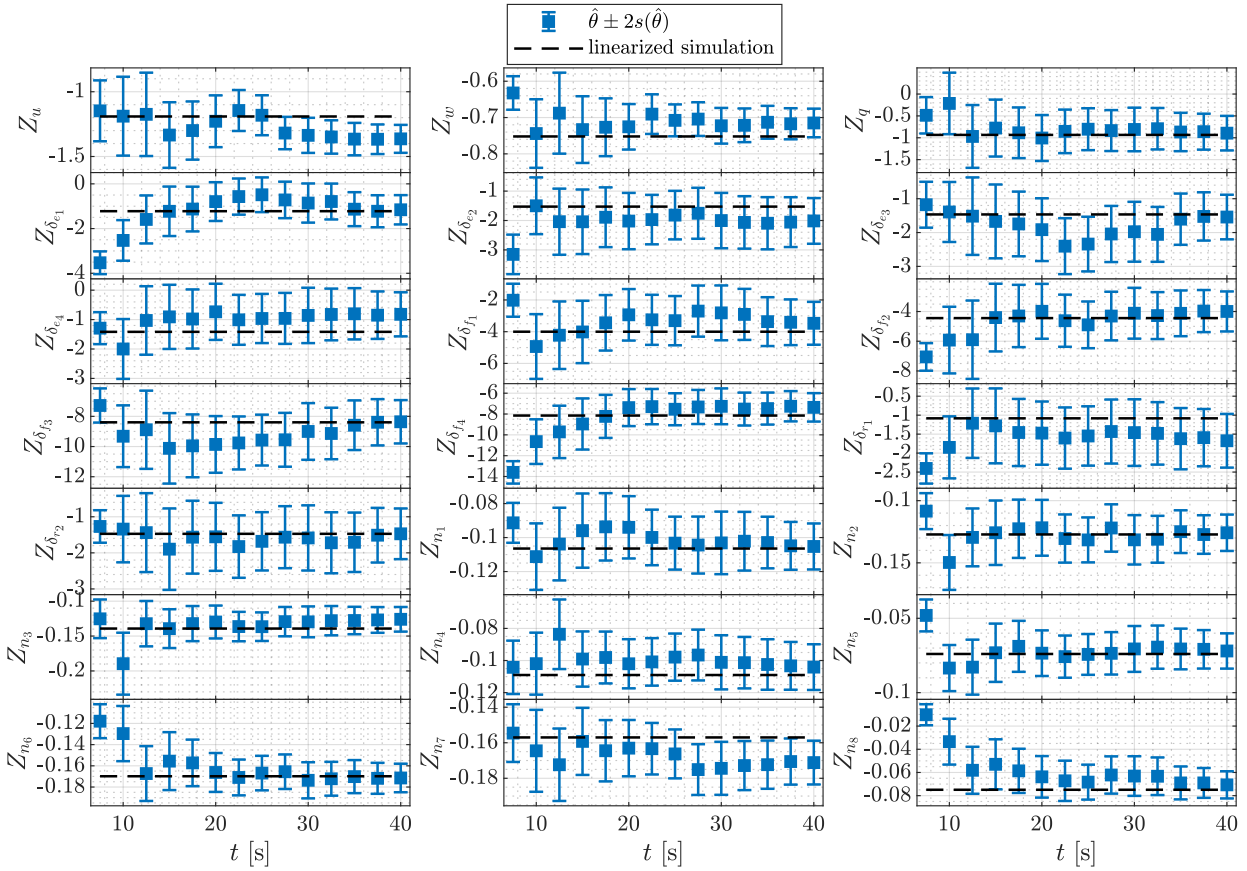

Figure 9.7: Variation of Z parameter estimates with maneuver time used for modeling at $u_o = 45$ ft/s.

Figure 9.8 shows the validation RMSE (RMSE_v) in the time domain for each response variable against the amount of maneuver time used for model identification. The last 20 seconds of data from the maneuver shown in Figures 9.5-9.6 were withheld from model identification and used to compute the RMSE_v metric at each modeling time length. The amount of time for RMSE_v to nearly level off is different for each response, but all responses appear to have a small RMSE_v reduction rate by the time 40 seconds has elapsed, indicating that a longer maneuver would provide little additional benefit. Similar results were obtained at other flight conditions.

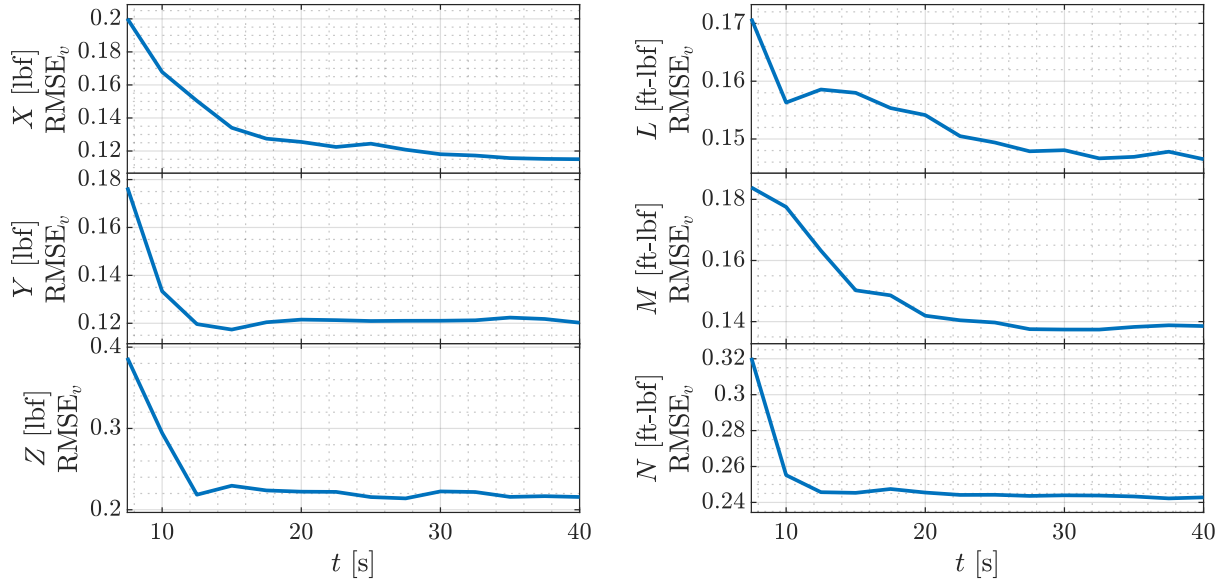

Figure 9.8: Variation of validation RMSE with maneuver time used for modeling at $u_o = 45$ ft/s.

In view of Figures 9.7-9.8, and also with the knowledge that 40 seconds is the amount of time needed to complete two full periods of the lowest frequency sinusoidal component of the multisine maneuver ($f_{\min} = 0.05$ Hz), 40 seconds was selected as the amount of maneuver time to use for modeling at each flight condition. The same data collection time was selected in Chapter 8 for LA-8 wind-tunnel experiments using multisine inputs following similar reasoning. A 60-second maneuver was executed at each reference flight condition used for model identification, where the first 40 seconds were used to identify the local aero-propulsive model, and the last 20 seconds of the maneuver were used as validation data to test the model prediction capability. This maneuver time length worked well across the LA-8 flight envelope, as will be shown in Section 9.5.2.

Figure 9.9 shows the model fit in the frequency domain using the first 40 seconds of the maneuver shown in Figures 9.5-9.6. A good model fit is observed for each response. The R^2 metric shown on the plot for each response is high, indicating that most of the variation of the response variable about its mean is characterized by the model. Figure 9.10 shows the model fit and model prediction compared to the smoothed aero-propulsive forces and moments in the time domain using the same maneuver. The model fit and model predictions are close to the responses calculated from the simulated flight data, indicating that the model is able to characterize a large amount of the variation in each response. The local model fit and prediction capability were similar for the other reference flight conditions across the LA-8 flight envelope.

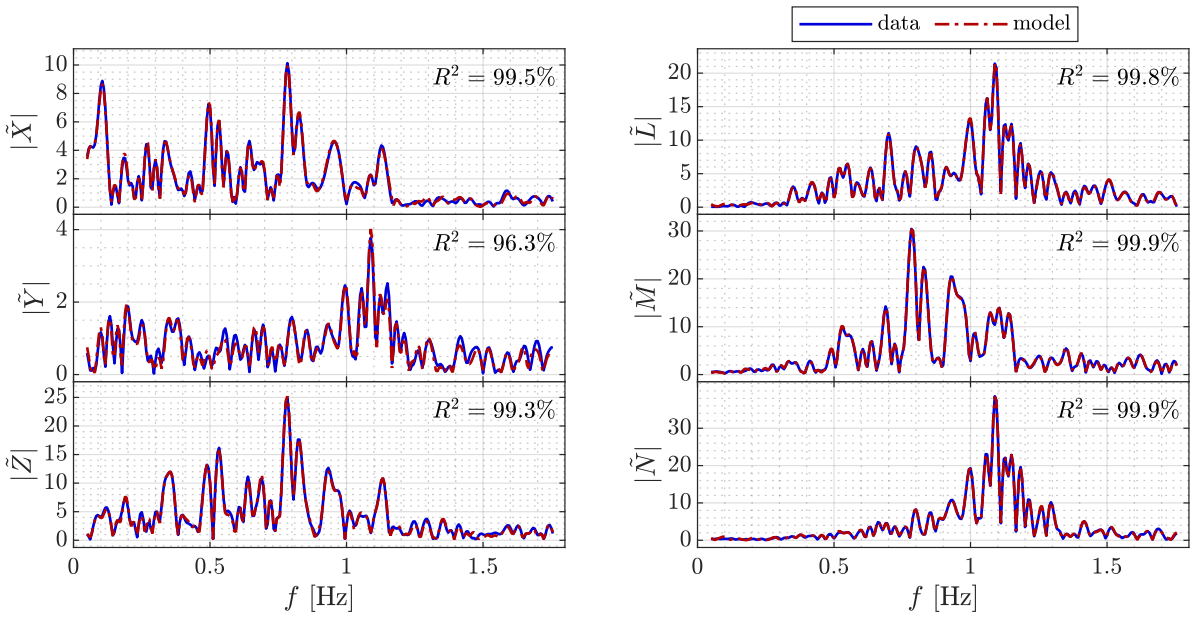

Figure 9.9: Comparison of modeling response data and model fit in the frequency domain at $u_o = 45$ ft/s.

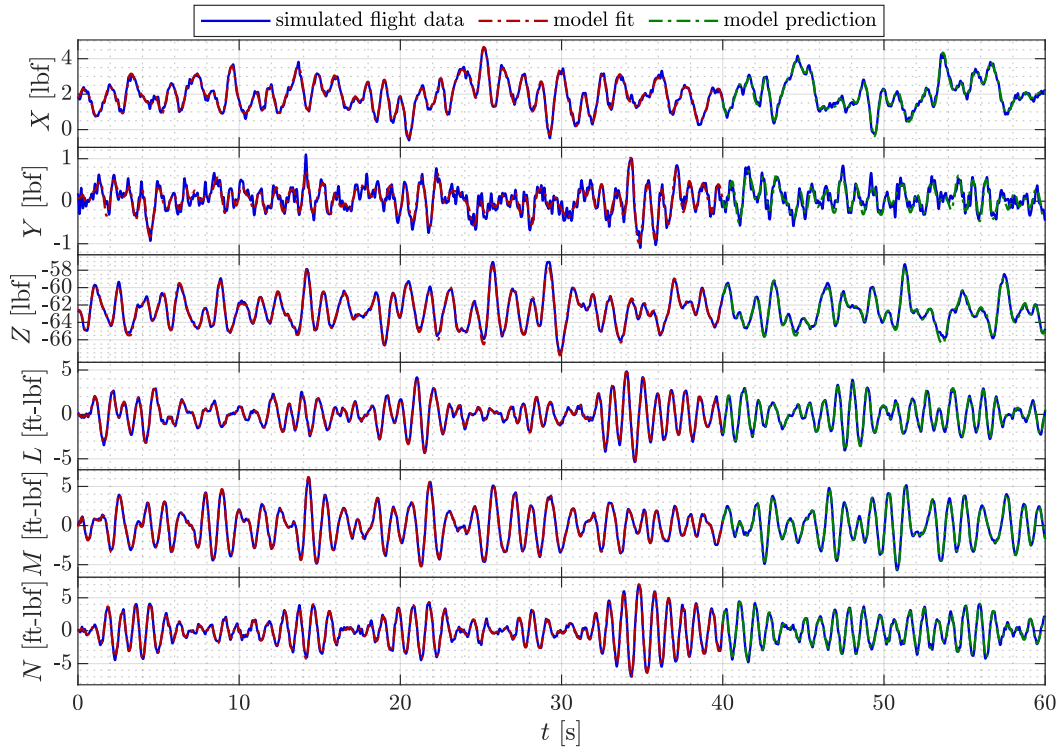

Figure 9.10: Model fit and model prediction in the time domain for a simulated LA-8 maneuver at $u_o = 45$ ft/s.

9.5.2 Global Modeling Results

Similar execution of a 60-second multisine maneuver and the subsequent analysis shown in the previous subsection were used to develop a local model at several flight conditions throughout the LA-8 flight envelope listed in Table 9.3. The same input design and input injection amplitudes were applied at each flight condition. The model fit and model predictions in the time domain for seven different flight conditions through the LA-8 transition envelope are shown in Figure 9.11. The corresponding time-domain R^2 values computed for each response using the modeling and validation data at each reference flight condition are shown in Table 9.4. A good model fit and good model predictions are generally observed for the dominant responses at each flight condition. Figure 9.12 shows the RMSE value for each response for both modeling data and validation data. Observing that the RMSE_m value for each response holds a similar value to the corresponding RMSE_v value, the RMSE_m values are an accurate representation of prediction performance suggesting that modeling was successful.

Table 9.3: Reference flight conditions for simulated LA-8 flight-test system identification experiments

u [ft/s]	δ_{w_1} [deg]	δ_{w_2} [deg]
0	83.9	82.0
9	78.2	75.3
18	65.2	62.5
27	54.3	53.8
36	39.6	39.9
45	25.1	25.0
54	16.0	15.4

Table 9.4: Time-domain R^2 values computed for the model identified at each reference flight condition (expressed as a percentage)

(a) Modeling data

u_o	X	Y	Z	L	M	N
0 ft/s	54.7	40.7	98.6	99.8	99.8	99.4
9 ft/s	91.1	43.7	98.6	99.6	99.8	99.1
18 ft/s	94.4	76.2	98.1	99.5	99.8	98.8
27 ft/s	97.5	82.7	98.0	99.4	99.8	98.9
36 ft/s	97.8	80.3	97.9	99.2	99.7	98.1
45 ft/s	97.7	86.1	99.0	99.2	99.6	98.9
54 ft/s	97.8	92.4	99.5	98.9	99.4	99.0

(b) Validation data

u_o	X	Y	Z	L	M	N
0 ft/s	41.9	37.2	98.9	99.6	99.9	98.7
9 ft/s	89.0	39.4	98.6	99.3	99.8	98.7
18 ft/s	91.4	65.2	97.6	99.5	99.8	98.3
27 ft/s	97.1	66.8	98.3	99.4	99.8	98.8
36 ft/s	98.1	64.0	97.3	99.0	99.8	97.5
45 ft/s	98.3	78.5	98.3	99.1	99.6	98.4
54 ft/s	97.2	90.3	99.3	98.5	99.4	98.5

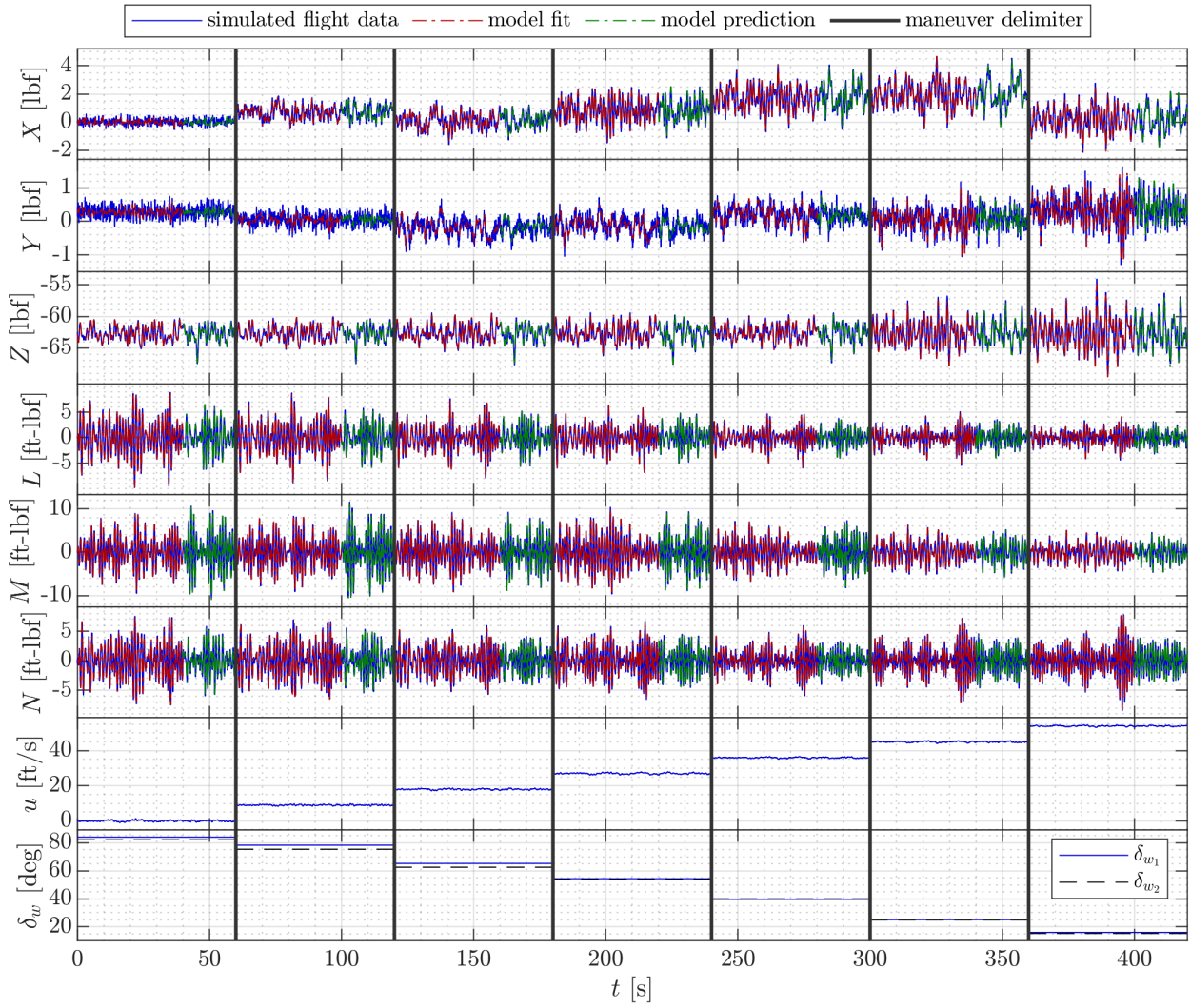

Figure 9.11: Model fit and model prediction for the aero-propulsive forces and moments at several reference conditions throughout the LA-8 transition envelope.

Although maneuvering between flight conditions is not shown in Figure 9.11, the plots still reflect how a practical flight test for the LA-8 aircraft would occur. The testing would start in a hover flight condition to develop an initial model and then testing would move gradually through transition to eventually develop models through the nominal flight envelope. This could occur in a single flight, could involve the aircraft returning to the ground between test points, or could be some combination of the two strategies. This approach would work well alongside safe envelope expansion flight testing and could be used to aid in tuning a flight controller to achieve a safe transition. Note that the forward airspeed conditions tested for this study ranged from 0 to 54 ft/s and the wing angles ranged from approximately 83 deg (the trimmed hover setting) to 15 deg. For an actual system identification flight test of the LA-8 vehicle, modeling would be performed through wing angles of 0 deg (forward flight);

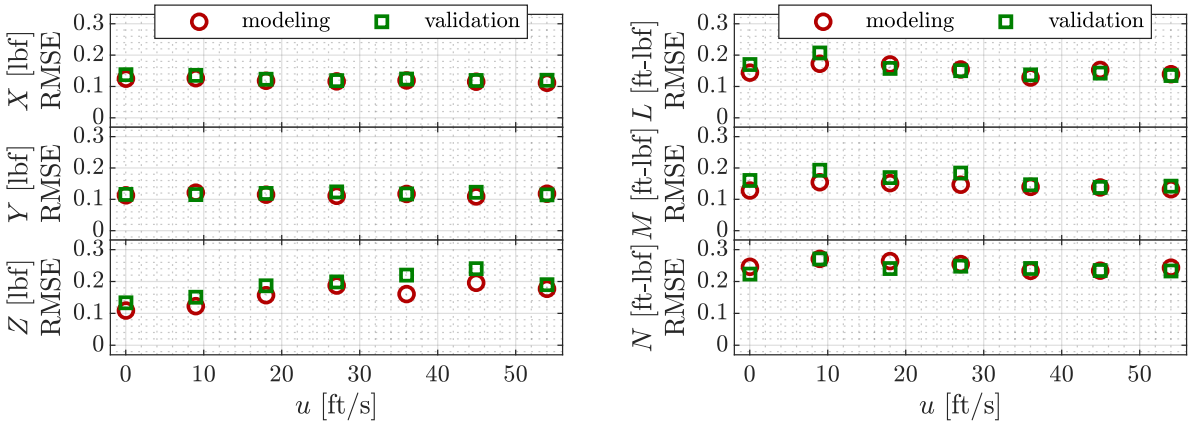

Figure 9.12: Modeling and validation RMSE for each response variable against reference forward speed.

however, for this simulated study, the possible flight conditions were limited by the range of validity of the wind-tunnel-derived aero-propulsive models currently implemented in the LA-8 simulation.

Figure 9.13 shows the Z parameter estimates and error bars of $\pm 2s(\hat{\theta})$ computed using complex least-squares regression for each tested flight condition. The solid line connecting the parameters is computed using shape-preserving piecewise cubic interpolation [92, 93] with the `pchip` MATLAB® function [90]; this interpolation method is preferred over cubic spline interpolation for blending parameter estimates because of its tendency to avoid overshoot and oscillatory behavior. Blending local model parameter estimates using this method shows how a continuous simulation can be formed using local models identified at several different reference conditions. The linearized parameters computed directly from the nonlinear LA-8 simulation at each condition are also shown for comparison. The identified Z parameters show good concurrence with the linearized LA-8 simulation parameters across the flight envelope. Similar results were obtained for the parameters corresponding to the other aero-propulsive forces and moments.

Acknowledgment of Collaborative Research

The research presented in this chapter was primarily conducted by the author, but included important collaborative contributions with other individuals. Eugene Morelli provided technical guidance on the eVTOL aircraft system identification approach and offered many helpful suggestions during manuscript preparation. Jacob Cook developed the LA-8 aircraft flight controller and integrated the controller into the simulation used for this work. Vehicle simulation development support was provided by Thomas Britton. The author gratefully acknowledges and appreciates these contributions which made the research described

in this chapter possible.

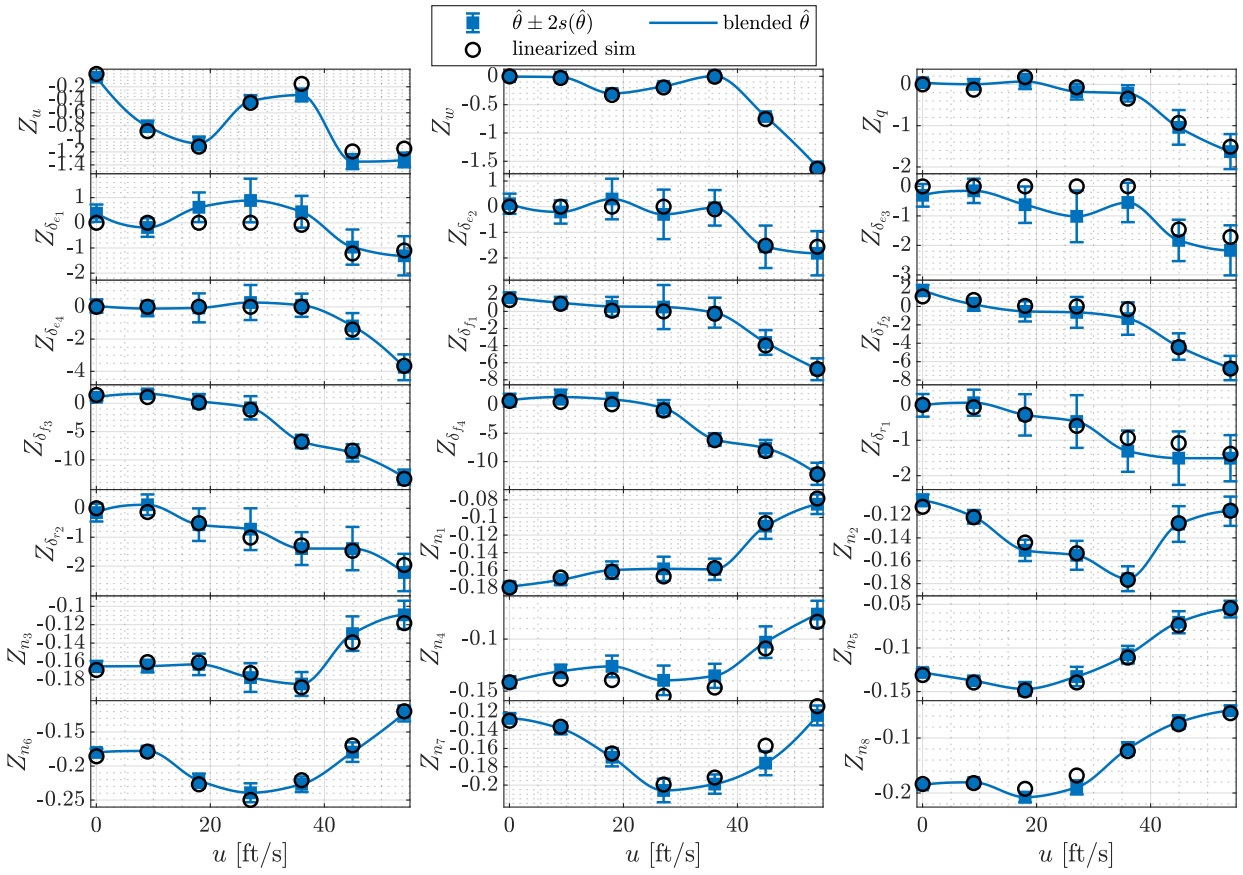

Figure 9.13: Variation of Z parameter estimates with forward speed across the LA-8 transition flight envelope.

Chapter 10

Part II Conclusions

Electric vertical takeoff and landing (eVTOL) vehicle configurations present new challenges for aircraft modeling and are currently an important area of research. Attributes of eVTOL vehicles overlap with both fixed-wing and rotary-wing aircraft, but also include complex vehicle-specific phenomena, such as many available control effectors and complex propulsion-airframe interaction effects. The mathematical models developed to describe eVTOL vehicle aerodynamics must be able to characterize many control effectors and complex aero-propulsive interactions, while also being amendable to drastically changing aerodynamics at numerous different flight conditions across a wide flight envelope. The result is a large nonlinear modeling problem that must be accomplished within cost and time constraints.

Aero-propulsive modeling for eVTOL vehicles is a crucial area of research because of a high demand for accurate vehicle simulations and the fact that existing system identification methods for conventional aircraft must be applied differently for modeling these unique, complex aircraft configurations. To address these challenges, Part II of this dissertation presented several aircraft system identification advancements for accurate and efficient aero-propulsive modeling for eVTOL vehicles. The LA-8 tandem tilt-wing eVTOL aircraft was used as a research testbed for this work in wind-tunnel testing and simulated flight-test experiments.

Chapter 6 developed and evaluated aero-propulsive modeling approaches for eVTOL aircraft using wind-tunnel data to support flight dynamics simulation development. Established model identification strategies for fixed-wing and rotary-wing aircraft were summarized and used to postulate new eVTOL aircraft modeling strategies. Powered-airframe wind-tunnel data were acquired at multiple dynamic pressure settings using design of experiments and response surface methodology techniques facilitating efficient, statistically-rigorous data collection that enabled accurate characterization of the LA-8 aircraft. One model identification approach used the powered-airframe wind-tunnel data to develop a model of the dimensional forces and moments exerted on the aircraft. A second approach used wind-tunnel-derived isolated propulsion models in concert with a full-airframe model identified using the same powered-airframe wind-tunnel data. Both approaches proposed a set of modeling explanatory variables and response variables tailored to tilt-wing eVTOL aircraft. Many control effectors and complex vehicle interactions result in a large number of potential model terms and challenges in identifying an adequate model structure. A practical and efficient model structure identification strategy was proposed and shown to be effective. Final models were

shown to have good predictive capability and small normalized model fit error.

In Chapter 7, several experiment designs were described and evaluated for modeling the aerodynamics of distributed propulsion aircraft in the form of a response surface model including linear, two-factor interaction, and pure quadratic model terms. Evaluation of single block foundational experiment designs revealed that I-optimal and A-optimal designs generally have the highest statistical power, lowest correlation among candidate model terms, lowest prediction variance across the design space, and yield the most precise parameter estimates. However, the single block designs were noted to place most of the design points near the exterior of the design space, which can result in model bias errors in the interior of the design space. To resolve this shortcoming, two sequential experiment designs containing nested designs that provide more coverage of the interior of the design space were investigated. The first sequential design approach used ordinary and nested minimum run resolution V, face-centered central composite designs as its base and represents a legacy design approach that has been applied previously to characterize complex aircraft. The second sequential design approach used a regular I-optimal design and a nested I-optimal design as its base with the same number of test points as the central composite designs. The nested I-optimal design was a new experiment design approach proposed for complex aircraft aero-propulsive characterization. Design evaluation metrics available prior to conducting an experiment were used to compare the two design approaches and revealed that the I-optimal base design had better statistical power for the candidate model terms, lower correlation among candidate model terms, and was expected to yield models with better prediction capability and more precise parameter estimates. Each set of sequential test matrices was applied in simulated LA-8 wind-tunnel experiments to develop a model of the dimensional forces and moments exerted on the aircraft at a reference airspeed condition. Modeling results obtained from the simulated wind-tunnel data suggested that the I-optimal based design provides improved prediction capability for data not used in the modeling process compared to the design blocks built on the face-centered central composite design. The results also indicated that an adequate model was obtained earlier in the block design sequence for the I-optimal base design. Based on the design evaluation metrics and modeling results, the nested I-optimal design approach is recommended for future aero-propulsive characterization experiments for complex distributed propulsion aircraft.

A novel, hybrid wind-tunnel testing and model identification strategy was developed in Chapter 8 and applied for eVTOL aircraft aero-propulsive modeling to enable rapid flight dynamics simulation development. A wind-tunnel experiment was developed in two parts. A four-factor static experiment was designed in a set of test blocks allowing identification of response surface models of increasing complexity for slow-moving airflow and wing angle test variables. A dynamic experiment composed of 18 simultaneous orthogonal phase-optimized multisine signals was designed for the propulsors and control surfaces, and executed at each set point. Several multisine designs were compared varying the fundamental period, which indicated that maneuvers with a longer fundamental period would be beneficial for model identification. A cubic I-optimal response surface design for the static test factors executed

simultaneously with dynamic excitations running for 40 seconds at each static test point was found to be a good testing strategy for model development, balancing test time and model prediction capability. Using this approach, all data collection at a reference airspeed condition can be completed in under 48 minutes, which is significantly faster than previous eVTOL aircraft modeling efforts using purely static test techniques. The model identification approach consisted of two parts in accordance with the data collection strategy. First, a local model was identified at each set point as a function of the dynamically changing explanatory variables using multivariate orthogonal function modeling and ordinary least-squares regression in the frequency domain. The model structure for each force and moment component was chosen to be identical for each set point based on the model terms deemed significant for a majority of the set points. Second, response surface models were developed for each model parameter associated with the dynamic test variables identified in the first stage of modeling as a function of the static test variables, using multivariate orthogonal function modeling and weighted least-squares regression with available uncertainty estimates. The identified models were shown to have good predictive capability and small normalized model fit error. Additionally, the model form supports parameterization of nonlinear aero-propulsive effects that cannot be captured in alternative modeling approaches.

Chapter 9 developed a flight-test system identification methodology for eVTOL aircraft leveraging system identification techniques for fixed-wing and rotary-wing aircraft, as well as previous eVTOL aircraft aero-propulsive characterization studies based on wind-tunnel data. The proposed method was evaluated using a high-fidelity LA-8 flight dynamics simulation. A flight-test experiment design for the LA-8 was developed using orthogonal phase-optimized multisine signals designed for each individual control surface and propulsor. Because the aircraft is unstable, system identification maneuvers were executed with the flight control system active, but the strategy still effectively excited the LA-8 aircraft dynamics allowing accurate modeling throughout the flight envelope. A 40-second modeling maneuver was shown to be an adequate length for accurate local model identification for the investigated vehicle and demonstrates the utility of using multiple-input orthogonal optimized multisine maneuvers for efficient eVTOL aircraft system identification. Model parameters in a linear aero-propulsive model structure used with the nonlinear aircraft equations of motion were estimated at several different flight conditions throughout the LA-8 flight envelope. The model structure is appropriate for capturing eVTOL aircraft characteristics in small perturbation maneuvers from a trimmed flight condition; however, the approach can also be readily extended to develop nonlinear aero-propulsive models that can expand the region of model validity. The identified models were shown to have good predictive capability, small model fit error, and good agreement with linearized simulation parameters. A blending method was shown which allows development of a global aero-propulsive model through the nominal flight envelope of the vehicle. Model development flight-test strategies were discussed allowing safe envelope expansion and sequential flight controller tuning for a new vehicle.

The work described in Part II of this dissertation provides progress in eVTOL aircraft modeling research using experimental techniques that can be applied for many current and

future vehicles. The methods allow accurate identification of dynamic models for complex eVTOL aircraft configurations with significant aero-propulsive coupling and many control effectors using a short amount of wind-tunnel and/or flight-test time. The methods were developed using a tandem tilt-wing eVTOL vehicle but can be readily applied to many other transitioning eVTOL vehicles, such as tilt-rotor and lift+cruise configurations, with straightforward modifications. The methods are also readily scalable to vehicles with more control effectors than the LA-8 aircraft studied in this dissertation, which had 20 independent control effectors. The accurate aero-propulsive models developed using the techniques described in this dissertation enable development of high-fidelity eVTOL aircraft flight dynamics simulations that can be used to foster advancement of many other pertinent Advanced Air Mobility technology areas. The research advancements presented in this dissertation support revolutionary eVTOL vehicle technology development, enabling progress towards realizing future Urban Air Mobility and Regional Air Mobility transportation missions.

Bibliography

[1] Shakhatreh, H., Sawalmeh, A. H., Al-Fuqaha, A., Dou, Z., Almaita, E., Khalil, I., Othman, N. S., Khreishah, A., and Guizani, M., "Unmanned Aerial Vehicles (UAVs): A Survey on Civil Applications and Key Research Challenges," *IEEE Access*, Vol. 7, 2019, pp. 48572–48634. https://doi.org/10.1109/ACCESS.2019.2909530.

[2] Dorobantu, A., Murch, A., Mettler, B., and Balas, G., "System Identification for Small, Low-Cost, Fixed-Wing Unmanned Aircraft," *Journal of Aircraft*, Vol. 50, No. 4, 2013, pp. 1117–1130. https://doi.org/10.2514/1.C032065.

[3] Hoffer, N. V., Coopmans, C., Jensen, A. M., and Chen, Y., "A Survey and Categorization of Small Low-Cost Unmanned Aerial Vehicle System Identification," *Journal of Intelligent & Robotic Systems*, Vol. 74, No. 1, 2014, pp. 129–145. https://doi.org/10.1007/s10846-013-9931-6.

[4] Arifianto, O., and Farhood, M., "Development and Modeling of a Low-Cost Unmanned Aerial Vehicle Research Platform," *Journal of Intelligent & Robotic Systems*, Vol. 80, No. 1, 2015, pp. 139–164. https://doi.org/10.1007/s10846-014-0145-3.

[5] Grymin, D. J., and Farhood, M., "Two-Step System Identification and Trajectory Tracking Control of a Small Fixed-Wing UAV," *Journal of Intelligent & Robotic Systems*, Vol. 83, No. 1, 2016, pp. 105–131. https://doi.org/10.1007/s10846-015-0298-8.

[6] Hale, L. E., Patil, M., and Roy, C. J., "Aerodynamic Parameter Identification and Uncertainty Quantification for Small Unmanned Aircraft," *Journal of Guidance, Control, and Dynamics*, Vol. 40, No. 3, 2017, pp. 680–691. https://doi.org/10.2514/1.G000582.

[7] Alabsi, M. I., and Fields, T. D., "Real-Time Closed-Loop System Identification of a Quadcopter," *Journal of Aircraft*, Vol. 56, No. 1, 2019, pp. 324–335. https://doi.org/10.2514/1.C034219.

[8] Venkataraman, R., and Seiler, P., "System Identification for a Small, Rudderless, Fixed-Wing Unmanned Aircraft," *Journal of Aircraft*, Vol. 56, No. 3, 2019, pp. 1126–1134. https://doi.org/10.2514/1.C035141.

[9] Cunningham, M. A., and Hubbard, J. E., "Open-Loop Linear Model Identification of a Multirotor Vehicle with Active Feedback Control," *Journal of Aircraft*, Vol. 57, No. 6, 2020, pp. 1044–1061. https://doi.org/10.2514/1.C035834.

[10] Perry, A. T., Bretl, T., and Ansell, P. J., "System Identification of a Subscale Distributed Electric Propulsion Aircraft," *Journal of Aircraft*, Published online 20 September 2022, pp. 1–14 (Article in Advance). https://doi.org/10.2514/1.C036616.

[11] Johnson, W., Silva, C., and Solis, E., "Concept Vehicles for VTOL Air Taxi Operations," *AHS Technical Conference on Aeromechanics Design for Transformative Vertical Flight*, Jan. 2018.

[12] Silva, C., Johnson, W., Antcliff, K. R., and Patterson, M. D., "VTOL Urban Air Mobility Concept Vehicles for Technology Development," *2018 Aviation Technology, Integration, and Operations Conference*, AIAA Paper 2018-3847, Jun. 2018. https://doi.org/10.2514/6.2018-3847.

[13] Saeed, A. S., Younes, A. B., Cai, C., and Cai, G., "A Survey of Hybrid Unmanned Aerial Vehicles," *Progress in Aerospace Sciences*, Vol. 98, 2018, pp. 91–105. https://doi.org/10.1016/j.paerosci.2018.03.007.

[14] Kim, H. D., Perry, A. T., and Ansell, P. J., "A Review of Distributed Electric Propulsion Concepts for Air Vehicle Technology," *2018 AIAA/IEEE Electric Aircraft Technologies Symposium*, AIAA Paper 2018-4998, Jul. 2018. https://doi.org/10.2514/6.2018-4998.

[15] Johnson, W., and Silva, C., "NASA Concept Vehicles and the Engineering of Advanced Air Mobility Aircraft," *The Aeronautical Journal*, Vol. 126, No. 1295, 2022, pp. 59–91. https://doi.org/10.1017/aer.2021.92.

[16] "eVTOL Aircraft Directory," *Electric VTOL News™*, https://evtol.news/aircraft, Accessed 23 April 2023.

[17] Patterson, M. D., Antcliff, K. R., and Kohlman, L. W., "A Proposed Approach to Studying Urban Air Mobility Missions Including an Initial Exploration of Mission Requirements," *AHS International 74th Annual Forum & Technology Display*, American Helicopter Society, Fairfax, VA, May 2018.

[18] Antcliff, K. R., Whiteside, S. K. S., Kohlman, L. W., and Silva, C., "Baseline Assumptions and Future Research Areas for Urban Air Mobility Vehicles," *AIAA SciTech 2019 Forum*, AIAA Paper 2019-0528, Jan. 2019. https://doi.org/10.2514/6.2019-0528.

[19] Morelli, E. A., and Klein, V., *Aircraft System Identification: Theory and Practice*, 2nd ed., Sunflyte Enterprises, Williamsburg, VA, 2016.

[20] Jategaonkar, R. V., *Flight Vehicle System Identification: A Time-Domain Methodology*, 2nd ed., American Institute of Aeronautics and Astronautics, Reston, VA, 2015. https://doi.org/10.2514/4.102790.

[21] Tischler, M. B., and Remple, R. K., *Aircraft and Rotorcraft System Identification: Engineering Methods With Flight-Test Examples*, 2nd ed., American Institute of Aeronautics and Astronautics, Reston, VA, 2012. https://doi.org/10.2514/4.868207.

[22] Simmons, B. M., Gresham, J. L., and Woolsey, C. A., "Flight-Test System Identification Techniques and Applications for Small, Low-Cost, Fixed-Wing Aircraft," *Journal of Aircraft*, Accepted for publication 21 March 2023. https://doi.org/10.2514/1.C037260.

[23] Simmons, B. M., Gresham, J. L., and Woolsey, C. A., "Aero-Propulsive Modeling for Propeller Aircraft Using Flight Data," *AIAA SciTech 2022 Forum*, AIAA Paper 2022-2171, Jan. 2022. https://doi.org/10.2514/6.2022-2171.

[24] Simmons, B. M., Gresham, J. L., and Woolsey, C. A., "Aero-Propulsive Modeling for Propeller Aircraft Using Flight Data," *Journal of Aircraft*, Vol. 60, No. 1, 2023, pp. 81–96. https://doi.org/10.2514/1.C036773.

[25] Simmons, B. M., Gresham, J. L., and Woolsey, C. A., "Nonlinear Dynamic Model Identification for Aircraft with Unknown Mass Properties Using Flight Data," *AIAA SciTech 2023 Forum*, AIAA Paper 2023-0040, Jan. 2023. https://doi.org/10.2514/6.2023-0040.

[26] Simmons, B. M., Gresham, J. L., and Woolsey, C. A., "Nonlinear Dynamic Modeling for Aircraft with Unknown Mass Properties Using Flight Data," *Journal of Aircraft*, Published online 21 February 2023, pp. 1–13 (Article in Advance). https://doi.org/10.2514/1.C037259.

[27] Simmons, B. M., and Murphy, P. C., "Wind Tunnel-Based Aerodynamic Model Identification for a Tilt-Wing, Distributed Electric Propulsion Aircraft," *AIAA SciTech 2021 Forum*, AIAA Paper 2021-1298, Jan. 2021. https://doi.org/10.2514/6.2021-1298.

[28] Simmons, B. M., and Murphy, P. C., "Aero-Propulsive Modeling for Tilt-Wing, Distributed Propulsion Aircraft Using Wind Tunnel Data," *Journal of Aircraft*, Vol. 59, No. 5, 2022, pp. 1162–1178. https://doi.org/10.2514/1.C036351.

[29] Simmons, B. M., "Evaluation of Response Surface Experiment Designs for Distributed Propulsion Aircraft Aero-Propulsive Modeling," *AIAA SciTech 2023 Forum*, AIAA Paper 2023-2251, Jan. 2023. https://doi.org/10.2514/6.2023-2251.

[30] Simmons, B. M., Morelli, E. A., Busan, R. C., Hatke, D. B., and O'Neal, A. W., "Aero-Propulsive Modeling for eVTOL Aircraft Using Wind Tunnel Testing with Multisine Inputs," *AIAA AVIATION 2022 Forum*, AIAA Paper 2022-3603, Jun. 2022. https://doi.org/10.2514/6.2022-3603.

[31] Simmons, B. M., "System Identification for eVTOL Aircraft Using Simulated Flight Data," *AIAA SciTech 2022 Forum*, AIAA Paper 2022-2409, Jan. 2022. https://doi.org/10.2514/6.2022-2409.

[32] Simmons, B. M., "System Identification Approach for eVTOL Aircraft Demonstrated Using Simulated Flight Data," *Journal of Aircraft*, Published online 30 January 2023, pp. 1–16 (Article in Advance). https://doi.org/10.2514/1.C036896.

[33] Simmons, B. M., "System Identification of a Nonlinear Flight Dynamics Model for a Small, Fixed-Wing UAV," Master's thesis, Virginia Tech, Blacksburg, VA, Apr. 2018.

[34] Simmons, B. M., McClelland, H. G., and Woolsey, C. A., "Nonlinear Model Identification Methodology for Small, Fixed-Wing, Unmanned Aircraft," *Journal of Aircraft*, Vol. 56, No. 3, 2019, pp. 1056–1067. https://doi.org/10.2514/1.C035160.

[35] Simmons, B. M., "System Identification for Propellers at High Incidence Angles," *AIAA SciTech 2021 Forum*, AIAA Paper 2021-1190, Jan. 2021. https://doi.org/10.2514/6.2021-1190.

[36] Simmons, B. M., and Hatke, D. B., "Investigation of High Incidence Angle Propeller Aerodynamics for Subscale eVTOL Aircraft," NASA TM–20210014010, May 2021.

[37] Simmons, B. M., "System Identification for Propellers at High Incidence Angles," *Journal of Aircraft*, Vol. 58, No. 6, 2021, pp. 1336–1350. https://doi.org/10.2514/1.C036329.

[38] Simmons, B. M., "Efficient Variable-Pitch Propeller Aerodynamic Model Development for Vectored-Thrust eVTOL Aircraft," *AIAA AVIATION 2022 Forum*, AIAA Paper 2022-3817, Jun. 2022. https://doi.org/10.2514/6.2022-3817.

[39] Simmons, B. M., Buning, P. G., and Murphy, P. C., "Full-Envelope Aero-Propulsive Model Identification for Lift+Cruise Aircraft Using Computational Experiments," *AIAA AVIATION 2021 Forum*, AIAA Paper 2021-3170, Aug. 2021. https://doi.org/10.2514/6.2021-3170.

[40] Thurman, C. S., Boyd Jr., D. D., and Simmons, B. M., "Comparison of Prediction Modeling Methodologies for Aeroacoustic Characterization of Hovering sUAS Rotors," *AIAA SciTech 2023 Forum*, AIAA Paper 2023-0027, Jan. 2023. https://doi.org/10.2514/6.2023-0027.

[41] Simmons, B. M., Geuther, S. C., and Ahuja, V., "Validation of a Mid-Fidelity Approach for Aircraft Stability and Control Characterization," *AIAA AVIATION 2023 Forum*, June 2023. To be published.

[42] Gresham, J. L., Simmons, B. M., Fahmi, J.-M. W., and Woolsey, C. A., "Remote Uncorrelated Pilot Inputs for Nonlinear Aerodynamic Model Identification from Flight Data," *AIAA AVIATION 2021 Forum*, AIAA Paper 2021-2792, Aug. 2021. https://doi.org/10.2514/6.2021-2792.

[43] Gresham, J. L., Simmons, B. M., Fahmi, J.-M. W., Hopwood, J. W., and Woolsey, C. A., "Remote Uncorrelated Pilot Input Excitation Assessment for Unmanned Aircraft Aerodynamic Modeling," *Journal of Aircraft*, Published online 31 March 2023, pp. 1–13 (Article in Advance). https://doi.org/10.2514/1.C036942.

[44] Gresham, J. L., Simmons, B. M., Hopwood, J. W., and Woolsey, C. A., "Spin Aerodynamic Modeling for a Fixed-Wing Aircraft Using Flight Data," *AIAA SciTech 2022 Forum*, AIAA Paper 2022-1160, Jan. 2022. https://doi.org/10.2514/6.2022-1160.

[45] Gresham, J. L., Simmons, B. M., Hopwood, J. W., and Woolsey, C. A., "Spin Aerodynamic Modeling for a Fixed-Wing Aircraft Using Flight Data," Submitted to a journal for consideration.

[46] Busan, R. C., Murphy, P. C., Hatke, D. B., and Simmons, B. M., "Wind Tunnel Testing Techniques for a Tandem Tilt-Wing, Distributed Electric Propulsion VTOL Aircraft," *AIAA SciTech 2021 Forum*, AIAA Paper 2021-1189, Jan. 2021. https://doi.org/10.2514/6.2021-1189.

[47] Murphy, P. C., Simmons, B. M., Hatke, D. B., and Busan, R. C., "Rapid Aero Modeling for Urban Air Mobility Aircraft in Wind-Tunnel Tests," *AIAA SciTech 2021 Forum*, AIAA Paper 2021-1644, Jan. 2021. https://doi.org/10.2514/6.2021-1644.

[48] Murphy, P. C., Buning, P. G., and Simmons, B. M., "Rapid Aero Modeling for Urban Air Mobility Aircraft in Computational Experiments," *AIAA SciTech 2021 Forum*, AIAA Paper 2021-1002, Jan. 2021. https://doi.org/10.2514/6.2021-1002.

[49] "PX4 Autopilot," https://px4.io/, Accessed 04 June 2022.

[50] "System IDentification Programs for AirCraft (SIDPAC)," NASA Technology Transfer Program, https://software.nasa.gov/software/LAR-16100-1, Accessed 04 June 2022.

[51] "Kentland Experimental Aerial Systems (KEAS) Laboratory," https://www.aoe.vt.edu/research/facilities/keas.html, Accessed 04 June 2022.

[52] "WeatherSTEM, Virginia Tech Kentland Farm Conditions," https://montgomery.weatherstem.com/kentlandfarm, Accessed 23 July 2022.

[53] Cotting, M. C., Murtha, J., Techy, L., and Woolsey, C., "Examples of Augmentation of an Atmospheric Flight Mechanics Curriculum Using UAVs," *AIAA Atmospheric Flight Mechanics Conference*, AIAA Paper 2009-5852, Aug. 2009. https://doi.org/10.2514/6.2009-5852.

[54] Murtha, J., Cotting, M. C., Wolek, A., Aarons, T., and Woolsey, C., "The Educational Impact of Creating a New UAV for Curriculum Enhancement," *AIAA Atmospheric Flight Mechanics Conference*, AIAA Paper 2009-5851, Aug. 2009. https://doi.org/10.2514/6.2009-5851.

[55] Cotting, M. C., Wolek, A., Murtha, J., and Woolsey, C., "Developmental Flight Testing of the SPAARO UAV," *48th AIAA Aerospace Sciences Meeting Including the New Horizons Forum and Aerospace Exposition*, AIAA Paper 2010-295, Jan. 2010. https://doi.org/10.2514/6.2010-295.

[56] Gresham, J. L., "Aerodynamic Modeling in Nonlinear Regions, including Stall Spins, for Fixed-Wing Unmanned Aircraft from Experimental Flight Data," Ph.D. Dissertation, Virginia Tech, Blacksburg, Virginia, Mar. 2022.

[57] Gresham, J. L., Fahmi, J.-M. W., Simmons, B. M., Hopwood, J. W., Foster, W., and Woolsey, C. A., "Flight Test Approach for Modeling and Control Law Validation for Unmanned Aircraft," *AIAA SciTech 2022 Forum*, AIAA Paper 2022-2406, Jan. 2022. https://doi.org/10.2514/6.2022-2406.

[58] "Cube Orange Flight Controller," *PX4 User Guide*, https://docs.px4.io/main/en/flight_controller/cubepilot_cube_orange.html, Accessed 23 July 2022.

[59] "MAVLink Developer Guide," https://mavlink.io/en/, Accessed 29 April 2023.

[60] "NSL@VT GitHub Repository," https://github.com/NSL-VT, Accessed 04 June 2022.

[61] Asper, G. D., and Simmons, B. M., "Rapid Flight Control Law Deployment and Testing Framework for Subscale VTOL Aircraft," NASA TM–20220011570, Sep. 2022.

[62] "Using the ECL EKF," *PX4 User Guide*, https://docs.px4.io/main/en/advanced_config/tuning_the_ecl_ekf.html, Accessed 23 July 2022.

[63] "National Weather Service Hourly Forecast," https://forecast.weather.gov/MapClick.php?lat=37.1971&lon=-80.5780&smap=1&unit=0&lg=en&FcstType=graphical, Accessed 01 May 2022.

[64] "QGroundControl," http://qgroundcontrol.com/, Accessed 04 June 2022.

[65] "FlightAware," *FlightAware PiAware*, https://flightaware.com/adsb/piaware/build/, Accessed 09 June 2022.

[66] Tangirala, A. K., *Principles of System Identification: Theory and Practice*, CRC Press, Boca Raton, FL, 2014.

[67] Ljung, L., *System Identification: Theory for the User*, PTR Prentice Hall, Upper Saddle River, NJ, 1999.

[68] Etkin, B., and Reid, L. D., *Dynamics of Flight: Stability and Control*, 3rd ed., John Wiley & Sons, Inc, New York, NY, 1996.

[69] Gainer, T. G., and Hoffman, S., "Summary of Transformation Equations and Equations of Motion Used in Free Flight and Wind Tunnel Data Reduction and Analysis," NASA SP-3070, 1972.

[70] Morelli, E. A., "Practical Aspects of the Equation-Error Method for Aircraft Parameter Estimation," *AIAA Atmospheric Flight Mechanics Conference and Exhibit*, AIAA Paper 2006-6144, Aug. 2006. https://doi.org/10.2514/6.2006-6144.

[71] Grauer, J. A., and Morelli, E. A., "Generic Global Aerodynamic Model for Aircraft," *Journal of Aircraft*, Vol. 52, No. 1, 2015, pp. 13–20. https://doi.org/10.2514/1.C032888.

[72] Stevens, B. L., Lewis, F. L., and Johnson, E. N., *Aircraft Control and Simulation: Dynamics, Controls Design, and Autonomous Systems*, 3rd ed., John Wiley & Sons, Hoboken, NJ, 2015.

[73] Phillips, W. F., *Mechanics of Flight*, 2nd ed., John Wiley & Sons, Hoboken, NJ, 2010.

[74] McClelland, H. G., "Towards Detecting Atmospheric Coherent Structures using Small Fixed-Wing Unmanned Aircraft," Ph.D. Dissertation, Virginia Tech, Blacksburg, Virginia, May 2019.

[75] González-Rocha, J., Woolsey, C. A., Sultan, C., and De Wekker, S. F. J., "Sensing Wind from Quadrotor Motion," *Journal of Guidance, Control, and Dynamics*, Vol. 42, No. 4, 2019, pp. 836–852. https://doi.org/10.2514/1.G003542.

[76] González-Rocha, J., Woolsey, C. A., Sultan, C., and De Wekker, S. F., "Model-based Wind profiling in the Lower Atmosphere with Multirotor UAS," *AIAA SciTech 2019 Forum*, AIAA Paper 2019-1598, 2019. https://doi.org/10.2514/6.2019-1598.

[77] Halefom, M. H., Gresham, J. L., and Woolsey, C. A., "Wind Estimation from an Unsteady Aerodynamic Aircraft Motion Model," *AIAA SciTech 2022 Forum*, AIAA Paper 2022-0554, Jan. 2022. https://doi.org/10.2514/6.2022-0554.

[78] Chen, Y.-C., and Woolsey, C. A., "Nonlinear, Model-Based Disturbance Estimation for Fixed-Wing Aircraft," *AIAA SciTech 2021 Forum*, AIAA Paper 2021-0018, Jan. 2021. https://doi.org/10.2514/6.2021-0018.

[79] Fahmi, J.-M., and Woolsey, C. A., "Port-Hamiltonian Flight Control of a Fixed-Wing Aircraft," *IEEE Transactions on Control Systems Technology*, Vol. 30, No. 1, 2022, pp. 408–415. https://doi.org/10.1109/TCST.2021.3059928.

[80] Hopwood, J. W., Gresham, J. L., and Woolsey, C. A., "Robust Stall Spin Flight Path Control with Flight Test Validation," *Journal of Guidance, Control, and Dynamics*, Vol. 46, No. 3, 2023, pp. 553–559. https://doi.org/10.2514/1.G007016.

[81] Fahmi, J.-M. W., Gresham, J. L., and Woolsey, C. A., "Experimental Validation of Port-Hamiltonian-Based Control for Fixed-Wing Unmanned Aircraft," *Journal of Guidance, Control, and Dynamics*, Published online 25 April 2023, pp. 1–7 (Article in Advance). https://doi.org/10.2514/1.G007018.

[82] Morelli, E. A., "Multiple Input Design for Real-Time Parameter Estimation in the Frequency Domain," *13th IFAC Conference on System Identification*, Aug. 2003. https://doi.org/10.1016/S1474-6670(17)34833-4.

[83] Morelli, E. A., "Flight-Test Experiment Design for Characterizing Stability and Control of Hypersonic Vehicles," *Journal of Guidance, Control, and Dynamics*, Vol. 32, No. 3, 2009, pp. 949–959. https://doi.org/10.2514/1.37092.

[84] Morelli, E. A., "Flight Test Maneuvers for Efficient Aerodynamic Modeling," *Journal of Aircraft*, Vol. 49, No. 6, 2012, pp. 1857–1867. https://doi.org/10.2514/1.C031699.

[85] Morelli, E. A., "Practical Aspects of Multiple-Input Design for Aircraft System Identification Flight Tests," *AIAA AVIATION 2021 Forum*, AIAA Paper 2021-2795, Aug. 2021. https://doi.org/10.2514/6.2021-2795.

[86] Brandon, J. M., and Morelli, E. A., "Nonlinear Aerodynamic Modeling From Flight Data Using Advanced Piloted Maneuvers and Fuzzy Logic," NASA TM–2012-217778, Oct. Oct. 2012.

[87] Morelli, E. A., Cunningham, K., and Hill, M. A., "Global Aerodynamic Modeling for Stall/Upset Recovery Training Using Efficient Piloted Flight Test Techniques," *AIAA Modeling and Simulation Technologies (MST) Conference*, AIAA Paper 2013-4976, Aug. 2013. https://doi.org/10.2514/6.2013-4976.

[88] Brandon, J. M., and Morelli, E. A., "Real-Time Onboard Global Nonlinear Aerodynamic Modeling from Flight Data," *Journal of Aircraft*, Vol. 53, No. 5, 2016, pp. 1261–1297. https://doi.org/10.2514/1.C033133.

[89] "ULog File Format," *PX4 User Guide*, https://docs.px4.io/main/en/dev_log/ulog_file_format.html, Accessed 23 July 2022.

[90] "MATLAB Documentation," *MathWorks*, https://www.mathworks.com/help/matlab/, Accessed 14 January 2023.

[91] Riseborough, P., "PX4 State Estimation Update," *PX4 Developer Summit*, June 2019, https://px4.io/px4-developer-summit-zurich-2019/, Accessed 30 April 2023.

[92] Fritsch, F. N., and Carlson, R. E., "Monotone Piecewise Cubic Interpolation," *SIAM Journal on Numerical Analysis*, Vol. 17, No. 2, 1980, pp. 238–246. https://doi.org/10.1137/0717021.

[93] Moler, C. B., *Numerical Computing with MATLAB*, Society for Industrial and Applied Mathematics, Philadelphia, PA, 2004. https://doi.org/10.1137/1.9780898717952.

[94] Gustafsson, F., "Determining the Initial States in Forward-Backward Filtering," *IEEE Transactions on Signal Processing*, Vol. 44, No. 4, 1996, pp. 988–992. https://doi.org/10.1109/78.492552.

[95] Grauer, J. A., "Position Corrections for Airspeed and Flow Angle Measurements on Fixed-Wing Aircraft," NASA TM-2017-219795, Nov. 2017.

[96] Steers, S. T., and Iliff, K. W., "Effects of Time-Shifted Data on Flight-Determined Stability and Control Derivatives," NASA TN D-7830, Mar. 1975.

[97] Morelli, E. A., "Dynamic Modeling from Flight Data with Unknown Time Skews," *Journal of Guidance, Control, and Dynamics*, Vol. 40, No. 8, 2017, pp. 2084–2092. https://doi.org/10.2514/1.G002008.

[98] Morelli, E. A., "Estimating Noise Characteristics from Flight Test Data using Optimal Fourier Smoothing," *Journal of Aircraft*, Vol. 32, No. 4, 1995, pp. 689–695. https://doi.org/10.2514/3.46778.

[99] Morelli, E. A., and Klein, V., "Accuracy of Aerodynamic Model Parameters Estimated from Flight Test Data," *Journal of Guidance, Control, and Dynamics*, Vol. 20, No. 1, 1997, pp. 74–80. https://doi.org/10.2514/2.3997.

[100] Morelli, E. A., and Grauer, J. A., "Practical Aspects of Frequency-Domain Approaches for Aircraft System Identification," *Journal of Aircraft*, Vol. 57, No. 2, 2020, pp. 268–291. https://doi.org/10.2514/1.C035599.

[101] Morelli, E. A., "High Accuracy Evaluation of the Finite Fourier Transform Using Sampled Data," NASA TM-110340, Jun. 1997.

[102] Morelli, E. A., "Global Nonlinear Aerodynamic Modeling Using Multivariate Orthogonal Functions," *Journal of Aircraft*, Vol. 32, No. 2, 1995, pp. 270–277. https://doi.org/10.2514/3.46712.

[103] Klein, V., Batterson, J. G., and Murphy, P. C., "Determination of Airplane Model Structure from Flight Data by Using Modified Stepwise Regression," NASA TP-1916, Oct. 1981.

[104] Barron, A. R., "Predicted Squared Error: A Criterion for Automatic Model Selection," *Self-Organizing Methods in Modeling*, Farlow, S. J., Ed., Marcel Dekker, Inc., New York, NY, 1984, pp. 87–104.

[105] Morelli, E. A., "Real-Time Global Nonlinear Aerodynamic Modeling for Learn-To-Fly," *AIAA Atmospheric Flight Mechanics Conference*, AIAA Paper 2016-2010, Jan. 2016. https://doi.org/10.2514/6.2016-2010.

[106] Morelli, E. A., "Practical Aspects of Real-Time Modeling for the Learn-To-Fly Concept," *2018 Atmospheric Flight Mechanics Conference*, AIAA Paper 2018-3309, Jun. 2018. https://doi.org/10.2514/6.2018-3309.

[107] Morelli, E. A., "Transfer Function Identification using Orthogonal Fourier Transform Modeling Functions," *AIAA Atmospheric Flight Mechanics (AFM) Conference*, AIAA Paper 2013-4749, Aug. 2013. https://doi.org/10.2514/6.2013-4749.

[108] Morelli, E. A., and Cooper, J., "Frequency-Domain Method for Automated Simulation Updates Based on Flight Data," *Journal of Aircraft*, Vol. 52, No. 6, 2015, pp. 1995–2008. https://doi.org/10.2514/1.C033121.

[109] Belsley, D. A., Kuh, E., and Welsch, R. E., *Regression Diagnostics: Identifying Influential Data and Sources of Collinearity*, John Wiley & Sons, Hoboken, NJ, 2004.

[110] Tischler, M. B., and Barlow, J. B., "Determination of the Spin and Recovery Characteristics of a General Aviation Design," *Journal of Aircraft*, Vol. 18, No. 4, 1981, pp. 238–244. https://doi.org/10.2514/3.57487.

[111] Bihrle, W., and Barnhart, B., "Spin Prediction Techniques," *Journal of Aircraft*, Vol. 20, No. 2, 1983, pp. 97–101. https://doi.org/10.2514/3.44837.

[112] Murch, A. M., and Foster, J. V., "Recent NASA Research on Aerodynamic Modeling of Post-Stall and Spin Dynamics of Large Transport Airplanes," *45th AIAA Aerospace Sciences Meeting and Exhibit*, AIAA Paper 2007-463, Jan. 2007. https://doi.org/10.2514/6.2007-463.

[113] Craig, A., and Romani, D., Jr., "Unsteady Aerodynamics in Airplane Stall-Spin Departure," *31st Aerospace Sciences Meeting*, AIAA Paper 1993-0622, Jan. 1993. https://doi.org/10.2514/6.1993-622.

[114] Brandt, J. B., and Selig, M. S., "Propeller Performance Data at Low Reynolds Numbers," *49th AIAA Aerospace Sciences Meeting including the New Horizons Forum and Aerospace Exposition*, AIAA Paper 2011-1255, Jan. 2011. https://doi.org/10.2514/6.2011-1255.

[115] Deters, R. W., Ananda, G. K., and Selig, M. S., "Reynolds Number Effects on the Performance of Small-Scale Propellers," *32nd AIAA Applied Aerodynamics Conference*, AIAA Paper 2014-2151, Jun. 2014. https://doi.org/10.2514/6.2014-2151.

[116] Dantsker, O. D., Caccamo, M., Deters, R. W., and Selig, M. S., "Performance Testing of Aero-Naut CAM Folding Propellers," *AIAA AVIATION 2020 Forum*, AIAA Paper 2020-2762, Jun. 2020. https://doi.org/10.2514/6.2020-2762.

[117] Kimberlin, R. D., *Flight Testing of Fixed-Wing Aircraft*, American Institute of Aeronautics and Astronautics, Reston ,VA, 2003. https://doi.org/10.2514/4.861840.

[118] Gong, A., Maunder, H., and Verstraete, D., "Development of an in-flight thrust measurement system for UAVs," *53rd AIAA/SAE/ASEE Joint Propulsion Conference*, AIAA Paper 2017-5092, Jul. 2017. https://doi.org/10.2514/6.2017-5092.

[119] Sabzehparvar, M., "In-Flight Thrust Measurements of Propeller-Driven Airplanes," *Journal of Aircraft*, Vol. 42, No. 6, 2005, pp. 1543–1547. https://doi.org/10.2514/1.12837.

[120] Bazin, J. M., Fields, T. D., and Smith, A. J., "Feasibility of In-Flight Quadrotor Individual Motor Thrust Measurements," *AIAA Atmospheric Flight Mechanics Conference*, AIAA Paper 2016-1760, Jan. 2016. https://doi.org/10.2514/6.2016-1760.

[121] Bronz, M., and Hattenberger, G., "Aerodynamic Characterization of an Off-the-Shelf Aircraft via Flight Test and Numerical Simulation," *AIAA Flight Testing Conference*, AIAA Paper 2016-3979, Jun. 2016. https://doi.org/10.2514/6.2016-3979.

[122] Bronz, M., Garcia de Marina, H., and Hattenberger, G., "In-Flight Thrust Measurement using On-Board Force Sensor," *AIAA Atmospheric Flight Mechanics Conference*, AIAA Paper 2017-0698, Jan. 2017. https://doi.org/10.2514/6.2017-0698.

[123] Bergmann, D. P., Denzel, J., Pfeifle, O., Notter, S., Fichter, W., and Strohmayer, A., "In-flight Lift and Drag Estimation of an Unmanned Propeller-Driven Aircraft," *Aerospace*, Vol. 8, No. 2, 2021. https://doi.org/10.3390/aerospace8020043.

[124] Pfeifle, O., Fichter, W., Bergmann, D., Denzel, J., Strohmayer, A., Schollenberger, M., and Lutz, T., "Precision Performance Measurements of Fixed-Wing Aircraft with Wing Tip Propellers," *AIAA Aviation 2019 Forum*, AIAA Paper 2019-3088, Jun. 2019. https://doi.org/10.2514/6.2019-3088.

[125] Pfeifle, O., Notter, S., Fichter, W., Paul Bergmann, D., Denzel, J., and Strohmayer, A., "Verifying the Effect of Wingtip Propellers on Drag Through In-Flight Measurements," *Journal of Aircraft*, Vol. 59, No. 2, 2022, pp. 474–483. https://doi.org/10.2514/1.C036490.

[126] Ahsun, U., Badar, T., Tahir, S., and Aldosari, S., "Real-time Identification of Propeller-Engine Parameters for Fixed Wing UAVs," *IFAC-PapersOnLine*, Vol. 48, No. 28, 2015, pp. 1082–1087. https://doi.org/10.1016/j.ifacol.2015.12.275.

[127] Perez, T., de Lamberterie, P., Donaire, A., and Herrero, E. R., "Parameter Estimation of Thrust Models of Uninhabited Airborne Systems," *IFAC Proceedings Volumes*, Vol. 43, No. 16, 2010, pp. 354–359. https://doi.org/10.3182/20100906-3-IT-2019.00062.

[128] Gremillion, G., and Humbert, J. S., "System Identification of a Quadrotor Micro Air Vehicle," *AIAA Atmospheric Flight Mechanics Conference*, AIAA Paper 2010-7644, Aug. 2010. https://doi.org/10.2514/6.2010-7644.

[129] Wei, W., Cohen, K., and Tischler, M. B., "System Identification and Controller Optimization of a Quadrotor UAV," *AHS 71st Annual Forum*, May 2015.

[130] Niermeyer, P., Raffler, T., and Holzapfel, F., "Open-Loop Quadrotor Flight Dynamics Identification in Frequency Domain via Closed-Loop Flight Testing," *AIAA Guidance, Navigation, and Control Conference*, AIAA Paper 2015-1539, Jan. 2015. https://doi.org/10.2514/6.2015-1539.

[131] Tobias, E. L., Sanders, F. C., and Tischler, M. B., "Full-Envelope Stitched Simulation Model of a Quadcopter Using STITCH," *AHS International 74th Annual Forum & Technology Display*, May 2018.

[132] Sun, S., de Visser, C. C., and Chu, Q., "Quadrotor Gray-Box Model Identification from High-Speed Flight Data," *Journal of Aircraft*, Vol. 56, No. 2, 2019, pp. 645–661. https://doi.org/10.2514/1.C035135.

[133] Gong, A., Sanders, F. C., Hess, R. A., and Tischler, M. B., "System Identification and Full Flight-Envelope Model Stitching of a Package-Delivery Octocopter," *AIAA SciTech 2019 Forum*, AIAA Paper 2019-1076, Jan. 2019. https://doi.org/10.2514/6.2019-1076.

[134] Cho, S. H., Bhandari, S., Sanders, F. C., Cheung, K. K., and Tischler, M. B., "System Identification and Controller Optimization of Coaxial Quadrotor UAV in Hover," *AIAA SciTech 2019 Forum*, AIAA Paper 2019-1075, Jan. 2019. https://doi.org/10.2514/6.2019-1075.

[135] Yuksek, B., Saldiran, E., Cetin, A., Yeniceri, R., and Inalhan, G., "System Identification and Model-Based Flight Control System Design for an Agile Maneuvering Quadrotor Platform," *AIAA SciTech 2020 Forum*, AIAA Paper 2020-1835, Jan. 2020. https://doi.org/10.2514/6.2020-1835.

[136] Kaputa, D. S., and Owens, K. J., "Quadrotor Drone System Identification via Model-Based Design and In-Flight Sine Wave Injections," *AIAA SciTech 2020 Forum*, AIAA Paper 2020-1238, Jan. 2020. https://doi.org/10.2514/6.2020-1238.

[137] Murphy, P. C., and Landman, D., "Experiment Design for Complex VTOL Aircraft with Distributed Propulsion and Tilt Wing," *AIAA Atmospheric Flight Mechanics Conference*, AIAA Paper 2015-0017, Jan. 2015. https://doi.org/10.2514/6.2015-0017.

[138] Perry, A. T., Ansell, P. J., and Kerho, M. F., "Aero-Propulsive and Propulsor Cross-Coupling Effects on a Distributed Propulsion System," *Journal of Aircraft*, Vol. 55, No. 6, 2018, pp. 2414–2426. https://doi.org/10.2514/1.C034861.

[139] Perry, A. T., Bretl, T., and Ansell, P. J., "Aeropropulsive Coupling Effects on a General-Aviation Aircraft with Distributed Electric Propulsion," *Journal of Aircraft*, Vol. 58, No. 6, 2021, pp. 1351–1363. https://doi.org/10.2514/1.C036048.

[140] Morelli, E. A., "Autonomous Real-Time Global Aerodynamic Modeling in the Frequency Domain," *AIAA SciTech 2020 Forum*, AIAA Paper 2020-0761, Jan. 2020. https://doi.org/10.2514/6.2020-0761.

[141] McCormick, B. W., *Aerodynamics, Aeronautics, and Flight Mechanics*, 2nd ed., John Wiley & Sons, New York, NY, 1995.

[142] Dommasch, D. O., *Elements of Propeller and Helicopter Aerodynamics*, Pitman Publishing Corporation, New York, NY, 1953.

[143] Greitzer, E. M., Spakovszky, Z. S., and Waitz, I. A., "Thermodynamics and Propulsion," *Lecture Notes, Massachusetts Institute of Technology*, 2006. http://web.mit.edu/16.unified/www/FALL/thermodynamics/notes/node86.html, Accessed 07 November 2021.

[144] Singleton, J. D., and Yeager, W. T., "Important Scaling Parameters for Testing Model-Scale Helicopter Rotors," *Journal of Aircraft*, Vol. 37, No. 3, 2000, pp. 396–402. https://doi.org/10.2514/2.2639.

[145] Leishman, J. G., *Principles of Helicopter Aerodynamics*, 2nd ed., Cambridge University Press, Cambridge, England, U.K., 2016.

[146] Johnson, W., *Rotorcraft Aeromechanics*, Cambridge University Press, Cambridge, England, U.K., 2013.

[147] Ribner, H. S., "Propellers in Yaw," NACA TR-820, 1945.

[148] Ribner, H. S., "Formulas for Propellers in Yaw and Charts of the Side-Force Derivative," NACA TR-819, 1945.

[149] Crigler, J. L., and Gilman Jr., J., "Calculation of Aerodynamic Forces on a Propeller in Pitch or Yaw," NACA TN-2585, Jan. 1952.

[150] De Young, J., "Propeller at High Incidence," *Journal of Aircraft*, Vol. 2, No. 3, 1965, pp. 241–250. https://doi.org/10.2514/3.43646.

[151] Smith, H. R., "Engineering Models of Aircraft Propellers at Incidence," Ph.D. thesis, University of Glasgow, Glasgow, Scotland, U.K., Jan. 2015.

[152] McCormick, B. W., Aljabri, A. S., Jumper, S. J., and Martinovic, Z. N., "The Analysis of Propellers Including Interaction Effects," NASA CR-158111, 1979.

[153] Theys, B., Dimitriadis, G., Hendrick, P., and De Schutter, J., "Experimental and Numerical Study of Micro-Aerial-Vehicle Propeller Performance in Oblique Flow," *Journal of Aircraft*, Vol. 54, No. 3, 2017, pp. 1076–1084. https://doi.org/10.2514/1.C033618.

[154] Leng, Y., Yoo, H., Jardin, T., Bronz, M., and Moschetta, J.-M., "Aerodynamic Modeling of Propeller Forces and Moments at High Angle of Incidence," *AIAA SciTech 2019 Forum*, AIAA Paper 2019-1332, Jan. 2019. https://doi.org/10.2514/6.2019-1332.

[155] Fei, X., Litherland, B. L., and German, B. J., "Development of an Unsteady Vortex Lattice Method to Model Propellers at Incidence," *AIAA Journal*, Vol. 60, No. 1, 2022, pp. 176–188. https://doi.org/10.2514/1.J060133.

[156] McLemore, H. C., and Cannon, M. D., "Aerodynamic Investigation of a Four-Blade Propeller Operating through an Angle-of-Attack Range from 0° to 180°," NACA TN-3228, Jun. 1954.

[157] Yaggy, P. F., and Rogallo, V. L., "A Wind-Tunnel Investigation of Three Propellers Through an Angle-of-Attack Range from 0° to 85°," NASA TN D-318, May 1960.

[158] Kuhn, R. E., and Draper, J. W., "Investigation of the Aerodynamic Characteristics of a Model Wing-Propeller Combination and of the Wing and Propeller Separately at Angles of Attack up to 90 Degrees," NACA TR-1263, 1956.

[159] Theys, B., Dimitriadis, G., Andrianne, T., Hendrick, P., and De Schutter, J., "Wind Tunnel Testing of a VTOL MAV Propeller in Tilted Operating Mode," *2014 International Conference on Unmanned Aircraft Systems (ICUAS)*, May 2014, pp. 1064–1072. https://doi.org/10.1109/ICUAS.2014.6842358.

[160] Leng, Y., Jardin, T., Bronz, M., and Moschetta, J.-M., "Experimental Analysis of Propeller Forces and Moments at High Angle of Incidence," *AIAA SciTech 2019 Forum*, AIAA Paper 2019-1331, Jan. 2019. https://doi.org/10.2514/6.2019-1331.

[161] Brandt, J. B., Deters, R. W., Ananda, G. K., Dantsker, O. D., and Selig, M. S., *UIUC Propeller Database*, Vol. 3, University of Illinois at Urbana-Champaign, 2020. https://m-selig.ae.illinois.edu/props/propDB.html, Accessed 16 October 2021.

[162] Grauer, J. A., Morelli, E. A., and Murri, D. G., "Flight-Test Techniques for Quantifying Pitch Rate and Angle-of-Attack Rate Dependencies," *Journal of Aircraft*, Vol. 54, No. 6, 2017, pp. 2367–2377. https://doi.org/10.2514/1.C034407.

[163] McCormick Jr., B. W., *Aerodynamics of V/STOL Flight*, Dover Publications, Inc., Mineola, NY, 1999.

[164] Gallais, P., *Atmospheric Re-Entry Vehicle Mechanics*, Springer, New York, 2007.

[165] Morelli, E. A., "Determining Aircraft Moments of Inertia from Flight Test Data," *Journal of Guidance, Control, and Dynamics*, Vol. 45, No. 1, 2022, pp. 4–14. https://doi.org/10.2514/1.G006072.

[166] Khan, W., and Nahon, M., "Development and Validation of a Propeller Slipstream Model for Unmanned Aerial Vehicles," *Journal of Aircraft*, Vol. 52, No. 6, 2015, pp. 1985–1994. https://doi.org/10.2514/1.C033118.

[167] Brandt, J. B., Deters, R. W., Ananda, G. K., Dantsker, O. D., and Selig, M. S., *UIUC Propeller Database*, Vol. 1, University of Illinois at Urbana-Champaign, 2015. https://m-selig.ae.illinois.edu/props/propDB.html, Accessed 16 October 2021.

[168] "APC Propeller Performance Data," https://www.apcprop.com/technical-information/performance-data/, Accessed 01 May 2021.

[169] Hall, D. K., Huang, A. C., Uranga, A., Greitzer, E. M., Drela, M., and Sato, S., "Boundary Layer Ingestion Propulsion Benefit for Transport Aircraft," *Journal of Propulsion and Power*, Vol. 33, No. 5, 2017, pp. 1118–1129. https://doi.org/10.2514/1.B36321.

[170] Pegram, J. P., and Anemaat, W. A., "Preliminary Estimation of Airplane Moments of Inertia using CAD Solid Modeling," SAE Technical Paper 2000-01-1700, May 2000. https://doi.org/10.4271/2000-01-1700.

[171] Jordan, T., Langford, W., and Hill, J., "Airborne Subscale Transport Aircraft Research Testbed - Aircraft Model Development," *AIAA Guidance, Navigation, and Control Conference and Exhibit*, AIAA Paper 2005-6432, Aug. 2005. https://doi.org/10.2514/6.2005-6432.

[172] Parikh, K., Dogan, A., Subbarao, K., Reyes, A., and Huff, B., "CAE Tools for Modeling Inertia and Aerodynamic Properties of an RC Airplane," *AIAA Atmospheric Flight Mechanics Conference*, AIAA Paper 2009-6043, Aug. 2009. https://doi.org/10.2514/6.2009-6043.

[173] Mutluay, T., "The Development of an Inertia Estimation Method to Support Handling Quality Assessment," Master's thesis, Delft University of Technology, Delft, Netherlands, Sep. 2015.

[174] McDonald, R. A., and Gloudemans, J. R., "Open Vehicle Sketch Pad: An Open Source Parametric Geometry and Analysis Tool for Conceptual Aircraft Design," *AIAA SciTech 2022 Forum*, AIAA Paper 2022-0004, Jan. 2022. https://doi.org/10.2514/6.2022-0004.

[175] Green, M. W., "Measurement of the Moments of Inertia of Full Scale Airplanes," NACA TN 265, 1927.

[176] Miller, M. P., "An Accurate Method of Measuring the Moments of Inertia of Airplanes," NACA TN 351, 1930.

[177] Soulé, H. A., and Miller, M. P., "The Experimental Determination of the Moments of Inertia of Airplanes," NACA Report No. 467, 1933.

[178] Gracey, W., "Experimental Determination of the Moments of Inertia of Airplanes by a Simplified Compound-Pendulum Method," NACA TN 1629, 1948.

[179] Turner, H. L., "Measurement of the Moments of Inertia of an Airplane by a Simplified Method," NACA TN 2201, 1950.

[180] Wener, N. L., "Measurement of Aircraft Moments of Inertia," AGARD Report 248, 1959.

[181] Wolowicz, C. H., and Yancy, R. B., "Experimental Determination of Airplane Mass and Inertial Characteristics," NASA TR R-433, 1974.

[182] de Jong, R., and Mulder, J. A., "Accurate Estimation of Aircraft Inertia Characteristics from a Single Suspension Experiment," *Journal of Aircraft*, Vol. 24, No. 6, 1987, pp. 362–370. https://doi.org/10.2514/3.45454.

[183] Jardin, M. R., and Mueller, E. R., "Optimized Measurements of Unmanned-Air-Vehicle Mass Moment of Inertia with a Bifilar Pendulum," *Journal of Aircraft*, Vol. 46, No. 3, 2009, pp. 763–775. https://doi.org/10.2514/1.34015.

[184] Previati, G., Gobbi, M., and Mastinu, G., "Method for the Measurement of the Inertia Properties of Bodies with Aerofoils," *Journal of Aircraft*, Vol. 49, No. 2, 2012, pp. 444–452. https://doi.org/10.2514/1.C031369.

[185] Lehmkühler, K., Wong, K., and Verstraete, D., "Methods for Accurate Measurements of Small Fixed Wing UAV Inertial Properties," *The Aeronautical Journal*, Vol. 120, No. 1233, 2016, pp. 1785–1811. https://doi.org/10.1017/aer.2016.105.

[186] Lorenzetti, J. S., Bañuelos, L., Clarke, R., Murillo, O. J., and Bowers, A., "Determining Products of Inertia for Small Scale UAVs," *55th AIAA Aerospace Sciences Meeting*, AIAA Paper 2017-0547, Jan. 2017. https://doi.org/10.2514/6.2017-0547.

[187] Dantsker, O. D., Vahora, M., Imtiaz, S., and Caccamo, M., "High Fidelity Moment of Inertia Testing of Unmanned Aircraft," *2018 Applied Aerodynamics Conference*, AIAA Paper 2018-4219, Jun. 2018. https://doi.org/10.2514/6.2018-4219.

[188] Grauer, J. A., and Morelli, E. A., "Dynamic Modeling Accuracy Dependence on Errors in Sensor Measurements, Mass Properties, and Aircraft Geometry," *51st AIAA Aerospace Sciences Meeting including the New Horizons Forum and Aerospace Exposition*, AIAA Paper 2013-0949, Jan. 2013. https://doi.org/10.2514/6.2013-949.

[189] Grauer, J. A., and Morelli, E. A., "Dependence of Dynamic Modeling Accuracy on Sensor Measurements, Mass Properties, and Aircraft Geometry," NASA TM–2013–218056, Nov. 2013.

[190] Yechout, T. R., Morris, S. L., Bossert, D. E., and Hallgren, W. F., *Introduction to Aircraft Flight Mechanics*, American Institute of Aeronautics and Astronautics, Reston, Virginia, 2003. https://doi.org/10.2514/4.102547.

[191] North, D. D., Busan, R. C., and Howland, G., "Design and Fabrication of the Langley Aerodrome No. 8 Distributed Electric Propulsion VTOL Testbed," *AIAA SciTech 2021 Forum*, AIAA Paper 2021-1188, Jan. 2021. https://doi.org/10.2514/6.2021-1188.

[192] McSwain, R. G., Geuther, S. C., Howland, G., Patterson, M. D., Whiteside, S. K., and North, D. D., "An Experimental Approach to a Rapid Propulsion and Aeronautics Concepts Testbed," NASA TM–2020-220437, Jan. 2020.

[193] Geuther, S. C., and Fei, X., "LA-8 Computational Analysis and Validation Studies Using FlightStream," *AIAA SciTech 2021 Forum*, AIAA Paper 2021-1191, Jan. 2021. https://doi.org/10.2514/6.2021-1191.

[194] Ahuja, V., and Hartfield, R. J., "Reduced-Order Aerodynamics with the Method of Integrated Circulation," *AIAA SciTech 2022 Forum*, AIAA Paper 2022-0005, Jan. 2022. https://doi.org/10.2514/6.2022-0005.

[195] Geuther, S. C., North, D. D., and Busan, R. C., "Investigation of a Tandem Tilt-Wing VTOL Aircraft in the NASA Langley 12-Foot Low-Speed Tunnel," NASA TM–2020–5003178, Jun. 2020.

[196] Stratton, M., and Landman, D., "Wind Tunnel Test and Empirical Modeling of Tilt-Rotor Performance for eVTOL Applications," *AIAA SciTech 2021 Forum*, AIAA Paper 2021-0834, Jan. 2021. https://doi.org/10.2514/6.2021-0834.

[197] Stratton, M. C., "Empirical Modeling of Tilt-Rotor Aerodynamic Performance," Master's thesis, Old Dominion University, 2021. https://doi.org/10.25777/mh0a-e343.

[198] Cook, J., and Gregory, I., "A Robust Uniform Control Approach for VTOL Aircraft," *VFS Autonomous VTOL Technical Meeting and Electric VTOL Symposium*, Jan. 2021.

[199] North, D. D., "Flight Testing of a Scale Urban Air Mobility Technology Testbed," *AIAA SciTech 2021 Forum*, AIAA Presentation, Jan. 2021. URL https://ntrs.nasa.gov/citations/20205010998, accessed April 2022.

[200] Borer, N. K., Patterson, M. D., Viken, J. K., Moore, M. D., Clarke, S., Redifer, M. E., Christie, R. J., Stoll, A. M., Dubois, A., Bevirt, J., Gibson, A. R., Foster, T. J., and Osterkamp, P. G., "Design and Performance of the NASA SCEPTOR Distributed Electric Propulsion Flight Demonstrator," *16th AIAA Aviation Technology, Integration, and Operations Conference*, AIAA Paper 2016-3920, Jun. 2016. https://doi.org/10.2514/6.2016-3920.

[201] Stoll, A. M., Bevirt, J., Moore, M. D., Fredericks, W. J., and Borer, N. K., "Drag Reduction Through Distributed Electric Propulsion," *14th AIAA Aviation Technology, Integration, and Operations Conference*, AIAA Paper 2014-2851, Jun. 2014. https://doi.org/10.2514/6.2014-2851.

[202] Holsten, J., Ostermann, T., and Moormann, D., "Design and Wind Tunnel Tests of a Tiltwing UAV," *CEAS Aeronautical Journal*, Vol. 2, No. 1, 2011, pp. 69–79. https://doi.org/10.1007/s13272-011-0026-4.

[203] Ostermann, T., Holsten, J., Dobrev, Y., and Moormann, D., "Control Concept of a Tiltwing UAV During Low Speed Manoeuvring," *28th International Congress of the Aeronautical Sciences*, ICAS Paper 2012-11.1.2, 2012.

[204] Small, E., Fresk, E., Andrikopoulos, G., and Nikolakopoulos, G., "Modelling and Control of a Tilt-Wing Unmanned Aerial Vehicle," *24th Mediterranean Conference on Control and Automation (MED)*, IEEE, Piscataway, NJ, Jun. 2016, pp. 1254–1259. https://doi.org/10.1109/MED.2016.7536050.

[205] Haviland, S. T., Bershadsky, D., and Johnson, E. N., "Dynamic Modeling and Analysis of a VTOL Freewing Concept," *AIAA Atmospheric Flight Mechanics Conference*, AIAA Paper 2016-1289, Jan. 2016. https://doi.org/10.2514/6.2016-1289.

[206] Hartmann, P., Meyer, C., and Moormann, D., "Unified Velocity Control and Flight State Transition of Unmanned Tilt-Wing Aircraft," *Journal of Guidance, Control, and Dynamics*, Vol. 40, No. 6, 2017, pp. 1348–1359. https://doi.org/10.2514/1.G002168.

[207] Cook, J. W., and Hauser, J., "A Strip Theory Approach to Dynamic Modeling of eVTOL Aircraft," *AIAA SciTech 2021 Forum*, AIAA Paper 2021-1720, Jan. 2021. https://doi.org/10.2514/6.2021-1720.

[208] Rohr, D., Stastny, T., Verling, S., and Siegwart, R., "Attitude and Cruise Control of a VTOL Tiltwing UAV," *IEEE Robotics and Automation Letters*, Vol. 4, No. 3, 2019, pp. 2683–2690. https://doi.org/10.1109/LRA.2019.2914340.

[209] Chauhan, S. S., and Martins, J. R. R. A., "Tilt-Wing eVTOL Takeoff Trajectory Optimization," *Journal of Aircraft*, Vol. 57, No. 1, 2020, pp. 93–112. https://doi.org/10.2514/1.C035476.

[210] Oner, K. T., Cetinsoy, E., Unel, M., Aksit, M. F., Kandemir, I., and Gulez, K., "Dynamic Model and Control of a New Quadrotor Unmanned Aerial Vehicle with Tilt-Wing Mechanism," *International Journal of Aerospace and Mechanical Engineering*, Vol. 2, No. 9, 2008, pp. 1008–1013.

[211] Muraoka, K., Okada, N., and Kubo, D., "Quad Tilt Wing VTOL UAV: Aerodynamic Characteristics and Prototype Flight," *AIAA Infotech@Aerospace Conference*, AIAA Paper 2009-1834, Apr. 2009. https://doi.org/10.2514/6.2009-1834.

[212] Öner, K. T., Çetinsoy, E., Sirimoğlu, E., Hançer, C., Ünel, M., Akşit, M. F., Gülez, K., and Kandemir, I., "Mathematical Modeling and Vertical Flight Control of a Tilt-Wing UAV," *Turkish Journal of Electrical Engineering & Computer Sciences*, Vol. 20, No. 1, 2012, pp. 149–157. https://doi.org/10.3906/elk-1007-624.

[213] Sato, M., and Muraoka, K., "Flight Test Verification of Flight Controller for Quad Tilt Wing Unmanned Aerial Vehicle," *AIAA Guidance, Navigation, and Control (GNC) Conference*, AIAA Paper 2013-5100, Aug. 2013. https://doi.org/10.2514/6.2013-5100.

[214] Masuda, K., and Uchiyama, K., "Flight Controller Design Using μ-synthesis for Quad Tilt-Wing UAV," *AIAA SciTech 2019 Forum*, AIAA Paper 2019-1918, Jan. 2019. https://doi.org/10.2514/6.2019-1918.

[215] May, M. S., Milz, D., and Looye, G., "Dynamic Modeling and Analysis of Tilt-Wing Electric Vertical Take-Off and Landing Vehicles," *AIAA SciTech 2022 Forum*, AIAA Paper 2022-0263, San Diego, CA & Virtual, Jan. 2022. https://doi.org/10.2514/6.2022-0263.

[216] Perdolt, D., Milz, D., May, M., and Thiele, M., "Efficient Mid-Fidelity Aerodynamic Modeling of a Tilt-Wing eVTOL for Control Applications," *33th Congress of the International Council of the Aeronautical Sciences*, ICAS Paper 2022-0860, Sep. 2022.

[217] May, M. S., Milz, D., and Looye, G., "Semi-Empirical Aerodynamic Modeling Approach for Tandem Tilt-Wing eVTOL Control Design Applications," *AIAA SciTech 2023 Forum*, AIAA Paper 2023-1529, Jan. 2023. https://doi.org/10.2514/6.2023-1529.

[218] Rothhaar, P. M., Murphy, P. C., Bacon, B. J., Gregory, I. M., Grauer, J. A., Busan, R. C., and Croom, M. A., "NASA Langley Distributed Propulsion VTOL Tilt-Wing Aircraft Testing, Modeling, Simulation, Control, and Flight Test Development," *14th AIAA Aviation Technology, Integration, and Operations Conference*, AIAA Paper 2014-2999, Jun. 2014. https://doi.org/10.2514/6.2014-2999.

[219] Busan, R. C., Rothhaar, P. M., Croom, M. A., Murphy, P. C., Grafton, S. B., and O'Neal, A. W., "Enabling Advanced Wind-Tunnel Research Methods Using the NASA Langley 12-Foot Low Speed Tunnel," *14th AIAA Aviation Technology, Integration, and Operations Conference*, AIAA Paper 2014-3000, Jun. 2014. https://doi.org/10.2514/6.2014-3000.

[220] Cooper, J. R., Ackerman, K. A., Rothhaar, P. M., and Gregory, I. M., "Autonomous Path-Following for a Tilt-Wing, Distributed Electric Propulsion, Vertical Take-Off and Landing Unmanned Aerial System in Hover Mode," NASA TM–2018–220109, Nov. 2018.

[221] McSwain, R. G., Glaab, L. J., and Theodore, C. R., "Greased Lightning (GL-10) Performance Flight Research – Flight Data Report," NASA TM–2017–219794, Nov. 2017.

[222] Fredericks, W. J., McSwain, R. G., Beaton, B. F., Klassman, D. W., and Theodore, C. R., "Greased Lightning (GL-10) Flight Testing Campaign," NASA TM–2017–219643, Jul. 2017.

[223] Morelli, E. A., and Klein, V., "Application of System Identification to Aircraft at NASA Langley Research Center," *Journal of Aircraft*, Vol. 42, No. 1, 2005, pp. 12–25. https://doi.org/10.2514/1.3648.

[224] Hamel, P. G., and Jategaonkar, R. V., "Evolution of Flight Vehicle System Identification," *Journal of Aircraft*, Vol. 33, No. 1, 1996, pp. 9–28. https://doi.org/10.2514/3.46898.

[225] Jategaonkar, R., Fischenberg, D., and von Gruenhagen, W., "Aerodynamic Modeling and System Identification from Flight Data-Recent Applications at DLR," *Journal of Aircraft*, Vol. 41, No. 4, 2004, pp. 681–691. https://doi.org/10.2514/1.3165.

[226] Iliff, K. W., "Parameter Estimation for Flight Vehicles," *Journal of Guidance, Control, and Dynamics*, Vol. 12, No. 5, 1989, pp. 609–622. https://doi.org/10.2514/3.20454.

[227] Owens, B., Brandon, J., Croom, M., Fremaux, M., Heim, G., and Vicroy, D., "Overview of Dynamic Test Techniques for Flight Dynamics Research at NASA LaRC," *25th AIAA Aerodynamic Measurement Technology and Ground Testing Conference*, AIAA Paper 2006-3146, Jun. 2006. https://doi.org/10.2514/6.2006-3146.

[228] Hamel, P. G., and Kaletka, J., "Advances in Rotorcraft System Identification," *Progress in Aerospace Sciences*, Vol. 33, No. 3-4, 1997, pp. 259–284. https://doi.org/10.1016/S0376-0421(96)00005-X.

[229] Altamirano, G. V., and McCrink, M. H., "Investigation of Longitudinal Aero-Propulsive Interactions of a Small Quadrotor Unmanned Aircraft System," *AIAA SciTech 2021 Forum*, AIAA Paper 2021-1310, Jan. 2021. https://doi.org/10.2514/6.2021-1310.

[230] "NASA Langley 12-Foot Low-Speed Tunnel," https://researchdirectorate.larc.nasa.gov/12-foot-low-speed-tunnel-12-ft-lst/, Accessed 12 January 2023.

[231] Montgomery, D. C., *Design And Analysis of Experiments*, 8th ed., John Wiley & Sons, Inc., Hoboken, NJ, 2013.

[232] Myers, R. H., Montgomery, D. C., and Anderson-Cook, C. M., *Response Surface Methodology: Process and Product Optimization Using Designed Experiments*, 4th ed., John Wiley & Sons, Hoboken, NJ, 2016.

[233] "Design-Expert®," Version 13, Stat-Ease, Inc., https://www.statease.com/software/design-expert/, Accessed 11 May 2022.

[234] Murphy, P. C., Hatke, D. B., Aubuchon, V. V., Weinstein, R., and Busan, R. C., "Preliminary Steps in Developing Rapid Aero Modeling Technology," *AIAA SciTech 2020 Forum*, AIAA Paper 2020-0764, Jan. 2020. https://doi.org/10.2514/6.2020-0764.

[235] Landman, D., Simpson, J., Mariani, R., Ortiz, F., and Britcher, C., "Hybrid Design for Aircraft Wind-Tunnel Testing Using Response Surface Methodologies," *Journal of Aircraft*, Vol. 44, No. 4, 2007, pp. 1214–1221. https://doi.org/10.2514/1.25914.

[236] DeLoach, R., "Assessment of Response Surface Models Using Independent Confirmation Point Analysis," *48th AIAA Aerospace Sciences Meeting Including the New Horizons Forum and Aerospace Exposition*, AIAA Paper 2010-741, Jan. 2010. https://doi.org/10.2514/6.2010-741.

[237] Murphy, P. C., and Brandon, J., "Efficient Testing Combining Design of Experiment and Learn-to-Fly Strategies," *AIAA Atmospheric Flight Mechanics Conference*, AIAA Paper 2017-0696, Jan. 2017. https://doi.org/10.2514/6.2017-0696.

[238] Foster, J. V., and Hartman, D., "High-Fidelity Multi-Rotor Unmanned Aircraft System (UAS) Simulation Development for Trajectory Prediction Under Off-Nominal Flight Dynamics," *17th AIAA Aviation Technology, Integration, and Operations Conference*, AIAA Paper 2017-3271, Jun. 2017. https://doi.org/10.2514/6.2017-3271.

[239] Goos, P., and Jones, B., *Optimal Design of Experiments*, John Wiley & Sons, West Sussex, England, U.K., 2011.

[240] Anderson, M. J., and Whitcomb, P. J., *RSM Simplified: Optimizing Processes Using Response Surface Methods for Design of Experiments*, 2nd ed., CRC Press, Boca Raton, FL, 2017. https://doi.org/10.1201/9781315382326.

[241] Anderson, M. J., and Whitcomb, P. J., *DOE Simplified: Practical Tools for Effective Experimentation*, 3rd ed., CRC Press, Boca Raton, FL, 2015. https://doi.org/10.1201/b18479.

[242] Montgomery, D. C., Peck, E. A., and Vining, G. G., *Introduction to Linear Regression Analysis*, 5th ed., John Wiley & Sons, Hoboken, NJ, 2012.

[243] "Stat-Ease Handbook for Experimenters," Version 13.00, Stat-Ease, Inc., Minneapolis, MN, Dec. 2020.

[244] Zahran, A., Anderson-Cook, C. M., and Myers, R. H., "Fraction of Design Space to Assess Prediction Capability of Response Surface Designs," *Journal of Quality Technology*, Vol. 35, No. 4, 2003, pp. 377–386. https://doi.org/10.1080/00224065.2003.11980235.

[245] Anderson, M. J., Adams, W. F., and Whitcomb, P. J., "How to Properly Size Response Surface Method Experiment (RSM) Designs for System Optimization," 2016. https://cdn.statease.com/media/public/documents/how_to_properly_size_experiments_aimed_at_system_optimization.pdf, Accessed 17 October 2022.

[246] Whitcomb, P., "FDS—A Power Tool for Designers of Optimization Experiments," *Stat-Teaser Newsletter*, Stat-Ease, Inc., Sep. 2008, pp. 1–3. https://cdn.statease.com/media/public/documents/statteaser-0908.pdf, Accessed 17 October 2022.

[247] Favaregh, N., and Landman, D., "Global Modeling of Pitch Damping from Flight Data," *AIAA Atmospheric Flight Mechanics Conference and Exhibit*, AIAA Paper 2006-6145, Aug. 2006. https://doi.org/10.2514/6.2006-6145.

[248] Omran, A., Newman, B., and Landman, D., "Global Aircraft Aero-Propulsive Linear Parameter-Varying Model Using Design of Experiments," *Aerospace Science and Technology*, Vol. 22, No. 1, 2012, pp. 31–44. https://doi.org/10.1016/j.ast.2011.05.008.

[249] Heim, E. H., Viken, E., Brandon, J. M., and Croom, M. A., "NASA's Learn-to-Fly Project Overview," *2018 Atmospheric Flight Mechanics Conference*, AIAA Paper 2018-3307, Jun. 2018. https://doi.org/10.2514/6.2018-3307.

[250] Riddick, S. E., "An Overview of NASA's Learn-to-Fly Technology Development," *AIAA SciTech 2020 Forum*, AIAA Paper 2020-0760, Jan. 2020. https://doi.org/10.2514/6.2020-0760.

[251] Morelli, E. A., and Smith, M. S., "Real-Time Dynamic Modeling: Data Information Requirements and Flight-Test Results," *Journal of Aircraft*, Vol. 46, No. 6, 2009, pp. 1894–1905. https://doi.org/10.2514/1.40764.

[252] Grauer, J., and Boucher, M., "Identification of Aeroelastic Models for the X-56A Longitudinal Dynamics Using Multisine Inputs and Output Error in the Frequency Domain," *Aerospace*, Vol. 6, No. 2, 2019, p. 24. https://doi.org/10.3390/aerospace6020024.

[253] Grauer, J. A., and Boucher, M., "System Identification of Flexible Aircraft: Lessons Learned from the X-56A Phase 1 Flight Tests," *AIAA SciTech 2020 Forum*, AIAA Paper 2020-1017, Jan. 2020. https://doi.org/10.2514/6.2020-1017.

[254] Morelli, E. A., and DeLoach, R., "Response Surface Modeling using Multivariate Orthogonal Functions," *39th AIAA Aerospace Sciences Meeting and Exhibit*, AIAA Paper 2001-0168, Jan. 2001. https://doi.org/10.2514/6.2001-168.

[255] Morelli, E. A., and DeLoach, R., "Wind Tunnel Database Development Using Modern Experiment Design and Multivariate Orthogonal Functions," *41st Aerospace Sciences Meeting and Exhibit*, AIAA Paper 2003-653, Jan. 2003. https://doi.org/10.2514/6.2003-653.

[256] Grauer, J. A., and Boucher, M. J., "Aircraft System Identification from Multisine Inputs and Frequency Responses," *Journal of Guidance, Control, and Dynamics*, Vol. 43, No. 12, 2020, pp. 2391–2398. https://doi.org/10.2514/1.G005131.

[257] Grauer, J. A., and Boucher, M. J., "Real-Time Estimation of Bare-Airframe Frequency Responses from Closed-Loop Data and Multisine Inputs," *Journal of Guidance, Control, and Dynamics*, Vol. 43, No. 2, 2020, pp. 288–298. https://doi.org/10.2514/1.G004574.

[258] Niemiec, R., Gandhi, F., Lopez, M. J. S., and Tischler, M. B., "System Identification and Handling Qualities Predictions of an eVTOL Urban Air Mobility Aircraft Using Modern Flight Control Methods," *Vertical Flight Society's 76th Annual Forum & Technology Display*, Oct. 2020.

[259] Gregory, I. M., Acheson, M. J., Bacon, B. J., Britton, T. C., Campbell, N. H., Cook, J. W., Holbrook, J. B., Moerder, D. D., Murphy, P. C., Neogi, N. A., Simmons, B. M., McMinn, J. D., and Buning, P. G., "Intelligent Contingency Management for Urban Air Mobility," *AIAA SciTech 2021 Forum*, AIAA Paper 2021-1000, Jan. 2021. https://doi.org/10.2514/6.2021-1000.

[260] Acheson, M. J., Cook, J., and Gregory, I., "Examination of Unified Control Approaches Incorporating Generalized Control Allocation," *AIAA SciTech 2021 Forum*, AIAA Paper 2021-0999, Jan. 2021. https://doi.org/10.2514/6.2021-0999.

[261] Weiss, S., Friehmelt, H., Plaetschke, E., and Rohlf, D., "X-31A System Identification Using Single-Surface Excitation at High Angles of Attack," *Journal of Aircraft*, Vol. 33, No. 3, 1996, pp. 485–490. https://doi.org/10.2514/3.46970.